

3D Characterisation of microcracks in concrete

A thesis submitted in fulfilment of the requirements for the degree of Doctor of Philosophy
and Diploma of Imperial College London

by

Monika Jolanta Mac

Concrete Durability Group
Department of Civil and Environmental Engineering
Imperial College London

December 2018

Declaration

I hereby declare that this thesis, submitted for the degree of Doctor of Philosophy and Diploma of Imperial College London is the result of my own work, and that all else is appropriately referenced.

The copyright of this thesis rests with the author and is made available under a Creative Commons Attribution Non-Commercial No Derivatives licence. Researchers are free to copy, distribute or transmit the thesis on the condition that they attribute it, that they do not use it for commercial purposes and that they do not alter, transform or build upon it. For any reuse or redistribution, researchers must make clear to others the licence terms of this work.

Signature:

Date: December, 2018

Abstract

The nature of microcracks that developed in concrete is not well understood. One reason for this is the lack of suitable techniques to detect and characterise the microcracks. Conventional methods include imaging polished cross sections with scanning electron microscopy and optical microscopy. However, these techniques only provide a two-dimensional representation of a three-dimensional structure, which significantly reduces the insights from such analysis. Another reason is that the development of microcracks may be associated with various complex forms of concrete deterioration during service life, e.g. due to mechanical loading, drying, thermal effects and chemical reactions. This complicates laboratory scale experiments and inducing “realistic” microcracks in concrete samples becomes very difficult.

The aim of this study is to develop new techniques for three-dimensional quantitative characterisation of microcracks and to apply these to understand the properties of microcracks in concrete. A thorough literature review was conducted to identify the causes of microcracking in concrete, mechanisms of microcrack initiation and propagation, transport properties of micro-cracked concrete and methods to characterise microcracks in two dimensions (2D) and three dimensions (3D). Materials and experimental procedures for inducing different types of microcracks, sample preparation for imaging and image analysis of microcracks are discussed. The feasibility of three-dimensional techniques such as focused ion beam nanotomography (FIB-nt), broad ion beam combines with serial sectioning (BIB), X-ray microtomography (μ -CT) and laser scanning confocal microscopy (LSCM) for imaging microcracks were investigated. A new approach that combines LSCM with serial sectioning was proposed to enhance the capability of LSCM for imaging microcracks in 3D.

A major focus of this thesis was dedicated to microcracks induced by autogenous shrinkage because this has been previously neglected due to the dominant role of drying shrinkage. Nonetheless, the increasing use of high strength concretes containing low water/binder ratio, complex binder systems and multiple chemical admixtures in recent years has highlighted the problem of autogenous shrinkage in these concretes. This study presents a first attempt on direct characterisation and understanding of the microcracks caused by autogenous shrinkage in 3D. Various concrete samples were produced and sealed cured to induce autogenous shrinkage. The water/binder ratio, cement type and content, and aggregate particle size distribution were varied to vary the magnitude of autogenous shrinkage and degree of microcracking. Linear deformation measurement was performed to correlate autogenous shrinkage with degree of microcracking. Samples were imaged in 2D using laser scanning confocal microscope (LSCM) and in 3D with X-ray microtomography (μ -CT). Subsequently, 2D and 3D image analysis was employed to quantify microcracks $> 1 \mu\text{m}$ in width.

A major challenge was to isolate the microcracks that are inherently connected to pores and air voids. Therefore, an algorithm was developed to separate microcracks from pores, and to extract quantitative data such as crack density, orientation degree, distribution of width and length, as well as connectivity and tortuosity. The results show that use of supplementary cementitious materials and low water/binder ratio can increase linear deformation and the amount of the microcracks. The thesis discusses the effect of autogenous shrinkage on the characteristics of the induced microcracking, which is critical to understanding the transport properties and long-term durability of concretes containing supplementary cementitious materials.

Keywords: microcracking, 3D imaging techniques, image analysis, autogenous shrinkage

Acknowledgements

First of all, I would like to thank the TRANSCEND recruiting committee led by Professor Karen Scrivener, for having offered me the opportunity to pursue my PhD in such a unique collaborative environment within the TRANSCEND Marie Curie Initial Training Network programme. I would like to acknowledge the European Commission since the research leading to these results has received funding from the European Union Seventh Framework Programme (FP7 / 2007-2013) under grant agreement 264448.

I would also like to thank my supervisors, Dr Hong Wong and Professor Nick Buenfeld for their guidance and support throughout the study and at the same time for allowing me to do my research with freedom. Professor Karen Scrivener and Dr Hong Wong deserve a special mention for believing in me. This work would not have been completed without their encouragement and help.

Throughout the programme, I had invaluable opportunities to undertake secondments at several leading research institutions. I was initially hosted by the Centre for Research in Nano-Engineering at Polytechnic University of Catalonia – Barcelona TECH. I undertook secondments at Sika Schweiz AG in Zurich and ZAG, the Slovenian National Building and Civil Engineering Institute in Ljubljana and visited the Institute of Structural Geology, Tectonics and Geomechanics at RWTH Aachen University. At all of these places, I have been surrounded by many great people, to whom I would like to express my greatest gratitude. This applies especially to Professor Ignasi Cassanova, Professor Patricia Pardo and Dr Trifon Trifonov from UPC, Dr Emmanuel Gallucci and Dr Arndt Eberhard from Sika, Professor Andraž Legat and Dr Lidija Korat from ZAG, and Dr Guillaume Desbois and his students from RWTH. I thank all of them for their co-supervision, collaboration and all the ideas and suggestions to improve my experiments during the first years of my PhD. My thanks are also extended to the National History Museum in London for providing me access to their 3D CT-scanner, and to the Facility for Imaging by Light Microscopy at Imperial College London for the access to their two-photon microscope.

I appreciate all the assistance provided by the staff in the Department of Civil and Environmental Engineering at Imperial College: International Office, Central Library and Student Hub, but mostly, the help and engagement with our lab technician, Mr Andrew Morris.

I am deeply grateful to my TRANSCEND colleagues: Agata, Arnaud, Elena, Luis, Merlin, Noemi, Vadim, Serge-Henri, Mohamed, Wu-Min, Saeed, Mahsa, Zhidong, Xiaomeng and Pierre-Vincent and all Nanocem members. I thank you all for the shared moments during our training courses, meetings and discussions. Above all, thank you for the time we spent out of working hours, chatting, dinners, road trips, sightseeing and travelling. I also thank my office mates, colleagues and friends: Vanessa, Aneta, Agustin, Francesca, Elena, Nuria, Raul and Christian (Barcelona), Camille (Zurich), Lidija and Alenka (Ljubljana), Marcus, Ima, Fadhilah, Sukina, Zhigen, Saeed, Han, Libin and Alfredo (London), for their great company and invaluable support! Thanks for the lab help and technical discussions, for all the lunches, coffee-/ tea-breaks and dinners, and especially for the motivation to keep going. Thanks are also due to my friends that I left behind in Poland for their support and friendship.

And finally, I would like to thank my son Wojtek, my parents and sister and everyone in my family for being so supportive, understanding and loving during this long journey. This work is dedicated to you.

Notation

Abbreviations:

2D	two dimensions
3D	three dimensions
ASR	alkali – silica reaction
AU	Airy Unit
av	air voids
BIB	broad ion beam
DSLR	digital single-lens reflex
FIB-nt	focused ion beam nanotomography
FOV	field of view
FT	Freeze -thaw
GGBS	ground granulated blast furnace slag
HPC	high-performance concrete
LICM	line intercept count method
LSCM	laser scanning confocal microscope
MG	morphological gradient
MSA	maximum size of aggregates
OM	optical microscope
OPC	ordinary Portland cement
PSF	point-spread function
PMT	photomultiplier tube
REV	representative elementary volume
RH	relative humidity
SC	sealed curing
SCMs	supplementary cementitious materials
SEM	scanning electron microscope
SF	silica fume
SLR	single-lens reflex
SSD	surface dry condition
UHPC	ultra-high-performance concrete
UV	ultraviolet light
VFA	voxel face area
XRF	X-ray fluorescence
μ-CT	X-ray micro-computed tomography

Roman letters:

A_A	area fraction
A_{crack}	total area of the microcracks
A_{image}	area of the image
$A_{\text{ind. crack}}$	area of an individual microcrack
AR	aspect ratio
C_1	connectivity of the largest microcrack
C_{10}	connectivity of the 10 largest microcrack
C_2S	dicalcium silicate
C_3A	tricalcium aluminate
C_3S	tricalcium silicate
C_4AF	tetracalcium aluminoferrite
$C_{\text{ind.}}$	connectivity of individual microcrack
DA	degree of anisotropy
D_{CN}	density of connections
D_D	crack dendritic density
D_N	numerical density
E	elongation
L	crack length
l	the length of the centroid path curve
L_0	initial length reading
L_{distance}	Euclidean distance of skeletonised microcracks
L_{mean}	mean length
L_n	subsequent length readings
L_{total}	total crack length
n_1	refractive index of immersion oil
NA	numerical aperture
N_{crack}	total number of crack
P	pinhole aperture size
SA	surface area
SD	surface density
Shape AP	parameter describing circularity of particle
SSA	specific surface area
V_{image}	image volume
$V_{\text{ind. crack}}$	volume of an individual microcrack
V_v	volume fraction
W	crack widths
W_{mean}	mean width

Greek letters:

ε	linear deformation (μ strain)
\bar{L}	spacing factor
\emptyset	diameter
\emptyset_{eq}	equivalent spherical diameter
λ	excitation wavelength
τ_{CP}	centroid path tortuosity
τ_{g}	geometric tortuosity
Ψ	sphericity
\oplus	dilation
\ominus	erosion
\bullet	closing

Contents

Declaration	2
Abstract.....	3
Acknowledgements	4
Notation	5
Contents.....	8
List of tables	12
List of figures.....	14
Chapter 1.....	25
<i>Introduction</i>	25
1.1 Research motivation	25
1.2 Objectives and scope	26
1.3 Thesis outline.....	27
Chapter 2.....	28
<i>Literature review</i>	28
2.1 Types and mechanisms of microcracking.....	28
2.2 Autogenous shrinkage microcracking.....	32
2.2.1 Autogenous shrinkage.....	32
2.2.2 Measurements of autogenous deformation	33
2.3 Methods for characterising microcracks	34
2.3.1 Optical microscopy	34
2.3.2 Laser scanning confocal microscopy	35
2.3.3 Scanning electron microscopy	35
2.3.4 Focused ion beam and broad ion beam with scanning electron microscopy	36
2.3.5 X-ray microtomography	37
2.4 Influence of microcracks on the bulk transport properties of concrete	38
2.5 Numerical modelling based on image analysis of microcracks	38
Chapter 3.....	40
<i>Methodology</i>	40
3.1 Materials, sample preparation and conditioning.....	40
3.1.1 Materials	40
3.1.2 Mix proportions	42
3.1.3 Mixing, casting and conditioning	43
3.2 Linear deformation measurement	45
3.3 2D and 3D microscopy techniques	46
3.3.1 Sample preparation for imaging.....	46

3.3.2 Imaging with LSCM	49
3.3.3 Imaging with X-ray microtomography	50
3.4 Image analysis	51
3.4.1 2D image analysis	52
3.4.2 3D image analysis	55
3.5 Summary	55
Chapter 4	57
<i>Assessment of 3D microscopy techniques for imaging microcracks</i>	57
4.1 Background	57
4.2 Strategies to generate microcracks	58
4.2.1. Materials, mix proportion and samples	59
4.2.2 Conditioning	60
4.2.3 Observation of microcracks	64
4.3 Focused ion beam nanotomography (FIB-nt)	68
4.3.1 Samples	68
4.3.2 Imaging procedure	68
4.3.3 Results	69
4.4 Broad ion beam (BIB) serial sectioning combined with SEM imaging	71
4.4.1 Samples	71
4.4.2 Imaging procedure	71
4.4.3 Results	72
4.5 Laser scanning confocal microscopy (LSCM)	74
4.5.1 Samples	74
4.5.2 Imaging procedure	74
4.5.3 Results	76
4.6 X-ray microtomography	77
4.6.1 Samples	77
4.6.2 Imaging procedure	78
4.6.3 Results	79
4.7 Comparison of imaging techniques for microcrack detection	79
4.8 Summary	81
Chapter 5	85
<i>Extending imaging depth of LSCM with serial sectioning</i>	85
5.1 Background	85
5.2 Principles of LSCM	86
5.3 Trials to increase imaging depth in conventional imaging	87
5.3.1 Fluorophore concentration	87
5.3.2 Theoretical Z resolution	88

5.3.3 Light compensation	89
5.3.4 Image processing methods.....	89
5.3.5 Two-photon microscopy.....	90
5.3.6 Transparent aggregates	91
5.4 Proposed method	92
5.4.1 Extending imaging depth (in Z direction) of LSCM.....	92
5.4.2 Extending imaging volume in XY plane.....	95
5.5 Application of the proposed method for imaging microcracks.....	97
5.5.1 Sample preparation	97
5.5.2 Imaging.....	97
5.5.3 Serial sectioning.....	98
5.5.4 Reconstructed image volume – single FOV	98
5.5.5 Reconstructed image volume – mosaic 2×2	100
5.6 Summary.....	101
Chapter 6.....	103
<i>Three-dimensional image analysis of microcracks.....</i>	<i>103</i>
6.1 Background.....	103
6.2 Image pre-processing and segmentation	104
6.2.1 Raw data	104
6.2.2 Cropping-out.....	105
6.2.3 Median filter	105
6.2.4 Segmentation	106
6.3 Separation algorithm.....	109
6.3.1 Separation of pores in coarse aggregates	109
6.3.2 Separation of air voids	114
6.3.3 Separation of microcracks	117
6.4 Quantitative measurement	118
6.4.1 Microcrack characteristics	120
6.4.2 Air voids characteristics.....	124
6.5 Results from image analyses.....	127
6.5.1 Comparison of microcrack characteristics from 3D and 2D image analysis	127
6.5.2 Comparison of air voids characteristics from 3D and 2D image analysis	132
6.6 Representative sample volume	135
6.7 Conclusion.....	140
Chapter 7.....	142
<i>Influence of various parameters on autogenous shrinkage-induced microcracking in concrete.....</i>	<i>142</i>
7.1 Background.....	142
7.2 Samples for shrinkage measurement and 2D microcrack analysis	143

7.3 Autogenous shrinkage	144
7.4 Two-dimensional characterisation of microcracks	146
7.4.1 Area fraction	148
7.4.2 Surface area	150
7.4.3 Width	151
7.4.4 Length	153
7.4.5 Density	154
7.4.6 Degree of anisotropy	155
7.5 Summary	156
Chapter 8	159
<i>3D characterisation of autogenous shrinkage-induced microcracks</i>	159
8.1 Background	159
8.2 Samples for analysis of microcracks in 3D	160
8.3 Three-dimensional characterisation of microcracks	161
8.3.1 Volume fraction	161
8.3.2 Surface area	164
8.3.3 Width	165
8.3.4 Length	170
8.3.5 Density	171
8.3.6 Degree of anisotropy	173
8.3.7 Connectivity	174
8.3.8 Tortuosity	175
8.4 Statistical approach	177
8.5 Comparison between 2D image analysis (LSCM and μ -CT) and 3D image analysis (μ -CT)	178
8.6 Summary	180
Chapter 9	182
9.1 Conclusions	182
9.2 Recommendations for further research	186
References	187
Appendices	196
APPENDIX I: Microcrack width - cumulative distribution curves (Chapter 7)	196
APPENDIX II: Microcrack length - cumulative distribution curves (Chapter 7)	199
APPENDIX III: 2D orientation of microcracks induced by autogenous shrinkage (Chapter 7)	202
APPENDIX IV: 3D orientation of microcracks induced by autogenous shrinkage (Chapter 8)	208
APPENDIX V: Publications arising from this research	212

List of tables

Table 3-1 Oxide composition of cementitious materials.....	40
Table 3-2 Loss on ignition, specific gravity and fineness of cementitious materials.....	40
Table 3-3 Specific gravity, moisture content and absorption values for fine and coarse aggregates.....	41
Table 3-4 Mix proportions.....	42
Table 4-1 Samples, materials and exposure conditions.....	59
Table 4-2 Mix proportions.....	60
Table 4-3 FOV and resolution for each objective lens.....	75
Table 5-1 Summary of reconstruction results.....	98
Table 6-1 List of measured parameters of microcracks in sample C/SF-14/SC. Note: *Voxel face area, **Iso-surface, ***LICM, •Local thickness, ••Rod model thickness, †Connectivity of the largest microcrack (C_1) and connectivity if the 10 largest microcracks (C_{10}).	128
Table 6-2 List of measured parameters of air voids in sample (C/SF-14/SC) from 3D and 2D analysis. Note: *Voxel face area, **Iso-surface, ***LICM.....	132
Table 7-1 Samples for linear shrinkage deformation measurements and 2D analysis of microcracks imaged with LSCM.....	143
Table 7-2 Specific surface area and surface density of microcracks. Note: * the same sample are listed several times to facilitate comparison between different groups of samples.....	150
Table 7-3 Average microcrack widths in μm with standard errors in brackets. Note: * same sample listed to facilitate comparison between different groups of samples.....	152
Table 7-4 Average microcrack lengths in mm with standard errors in brackets.....	153
Table 7-5 Degree of anisotropy of microcracks induced by autogenous shrinkage.....	156
Table 7-6 Overall trends of the measured parameters indicated by colour codes. AS – autogenous shrinkage, A_A – area fraction of microcracks, W – crack width, SSA – specific surface area, SD – surface density, $D_D =$	




dendritic density, L – crack length, DA – degree of anisotropy. Colour code:  increase,  decrease,  no change..... 157




Table 8-1 Samples for 3D analysis of microcracks with X-ray microtomography. * - the same mix, replicates. 160

Table 8-2 Average microcrack widths in μm with standard errors. (* - refers to relevant replicas)..... 167

Table 8-3 Average and total microcrack lengths in mm with standard errors. (* - refers to relevant replicas).170

Table 8-4 Characteristics of microcracks in three replicate samples (binder, w/b ratio and age replicas) and averages with standard deviations of the measured parameters..... 177

Table 8-5 Comparison of microcrack analysis using different methods: 3D ($\mu\text{-CT}$), 2D ($\mu\text{-CT}$) and 2D (LSCM) of three selected samples (0.30C-10/68-14, 0.30SF-10/68-14* - binder replica and 0.30S-10/68-14)..... 178

Table 8-6 Overall trends of the measured parameters indicated by colour codes. V_V – volume fraction, W – crack width, SSA – specific surface area, SD – surface density, D_D = dendritic density, L – crack length, DA – degree of anisotropy, C – connectivity, D_{CN} – density of connection, τ_g – geometric tortuosity, τ_{CP} – centroid path tortuosity. Colour code:  increase,  decrease,  no change. 181

List of figures

Figure 2-1 Common causes of cracking in concrete structures (Meyer, et al., 2006).....	28
Figure 2-2 Matrix (a) and bond (b) crack opening mechanism (Maruyama and Sasano, 2014).....	29
Figure 2-3 Typical microcrack pattern observed in concrete subjected to oven drying (Wong et al., 2009).....	30
Figure 2-4 Examples of crack pattern on the drying surface of cement paste (different drying regimes). Image size is 3×3 cm (Bisschop & Wittel, 2011).....	30
Figure 2-5 Methods to measure autogenous shrinkage (Hu et al, 2013).....	33
Figure 2-6 Principles of ion beam cross-sectioning methods with typical cross sections performed by BIB (a) and FIB (b) on a clay sample Desbois et al., 2010).....	36
Figure 2-7 Image acquisition with X-ray microtomography.....	37
Figure 3-1 Grading curves for fine and coarse aggregates.....	41
Figure 3-2 Sample designation.....	43
Figure 3-3 Geometry of the stud, end cap and postal tube used to prepare concrete cylinders for linear deformation measurement.....	44
Figure 3-4 Examples of mass change of sealed cured concrete cylindrical specimens.....	45
Figure 3-5 Linear deformation measurement using length comparator: a) calibration with invar bar, b) length measurement of cylindrical concrete specimen, and c) a photo of laboratory set up.....	46
Figure 3-6 Sample preparation for imaging using LSCM.....	47
Figure 3-7 Illustration of the impregnation procedure: a) impregnation under vacuum, b) application of additional pressure to push the resin farther into the sample.....	48
Figure 3-8 Preparation of epoxy impregnated flat polished concrete sections for microscopy. The images were obtained after: a) cutting and freeze drying, b) vacuum impregnation and c) grinding and polishing.....	48
Figure 3-9 Example of consecutive fluorescence images captured by LSCM at 10% edge overlap.....	50
Figure 3-10 An example of concrete core scanned by X-ray microtomography. The orthogonal views in XY, XZ and YZ directions with 3D rendering.....	51
Figure 3-11 Flow chart showing the main steps of image pre-processing.....	52

Figure 3-12 Image processing: A) raw data, B) grey scale LUT & invert & median filter 0.5, C) ALT Sauvola 20, D) manual tracing, E) traced microcracks, F) subtraction: (E)-(C), G) application of circularity factor (Shape AP: noise $\leq 1.5 >$ microcracks), H) accurate microcracks, I) closing 3 pixels' disc & fill holes & despeckle, J) local thickness measurement, K) dilating 10 pixels' disc & fill holes, L) skeletonisation.	53
Figure 3-13 Summary of overall experimental program.....	56
Figure 4-1 Geometry of cement paste samples.	61
Figure 4-2 Linear deformation of cement paste prisms: (a) CP/C-7, (b) CP/S-7 and (c) CP/SF-7 exposed to conditioning regime at five different RH: 35%, 50%, 65%, 80% and 100%.....	62
Figure 4-3 Ring test – mortar samples.	63
Figure 4-4 Strain development in mortar samples (M/C-1/50, M/S-1/50, M/SF-1/50) exposed to drying in the restrained ring test.	63
Figure 4-5 Linear deformation of sealed-cured concrete sample (C/SF-14/SC).....	64
Figure 4-6 Mass loss of concrete sample subjected to 84 cycles of freeze-thaw (C/C-14/84FT).....	64
Figure 4-7 Top and side view of cement paste (CP/C-7/30 and CP/C-7/105) and side view of mortar (M/C-7/30 and M/C-7/105) samples impregnated with resin after drying at 30°C and 105°C.....	65
Figure 4-8 Cracking of restrained cement paste rings after drying at a) 35%, b) 50%, c) 65% and d) 80% RH. 66	66
Figure 4-9 Microcrack pattern of concrete sample (C/SF-14/SC) subjected to autogenous shrinkage.....	67
Figure 4-10 Concrete samples impregnated with fluorescent resin after 42, 56 and 70 freeze-thaw cycles (C/FT/42, C/FT/56 and C/FT/70).	67
Figure 4-11 Zeiss Neon 40 FIB-SEM workstation at UPC – CRnE, Barcelona, Spain.	68
Figure 4-12 Sample positioning and cube preparation for FIB-nt.	68
Figure 4-13 Original and aligned images. Alignment according to the reference lines on the top of the sectioned cube.	69
Figure 4-14 Raw and wavelet-FFT filtered image of cement paste (CP/C-7/30) captured by FIB-nt.	69
Figure 4-15 Orthogonal views and 3D rendering of cement paste (CP/C-7/30) acquired using FIB-nt showing bond microcracks around unreacted cement grain.....	70
Figure 4-16 Orthogonal views and 3D rendering of mortar (M/C-7/30) acquired using FIB-nt showing matrix and bond cracks.	70

Figure 4-17 JEOL SM-09010 Ar-BIB cross-section polisher at RWTH Aachen University, Germany.	71
Figure 4-18 Schematic of Ar-BIB cross-sectioning.....	71
Figure 4-19 Five successively polished cross sections (left row), stitched BSE image (middle row) and SE image (right row) of M/C-7/30. Images collected at 500×, 1000× and 14000× magnification respectively.	72
Figure 4-20 Orthogonal views and 3D rendering of mortar (M/C-7/30) obtained from BIB serial sectioning combined with SEM-BSE imaging. XZ and YZ planes show very poor resolution of the technique.	73
Figure 4-21 Orthogonal views and 3D rendering of mortar (M/C-7/30) obtained from BIB serial sectioning combined with SEM-SE imaging. XZ and YZ planes show very poor resolution of the technique.	73
Figure 4-22 Leica TCS SP5 laser scanning confocal microscope at Civil and Environmental Engineering Department, Imperial College.	74
Figure 4-23 Confocal microscopy	74
Figure 4-24 2D confocal images of concrete after 84 cycles of freeze-thaw (C/C-14/56FT) captured using the 5×, 20×, 40× and 63× objective lens.....	75
Figure 4-25 Confocal image stack of a concrete (C/C-14/56FT) collected up to an imaging depth of 18 μm (20× objective lens, FOV 0.75×0.75 mm).	76
Figure 4-26 Orthogonal views and 3D rendering of concrete (C/C-14/56FT) obtained from LSCM with 40× objective lens. XZ and YZ planes show loss of signal with depth.	76
Figure 4-27 Metris X-Tek HMX ST 225 CT scanner in the Natural History Museum, London.	77
Figure 4-28 Principles of the X-ray microtomography.....	77
Figure 4-29 MicroXCT-400 Xradia CT scanner in ZAG, Ljubljana, Slovenia.	77
Figure 4-30 2D reconstructed slices of concrete (C/C-7/105 and C/SF-14/SC) from X-ray microtomography and scan settings. Images (a) to (c) obtained with X-Radia 400 CT scanner and image (d) with Metris X-Tek HMX ST 225.	78
Figure 4-31 3D rendering of concrete cores of a) Ø4 mm, b) Ø9 mm and c) Ø30 mm (C/C-4/105) imaged with X-Radia 400 CT scanner and d) Ø30mm (C/SF-14/SC) imaged with Metris X-Tek HMX ST 225 CT scanner with corresponding 2D slices showing example microcracks.	79
Figure 4-32 Area-matching micrographs obtained using four different imaging techniques. The sample is mortar M/C-7/105.....	80
Figure 4-33 Microcrack density and areal fraction as measured by four imaging techniques.	81

Figure 4-34 Microcrack width distribution and average crack width as measured by four imaging techniques.	81
Figure 4-35 Schematic presentation of microcracking caused by different mechanisms.	82
Figure 4-36 Overview of the 3D imaging methods examined showing the achievable image thickness and resolution in the Z direction.	83
Figure 5-1 a) Emission profile of EpoDye; b) Plot showing fluorescence intensity versus concentration of Struers EpoDye (excited by a 488 nm laser at intensities of 1%, 4% and 15%) (Yio et al., 2015).	88
Figure 5-2 Influence of pinhole size on the Z resolutions of a) 5× and b) 20×, 40× and 60× objective lenses.	88
Figure 5-3 Comparison between raw and processed images using light compensation by photomultiplier tube (PMT) or laser intensity. Images are of hardened cement paste.	89
Figure 5-4 Comparison between raw and processed images using histogram matching and deconvolution.	90
Figure 5-5 Comparison between a) confocal; and b) two-photon microscopy images acquired using a 63× water and 63× oil immersion objective lens with 488 nm and 930 nm laser, respectively.	91
Figure 5-6 Orthogonal view and 3D rendering of cement paste with glass ‘aggregates’ acquired by LSCM with 5× objective lens. XZ and YZ planes show loss of signal with depth underneath glass ‘aggregates’.	91
Figure 5-7 Intensity profile of images from a single z-stack showing signal degradation with increase in depth below sample surface. Well-focused images are selected for subsequent stitching.	93
Figure 5-8 Schematic diagram of the stitching process. Selected images from each z-stack are aligned a), stitched in pairs b), and then progressively combined (i.e. [1+2] + [2+3] + [3+4] + [4+5] + [...]) by stitching the overlapping regions c) to reconstruct an image volume d), (Yio, et al. 2015).	94
Figure 5-9 Demonstration of the stitching process on an air void filled with resin: a) selected images from two serial section z-stacks, b) alignment of the image stacks, c) close-up of the stitching outcome between z-stack number 1 and 2, and d) stitching of the overlapping regions.	94
Figure 5-10 Stitching 2 × 2 mosaic: a) A, B, C and D image tiles of a mosaic, b) stitched image tiles with overlapping region, c) reconstructed large image ABCD-mosaic.	96
Figure 5-11 Schematic diagram of the stitching process: a) imaged z-stack tiles of a mosaic ‘snake by rows’, b) stitched z-stack tiles with overlapping region of ~20%, and c) reconstructed thin image volume, used as a single z-stack for stitching in Z direction.	96
Figure 5-12 Plot of axial shift and correlation coefficient as a function of cumulative image thickness, (Yio, et al., 2015).	99

Figure 5-13 Plot showing R versus ΔZ for all samples, (Yio, et al., 2015)	99
Figure 5- 14 Orthogonal views of reconstructed image of concrete (C/C-14/56FT) with 3D rendering.	99
Figure 5- 15 Orthogonal views of the image volume reconstructed from the mosaic 2×2 . Total area in XY is $700 \times 700 \mu\text{m}^2$	100
Figure 5-16 Correction of uneven brightness in the XY plane of a large LSCM image: a) raw image b) flat field image generated by mean filtering of a) with a kernel size of 350 pixels, and c) corrected image. This image was captured with 20 \times objective lens as a 3×3 mosaic, with a stitched area of $2.43 \times 2.43 \text{ mm}^2$	101
Figure 6-1 Examples of morphological operations: a) original image, b) dilation, c) erosion, d) opening, e) closing, f) holes filling.	104
Figure 6-2 Cropping out: I) raw image 2011×2011 pixels with selected area for cropping; II) cropped image of 1320×1320 pixels; III) 3D median filter of radius 1 applied to reduce noise.	105
Figure 6-3 Demonstration of noise reduction using median filter with different radii: a) original image; b) filtered with radius 2; c) filtered with radius 4; d) noise (a)-(b).	105
Figure 6-4 Demonstration of various thresholding methods: a) Mean, b) Moments, c) Intermodes.	106
Figure 6-5 Comparison of images acquired by SEM-BSE and μ -CT (a) with their histograms (b).	107
Figure 6-6 Segmentation: IV) thresholding with overflow method (Wong et al, 2006) and grey scale histogram of the stack; V) binary image after segmentation.	108
Figure 6-7 Cumulative grey scale histogram of image III The grey value x at the intersection between y_1 and y_2 is used as the threshold according to the overflow method (Wong et al., 2006). Here $x = 98$ for $y_1 = y_2$	108
Figure 6-8 Algorithm to separate microcracks from pores in aggregates and air voids.	110
Figure 6-9 Edge detection: VI) detected edges by external morphological gradient with a 3 voxel half-kernel size ball as structuring element; VII) inverted image of VI; VIII) thresholded (binary) image of VII with overflow method (Wong et al, 2006) using threshold value 237.	111
Figure 6-10 Cumulative grey scale histogram of image V The grey value x at the intersection between y_1 and y_2 is used as the threshold according to the overflow method (Wong et al., 2006). Here $x = 237$ for $y_1 = y_2$. ..	111
Figure 6-11 Despeckling, dilation and hole filling: IX) removing small particles from image VIII with despeckle filter at 3 voxels; X) image after binary dilation using a ball structuring element with half-kernel size of 2 voxels; XI) image after filling image borders and holes specified at 26-connectivity.	112

Figure 6-12 Image processing: XII) Manual selection of connected structures (cracks and air voids); XIII) Segmented image with removed pores in aggregates, XIV) Result of subtraction (Image V - Image XIV).	113
Figure 6-13 Image processing: XV) Image after dilation, fill holes and fill image borders at 26-conectivity; XVI) Result of subtraction: (Image V) - (Image XV); XVII) Result of subtraction: (Image V) - (Image XVI) showing pores in aggregates, part A.	113
Figure 6-14 Image processing: XVIII) Manual selection of remaining porous aggregates, XIX) porous aggregates - part B, XX) Separated porous aggregates (sum of part A and B).	114
Figure 6-15 Separation of air voids: XXI) Image without porous aggregates obtained by subtraction (Image V - Image XX); XXII) Air voids separated remained after sieve analysis of image XXI (Air voids part A); XXIII) Result of subtraction: (Image XXI - Image XXII).	114
Figure 6-16 Image processing: XXIV) Image after binary erosion using a ball structuring element with half-kernel size of 3 voxels; XXV) Remaining air voids after sieve analysis of image XXIV with 3D shape factor between 0.5 and 1.5, binary dilated using ball structuring element with half-kernel size of 4 voxels; XXVI) Result of logical AND operation: (Image XXIII) AND (Image XXV), air voids part B.	115
Figure 6-17 Image processing: XXVII) Result of subtraction: (Image XXIII) - (Image XXVI); XXVIII) Image after binary erosion using a ball as a structuring element with half-kernel size of 6; XXIX) Manual selection of remaining air voids.	116
Figure 6-18 Image processing: XXX) Image after binary dilation using a ball as a structuring element with half-kernel size of 7; XXXI) Result of logical AND operation: (Image XXVII) AND (Image XXX), air voids part C; XXXI) All air voids: part A+B+C, result of addition: (Image XXII) + (Image XXVI) + (Image XXXI).	116
Figure 6-19 Image processing: XXXIII) Image without porous aggregates and air voids (Image XXI - Image XXXII); XXXIV) After binary closing using a ball structuring element with half-kernel size of 1 voxel to remove noise; XXXV) Large microcracks that remained after sieve analysis of XXXIV with 3D shape factor > 5 and size < 50,000 voxels.	117
Figure 6-20 Image processing: XXXVI) Remaining features after subtraction (Image XXXIV - Image XXXV); XXXVII) Manual selection of remaining microcracks; XXXVIII) Result of addition (Image XXXV/large microcracks/ + Image XXXVII /selected remaining microcracks/) to produce the final image containing all microcracks.	118
Figure 6-21 Overlaid image of selected a) pores in aggregates, b) air voids and c) microcracks (highlighted in red) on to the original image (III).	118
Figure 6-22 a) Segmented, b) labelled and c) skeletonised image of microcracks.	119

Figure 6-23 Labelling of air voids: a) segmented image, b) labelled air voids, c) labelled air voids into eight categories according to their size distribution (equivalent spherical diameter). The upper and lower images show the 2D slices and the 3D volume respectively.....	125
Figure 6-24 Labelling of microcracks: a) Segmented binary image; b) labelled microcracks with 3D interpretation; c) labelled microcracks with 2D interpretation.	127
Figure 6-25 Skeletonisation of microcracks: a) Segmented binary image, b) skeleton of microcracks with 3D interpretation and c) skeleton of microcracks with 2D interpretation.....	128
Figure 6-26 Estimation of a) surface area, b) specific surface area and c) surface density of microcracks by voxel face area, Iso-surface (triangular surface mesh) and LICM (line intercept count method) in 3D and 2D analysis.	129
Figure 6-27 Cumulative width distribution of microcracks from 2D (XY) and 3D image analyses.	130
Figure 6-28 Microcracks width distribution based on local thickness measurements in BoneJ. Colours indicate microcrack width range.	130
Figure 6-29 Cumulative length distribution of microcracks from 2D and 3D image analyses.	130
Figure 6-30 Microcracks length distribution based on the dendritic length of microcracks 3D skeleton.	130
Figure 6-31 Orientation of microcracks presented in 2D by means of rose of intercepts at 0°, 45° 90° and 135° angle (black lines) and with 3D visualisation of the MIL vector cloud in XY, XZ, YZ directions.	131
Figure 6-32 Estimation of a) surface area, b) specific surface area and c) surface density of air voids by three methods: voxel face area, Iso-surface (triangular surface mesh) and LICM (line intercept count method).	133
Figure 6-33 Air voids size distribution according to equivalent diameter, Feret width and length (3D).	134
Figure 6-34 Air voids shape factors: aspect ratio, sphericity and elongation (3D).	134
Figure 6-35 Orientation of air voids presented by means of rose of intercepts at 0°, 45° 90° and 135° angle (black lines) with 3D visualisation of the MIL vector cloud in XY, XZ, YZ directions.	135
Figure 6-36 Oscillation of measured parameters versus sample size.....	135
Figure 6-37 Determination of a representative sample volume for characterising microcracks and air voids. .	136
Figure 6-38 Effect of sample size on the measured volume fraction of microcracks and air voids.	136
Figure 6-39 Effect of sample size on the measured density of microcracks and air voids.	137
Figure 6-40 Effect of sample size on the measured specific surface area of microcracks and air voids.....	137
Figure 6-41 Effect of sample size on the measured surface density of microcracks and air voids.	137

Figure 6-42 Effect of sample size on measured connectivity and tortuosity of microcracks.....	138
Figure 6-43 Effect of sample size on the degree of anisotropy of microcracks and air voids.	138
Figure 6-44 Effect of sample size on the measured microcrack width and length.....	139
Figure 6-45 Effect of sample size on the measured air void size and shape.....	139
Figure 6-46 Effect of sample size on measured air void spacing factor.....	139
Figure 6-47 Steps in the separation algorithm: a) raw data, b) cropped image, c) binary image, d) pores in porous aggregates, e) air voids f) microcracks.	140
Figure 7-1 Linear deformation measurement of concrete mixes with different binders: a) Portland cement (C), b) silica fume (SF) and c) GGBS (S) and water to binder ratios of 0.20, 0.25, 0.30, 0.35, 0.40 and 0.45.....	145
Figure 7-2 Linear deformation measurement of concrete mixes with different binders: a) Portland cement (C), b) silica fume (SF) and c) GGBS (S) and maximum aggregate sizes of 5 mm, 10 mm and 20 mm.....	145
Figure 7-3 Linear deformation measurement of concrete mixes with different binders: a) Portland cement (C), b) silica fume (SF) and c) GGBS (S) and aggregate contents of 50%, 60% and 68%.....	145
Figure 7-4 Typical microcrack morphology in a concrete sample subjected to autogenous shrinkage showing bond and matrix microcracks at the aggregate – cement paste – air voids interfaces.....	147
Figure 7-5 Area fraction of microcracks measured in samples with different a) w/b ratio, b) age, c) maximum aggregate size, d) aggregate fraction and e) sample size.....	148
Figure 7-6 Microcrack density measured in samples with different a) w/b ratio, b) age, c) maximum aggregate size, d) aggregate fraction and e) sample size.....	154
Figure 8-1 Segmented microcracks in concretes with different binders a) 0.30C-10/68-14, b) 0.30SF-10/68-14- (w/b replica), c) 0.30S-10/68-14. (Scale in mm).....	162
Figure 8-2 Segmented microcracks in concretes with different water to binder ratio: a) 0.20SF-10/68-14, b) 0.25SF-10/68-14, c) 0.30SF-10/68-14-(w/c replica), d) 0.35SF-10/68-14, e) 0.40SF-10/68-14, f) 0.45SF-10/68-14. (Scale in mm).....	162
Figure 8-3 Segmented microcracks in concretes at different age: a) 0.30SF-10/68-1, b) 0.30SF-10/68-3, c) 0.30SF-10/68-7, d) 0.30SF-10/68-14- (age replica), e) 0.30SF-10/68-28. (Scale in mm).....	163

Figure 8-4 Volume fraction of microcracks in concretes with a) different binders, b) different water to binder ratio and c) at different age. (* - refers to relevant replicas).....	163
Figure 8-5 a) Specific surface area and b) surface density of microcracks in concrete with different binders obtained via voxel face area (VFA), triangular surface mesh (Iso-S) and line intercept count method (LICM). (* - refers to binder replica).	164
Figure 8-6 a) Specific surface area and b) surface density of microcracks in concrete with different water to binder ratio via voxel face area (VFA), triangular surface mesh (Iso-S) and line intercept count method (LICM). (* - refers to w/b ratio replica).	165
Figure 8-7 Estimation of a) specific surface area and b) surface density of microcracks in concrete at different age via voxel face area (VFA), triangular surface mesh (Iso-S) and line intercept count method (LICM). (* - refers to age replica).	165
Figure 8-8 Microcrack width distribution in concretes with different binders: a) 0.30C-10/68-14, b) 0.30SF-10/68-14- (binder replica), c) 0.30S-10/68-14 based on local thickness measurements in BoneJ. Colour indicates microcrack width range.	166
Figure 8-9 Microcrack width distribution in concretes with different water to binder ratios: a) 0.20SF-10/68-14, b) 0.25SF-10/68-14, c) 0.30SF-10/68-14- (w/b ratio replica), d) 0.35SF-10/68-14, e) 0.40SF-10/68-14 and f) 0.45SF-10/68-14 based on local thickness measurements in BoneJ. Colours indicates microcrack width range.	166
Figure 8-10 Microcrack width distribution in concretes at different age a) 0.30SF-10/68-1, b) 0.30SF-10/68-3, c) 0.30SF-10/68-7, d) 0.30SF-10/68-14-(age replica) and e) 0.30SF-10/68-28 based on local thickness measurements in BoneJ. Colour indicates microcrack width range.	167
Figure 8-11 Cumulative width distribution of microcracks in concretes with different a) type of binder, b) w/c ratio and c) age. (* - refers to relevant replicas).	169
Figure 8-12 Cumulative length distribution of microcracks in concretes with different a) type of binder, b) w/c ratio and c) age. (* - refers to relevant replicas).	169
Figure 8-13 Skeleton of microcracks in concretes with different binders a) 0.30C-10/68-14, b) 0.30SF-10/68-14- (binder replica), c) 0.30S-10/68-14.	171
Figure 8-14 Skeleton of microcracks in concretes with different water to binder ratios: a) 0.20SF-10/68-14, b) 0.25SF-10/68-14, c) 0.30SF-10/68-14- (w/b ratio replica), d) 0.35SF-10/68-14, e) 0.40SF-10/68-14, and f) 0.45SF-10/68-14.....	172
Figure 8-15 Skeleton of microcracks in concretes at different ages: a) 0.30SF-10/68-1, b) 0.30SF-10/68-3, c) 0.30SF-10/68-7, d) 0.30SF-10/68-14- (age replica) and e) 0.30SF-10/68-28.....	172

Figure 8-16 Dendritic density of microcracks in concretes with a) different binders, b) different water to binder ratios and c) at different ages. (*- refers to relevant replicas).....	173
Figure 8-17 Degree of anisotropy of microcracks in concrete with different c) type of binder, b) w/b ratio and c) age. The results were calculated for the whole 3D volume and with 2D interpretation in XY, XZ and YZ.	174
Figure 8-18 Connectivity of microcracks and density connections in concretes with different a) binders, b) w/b ratios and c) age. *- refers to relevant replicas.	176
Figure 8-19 Geometric (G) and centroid path tortuosity along X-, Y- and Z- axes for concretes with different a) binders, b) w/c ratio and c) age. *- refers to relevant replicas	176
Figure 9-1 Demonstration of fluorescence LSCM for real-time imaging of water penetration into a microcracked concrete subjected to cyclical freezing and thawing (in collaboration with Marcus Yio).....	183
Figure I- 1 Cumulative distribution of microcrack width in concretes with different w/b ratios (0.20, 0.25, 0.30, 0.35, 0.40, 0.45) and a) Portland cement (C), b) silica fume (SF) and c) GGBS (S) as binders.....	196
Figure I-2 Cumulative distribution of microcrack width in concretes at different ages (1, 3, 7, 14 and 28 days) and a) Portland cement (C), b) silica fume (SF) and c) GGBS (S) as binders.	197
Figure I-3 Cumulative distribution of microcrack width in concretes with different MSA (5 mm, 10mm, 20 mm) and a) Portland cement (C), b) silica fume (SF) and c) GGBS (S) as binders.	197
Figure I-4 Cumulative distribution of microcrack width in concretes with different aggregate fraction (50%, 60%, 68%) and a) Portland cement (C), b) silica fume (SF), c) GGBS (S) as binders.....	198
Figure I-5 Cumulative distribution of microcrack width in concretes with different sample sizes (Ø25 mm, Ø50 mm, Ø95 mm) and a) Portland cement (C), b) silica fume (SF) and c) GGBS (S) as binders.	198
Figure II-1 Cumulative distribution of microcrack length in concretes with different w/b ratio (0.20, 0.25, 0.30, 0.35, 0.40 and 0.45) and a) Portland cement (C), b) silica fume (SF) and c) GGBS (S) as binders.	199
Figure II-2 Cumulative distribution of microcrack length in concretes at different ages (1, 3, 7, 14 and 28 days) and a) Portland cement (C), b) silica fume (SF) and c) GGBS (S) as binders.	200
Figure II-3 Cumulative distribution of microcrack length in concretes with different MSA (5, 10 and 20 mm) and a) Portland cement (C), b) silica fume (SF) and c) GGBS (S) as binders.	200

Figure II-4 Cumulative distribution of microcrack length in concretes with different volume fraction of aggregates (50%, 60% and 68%) and a) Portland cement (C), b) silica fume (SF), c) GGBS (S) as binders.... 201

Figure II-5 Cumulative distribution of microcrack length in concretes with different sample size (25, 50 and 95 mm diameter) and a) Portland cement (C), b) silica fume (SF) and c) GGBS (S) as binders..... 201

Figure III-1 Orientation of microcracks in concretes with different binders and w/b ratio of a) 0.20, b) 0.25 c) 0.30, d) 0.35, e) 0.40 and f) 0.45, presented by means of rose of intercepts at 0°, 45° 90° and 135°. 203

Figure III-2 Orientation of microcracks in concretes with different binders at age of a) 1 day, b) 3 days c) 7 days, d) 14 days and e) 28 days, presented by means of rose of intercepts at 0°, 45° 90° and 135°. 204

Figure III-3 Orientation of microcracks in concretes with different binders and aggregate volume fraction of a) 50%, b) 60% and c) 68%, presented by means of rose of intercepts at 0°, 45° 90° and 135°. 205

Figure III-4 Orientation of microcracks in concretes with different binder types and MSA of a) 5 mm, b) 10 mm and c) 20 mm, presented by means of rose of intercepts at 0°, 45° 90° and 135°. 206

Figure III-5 Orientation of microcracks in concretes with different binders and sample sizes of a) 25 mm, b) 50 mm and c) 95 mm in diameter, presented by means of rose of intercepts at 0°, 45° 90° and 135°. 207

Figure IV-1 Orientation of microcracks in concretes with three different binders: a) 0.30C-10/68-14, b) 0.30SF-10/68-14- (binder replica), c) 0.30S-10/68-14 presented in 2D by means of rose of intercepts at 0°, 45° 90° and 135° angle (black lines) and 3D visualisation of the MIL vector cloud in XY, XZ and YZ directions. 208

Figure IV-2 Orientation of microcracks in concretes with different water to binder ratios: a) 0.20SF-10/68-14, b) 0.25SF-10/68-14, c) 0.30SF-10/68-14- (w/b ratio replica), d) 0.35SF-10/68-14, e) 0.40SF-10/68-14 and f) 0.45SF-10/68-14 presented in 2D by means of rose of intercepts at 0°, 45° 90° and 135° angle (black lines) and 3D visualisation of the MIL vector cloud in XY, XZ and YZ directions. 210

Figure IV-3 Orientation of microcracks in concretes at different ages: a) 0.30SF-10/68-1, b) 0.30SF-10/68-3, c) 0.30SF-10/68-7, d) 0.30SF-10/68-14-(age replica) and e) 0.30SF-10/68-28 presented in 2D by means of rose of intercepts at 0°, 45° 90° and 135° angle (black lines) and 3D visualisation of the MIL vector cloud in XY, XZ and YZ directions. 211

Chapter 1

Introduction

1.1 Research motivation

The microstructure of concrete has a great influence on its performance and research on the microstructure of concrete has attracted much attention in recent decades. This has been partly a result of the considerable developments in microscopy and image analysis techniques. Most studies on the microstructure of cement-based materials have been carried out by imaging fractured surfaces or polished cross sections with optical microscopes (OM) (Bisschop and Van Mier, 2002, Soroushiana et al., 2003) and scanning electron microscopes (SEM) (Soroushiana et al., 2003, Bisschop and Van Mier, 2002, Wong et al., 2006, Scrivener, 2004). However, these imaging methods require invasive specimen preparation procedures that may alter the microstructure or produce artefacts. Additionally, these techniques can only observe a two-dimensional cross-section of a three-dimensional structure. This is a major limitation that significantly reduces the insights that can be gained from such analyses. Thus, there is a real need to develop and explore three-dimensional imaging techniques for characterising the microstructure of cement-based materials. Such 3D imaging techniques hold great promise, yet many technical challenges remain.

Research has also been driven by the needs to understand various deterioration processes affecting concrete and to develop more durable and sustainable concretes. Many studies have been dedicated to understanding the deterioration processes in concrete. Nevertheless, there is a general lack of studies on the microcracking induced by these deterioration processes. The microcrack network, besides connected pores, plays a major role in transport processes due to the ability of liquids and gases to penetrate through them (Wu et al., 2017 and 2019; Abyaneh et al., 2016). Microcracks provide channels for deleterious substances to penetrate concrete, which would initiate and accelerate deterioration. In addition, microcracks can propagate to macrocracks, which can cause the ultimate failure of concrete structures. Therefore, the development of microcracks is a significant concern and more efforts should be given to characterising and understanding microcracking. Understanding the microstructure of cementitious systems and its impact on transport processes will enable us to develop more durable materials, improve performance prediction and prolong the service life of concrete structures.

It is also important to point out that microcracks in concrete range from few microns to hundreds of microns in width, depending on the origin of the microcrack. On one hand, this means that the 3D imaging technique would require a resolution of approximately 1 μm to fully detect the microcracks. On the other hand, a minimum representative volume of the sample should be imaged to accurately characterise the microcracks. The representative elementary volume (REV) at the cement paste scale for the purpose of characterisation 3D microstructure and transport processes is of the order $\sim 100 \times 100 \times 100 \mu\text{m}^3$ (Yio et al., 2017, 2019). The

volume of concrete for representative analysis depends on the largest aggregate size present and is around 2.5 times the maximum aggregate size according to Abyaneh et al. (2013) for crack-free concrete and around 5-10 times the maximum aggregate size for concrete containing drying-induced microcracks (Wu et al., 2015). This makes 3D characterisation of microcracks in concrete very challenging since none of the existing imaging technique can fulfil the requirement of imaging at high resolution (1 μm) to capture the microcracks in a sufficiently representative sample volume.

A primary attention of this work was put on characterising microcracks induced by autogenous shrinkage. This type of microcracking is mainly associated with low water to binder ratio concretes, such as high-performance concretes (HPC). The sensitivity of HPC to early-age cracking is often considered as its Achilles' heel and attracts much attention of researchers, even though no one has performed direct characterisation of these microcracks.

HPC has become increasingly used, especially in recent years, in civil engineering because of its excellent performance in terms of high workability, high strength and low permeability. These properties are obtained by employing a low water to cement ratio and incorporating mineral and chemical admixtures such as silica fume, fly ash, ground granulated blast furnace slag and superplasticiser (Neville and Aïtcin, 1998, Aïtcin, 1998). Unfortunately, such concretes are susceptible to microcracking caused by self-desiccation (reduction in internal relative humidity as the water is consumed during cement hydration) and autogenous shrinkage. Numerous studies have been performed to study the nature of autogenous shrinkage (Lura, 2003, Lura et al., 2003, Lura et al., 2009, Igarashi et al., 2000) and how internal curing can minimise microcracking caused by this phenomenon (Huo and Wong, 2006, Jiang et al., 2014). Several shrinkage-counteracting techniques have also been proposed. Examples include shrinkage reducing admixtures (SRA) and internal curing (IC) by means of lightweight aggregates (Lura, 2003, Zhutovsky and Kovler, 2012, Zhutovsky et al., 2013) or super-absorbent polymers (Craeye et al., 2011). Despite this, there is no fundamental study that explains the development of microcracks, characterise them and investigate their actual influence on bulk properties of concrete.

1.2 Objectives and scope

The overall aim of this project is to characterise microcracks in cement-based materials in three-dimensions (3D). The main sub-objectives are:

- Evaluate different ways of introducing microcracks to concrete samples in the laboratory environment.
- Develop and apply new 3D imaging techniques such as focused ion beam nanotomography (FIB-nt), broad ion beam serial sectioning (BIB), X-ray microtomography (μ -CT) and laser scanning confocal microscopy (LSCM) to image microcracks.
- Develop 3D image analysis methods to segment and extract quantitative data of the microcracks such as size distribution, density, connectivity, tortuosity and orientation.
- Apply the most suitable 3D imaging technique and image analysis method to study the characteristics of microcracks induced by autogenous shrinkage in concrete.

1.3 Thesis outline

Nine chapters are presented in this thesis. Chapter 1 introduces the research background, objectives and scope of the study. Chapter 2 presents a literature review on the topics relevant to the scope of this thesis. Chapter 3 describes the methodology of experimental work, including sample preparation, detailed protocols for microscopy techniques and image analysis procedures. The main findings of this study are presented in the next five chapters, i.e. Chapter 4, 5, 6, 7 and 8.

The aim of Chapter 4 is to examine the feasibility of three-dimensional microscopy techniques for imaging microcracks. Several types of sample containing different degrees of microcracking induced by drying shrinkage with internal and external restraints, autogenous shrinkage, and freeze-thaw cycles are investigated. Focused ion beam nanotomography (FIB-nt), broad ion beam serial sectioning (BIB), X-ray microtomography (μ -CT) and laser scanning confocal microscope (LSCM) are evaluated. The advantages and limitations of these techniques are discussed.

Chapter 5 presents a solution to extend the imaging depth of LSCM for cement-based materials, which is achieved by combining confocal imaging with a serial sectioning procedure. This new approach has been developed in collaboration with Marcus Yio, a PhD student in the group.

3D image analysis is very challenging especially for microcracks, partly because they share similar grey scale (brightness) values in the image histogram as pores and air voids. Chapter 6 proposes methods for image pre-processing which strongly depends on the imaging techniques and develops algorithms for segmentation and separation of microcracks from other porous features. This chapter also presents the characteristic parameters of microcracks that can be measured in such analysis.

The main objective of Chapter 7 is to determine the magnitude of autogenous shrinkage (by linear deformation measurements) for a range of concrete mixes and to understand its effect on microcracking. The 2D characteristics of early-age microcracking in concretes with different water to binder ratio, type of binder, age, maximum aggregate size, aggregate content and sample size are investigated. Additionally, degree of microcracking is correlated with degree of linear deformation.

Chapter 8 presents 3D characteristics of the microcracks induced by autogenous shrinkage using X-ray microtomography. Selected samples from Chapter 7 are scanned with Metris X-Tek HMX ST 225 CT, which is capable of achieving a voxel size resolution of 1/2000 of sample size. This allows for detection most of the microcracks caused by autogenous shrinkage. 3D image analysis is performed on the captured 3D images to quantify the propagation of microcracks as a function of time and effect of water to binder ratio and type of binder. The algorithm developed in Chapter 6 is applied to separate microcracks from pores, and to extract quantitative data such as crack density, areal fraction, average width and length, orientation degree and distribution of width, as well as connectivity and tortuosity.

Finally, the main findings from this thesis are summarised in Chapter 9, together with suggestions and recommendations for further research.

Chapter 2

Literature review

A literature review has been conducted to establish the state-of-the-art of research related to this project. The review covers the causes of microcracking, in particular, autogenous shrinkage induced microcracking, mechanisms of crack initiation and propagation, transport properties of microcracked concrete, and methods to characterise microcracks including 2D and 3D imaging techniques. These four sections are summarised, and the main references are given.

2.1 Types and mechanisms of microcracking

Microcracking occurs in concrete due to a variety of causes. They can be induced by external loads, or through the interaction between the concrete and its environment, or through physico-chemical degradation processes. Microcracks may propagate, become highly interconnected macrocracks and contribute to ultimate failure of concrete. They can provide channels for deleterious substances to penetrate concrete and thereby accelerate its deterioration.

The common types of cracks are listed in Figure 2-1:

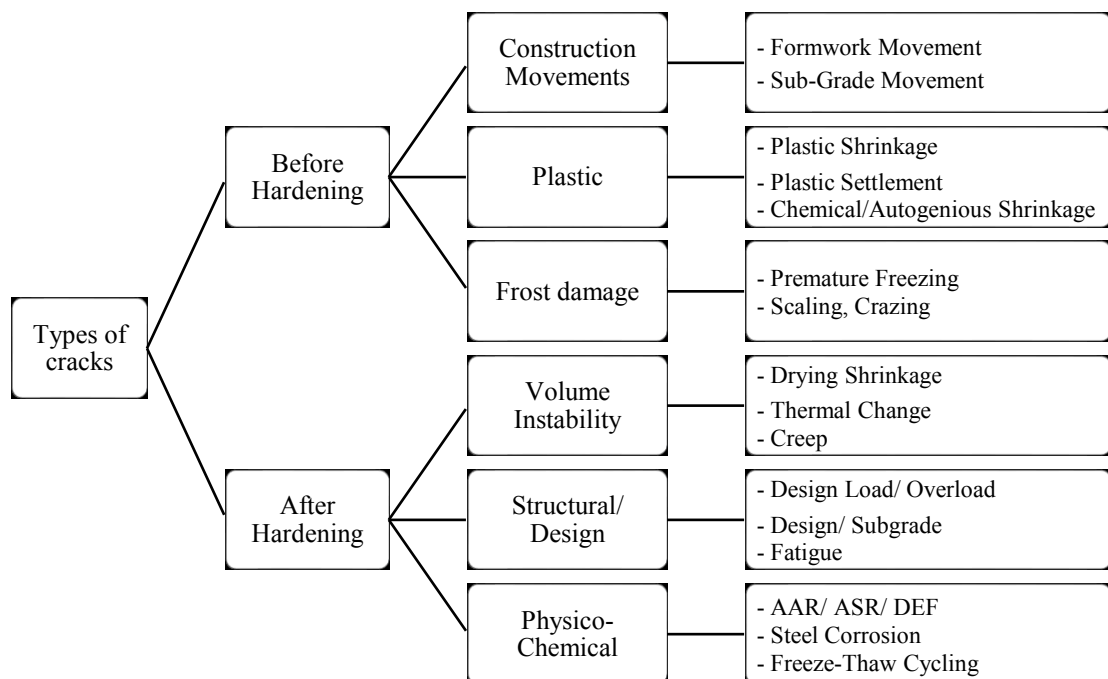


Figure 2-1 Common causes of cracking in concrete structures (Meyer, et al., 2006).

Cracks, which occur before hardening of concrete, primarily due to settlement, construction movements and excessive evaporation of water, are called plastic cracks. These can be minimized through proper attention to the mixture design, material placement and curing. Cracks that occur after the concrete has hardened may be due to various reasons such as mechanical loading, moisture and thermal gradients, and degradation reactions such as alkali-aggregate reactions, sulphate attack, freezing – thawing, and corrosion of reinforcement (Meyer, et al., 2006).

Although numerous factors influence whether or not concrete cracks, it can be stated according to elasticity theory (Goltermann, 1995) that cracking occurs when the tensile stress that develops in response to load or restrained volumetric changes exceeds the tensile strength of the material. According to fracture mechanics, the cracks will then propagate if the energy released during crack propagation is equal or larger than a critical fracture energy (Goltermann, 1995).

Cracks are either macrocracks, which are detectable by visual inspection, or microcracks, which can only be detected with the aid of a microscope. The focus of this research is microcracks, and these are commonly defined as cracks with widths above 1 μm and below few hundreds of microns ($<1\text{ mm}$).

Microcracks can also be classified according to their location in the heterogeneous concrete composite. Accordingly, three types of microcracks are distinguished: cracks that occur through the cement paste (matrix cracks), cracks at the interface between aggregate particle and cement paste matrix, i.e. at the Interfacial Transition Zone (bond/radial cracks) and cracks that occur through the aggregate particle. It is also observed that matrix cracks tend to propagate from the surface of one aggregate particle to the surface of a neighbouring aggregate particle. Such arrangement of microcracks is related to strain distribution in a stressed system. Maruyama and Sasano (2014) experimentally showed that the maximum stress occurs between cement paste and coarse aggregates (at the ITZ), where most of microcracks developed as matrix or bond cracks. This mechanism is illustrated in Figure 2-2.

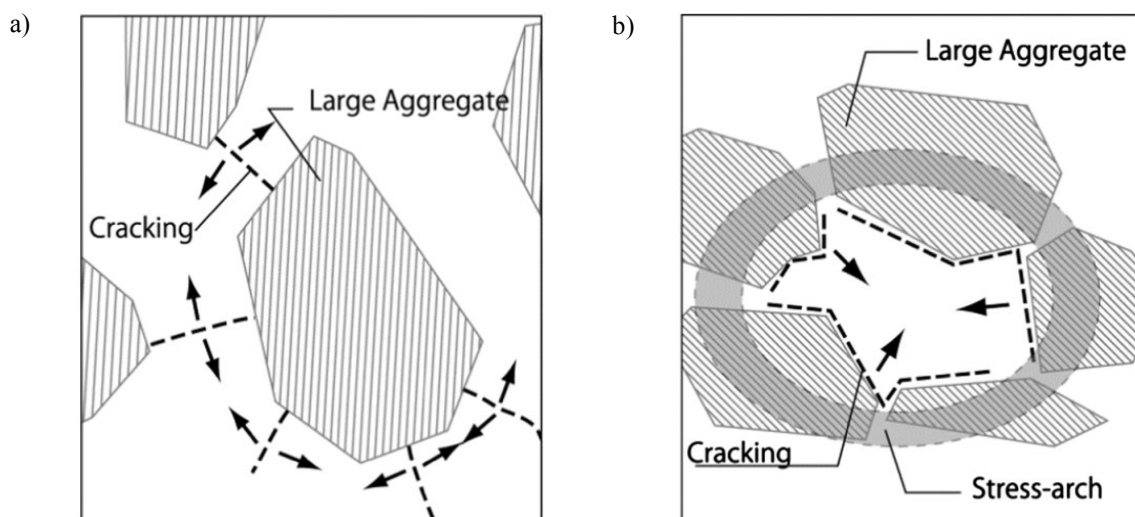


Figure 2-2 Matrix (a) and bond (b) crack opening mechanism (Maruyama and Sasano, 2014).

Many other authors have observed the same typical pattern of microcracks (e.g. Goltermann, 1995; Bisschop & van Mier, 2002; Wong et al., 2009). Figure 2-3 shows a SEM image of cracked concrete due to

drying shrinkage (Wong et al., 2009) with all three types of microcracks: bond cracks, crack through an aggregate and matrix cracks propagating from one aggregate particle to a neighbouring aggregate particle.

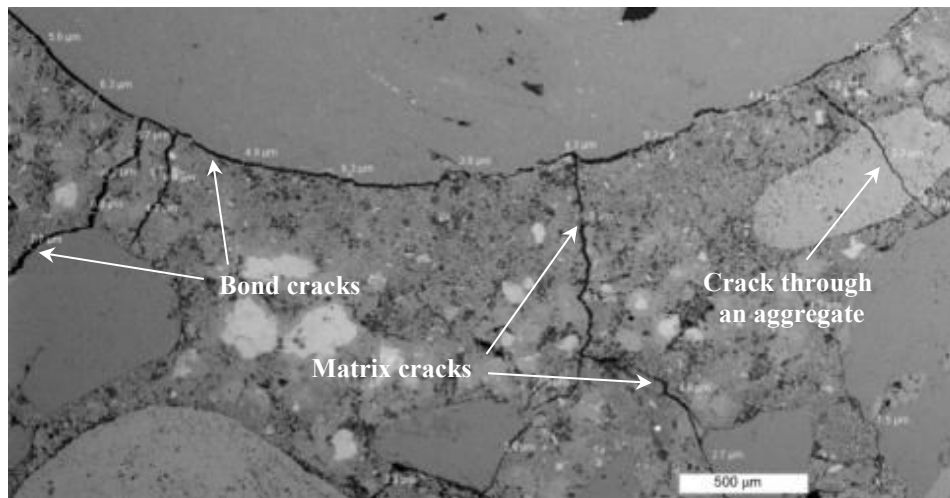


Figure 2-3 Typical microcrack pattern observed in concrete subjected to oven drying (Wong et al., 2009).

In practical construction, it has been found that microcracking is commonly caused by drying shrinkage. This is particularly true especially in concrete overlays and slabs where single-sided drying occurs, and shrinkage is restrained by internal or external restraints (Bissonnette et al., 1999). External restraint is caused by the surrounding of the structure while internal restraint is caused by two mechanisms: self-restraint and aggregate restraint. Self-restraint is a result of non-uniform shrinkage of the material caused by a moisture gradient that develops during drying. Important factors are the size and geometry of the sample (ratio of surface area to volume). In cement paste, this type of restraint causes tensile stresses near the drying surface and compressive stresses in the core of the sample. This leads to a development of microcracks that extend perpendicular to the drying surface with a limited depth, forming cell-like crack pattern on the drying surface as shown in Figure 2-4 (Bisshop & Wittel, 2011). The second type of internal restraint is caused by the presence of stiff aggregate particles in mortars and concretes. If the restraint caused by an aggregate particle in a shrinking matrix is large enough, radial and bond cracks will form around the aggregate particle (Goltermann, 1995). The size, surface roughness (bond), and volume fraction of the aggregates, and the contrast between the Young’s modulus of the aggregate and surrounding matrix are the main influencing parameters.

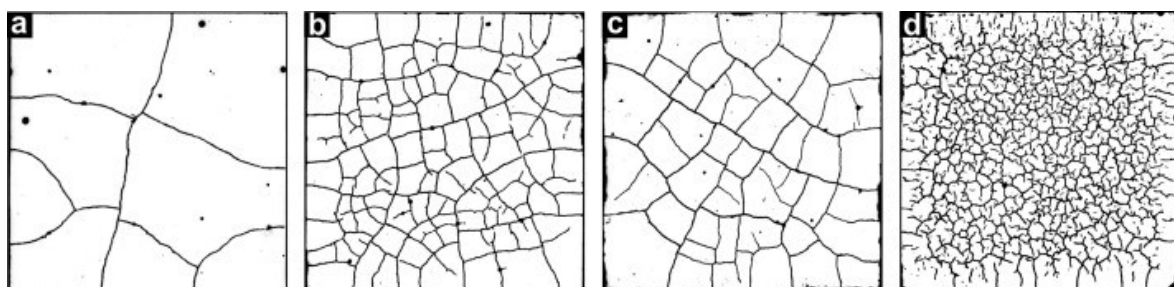


Figure 2-4 Examples of crack pattern on the drying surface of cement paste exposed to different drying regimes: (a) 5h drying at 95% RH; (b) 5h drying at 26% RH; (c) 2 months drying at 26% RH; (d) 5 h drying at 25% RH and 590 Pa (ESEM chamber). Image size is 3×3 cm (Bisshop & Wittel, 2011).

Drying induced microcracks occur mainly on the surface of concrete. However, they tend to penetrate to a depth of up to 10 mm (Wu, 2014, Wu et al., 2017 and 2019). Similar crack pattern is observed in surface crazing, although these are much shallower microcracks, usually less than 3 mm in depth (Mircea, 2009). Crazing cracks are a network of fine cracks induced by rapid evaporation of moisture (due to drying or cooling) from the surface of concrete and thus differential contraction between the surface and interior sections (White et al., 1928; Mircea, 2009). Crazing cracks develops at an early age, usually up to one week from casting.

Many concrete structures suffer from microcracking induced by physico-chemical processes. For instance, alkali-silica reactions (ASR), a chemical reaction that takes place between the alkaline pore solution of the cement paste and reactive silica in aggregate particles. ASR produces an expansive alkali – silica gel that gives rise to internal pressure, expansion and eventually cracking. The cracks propagate from the interior of the aggregate particles out into the surrounding cement paste (Lee, 1992).

External sulphate attack is another example, where cracking and scaling is caused by chemically-induced volume expansion of the concrete. Sulphate attack involves two chemical reactions. First, the sulphate ions from waste water or naturally occurring soil or ground water sulphate salts (e.g. sulphates of sodium, potassium, calcium, or magnesium) react with free calcium hydroxide released during hydration processes to form calcium sulphate (gypsum). Next, the gypsum combines with hydrated calcium aluminate to form calcium sulpho-aluminate (ettringite). Both products, particularly ettringite, result in volume increase followed by internal cracking starting from exposed to sulphates regions (Lee, 1992; Neville, 1995).

Chloride-induced corrosion of steel reinforcement is the most frequent and severe cause of deterioration of concrete structures. In general, ordinary Portland cement (OPC) concrete provides good protection to embedded reinforcing steel, which is attributed to the high alkalinity pore solution and to the relatively high electrical resistance of this concrete. Even then, this highly alkaline environment can be reduced over a period of time by carbonation and the electrical resistivity can be decreased by the presence of chemicals (e.g. chloride salts). Under such conditions, corrosion cells may be established between individual reinforcing rebars. Expansive corrosion products forming on the steel surface cause pressure at the interface between the reinforcement and concrete. This pressure eventually leads to cracking if the resultant tensile stress exceeds the tensile strength of the concrete. The cracks are usually parallel to the rebars and appear on the steel – concrete interface first, propagating afterwards through the concrete cover. The severity of cracking increases with the progression of corrosion processes (Lee, 1992; Kurdowski, 2002).

Highly saturated concrete members in areas of fluctuating water levels or under spraying conditions such as tops of walls, piers, parapets, and slabs enhance the vulnerability of concrete to the harmful effects of repeated cycles of freezing and thawing, which intensify during winter seasons. The volume expansion of approximately 9% of pore water on freezing in the capillary pores of the cement paste and aggregates causes an increase of internal pressure and damage by means of internal microcracking or surface scaling – related to use of deicing chemicals (Pigeon et al., 1996). The degree of deterioration strongly depends on the number of freeze – thaw cycles and also on the length of the freezing period. The cracks induced are in general, uniformly distributed and can become very well connected if the concrete is subjected to severe cyclic freezing and thawing (Promentilla and Sugiyama, 2010).

2.2 Autogenous shrinkage microcracking

The volume changes caused by autogenous shrinkage are inevitable in concrete. When the volume change is restrained either by external or internal restraints, internal stresses are produced. Autogenous shrinkage may lead to the occurrence of microcracking when the induced stresses exceed the tensile strength of concrete. This will subsequently accelerate the ingress of aggressive agents into concrete structures and therefore, degradation of concrete. Thus, it is of great importance to have a better understanding of the mechanism of microcracking induced by autogenous shrinkage, of their characteristic parameters (i.e. density, orientation, connectivity), as well as their influence on transport properties of microcracked concrete (i.e. sorptivity, diffusivity and permeability) that control the long-term durability of concrete structures.

2.2.1 Autogenous shrinkage

The autogenous shrinkage phenomenon was originally used to describe the shrinkage of concrete by itself that seemingly occurs without any external influences such as loads, moisture or temperature changes. A later definition of autogenous shrinkage was related to the changes in volume of concrete under a sealed condition (Davis, 1940). Nowadays, it is widely agreed that autogenous shrinkage is a macroscopic volume change caused by the hydration process of cement after initial setting that occurs without external loading or external drying. Autogenous shrinkage starts at very early ages as a result of chemical shrinkage (volume reduction due to the hydration process) and self-desiccation caused by internal consumption of water by the hydration reaction, lowering the internal relative humidity (Tazawa, 1998).

The contribution of autogenous shrinkage in typical concrete mixes has been previously neglected due to the dominant role of drying shrinkage. One of the first reports found in literature was the work done by Davis (1940). He observed that autogenous shrinkage in concrete using ordinary Portland cement at 28 days was about $40 \mu\epsilon$, much smaller than drying shrinkage which ranges from 400 to 800 $\mu\epsilon$. His study reported that autogenous shrinkage for ordinary concrete ranges between 50 to 100 $\mu\epsilon$ after 5 years of hardening.

Nonetheless, the increasing use of high strength and high-performance concretes containing low water/binder ratio, complex cementitious materials and multiple chemical admixtures in recent years has highlighted the problem of autogenous shrinkage in these concretes. Concretes with a lower water to cement ratio can achieve much higher autogenous shrinkage, as reported by Tazawa & Miyazawa (1995). In their experiment, a total shrinkage of almost 700 $\mu\epsilon$ was measured for high strength concrete with a water to cement ratio of 0.17. Similar results were achieved by the group of Äitcin (1998), they observed that autogenous shrinkage will develop rapidly if the w/c ratio is lower than 0.42. The effect of cementitious materials addition on autogenous shrinkage was also investigated. Silica fume modified cement pastes show much greater self-desiccation and autogenous shrinkage than Portland cement pastes (Jensen & Hansen 1996). Similarly, GGBS cement pastes exhibit lower internal RH and greater autogenous shrinkage than Portland cement paste (Hanehara et al., 1999). The severity of autogenous shrinkage may also be related to the following aspects: cement class and fineness, amount of tricalcium aluminate (C_3A) and tetracalcium aluminato ferrite (C_4AF) in Portland cement and temperature (Tazawa & Miyazawa, 1995).

2.2.2 Measurements of autogenous deformation

Autogenous shrinkage is associated with two phenomena: chemical shrinkage and self-desiccation effects. There are also two testing methods, direct and indirect to measure both effects. Direct methods measure either the volumetric or linear changes while indirect methods correlate the autogenous shrinkage with measurement of the porosity or changes in the relative humidity of cement-based materials. A summary of all the existing method is shown in Figure 2-5 (Hu et al., 2013).

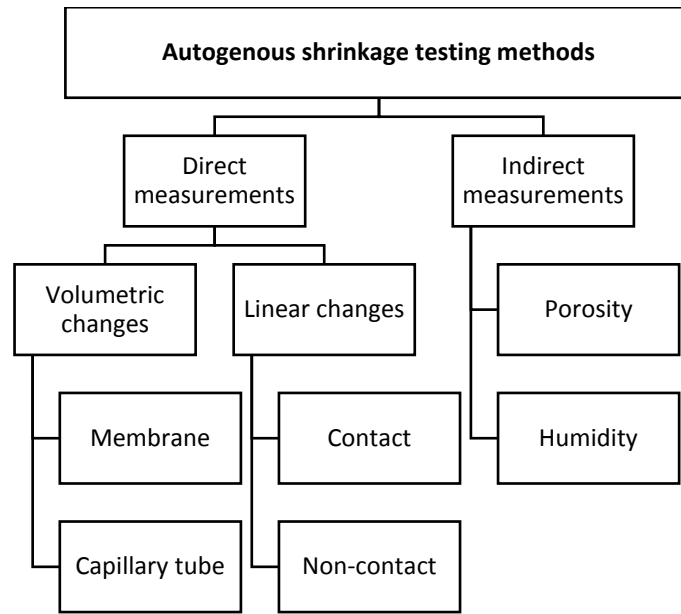


Figure 2-5 Methods to measure autogenous shrinkage (Hu et al., 2013).

Direct measurements are simpler and therefore more common. Volumetric methods are usually applied to establish the shrinkage of cement pastes, while linear changes are measured in concrete and mortar samples. Volumetric changes can be measured by using a membrane or a capillary tube. Membrane method is based on the change in buoyancy of cement paste when it is placed in a tight elastic membrane (e.g. a balloon) and immersed in water. The change in volume of the cement paste is measured by weighing the immersed sample over time. Here, re-absorption of bleeding water and thermal action may affect the results (Tazawa, 1998). The capillary tube method is based on Le Chatelier contractions of a cement paste placed in a tube. Autogenous shrinkage is measured with a pipette inserted on top of the paste that controls the water or oil movement laid in the cement paste. Here, thermal action and sample size may affect the results (Hu et al., 2013).

Linear deformation measurement can be carried out using contact or non-contact methods. In general, contact methods adopt gauges connected to semi-embedded studs located at both ends of specimens, or sensors (e.g. thermocouples), which are totally embedded in the sample to measure the length change over time (Hu et al., 2013). More advanced applications have replaced the gauges with linear variable differential transformers (LVDT) to obtain more accurate results (Amin, et al., 2010). Non-contact methods measure linear deformations using laser sensors equipped with computer system and current sensors. These measurements are carried out automatically and continuously, without producing constraints in the samples (Morioka et al., 1999).

Indirect methods are based on measuring internal humidity or porosity as the occurrence of autogenous shrinkage is closely related to relative humidity and pore pressure of specimens (Hu et al., 2013).

Among all the existing methods, linear measurements provide the most reliable method because factors such as bleeding, setting time, thermal action are taken into account during the testing (Hu et al., 2013). Therefore, the linear deformation contact method will be applied in the present work.

2.3 Methods for characterising microcracks

To-date, the nature of microcracks in cement-based materials is still relatively not well understood. One reason for this is the lack of suitable techniques to detect and characterise microcracks. Indirect methods for detecting microcracks include ultrasonic (Kesner et al., 2004; Jacobs & Whitcomb, 1997) and acoustic emission (Ohtsu et al., 1998; Ouyang et al., 1991). The ultrasonic method measures the propagation of sound waves through the concrete and the signal is then calibrated to give microcrack density. The acoustic emission technique works by detecting the sound waves produced by crack nucleation and propagation in real time. However, these methods provide limited information about size, position and geometry of the developed crack pattern. Therefore, they will not be used for characterisation of microcracks within this project.

Conventional methods for direct imaging of microcracks include optical microscopy (OM) and scanning electron microscopy (SEM) (Bisschop & van Mier, 2002; Bisschop, 2002; Litrowicz, 2006). However, both techniques are destructive as they require a cross-section through the material and the obtained measurements are only two-dimensional. More recently three-dimensional imaging methods using computed tomography based on conventional X-ray and synchrotron radiation have been introduced (Promentilla & Sugiyama, 2010; Landis et al., 2006; Gallucci et al., 2007). These techniques can image the true nature of cracks in 3D rather than its 2D projection. However, the resolution of these techniques is limited and decreases with increase in sample size.

In conventional image analysis of micrographs obtained from scanning electron microscopy and optical microscopy, parameters such as crack length, density, orientation degree and width are often measured (Litrowicz, 2006). However, three-dimensional parameters such as connectivity and tortuosity of microcracks, which are critical with respect to understanding transport phenomena are completely unattainable with these methods. The following sections provide a review of various 2D and 3D imaging techniques, and discuss their potential for characterizing microcracks.

2.3.1 Optical microscopy

Optical microscopy (OM), also called light microscopy, is an imaging technique by reflection on a polished sample, or by transmission through a polished thin section using a beam of visible light and a system of lenses. As cement-based materials are relatively opaque to photons within the visible wavelength (Coster & Chermant, 2001), reflected mode with ultraviolet (UV) light can be utilised to image microcracks in a sample impregnated with fluorescent epoxy resin. The areas that are filled with epoxy such as microcracks and pores

will appear bright and therefore distinguishable from the dark solid phases in concrete (Bisschop, 2002; Shiotani et al., 2003).

2.3.2 Laser scanning confocal microscopy

Laser scanning confocal microscopy (LSCM) is an extension of 2D optical microscopy. It is capable of collecting serial optical sections from a thick specimen to produce a 3D image. The principle of LSCM is explained in Section 5.2. Essentially, a highly focused laser beam is used as a light source and a pinhole is employed to remove out-of-focus light emanating from below and above the focal plane so as to give a very small focal volume. By scanning the light source across the sample and by displacing the focal plane in the Z-axis, a high-resolution 3D image can be built up from sequential thin optical slices.

The resolution of the confocal microscope is affected by several different factors (Head & Buenfeld, 2006), such as the properties of the objective lens and wavelength of the light source (laser). In ideal conditions, the resolution of LSCM approaches the wavelength of the light source (~ 500 nm) and so is sufficient to detect microcracks in concrete. However, the most problematic aspect of LSCM is that the intensity of the detected signal in concrete drops dramatically with depth and this limits the imaging depth to several microns. A maximum imaging depth of 12 μm was achieved by Head and Buenfeld (2006) in their experiment. Imaging depths of 13.5 μm and 18.2 μm were also reported in others work (Kurtis et al., 2003; Nichols & Lange, 2006). This is a major limitation of LSCM. Hence, a new approach combining serial sectioning and confocal microscopy is proposed in this study to overcome the imaging depth limitation of LSCM.

2.3.3 Scanning electron microscopy

A scanning electron microscope (SEM) produces images of a sample by scanning it with a focused high-energy beam of electrons. The electrons interact with atoms in the sample, producing various signals (radiations) that can be detected and that contain information about the sample surface topography and composition.

Two types of radiation, the secondary electrons and backscattered electrons are usually used for imaging. Secondary electrons are electrons caused by inelastic scattering. They emerge from a smaller sampling volume and are able to achieve a better spatial resolution than other signals. The intensity of secondary electrons relies on the local inclination of the specimen surface. Hence, topographic images can be produced by secondary electrons. Backscattered electrons (BSE) are elastically scattered electrons having a larger sampling volume and a lower spatial resolution compared to secondary electrons. However, the intensity of backscattered electrons increases with increase in the mean atomic number of the solid phases of a polished sample (Stutzman & Cliffron, 1999). This enables compositional imaging to be achieved. The phase with largest mean atomic number appears brightest in a BSE image, which enables quantitative analysis of the various phases in the microstructure. For cement-based materials, resin-filled pores and cracks will appear as the darkest phase. During the last two decades, backscattered electron imaging of polished surfaces has become a well-established method for studying the microstructure of cementitious materials (Scrivener, 2004; Wong, 2006).

2.3.4 Focused ion beam and broad ion beam with scanning electron microscopy

SEM imaging combined with ion beam processing such as focused ion beam nano-tomography (Giannuzzi & Stevie, 2005) and broad ion beam serial sectioning (Desbois et al., 2013) has been shown to be a versatile method for 3D investigation of microstructure of heterogeneous materials.

The Broad Ion Beam (BIB) method uses an argon gas source to produce an ion beam of approximately 500 μm in diameter. The ion beam irradiates the edge of the sample as shown in Figure 2-6 a. The sample is milled with the ion beam and imaged sequentially with the SEM. By using a standard BIB polisher, a minimum slice thickness of 10 μm is achievable. However, it was reported by Desbois et al. (2013) that the first BIB-cryo-SEM machine is capable of achieving a minimum slice thickness of 350 nm.

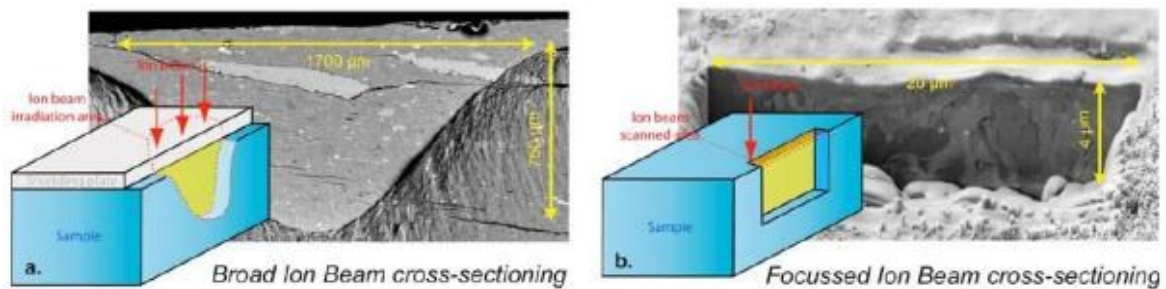


Figure 2-6 Principles of ion beam cross-sectioning methods with typical cross sections performed by BIB (a) and FIB (b) on a clay sample Desbois et al., 2010).

In comparison to BIB, the Focused Ion Beam (FIB) method uses a gallium metal source to produce a focused beam. It also does not require a shielding plate and the cross section produced by irradiating the region of interest is much smaller (tens of μm) as shown in Figure 2-6 b. The combination of an electron beam for imaging and an ion beam for exposing successive surfaces provides a suitable tool for 3D imaging with resolutions of about 10 nm in XY and Z directions for FIB (Trtik et al., 2010). The resolution for BIB is about 10 nm in XY, but its Z resolution is much coarser (affected by the slicing step).

FIB nano-tomography (FIB-nt) is now an established technique and combine a dual beam SEM-FIB systems are commercially available. However, its application to cement-based materials remains limited because of the very small imaged volume. Available studies have focused on characterising the particle size distribution and morphology of cement particles (Holzer et al., 2006; Münch et al., 2006), morphology and spatial arrangement of early hydration products (Holzer et al., 2007), surface roughness (Trtik et al., 2008), nanoscale porosity of hardened cement paste (Münch & Holzer, 2008), and 3D morphology of different solid phases in hardened cement pastes (Trtik et al., 2010).

It has been reported that the next generation of ion beam-SEM instrument uses a Xe plasma source FIB, which has higher probe current and sputtering rate than the conventional Ga^+ FIB. Thus, a larger area of up to $300 \times 300 \mu\text{m}^2$ can be achieved (Hrnčir et al., 2012). However, this is a relatively new technique and has not yet been tested on cement-based materials.

With the advancement of 3D imaging techniques such as X-ray nCT and Xe^+ plasma source FIB-nt, it may be possible in the future to characterise the pore structure in 3D at different length scales.

2.3.5 X-ray microtomography

X-ray micro-computed tomography (μ -CT) is a non-destructive 3D imaging technique, where hundreds of 2D projection radiographs are taken of a specimen at many different angles. These projections are then used to produce a 3D mathematically reconstructed image as shown in Figure 2-7.

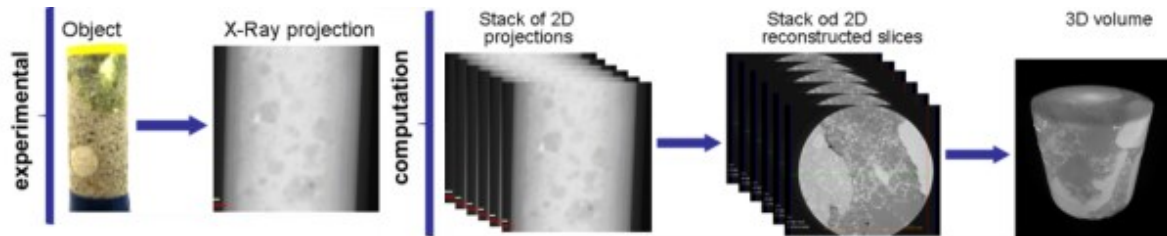


Figure 2-7 Image acquisition with X-ray microtomography.

μ -CT is able to scan a large sample volume from hundreds of μm^3 to tens of cm^3 . However, the resolution decreases with increase in sample volume. Spatial resolution is also affected by CT scanner characteristics and the linear attenuation coefficients of the sample (Hsieh, 2009). The important parameters are the X-ray source spot size, detector resolution, vibrational, electrical and thermal stability, magnification geometry, and imaging conditions. Image contrast depends on the absorption of X-rays of the different phases in a sample. As a consequence, low atomic number (low Z) materials, such as soft tissue and polymers, and materials of similar Z number, such as ceramic compounds do not provide sufficient imaging contrast, and therefore are difficult to segment for quantitative image analysis.

Conventional μ -CT scanners are capable of achieving a spatial resolution of $> 1 \mu\text{m}$. This has been applied in cement and concrete research in a number of applications for imaging large scale features, e.g. freeze-thaw induced microcracking (Promentilla & Sugiyama, 2010), quantitative measurements of crack growth under loading (Landis et al., 2006), in situ observation of cracking and fracture behaviour under progressive uniaxial compressive loading (Yang et al., 2017) and characterisation of deterioration due to sulfate attack (Naik et al., 2006; Stock et al., 2002), carbonation (Han et al., 2012) and leaching (Burlion et al., 2006). Synchrotron μ -CT with a better resolution of between 0.7 to 1.0 μm has been used to image pores in hardened cement paste (Gallucci et al., 2007) and anhydrous cement particles (Garboczi & Bullard, 2004).

Over the last few years, commercial X-ray CT systems continue to push the limits of tomographic imaging resolution. Recently, new laboratory-based systems are benefiting from developments in synchrotron facilities by employing new detector and focusing optic technologies (Zeiss, 2013). For instance, the Xradia VersaXRM uses a detector pixel size down to $\sim 150 \text{nm}$ to produce spatial resolutions $\sim 700 \text{nm}$ on samples several millimetres in size or at working distances measured in the several tens of millimetres (Merkle & Gelb, 2013). In addition, as a result of small effective pixel dimensions and tuneable detector and source positions, propagation phase contrast can effectively highlight interfaces in samples that exhibit low absorption contrast. However, it is unsure if such resolution can persist on cement-based materials.

2.4 Influence of microcracks on the bulk transport properties of concrete

Microcracks are inherent features of the microstructure in most concrete structures. This is due to the fact that the tensile strength of concrete is very low compared to its compressive strength. The presence and continuous development of microcracking affecting microstructure of concrete may also influence the bulk transport properties of concrete such as permeability, diffusivity and sorptivity. Thus, this topic has attracted attention of many researchers who are trying to isolate and investigate the effect of microcracking on the mass transport properties of concrete. Researchers have studied the relationships between water transport properties and different deterioration mechanisms causing microcracking e.g. carbonation, chloride-induced corrosion and freeze-thaw attack (Yang et al., 2006; Basheer et al., 2001). Generally, the rate of deterioration and severity of microcracking increases with transport properties, although the exact relationship varies depending on the test methods adopted (Basheer et al., 2001). There are studies, which investigated and compared the effects of microcracking on transport properties (Yang et al., 2006; Jacobsen et al., 1996; Wong et al., 2009; Chena et al., 2010). These studies have indicated that the presence of cracks could increase the permeability by several orders of magnitude.

Scheydt and Muller (2012) investigated the effect of microcracking induced by the autogenous shrinkage on the durability of ultra-high-performance concrete (UHPC). Their results confirm that high autogenous shrinkage leads to deformation and consequently to microcracking, which strongly affected the microstructure of dense UHPC. Their presence significantly increased the transport properties of the cracked-UHPC compared to crack free- (fibre reinforced) UHPC. This was proven by experiments on water absorption (an increase up to 90%), chloride ingress and chemical attack.

Samaha and Hover (1992) investigated transport properties of concrete under different loading levels. It was found that different types of loading induce different characteristics of cracking, and therefore direct correlation between loading level and transport properties are difficult to determine. Their work emphasised that transport properties of concrete are strongly influenced by the characteristics of cracking. A similar observation was described by Guayasamin (2015). He examined the influences of autogenous shrinkage induced microcracking on mass transport properties and found out that the depth and speed of water penetration in the prepared samples was affected by the orientation of cracking and its connectivity.

Moreover, different transport properties should be investigated separately since the influence of microcracking on each mechanism might not be the same (Wong et al., 2009). For instance, diffusivity and sorptivity of samples exposed to oven-dried samples were less sensitive compared to permeability, where the effect of drying-induced microcracks on transport properties was investigated.

2.5 Numerical modelling based on image analysis of microcracks

Researchers have proposed several approaches that combine numerical simulations and experimental imaging techniques to model complex microcracking in heterogeneous cementitious materials. For instance, Ren et al., (2018) performed a study where in situ X-ray computed micro-tomography was applied to characterise the 3D microstructure and cracking behaviour of concrete under progressive uniaxial compressive loading. The images were subsequently processed and used to build microscale realistic 3D finite element (FE) models. A finite element simulation of uniaxial compression was then conducted, and the results were compared to the in situ μ -CT compression test results. Following that, the same image-based model was used to simulate the effect of tensile loading to investigate cracking behaviour. A similar study was carried out by Nguyen (2015). He proposed a three-dimensional numerical model to predict the initiation and the propagation of microcracks at the scale of the actual microstructure of a real sample subjected to compression. The predictions were validated by direct comparison with the actual crack network characterized using 3D imaging techniques.

Chapter 3

Methodology

In this chapter, the materials and experimental procedures used in this thesis are described. Details of sample preparation, linear shrinkage measurement, imaging techniques and image analysis approaches are introduced. The described methodology is mainly related to the experiments presented in Chapter 7 and 8.

3.1 Materials, sample preparation and conditioning

3.1.1 Materials

Ordinary Portland cement CEM I 52.5 R, CEM I 52.5R with 9% by mass replacement of silica fume (SF), and pre-blended CEM III/B 42.5N with 70% ground granulated blast furnace slag (GGBS) were used as the main binders. The oxide composition (XRF), loss on ignition, specific gravity and fineness of CEM I, SF and CEM III are shown in Tables 3-1 and 3-2. The calculated Bogue composition of CEM I 52.5R was 53.1% C3S, 19.1% C2S, 10.8% C3A, 7.2% C4AF by mass.

Materials	Oxide composition (%)											
	CaO	SiO ₂	Al ₂ O ₃	Fe ₂ O ₃	MgO	Na ₂ O	K ₂ O	SO ₃	Cl-	TiO ₂	P ₂ O ₅	Mn ₂ O ₃
CEM I 52.5 R	63.4	20.8	5.4	2.4	1.5	0.3	0.7	2.9	<0.1	-	-	-
CEM I 32.5 R	63.4	20.6	5.6	2.4	1.6	0.2	0.7	2.9	< 0.1	-	-	-
CEM III/B 42.5N	48.0	29.2	8.9	1.2	4.8	0.2	0.6	2.6	0.1	-	-	-
Silica fume	0.15	98.7	0.31	0.02	0.04	0.09	0.30	-	-	0.39	0.02	0.01

Table 3-1 Oxide composition of cementitious materials.

Materials	Loss on ignition [%]	Specific gravity	Fineness[cm ² /g]
CEM I 52.5 R	2.1	2.910	3.06
CEM I 32.5 R	2.1	2.905	3.06
CEM III/B 42.5N	1.4	4.635	2.90
Silica fume	0.47	-	2.30

Table 3-2 Loss on ignition, specific gravity and fineness of cementitious materials.

Additionally, an ordinary Portland cement CEM I 32.5R was used for selected samples of cement pastes and mortars prepared for assessment of different 3D imaging techniques in Chapter 4. The calculated Bogue composition of CEM I 32.5R was 52.7% C₃S, 19.3% C₂S, 10.6% C₃A, 7.4% C₄AF by mass. The oxide composition, loss on ignition, specific gravity and fineness of CEM I 32.5R are presented in Tables 3-1 and 3-2.

A polycarboxylate-based superplasticiser admixture (Sika[®] ViscoCrete 20RM) that complies with British Standards (BS EN 934-2) was used to improve the workability of low water to binder mixes. It has a density of 1.01 kg/l and water-soluble chloride content and alkali content of <0.10% and <0.35% respectively.

Thames Valley sand with maximum particle size of 2.5 and 5 mm were used as fine aggregates, and Thames Valley gravel with maximum size of 5 mm, 10 mm and 20 mm were utilised as coarse aggregates. Additionally, CEN reference sand with maximum aggregate size of 2.5 mm was used to prepare mortars for evaluation of different strategies for introducing microcracks (Chapter 4). The particle size distributions of the fine and coarse aggregates are shown in Figure 3-1. The sieve analysis showed that gravel complied with British Standards overall grading (BS EN 12620), and the sand complied with the recommended medium grading (BS 882). The specific gravity at saturated and surface dry condition (SSD), 24-hour absorption, and moisture content of the aggregates are given in Table 3-3.

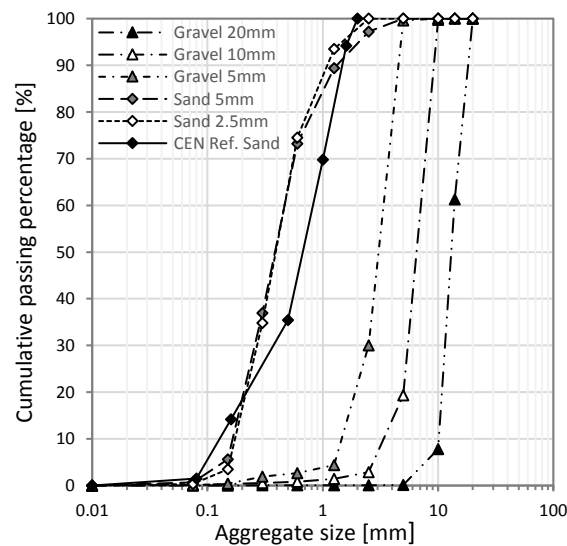


Figure 3-1 Grading curves for fine and coarse aggregates.

Aggregate type	Max agg size (mm)	Specific gravity	24-hr absorption (%)	Moisture content (%)
Sand	2.5	2.45	0.86	0.20
	5	2.56	0.80	0.20
Gravel	5	2.68	0.79	0.50
	10	2.70	0.76	0.45
	20	2.74	0.72	0.40

Table 3-3 Specific gravity, moisture content and absorption values for fine and coarse aggregates.

3.1.2 Mix proportions

Mixes prepared in this thesis are tabulated in Table 3-4:

Designation	w/b	MSA [mm]	Agg. vol fraction [%]	Water [kg/m ³]	CEM I [kg/m ³]	CEM III [kg/m ³]	Silica fume [kg/m ³]	Sand [kg/m ³]	Gravel [kg/m ³]	SP [kg/m ³]
0.20C-10/68	0.20	10	68	117	586	-	-	718	1077	12
0.25C-10/68	0.25	10	68	136	542	-	-	718	1077	8
0.30C-10/68	0.30	10	68	151	503	-	-	718	1077	5
0.35C-10/68	0.35	10	68	165	470	-	-	718	1077	2
0.40C-10/68	0.40	10	68	176	441	-	-	718	1077	-
0.45C-10/68	0.45	10	68	186	413	-	-	718	1077	-
0.30C-5/68	0.30	5	68	151	503	-	-	702	1053	5
0.30C-20/68	0.30	20	68	151	503	-	-	724	1086	5
0.30C-10/50	0.30	10	60	188	625	-	-	636	954	6
0.30C-10/60	0.30	10	50	236	786	-	-	528	792	8
0.20SF-10/68	0.20	10	68	117	534	-	53	718	1077	12
0.25SF-10/68	0.25	10	68	133	485	-	48	718	1077	8
0.30SF-10/68	0.30	10	68	149	451	-	45	718	1077	5
0.35SF-10/68	0.35	10	68	162	422	-	42	718	1077	3
0.40SF-10/68	0.40	10	68	174	396	-	39	718	1077	-
0.45SF-10/68	0.45	10	68	183	371	-	37	718	1077	-
0.30SF-5/68	0.30	5	68	149	451	-	45	702	1053	5
0.30SF-20/68	0.30	20	68	149	451	-	45	724	1086	5
0.30SF-10/50	0.30	10	60	185	560	-	56	636	954	6
0.30SF-10/60	0.30	10	50	232	703	-	70	528	792	8
0.20S-10/68	0.20	10	68	113	-	567	-	718	1077	11
0.25S-10/68	0.25	10	68	132	-	526	-	718	1077	8
0.30S-10/68	0.30	10	68	147	-	489	-	718	1077	5
0.35S-10/68	0.35	10	68	160	-	458	-	718	1077	2
0.40S-10/68	0.40	10	68	172	-	430	-	718	1077	-
0.45S-10/68	0.45	10	68	181	-	403	-	718	1077	-
0.30S-5/68	0.30	5	68	147	-	489	-	702	1053	5
0.30S-20/68	0.30	20	68	147	-	489	-	724	1086	5
0.30S-10/50	0.30	10	60	182	-	608	-	636	954	6
0.30S-10/60	0.30	10	50	229	-	764	-	528	792	8
Ref0.50C-10/68	0.50	10	68	194	388	-	-	718	1077	-

Table 3-4 Mix proportions.

Absolute volume method was used to determine the proportions of cements, silica fume, tap water, fine aggregate, coarse aggregates and superplasticiser for all mixes. This method assumes that the volume of a fully compacted sample equals the sum of the volumes of all ingredients (Neville, 1995). Samples were carefully compacted layer by layer on a vibrated table to remove entrapped air. However, it is difficult to achieve a full compaction especially for concretes with low water to binder. Hence, an entrapped air content of 1-2% vol. was assumed for each mix.

Table 3-3 shows that all of the aggregates used had moisture content lower than the 24-hr absorption. Therefore, it is important that the mix design considers the amount of water absorbed by the aggregates when the concrete is in the fresh state. This is to ensure that the targeted free w/b ratio is achieved. The additional water required to bring the aggregates to SSD condition is the difference between 24-hr absorption and moisture content.

Trials were carried out to determine the amount of superplasticiser required to achieve good compaction for stiff mixes. The amount of superplasticiser used was 2%, 1.5%, 1% and 0.5% by mass of the binder for concrete mixes with w/b of 0.20, 0.25, 0.30 and 0.35 respectively. Concrete mixes with w/b ratio of 0.40 and 0.45 did not required application of superplasticiser.

The following samples were prepared:

- CEM I, CEM I with 9% of silica fume and CEM III concrete samples with w/b ratio of 0.20, 0.25, 0.30, 0.35, 0.40 and 0.45 (MSA: 10 mm, aggregate fraction: 68%, age: 14 days). These samples were used to study the effect of water to binder ratio on autogenous shrinkage and shrinkage induced microcracking.
- CEM I, CEM I with 9% of silica fume and CEM III concrete samples with aggregate volume fraction of 50%, 60% and 68% and MSA at 5 mm, 10 mm and 20 mm (w/b: 0.30, age: 14 days). These samples were cast to study the effect of aggregate size and aggregate content on autogenous shrinkage deformation and autogenous shrinkage-induced microcracking.
- CEM I, CEM I with 9% of silica fume and CEM III concrete samples (w/b: 0.30, MSA: 10 mm, aggregate fraction: 68%). For each mix, five replicates were prepared and imaged after 1, 3, 7, 14 and 28 days from casting, in order to study the effect of age on microcracking induced by autogenous shrinkage.
- CEM I, CEM I with 9% of silica fume and CEM III concrete samples (w/c: 0.30, age: 14 days, MSA: 10 mm, aggregate volume fraction: 68%). These samples were cast into cylindrical moulds of 65 mm height and diameter of 95, 50 and 25 mm to study the influence of sample size on characteristics of microcracks caused by autogenous shrinkage.

The sample designation used in this thesis is shown in Figure 3-2.

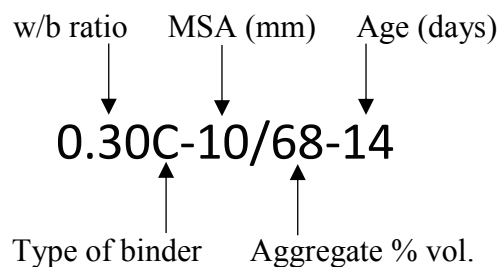


Figure 3-2 Sample designation.

3.1.3 Mixing, casting and conditioning

Cement and aggregates were first dry mixed for around 30 seconds in a 30-litre capacity pan mixer. Water was then added and mixed for a further 3 minutes. For mixes with low water to binder ratio (w/b = 0.20, 0.25, 0.30, 0.35) that required superplasticiser, the admixture was mixed with the batch water before adding into the dry ingredients. For mixes containing silica fume, the silica fume was first dispersed in water or in water with superplasticiser and then mixed with dry ingredients. A vibrating table with adjustable frequency was used

for compaction. Samples were cast in moulds, compacted in three layers and each layer was vibrated until no significant release of air bubbles. All the mixes produced were easily compacted with no evidence of significant bleeding or segregation.

Because the work presented in Chapter 7 was dedicated to the study of microcracking induced by autogenous shrinkage, it was essential to isolate this phenomenon from other external influences such as drying shrinkage. Therefore, the specimens were sealed to prevent moisture exchange with the environment from the moment of casting until the end of the experiments. This was achieved by casting samples in polythene lined postal tubes with end caps, or in plastic containers with lids as moulds. This approach is also advantageous from an economical and practical consideration since the study required the preparation of a large number of samples cast in single-use moulds.

The test methods employed in this thesis required specified sample size and geometry. Three replicate cylinders were cast for linear deformation measurements and disc-shaped samples were prepared for 2D imaging with LSCM and 3D imaging with X-ray microtomography. In total, 90 cylindrical samples and 48 disc samples were prepared and tested.

Cylindrical specimens were cast in purpose-made moulds with diameter of 78 mm and height of 300 mm for linear deformation measurement. The moulds were made of stiff cardboard postal tubes (3-inch size) with plastic end caps. The tubes were internally lined with a waterproof polythene sheet to avoid leakage and reduce friction between sample and mould. A hole of approximately 6 mm in diameter was drilled in the middle of each end cap. This was done to allow a steel stud ($\text{Ø}5$ mm and 16.5 mm length) to be attached through each end cap which is then sealed using melting wax. During casting, the moulds were filled with fresh concrete and compacted in three layers, then sealed with the end caps. This produces samples with half of the stud embedded in concrete and the other half protruded to allow length change measurements. Small sized studs were chosen to ensure good bonding and to avoid generating large restraints when the concrete shrinks. Geometry of the stud, end cap and tube are shown in Figure 3-3.

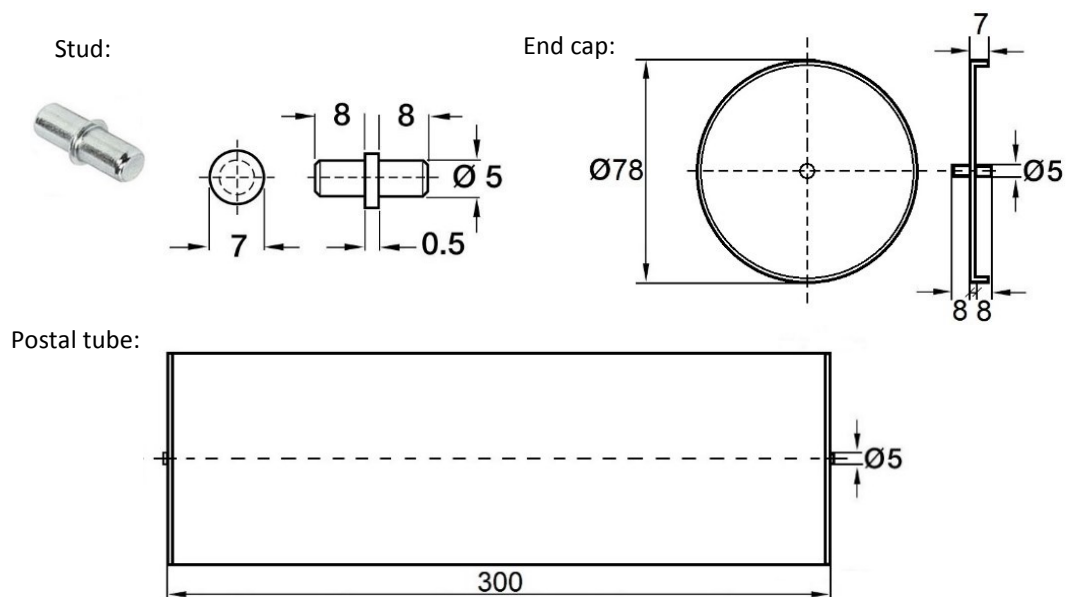


Figure 3-3 Geometry of the stud, end cap and postal tube used to prepare concrete cylinders for linear deformation measurement. (All dimensions in mm).

The cylinders were placed horizontally in a temperature-controlled laboratory at $21 \pm 1^\circ\text{C}$, 50% RH for sealed curing. The mass of the cylinders was frequently monitored in order to check that the sealed curing is effective. Figure 3-4 presents the mass changes plotted over time for three exemplary mixes. Results show that a small amount of mass loss has occurred. At the age of 70 days, concrete with neat CEM I, CEM I with silica fume and CEM III lost about 0.33%, 0.32% and 0.37% respectively. This is a negligible amount, perhaps caused by a slight but inevitable moisture loss to the environment. It can be also explained as a drift in accuracy of the laboratory scales ($\pm 0.1\text{g}$).

Cylindrical samples were also prepared in plastic containers of 95 mm diameter and 65 mm height or 30 mm diameter and 65 mm height for 2D imaging with LSCM and 3D imaging with X-ray microtomography respectively. These containers were sealed with plastic lids and additionally wrapped with a cling film to prevent any moisture exchange with the environment. The sealed samples were then placed in a temperature-controlled laboratory at $21 \pm 1^\circ\text{C}$, 50% RH for sealed curing until the required age.

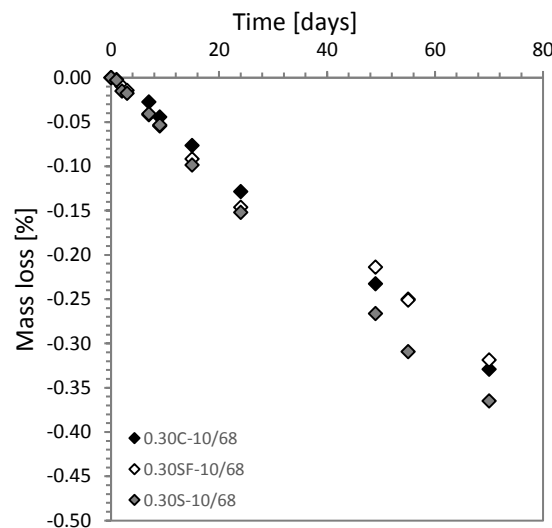


Figure 3-4 Examples of mass change of sealed cured concrete cylindrical specimens.

3.2 Linear deformation measurement

Quantification of autogenous shrinkage was carried out to assess the possibility of internal cracking due to volumetric changes in concrete. In this study, the linear contact method was adopted to measure longitudinal deformation of the cylindrical concrete specimens. The measurement was carried out on a length comparator device with a 1/1000 mm digital gauge and a 300 mm invar bar used for calibration purposes. A schematic illustration of this set up is presented in Figure 3-5 a). Additionally, a thermometer and hygrometer were used to monitor the temperature and humidity of the laboratory.

The device was calibrated with the 300 mm invar bar prior to each length measurement. The specimen with embedded two steel studs at each end was placed at the bottom end of the length comparator and aligned with the upper indicator spindle, which was slowly released until it touched the upper steel stud of the specimen. This is shown in Figure 3-5 b) and c). When the reading from the digital gauge stabilises, the actual length of the specimen is the reading plus 300 mm (the invar bar length).

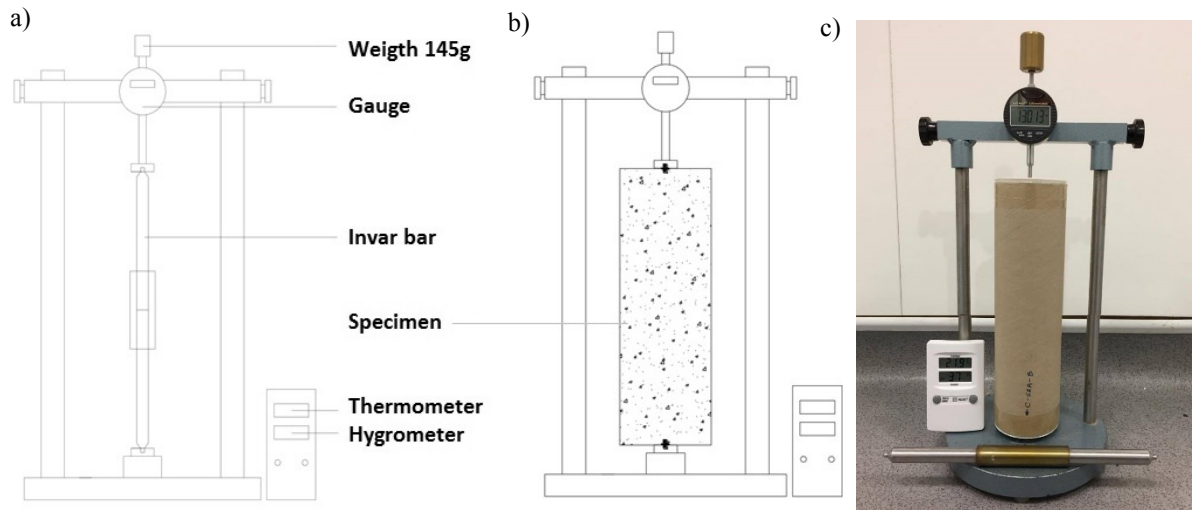


Figure 3-5 Linear deformation measurement using length comparator: a) calibration with invar bar, b) length measurement of cylindrical concrete specimen, and c) a photo of laboratory set up.

The initial length measurement (L_0) was taken after initial set of concrete, which is approximately 6 to 12 hours after casting depending on the type of binder used in the concrete mix. Subsequent readings (L_n) were taken daily for the first two to three weeks and then weekly or longer for a total period of at least 70 days. Three replicate specimens were prepared and measured for each concrete mix, and the device was calibrated (reset) with invar bar after each reading.

Based on the measurements, linear deformation was calculated using Equation 3-1

$$\varepsilon = \frac{L_0 - L_n}{L_0} \times 1000000 \quad (\text{Eq. 3-1}).$$

Where, ε is the linear deformation (μstrain), and L_0 with L_n are respectively, the first and the subsequent readings after the initial set of concrete (mm). An average linear deformation was calculated from the three measurements over time for each concrete mix.

3.3 2D and 3D microscopy techniques

Laser scanning confocal microscopy (LSCM) and X-ray microtomography ($\mu\text{-CT}$) were used to image microcracks in two and three-dimensions. The following sections explain in detail the sample preparation and imaging procedures for both techniques.

3.3.1 Sample preparation for imaging

LSCM is able to image only microcracks and pores that are filled with fluorescent resin. Therefore, an appropriate sample preparation is required prior to imaging using this technique to ensure that all microcracks present in the sample are captured. Figure 3-6 shows a flow chart summarising the sample preparation procedure.

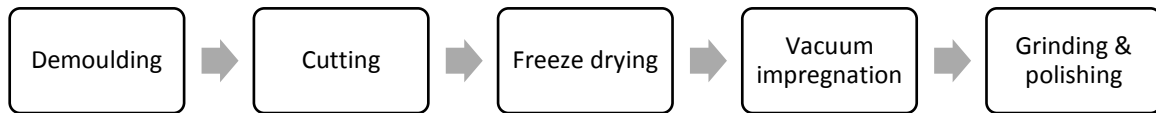


Figure 3-6 Sample preparation for imaging using LSCM.

At the required age, the disc-shaped sample is removed from its mould and sectioned with a diamond saw to extract a $65 \times 95 \times 8$ mm slice from the centre. This is so that the degree of internal microcracking can be observed on the cross-section. The slice is then dried prior to impregnation with fluorescent resin. There are a number of drying methods available and this requires careful consideration for this study. Severe drying techniques such as oven drying (typically at temperatures ~ 50 to 105°C), drying at low relative humidity and microwave drying can remove evaporable water effectively, but they can also alter the microstructure by accelerating cement hydration and increasing capillary pressure. In addition, they may induce microcracking as a result of tensile stresses deformation from differential thermal expansion or volumetric shrinkage between the aggregates and hardened cement paste (Zhang and Scherer, 2011). Vacuum drying also induces tensile stresses and microcracking similar to those found in oven-dried samples as reported by Gallé (2001). Additionally, this technique is slow and thus cannot effectively arrest early age hydration at the desired time. Other techniques such as D-drying, P-drying and solvent exchange methods are time consuming and may last up to several weeks depending on sample size, porosity and diffusivity of the solvent (Zhang and Scherer, 2011). The long time needed for D- or P-drying or solvent exchange to be complete for concrete slices of $65 \times 95 \times 8$ mm is unacceptable, especially when the samples ought to be examined at the age of 1, 3, 7 and 14 days.

Considering the factors above, it was decided that the most appropriate method is freeze-drying, which removes water by sublimation. The sample is first rapidly frozen by immersion in liquid nitrogen (-196°C). The frozen sample is then placed into a freeze dryer under vacuum, where the solid ice crystals sublime directly to vapour without passing through the liquid state. This eliminates the risk of damage caused by capillary stresses induced by pore water meniscus (Zhang and Scherer, 2011). The freezing process itself could potentially be damaging because of stresses from volume expansion, hydraulic pressure, and crystallization pressure (Marchand, et al., 1995). However, the risk of this is reduced because rapid freezing avoids the formation of large ice crystals in the pore structure. As observed using SEM in a study by Collier et al. (2008), the microcracks present in freeze-dried samples are very small, approximately of $0.1 \mu\text{m}$ in width, which is beyond the detectability by X-ray microtomography or LSCM.

The cut slices were weighed and immersed directly in liquid nitrogen (-196°C) for approximately 20-30 min until there was no significant bubbling. This indicates that the freezing process has completed. The frozen slices were then transferred into a Lyotrap freeze dryer and kept at -30°C and ~ 7 kPa pressure. Under these conditions, water will be removed effectively within 5 to 7 days, depending on the sample composition (especially, the water to binder ratio) and curing age. Typically, $\sim 70\%$ of the removable water is sublimated in the first 24 hours according to the daily weight measurements. After drying, the slices were allowed to return to room temperature and atmospheric pressure gradually, and then impregnated with fluorescent resin following a 2-step impregnation method developed by Wong and Buenfeld (2006).

A low-viscosity fluorescein-dyed epoxy resin was prepared by adding a fluorescein dye (Struers Epodye) into epoxy resin (Araldite AY103) at 5 grams per 1 litre of resin and mixed with a magnetic stirrer for one day to ensure uniform dispersion of the dye. The fluorescent epoxy was then heated up to 40°C prior to mixing with hardener and toluene. The proportion of resin: hardener: toluene used was 25: 3: 1.5 by mass. Toluene was used to reduce viscosity of the resin. The edge and bottom sides of the slice were sealed with two layers of waterproof adhesive tape, and then de-aired in vacuum (1 bar below atmosphere) for 40 minutes. Next, the prepared resin was poured onto the sample to cover its entire surface without breaking its vacuum. The vacuum was then released and a compressed air at 0.25 MPa above atmospheric pressure was applied to push the resin further into the sample. Figure 3-7 schematically shows the epoxy impregnation procedure. The impregnated sample was cured at room temperature for 2 days to allow proper hardening of the epoxy. The fluorescent epoxy resin penetrates the sample via microcracks and pores, and protects the sample from further damage during subsequent grinding and polishing operations.

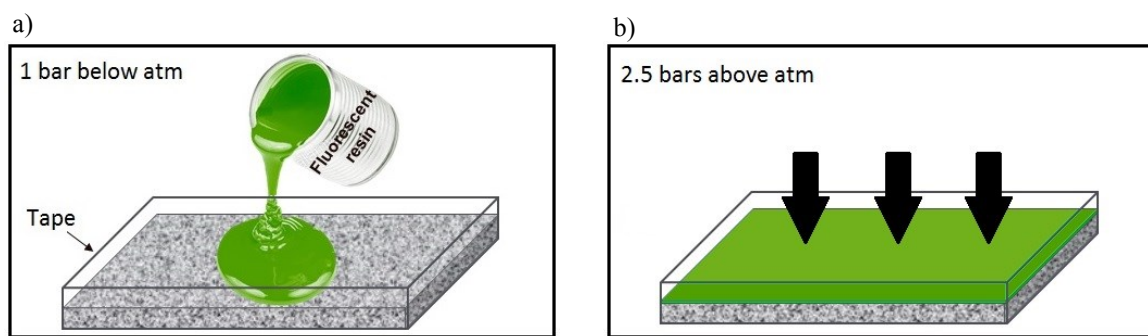


Figure 3-7 Illustration of the impregnation procedure: a) impregnation under vacuum, b) application of additional pressure to push the resin farther into the sample.

After the resin has hardened, the impregnated slice was ground and polished on the Struers LaboPol-5 polishing machine at successively finer size. The slice was ground using diamond disc (Struers MD –Piano) of grit sizes 120, 240, 500 and 1200, and then polished with diamond pastes of 9, 6, 3 and 1 µm fineness on polishing cloths to obtain a flat surface for imaging. Figure 3-8 shows examples concrete slices after a) freeze drying, b) vacuum impregnation and c) grinding and polishing.

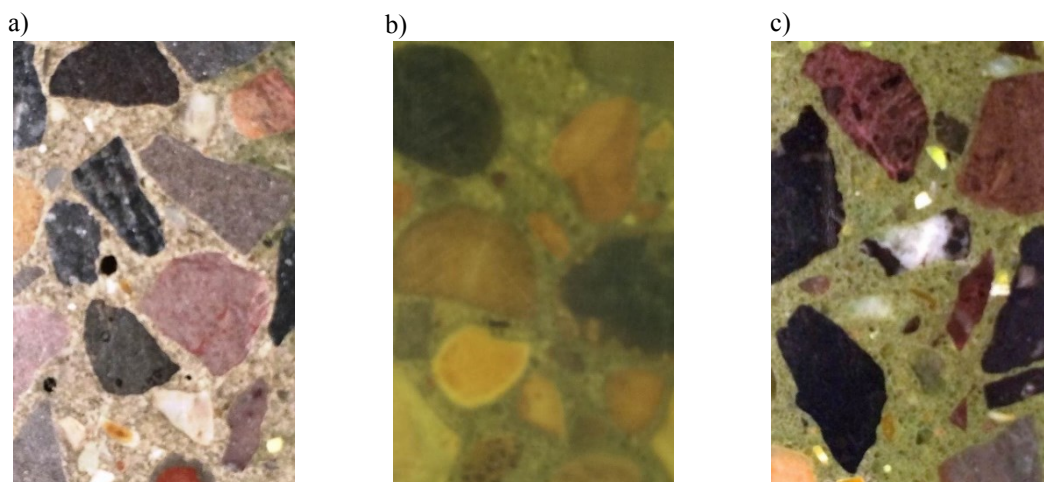


Figure 3-8 Preparation of epoxy impregnated flat polished concrete sections for microscopy. The images were obtained after: a) cutting and freeze drying, b) vacuum impregnation and c) grinding and polishing.

Sample preparation for microscopy may induce some additional microcracking, especially during the initial diamond saw cutting and freeze-drying with liquid nitrogen steps. However, the possibility of preparation-induced microcracking is reduced by epoxy impregnation because the hardened epoxy provides protection and preserves the microstructure. Furthermore, if the mechanical grinding and polishing stages produce new microcracks, these would not be epoxy-filled and therefore will not be imaged with LSCM.

A reference sample was prepared in order to assess the potential damage caused by sample preparation. The reference sample was prepared with CEM I 52.5R, coarse (10 mm) and fine (5 mm) aggregate at 68% vol. fraction and water to cement ratio of 0.50. It was cast in a cylindrical mould ($\text{\O}100$ mm, height 50 mm), demoulded after initial 24 hours and cured in saturated calcium hydroxide for 14 days. The sample was then sectioned, freeze-dried, epoxy impregnated, ground and polished following the same procedures that were applied to sealed-cured samples. A proper wet curing and high w/c ratio should minimise autogenous shrinkage and avoid internal cracking, so any microcracks present in the reference sample is likely due to sample preparation. The polished sample was imaged using LSCM, and microcracks were characterised by image analysis (see Sections 3.3.2 and 3.4.1 for more details). The results show that the reference samples contained some amount of microcracking, but these are small, short, and spatially distributed. The measured dendritic density and area fraction of these microcracks is only 0.06 mm/mm² and 0.07% respectively. About 95% of all microcracks have widths below 20 μm (average width 11.5 μm) and 90% have lengths below 250 μm (average length 121 μm). These values have to be kept in mind when characterising autogenous shrinkage-induced microcracks. Unfortunately, there is no other way to omit this problem since fluorescence microscopy requires fluorescent resin impregnation.

X-ray microtomography requires a much simpler sample preparation. This is because the technique is non-destructive and does not require special sample preparation techniques. Furthermore, the sample can be imaged as is, without requiring any pre-drying unlike fluorescence microscopy. It can image any shape and sample volume in a range from hundreds of μm^3 to tens of cm^3 . However, the resolution decreases with increase in sample volume. Therefore, it was decided that 30 mm diameter cores of concrete will be prepared for scanning. The samples were either cast into a plastic container of $\text{\O}30$ mm and height 65 mm or drilled from larger volume (cylindrical samples of $\text{\O}95$ mm, height 65 mm).

3.3.2 Imaging with LSCM

Laser scanning confocal microscopy (LSCM) was used to image and characterise microcracks in two-dimensions in this study because it can image a large area of the sample cross-section at a good resolution and in a relatively short time. The fluorescent resin impregnated samples were imaged using a Leica TCS SP5 LSCM with an objective lens of 5 \times magnification. The theoretical resolution and achievable field of view of the objective lens is 1.30 μm and 3.10 \times 3.10 mm², respectively. Each sample was placed on the motorized scanning stage of the microscope. Then, the sample was levelled to ensure even brightness and focus of the captured images, while the entire area (65 \times 95 mm²) was imaged. This was achieved using several layers of adhesive tape on the underside of the sample.

An argon laser line of 488 nm was used to excite the fluorophores in the fluorescent resin impregnated sample and the beam splitter was configured to a range of 500 nm to 600 nm to allow the emitting fluorescence to be collected by the PMT. The laser intensity was set to 15% and the PMT sensitivity was adjusted correspondingly to prevent oversaturation. The pinhole aperture was maintained at 1 Airy unit and a zoom factor of 1× was adopted while imaging, which corresponds to 50× overall magnification. The images were digitised to 2048 × 2048 pixels at a pixel spacing of 1.5144 µm. The entire surface area of the sample was captured in tiles with 10% of overlapping, and this required 600 images (a mosaic of 20 × 30 images) per sample.

These settings were kept consistent for all samples to ensure repeatability. An example of three consecutive fluorescent images captured using the LSCM at 10% overlap is shown in Figure 3-9. The images captured in tile scans were aligned and then stitched to produce a large montage of the entire epoxy-intruded area using Image J with Grid/Collection Stitching plugin (Stitching plugin).

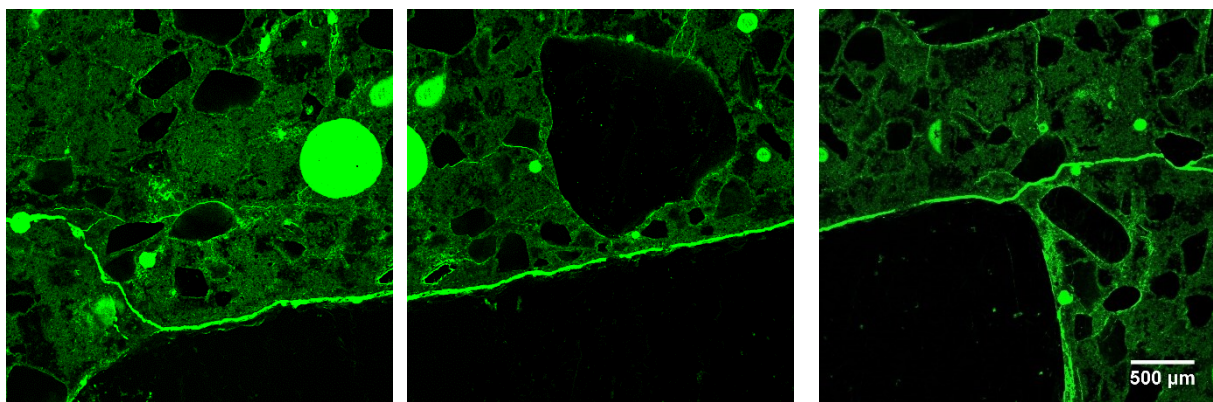


Figure 3-9 Example of consecutive fluorescence images captured by LSCM at 10% edge overlap.

3.3.3 Imaging with X-ray microtomography

X-ray microtomography was carried out using the Metris X-Tek HMX ST 225 CT scanner available in the Natural History Museum in London. The concrete core was mounted on the rotating stage between the cone beam of the X-ray source and the detector that has a matrix of 2000 × 2000 pixels. The stage was positioned in a way to achieve maximal geometrical magnification while maintaining an optimal fitting of the whole sample into the field of view. This was obtained (for Ø30mm cylindrical samples) at the X-ray source to sample distance and sample to detector distance of 91.5 mm and 1088 mm, respectively. The rotation step was set at 0.1146°, thus 3142 projections were acquired with exposure time of 1.25 seconds per frame. The voltage and current of the X-ray source were set at 220 kV and 200 µA respectively, due to high density of the scanned material. Additionally, a 5 mm thick copper filter was applied to improve image quality by removing low-energy X-rays which do not provide useful information.

The imaging process was completed within 65 min per sample. This was followed by an automated mathematical image reconstruction using the PRO Metris X-Tek software, which is accomplished by correcting for centre shift (offset of the axis of rotation) and beam hardening effects (an increase in mean X-ray energy of the X-ray beam as it passes through the scanned object). The reconstructed image volume with 15.52 µm voxel

size resolution was achieved and the result was saved as 2D reconstructed slices in 16-bit tiff files. An example of the reconstructed 3D image is presented in Figure 3-10 in orthogonal views and as a 3D rendering.

All concrete cores were scanned with the same settings and their 3D images were processed by means of an image analysis to quantify the observed microcracks in 3D.

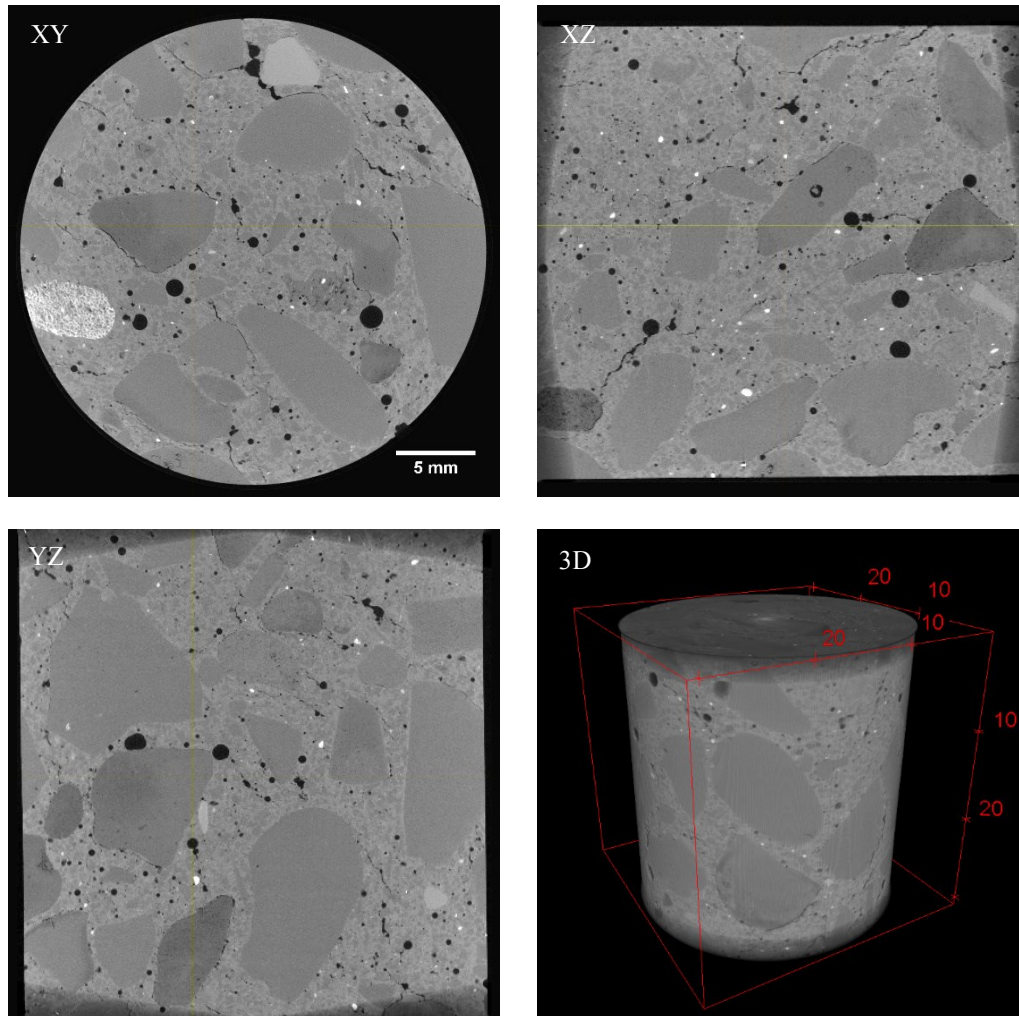


Figure 3-10 An example of concrete core scanned by X-ray microtomography. The orthogonal views in XY, XZ and XY directions with 3D rendering.

3.4 Image analysis

Microcracks were imaged in two and three dimensions using fluorescence LSCM and X-ray microtomography respectively. The characteristics of the microcracking were obtained by applying quantitative image analysis. This generally consists of: a) image pre-processing, where the microcracks are segmented and separated from other porous features based on size and shape characteristics, and b) quantifying parameters such as the microcrack density, area/volume fraction, surface area, distribution of crack widths and lengths, orientation/degree of anisotropy, connectivity and tortuosity (in the case of 3D imaging).

3.4.1 2D image analysis

Images collected with LSCM were pre-processed to obtain binary images that consists of only microcracks. Figure 3-11 presents a flow chart summarising the main steps in this process and Figure 3-12 presents example images at different stages of the procedure.

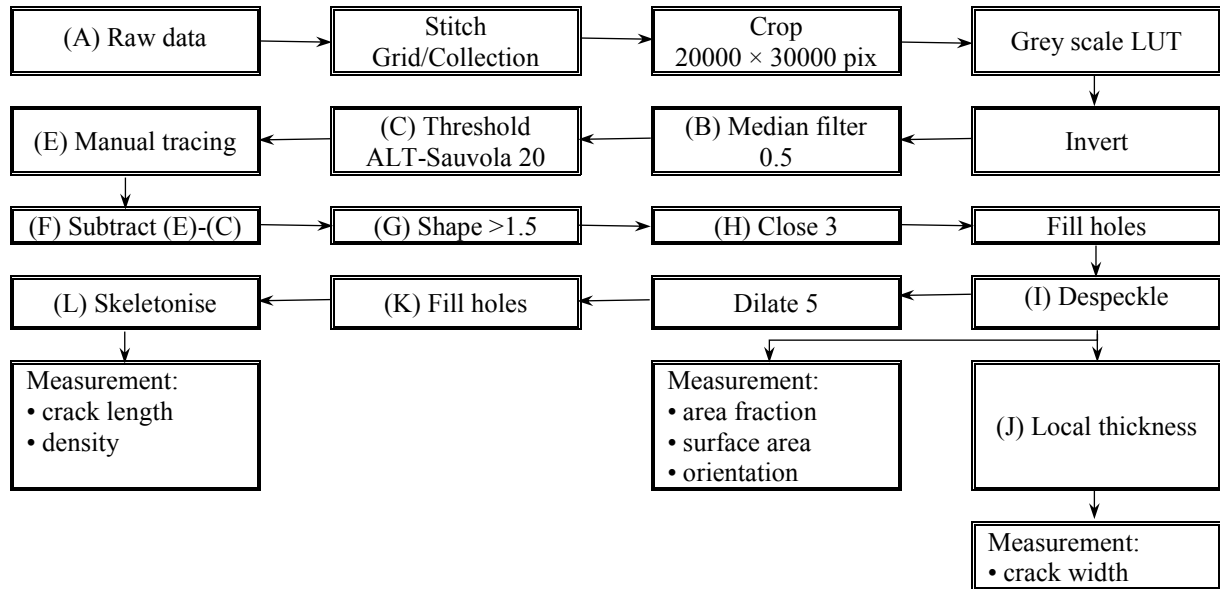


Figure 3-11 Flow chart showing the main steps of image pre-processing.

The raw data (Figure 3-12-A) were first stitched into a montage image of the entire area of the sample. Then a sub-area was cropped to exclude edges because these tend to be out of focus and noisy. The cropped images were converted to grey scale and inverted to highlight features of interest. Additionally, a median filter of 0.5×0.5 was applied to remove noise. An example is shown in Figure 3-12B.

The grey scale images were subsequently thresholded with an auto local threshold, which applies different threshold values to different parts of the image. This type of segmentation method was chosen because imaging such a huge area inevitably produces images with slight variation in brightness intensity. The Sauvola method (Sauvola and Pietaksinen, 2000) with radius of 20 pixels was adopted to all images and the method was implemented in Image J. An example of thresholded image is shown in Figure 3-12-C.

In the next step, the microcracks were separated from other porous features by manual tracing. The tracing was done on the thresholded image enlarged to 1:1 scale montage image in Avizo Fire with a Brush tool. Using different brush sizes and referencing grey scale images as a mask enable us to select only those regions with microcracks that are clearly visible in the enlarged image and can be differentiated from other porous regions. The adopted microcrack separation procedure is a very time consuming process, but is the most reliable method. The tracing procedure and traced microcracks are presented in Figures 3-12-D and 3-12-E respectively.

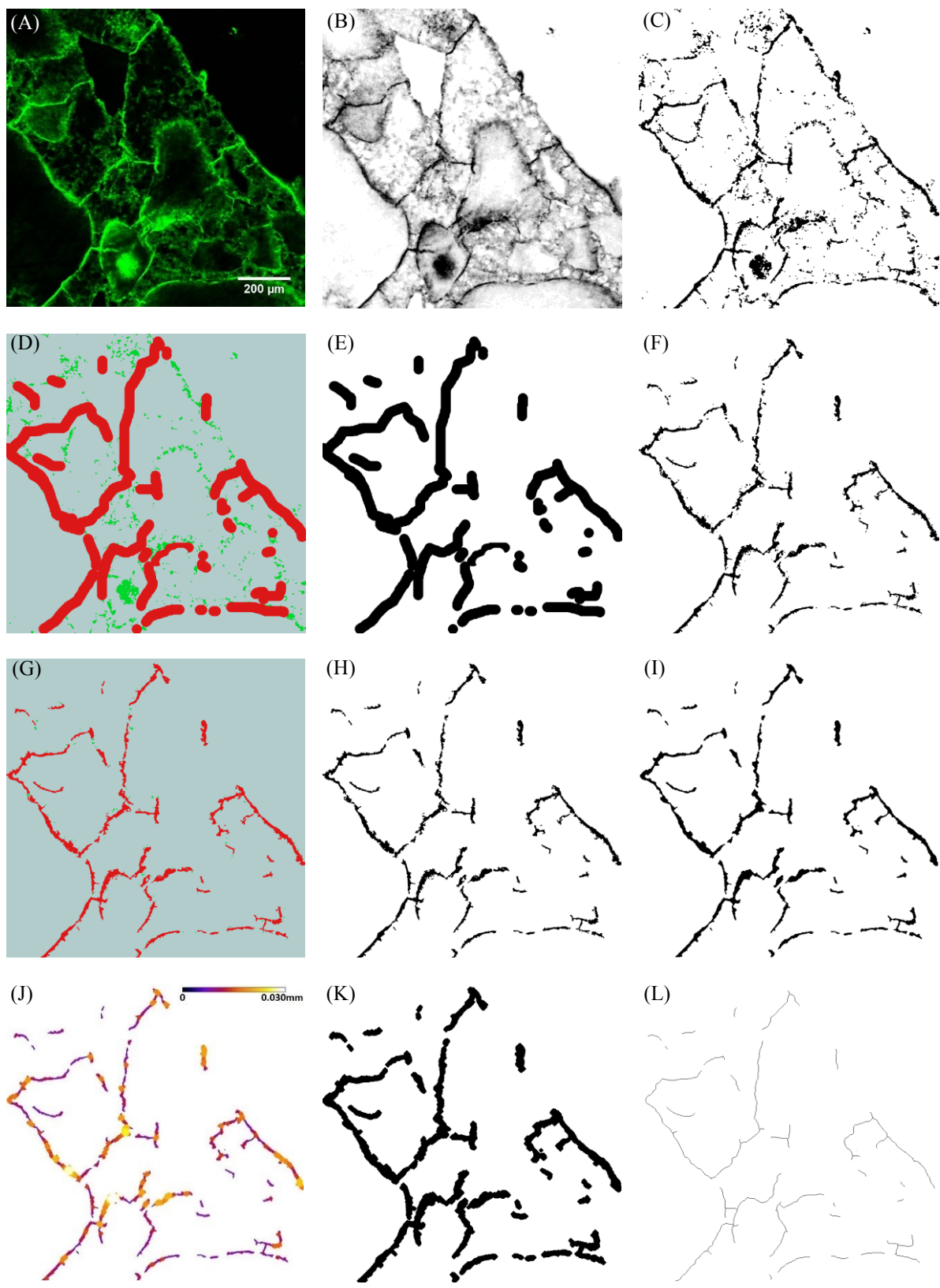


Figure 3-12 Image processing: A) raw data, B) grey scale LUT & invert & median filter 0.5, C) ALT Sauvola 20, D) manual tracing, E) traced microcracks, F) subtraction: (E)-(C), G) application of circularity factor (Shape AP: noise $\leq 1.5 >$ microcracks), H) accurate microcracks, I) closing 3 pixels' disc & fill holes & despeckle, J) local thickness measurement, K) dilating 10 pixels' disc & fill holes, L) skeletonisation.

The microcracks were then obtained by subtracting the thresholded image (C) from the traced image (E). The result of the subtraction may still include some undesirable features, such as those seen in Figure 3-13-F. To remove these features, the image was labelled and analysed with sieve analysis in Avizo Fire. In the sieved analysis, a parameter describing circularity of particle (Shape AP) was measured and set to distinguish all circular particles ($\text{Shape AP} \leq 1.5$) coloured in green from elongated microcrack ($\text{Shape AP} > 1.5$) coloured in red. The result of the sieve analysis is presented in Figure 3-12-G.

The images with circular particles removed (e.g. Figure 3-12-H) were subsequently subjected to two morphological operations: closing with three-pixel sized disc as structuring element and filling holes. Additionally, a despeckle filter was applied to remove any remaining noise. The result (shown in Figure 3-12-I) is the final binary image of the microcracks, which is used to measure parameters as area fraction, surface area and orientation of the microcracks.

The quantitative analysis of the microcrack width was carried out by applying local thickness measurements on separated images (Figure 3-12-J). Crack length and density measurements were performed on skeletonised microcracks. To do this, binary images of the microcracks were dilated with ten-pixel sized disc as structuring element and all remaining holes were filled as shown in Figure 3-12-K. This procedure smooths jagged edges of the microcracks, enabling precise skeletonisation. The skeletonised microcracks are presented in Figure 3-12-L.

The main quantified parameters are:

- Area fraction (A_A) was calculated as the ratio between the total area of the microcracks (A_{crack}) to the area of the image (A_{image}).
- Crack density (D_D) was defined as the total length of skeletonised microcracks divided by image area. It can be also expressed as the number of microcracks (N_{crack}) per image area.
- Surface area of the microcracks (SA) was estimated using line intercept count method (LICM) (Huang and Klette, 2004) implemented in Avizo Fire software. This method generates a line probe and searches for an object boundary, then it counts the object-probe intercepts and finally estimates surface area by stereology. From the surface area measurement, two other parameters can be calculated: specific surface area (SSA), which is the ratio between the SA to the total area of the microcracks, and surface density (SD), which is the ratio between the SA of the microcracks to the image area.
- Distribution of crack widths (W) was obtained using local thickness measurement implemented in BoneJ (Doube et al., 2010). It estimates local thicknesses by fitting maximal circle to every point in the structure (Dougherty and Kunzelmann, 2007, Hildebrand and Rüeggsegger, 1997). The circle diameter at each point represents the microcrack width. From these local thicknesses, a mean width (W_{mean}) and distribution of microcrack width can be obtained.
- Length of the microcracks (L) was measured as dendritic length of the skeletonised microcracks, which is the skeletonised crack area divided by the pixel size. Measured values

for each microcrack were used to calculate a mean length (L_{mean}) and distribution of microcrack length.

- Degree of anisotropy (DA), which determines the microcrack orientation, was measured by the intercept method and presented by means of rose of intercepts (Launeau and Robin, 1996). This method is based on counting intercepts between microcracks and test lines drawn on the image montage at regular intervals and at angles: 0° , 45° , 90° , 135° . The total number of intercepts for each angle is divided by the total length of the test line and the results are plotted on a rose diagram.

3.4.2 3D image analysis

3D image analysis is the focus of Chapter 6 and therefore the details of the methodology will be presented in that chapter. Briefly, image pre-processing with algorithm for separating microcracks are proposed and parametrisation approaches are consequently applied to the three-dimensional images. For more details, please refer to Chapter 6.

3.5 Summary

This chapter describes the experimental methods and procedures used in this thesis. Details of materials, mix proportion, sample preparation, conditioning regime to induce microcracking, 2D and 3D imaging techniques with respective sample preparation for imaging and image analysis were presented. The overall experimental programme is summarised in Figure 3-13.

The magnitude of the autogenous shrinkage indicates if the concrete is exposed to a higher risk of internal microcracking. Results from the linear deformation measurements due to autogenous shrinkage will be discussed in Section 7.3.

The autogenous shrinkage induced microcracks were characterised in two-dimensions using fluorescence imaging and image analysis. Samples were impregnated with a fluorescent epoxy, and then imaged with LSCM. The stitched montage images were used to quantify the microcracks in terms of length, width, orientation, density, surface area and area fraction. Results from the analysis will be presented in Section 7.4.

X-ray microtomography was used to image the sample in three-dimensions, but at lower spatial resolution compared to LSCM. The proposed image analysis with developed separation algorithm (Chapter 6) was applied to quantify the microcracks. This includes parameters that cannot be obtained in 2D analysis such as connectivity and tortuosity. The 3D analysis of microcracks will be discussed in Chapter 8.

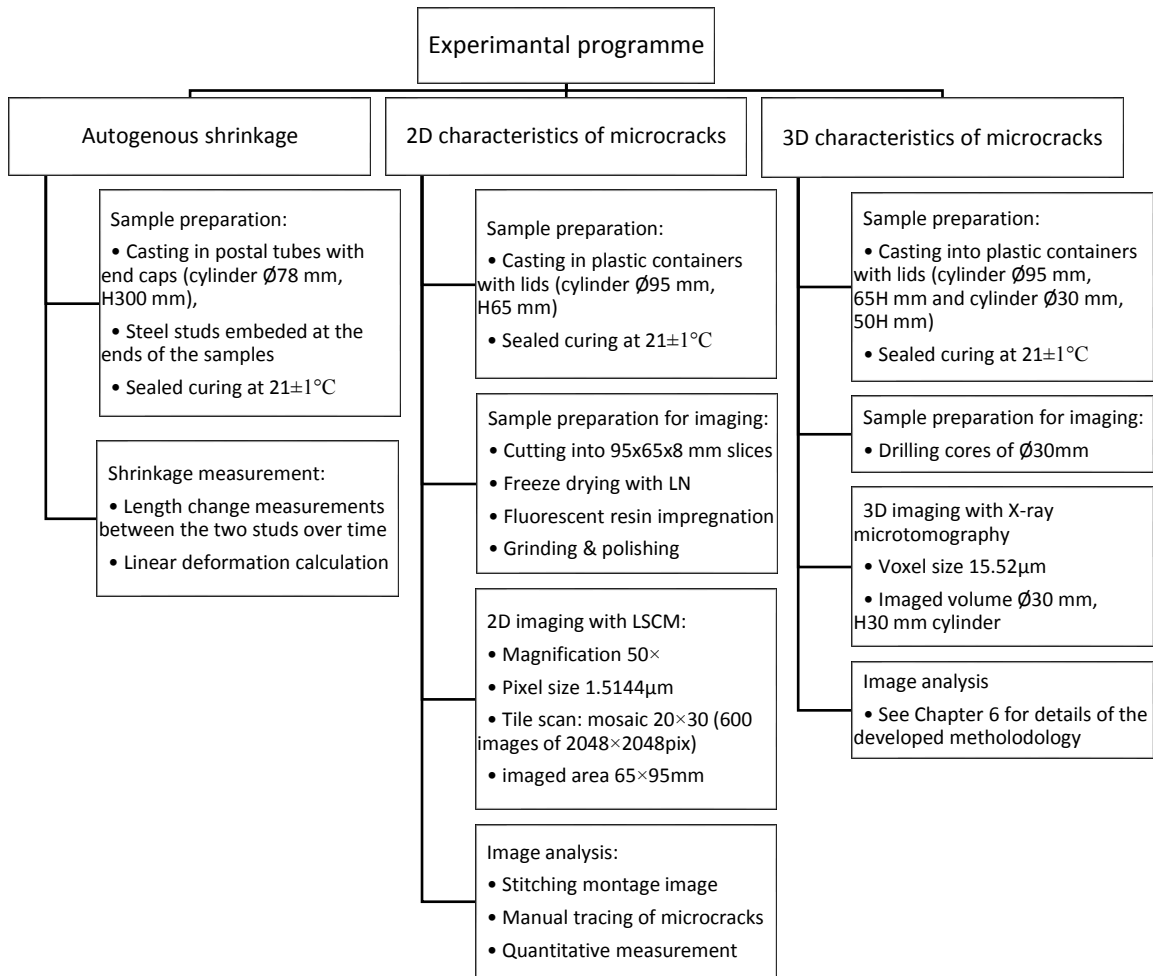


Figure 3-13 Summary of overall experimental programme.

Chapter 4

Assessment of 3D microscopy techniques for imaging microcracks

The aim of this Chapter is to evaluate different ways for inducing microcracking in concrete in the laboratory environment and to examine the feasibility of three-dimensional microscopy techniques for imaging the microcracks. Several types of samples containing different degrees of microcracking induced by drying shrinkage with internal and external restraints, autogenous shrinkage, and freeze-thaw cycles are investigated. A range of three-dimensional microscopy techniques is evaluated including focused ion beam nanotomography (FIB-nt), broad ion beam serial sectioning (BIB), X-ray microtomography (μ -CT) and laser scanning confocal microscope (LSCM). The advantages and limitations of these techniques are discussed.

4.1 Background

Concrete as a widely used construction material is subjected to various forms of deterioration during its service life due to mechanical loading, moisture and thermal gradients, and degradation mechanisms such as alkali-aggregate reactions, sulphate attack, freezing–thawing, and corrosion of reinforcement. These are very often associated with development of microcracks. To-date, the nature of microcracks in cement-based materials is still relatively poorly understood. The main reason for this is the lack of suitable techniques to detect and characterise microcracks. Conventional methods for detecting and characterising microcracks include imaging polished cross sections with scanning electron microscopes (SEM) and optical microscopes (OM). However, these techniques can only observe a two-dimensional cross-section of a three-dimensional structure. This is a major limitation and significantly reduces the insights that can be gained from such analyses. Consequently, three-dimensional imaging techniques should be exploited to fully characterize microcracks.

Focus ion beam (FIB) nanotomography is a well-known and established 3D imaging technique. Nowadays, dual beam SEM-FIB systems are available in many microscopy laboratories. However, only a small number of investigations have applied this technique to cement-based materials.

The next generation of ion beam-SEM instrumentation will probably include a broad ion beam (BIB) source in addition to FIB. The first BIB-cryo-SEM microscope was installed at RWTH Aachen University in Germany (Desbois et al., 2013). As it is a relatively new technique, this instrument has so far only been applied for investigating the microstructure of sedimentary rocks (Desbois et al, 2009 & 2013).

3D imaging with the laser scanning confocal microscopy (LSCM) has been widely applied in biological sciences. However, until now, only a few studies have used this technique in cement and concrete research. This is mainly due to the imaging depth of LSCM in concrete being limited to several microns. Using

the fluorescent mode of the LSCM, 3D imaging of capillary pores, 'Hadley' grains and microcracks in concrete was performed by Head and Buenfeld (2006) and Head et al. (2006, 2008). Various studies have also used the reflected mode of LSCM for characterization of surface roughness of cement-based materials, for example Kurtis et al. (2003), Ficker et al. (2010) and Lange et al. (1993).

X-ray microtomography is a widely used technique in almost every field of materials science. This is mainly because of its non-destructive nature and its ability to image a wide range of material types and sample sizes in three dimensions. Also in cement and concrete research, this method has found a number of applications, including characterization of microstructure of deteriorated mortars due to sulphate attack (Naik et al., 2006), carbonation processes (Han et al., 2012), freezing-thaw action (Promentilla & Sugiyama, 2010) and calcium leaching (Burlion et al., 2006), characterization of pore structure in cement paste (Promentilla et al., 2008) and concrete (Lu et al., 2006), quantitative measurements of crack growth under loading (Landis et al., 2006) and characterization of cement hydration products (Gallucci et al., 2007).

All of these three-dimensional microscopy techniques will be examined in this Chapter to evaluate their feasibility for imaging microcracks in cement-based materials.

4.2 Strategies to generate microcracks

Microcracking is often caused by restrained drying shrinkage. This is particularly true in concrete overlays and slabs where single-sided drying occurs, and the resultant shrinkage is resisted by internal or external restraints. Consequently, one-directional drying at various temperature and relative humidity conditions was chosen as the first strategy to generate microcracks. Several types of sample were prepared. Neat cement pastes and mortars were subjected to drying in a ventilated oven at 30°C and 105°C. Moreover, cement pastes and mortars cast against steel cylinders/rings, which act as an external restraint, were exposed to drying at various relative humidity levels.

A second major source of microcracking is autogenous shrinkage, which is defined as volume change that occurs without any moisture transfer between the sample and the environment (Lura et al., 2003). This is a result of self-desiccation of concrete due to the reduction in internal relative humidity as water is consumed during cement hydration. In normal strength concrete mixes, the magnitude of autogenous shrinkage is relatively small compared to drying shrinkage and so is often ignored. This is not the case for high strength concrete. The increasing use of high strength and high performance concretes containing low water/binder ratio, supplementary cementitious materials and multiple chemical admixtures has highlighted the problem of autogenous shrinkage in these concretes. For this reason, a second proposed strategy for generating microcracks is by producing concrete samples with very low water to binder ratio followed by sealed curing to induce autogenous shrinkage.

Another damaging action affecting concrete is temperature change. Cyclic freeze-thaw is one of the major causes of deterioration of concrete structures especially in regions that experience sub-zero temperature conditions such as the Arctic zone, Scandinavia, Canada, Russia and Northern China. Progressive deterioration due to freezing and thawing of saturated concrete starts with surface scaling and can lead to very severe internal

cracking and ultimate collapse. This is the last alternative strategy to generate microcracks that will be considered, where water saturated concrete samples were prepared and exposed to cyclic frost attack.

4.2.1. Materials, mix proportion and samples

Sample preparation (materials, mix design, mixing, and curing) and drying conditions are explained as follows. Cement paste, mortar and concrete samples were prepared at three w/c ratios of 0.25, 0.4 and 0.5 with CEM I 32,5R, CEM I 52,5R CEM III/B 42,5N and silica fume as binders. Properties of the cementitious materials including their oxides composition are given in Table 3-1 in Section 3.1.

Sample	Sample type	Binder	Aggregate type	Aggregate fraction	Max agg. size [mm]	Sample dimensions	Age [days]	Exposure
CP/C-7/30	Cement Paste	CEM I 32,5R	-	-	-	Cylinder Ø100mm, H25mm	7	Oven 30°C
M/C-7/30	Mortar	CEM I 32,5R	CEN Ref. sand	67%	2	Cylinder Ø100mm, H25mm	7	Oven 30°C
CP/C-7/105	Cement Paste	CEM I 32,5R	-	-	-	Cylinder Ø100mm, H25mm	7	Oven 105°C
M/C-7/105	Mortar	CEM I 32,5R	CEN Ref. sand	67%	2	Cylinder Ø100mm, H25mm	7	Oven 105°C
C/C-28/105	Concrete	CEM I 32,5R	Thames Valley sand limestone	67%	10	Cylinder Ø100mm, H50mm	7	Oven 105°C
CP/C(S,SF) -1 (3,7) /35 (50, 65, 80)	Cement Paste	CEM I 32,5R CEM III/B 42,5N CEM I 32,5R +10% SF	-	-	-	Ring Ø _{out} 65mm Ø _{in} 15mm H10mm	1 3 7	Climate chamber T=23°C RH=35% RH=50% RH=65% RH=80%
M/C(S, SF) -1 (3,7)/50	Mortar	CEM I 32,5R CEM III/B 42,5N CEM I 32,5R +10% SF	CEN Ref. sand	67%	2	Ring Ø _{out} 240mm Ø _{in} 200mm H40mm	1 3 7	Fog room T=23°C RH=50%
C/C-14/42FT (56FT,70FT)	Concrete	CEM I 52,5R	Thames Valley sand gravel	68%	10	Cylinder Ø100mm, H50mm	14	Freeze-thaw: 42, 56,70, 84 cycles
C/SF-14/SC	Concrete	CEM I 52,5R +9% SF	Thames Valley sand gravel	60%	10	Cylinder Ø95mm, H65mm	14	Sealed, room tem.

Table 4-1 Samples, materials and exposure conditions.

CEN Reference sand (< 2 mm), Thames Valley sand (< 5 mm), Thames Valley gravel (< 10 mm) and limestone (< 10 mm) were used as fine and coarse aggregate. The volume of entrapped air voids, moisture content of aggregates and their absorption of water were assumed to be negligible. The specific gravity of aggregates, CEM I, CEM III, silica fume and water are 2.65, 3.06, 2.90, 2.30 and 1.00 respectively. The sand to total aggregate mass ratio was selected as 0.4 to obtain a good workability. A superplasticiser (Sika Visco

Crete® 20 HE) was used in mixes containing silica fume. Table 4-1 lists the samples, materials and exposure conditions used for all samples. Table 4-2 lists the mix proportions for all samples designed according to the absolute volume method (Neville, 1995). Mixes were prepared, and all samples were exposed to the specified exposure conditions to generate different types of microcracking.

Sample	w/c	Cement CEM I C:kg/m ³	Cement CEM III S:kg/m ³	Silica fume SF: kg/m ³	Water w: kg/m ³	Sand s :kg/m ³	Gravel g :kg/m ³	Limestone l:kg/m ³	Admixture sp: kg/m ³
CP/C	0.4	1376	-	-	550	-	-	-	-
CP/S	0.4	-	1343	-	537	-	-	-	-
CP/SF	0.4	1220	-	135.6	542	-	-	-	1.356
M/C	0.5	510	-	-	255	1531	-	-	-
M/S	0.5	-	506	-	253	1518	-	-	-
M/SF	0.5	457	-	51	254	1523	-	-	0.508
C/C-105	0.5	399	-	-	200	702	-	1053	-
C/C-FT	0.5	388	-	-	194	712	1068	-	-
C/SF	0.25	488	-	49	134	712	1068	-	5

Table 4-2 Mix proportions.

4.2.2 Conditioning

Samples were conditioned in the following regimes: Regimes A, B, and C were designed to produce microcracking from internally restrained and externally (by steel disc/ring) restrained drying shrinkage. In regimes D and E, samples were subjected respectively to autogenous shrinkage and cyclic freezing and thawing.

A) Oven drying at 30°C and 105°C

Disc samples of cement paste and mortar with diameter of 100 mm and thickness of 25 mm were prepared and cured for 7 days in a fog room. The curved surface of each sample was then sealed with waterproof adhesive tape to simulate one-directional drying. Following that, one sample of cement paste (CP/C-7/30) and another sample of mortar (M/C-7/30) were placed in a ventilated oven at 30°C and their replicates (CP/C-7/105 and M/C-7/105) were placed in another oven at 105°C. Moisture content of the sample was frequently monitored until the mass change between the last two measurements was less than 0.2%, at which moisture equilibrium was considered to be complete. Afterwards, one of the exposed drying surfaces of each sample was vacuum impregnated with fluorescent epoxy resin to facilitate visibility of the formed microcracks.

B) Drying at relative humidity of 35%, 50%, 65% and 80%, and temperature of 23°C

Cement pastes with three different binders: CEM I, CEM III and CEM I + 10% of silica fume (CP/C, CP/S, CP/SF) were cast around steel cylinders as shown on Figure 4-1, and cured in a fog room for 1, 3 and 7 days. Twelve replicate samples were prepared for each binder and curing period. The geometry of the samples

was designed to induce more severe cracking by placing rigid object (steel cylinder) in the middle of the shrinking matrix. This simulated drying shrinkage with external restraint. At the end of curing, flat surfaces of the samples were sealed with adhesive foil to allow circumferential drying through the curved surface. The samples were then exposed to drying in four climate chambers (three replicate samples in each chamber) at relative humidity levels of 35%, 50%, 65% and 80%, and the temperature of 23°C, and their weight loss was frequently measured.

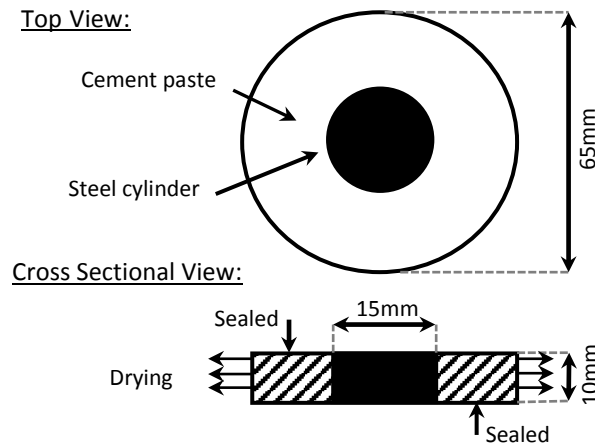


Figure 4-1 Geometry of cement paste samples.

Moreover, the same cement pastes were cast into prisms with dimensions of 160×40×10 mm for linear deformation measurement. Three replicate prisms with embedded steel studs at their ends were prepared and exposed to drying in the climate chambers. Additionally, one set of prisms were constantly cured in the fog room. Length change between the two studs of each prism was regularly measured by a length comparator device. The details of this procedure and calculation of the deformation are presented in Section 3.2.

The measured linear deformation of cement pastes are shown in Figures 4-2 (a), (b) and (c) respectively for different binder types and conditioning humidity. Until the age of 7 days, all prisms were cured in the fog room and in this period, the highest shrinkage occurred in CEM III pastes. This is associated with high chemical and autogenous shrinkage of systems containing GGBS compared to ordinary Portland cement. After the first 7 days, samples were dried in climate chambers and the prisms started to shrink significantly. The highest shrinkage rates were observed in the first 14 days of drying. Lower conditioning relative humidity produced higher shrinkage. For example, the shrinkage in samples dried at 35% RH was about 1000 $\mu\epsilon$ higher than similar samples dried at 80% RH after 57 days of drying. Samples containing SCMs had greater shrinkage compared to CEM I pastes. On the contrary, samples that were continuously cured in the fog room showed very little shrinkage. In fact, CEM I pastes showed a small amount of expansion. Linear deformation measurement indicates tendency to cracking when the measured strains are high. Based on these observations, microcracking would be expected in samples with steel cylinders acting as external restraint to the surrounding shrinking matrix, particularly in samples that were dried at low relative humidity.

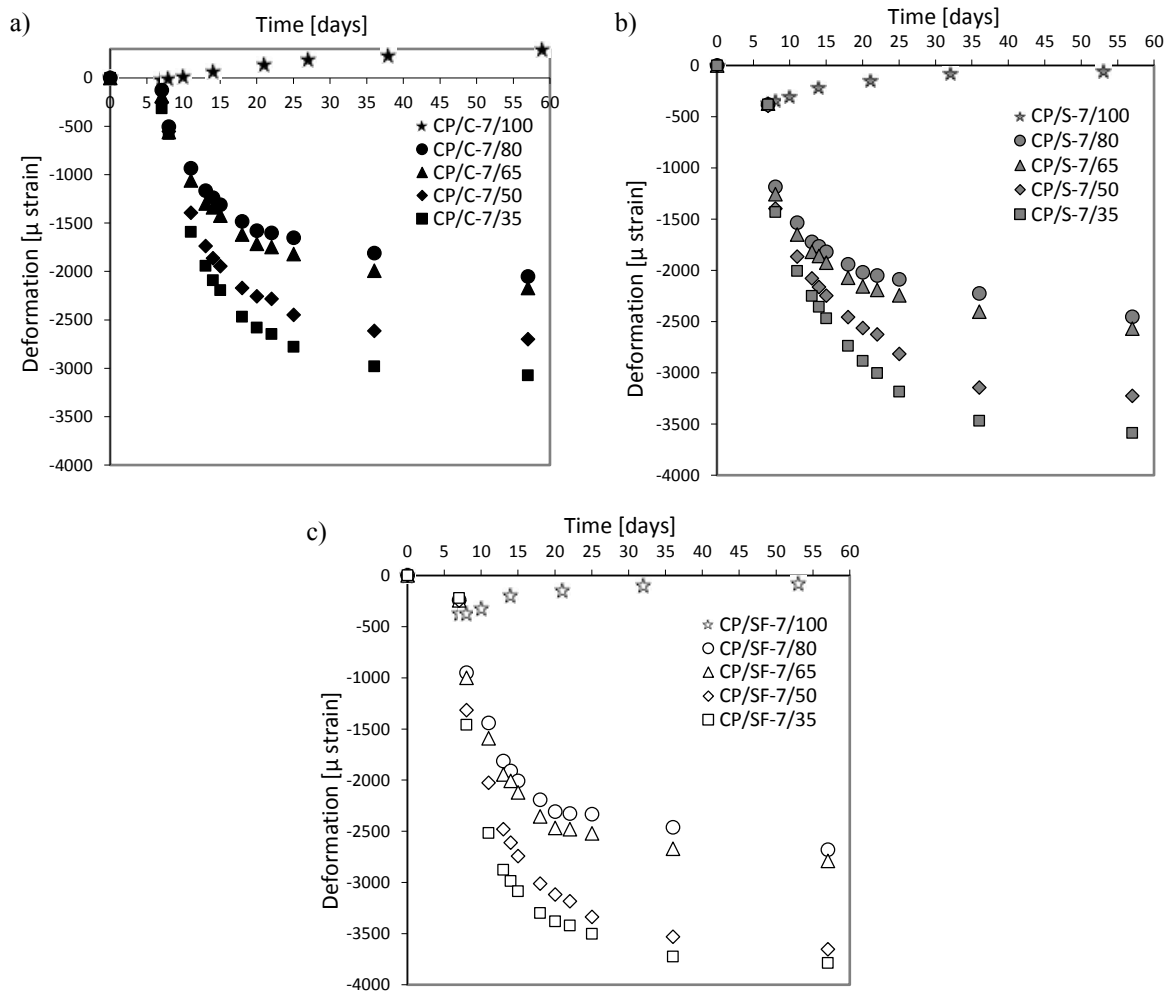


Figure 4-2 Linear deformation of cement paste prisms: (a) CP/C-7, (b) CP/S-7 and (c) CP/SF-7 exposed to conditioning regime at five different RH: 35%, 50%, 65%, 80% and 100%.

C) Drying at relative humidity of 50% and temperature of 23°C – restrained ring test

This was carried out in accordance with ASTM C1581/C1581M, a widely used standard test to assess the potential for early-age cracking in concrete. Mortar or concrete is cast in a cylindrical mould around a steel ring, which acts as the restraining support. The geometry of the sample and steel ring is shown in Figure 4-3. Three mortar mixes (M/C-1/50, M/S-1/50, M/SF-1/50) were prepared for the test and cured in sealed plastic bags for 24 hours. Following that, the samples were demoulded and exposed to circumferential drying at 50% relative humidity and 23°C by sealing the top and bottom surfaces of the samples with silicon. Each steel ring was equipped with four strain gauges and linked to a data acquisition system that records strain at every 15 minutes interval from the time of casting. Therefore, the exact moment of cracking and the strain at the time of cracking can be obtained. Example results are presented in Figure 4-4, where the relief in strain development indicates the time when cracking occurs. It was observed that samples containing slag and silica fume cracked approximately at the same time, after four days of drying with almost completely relief in strain, while mortars containing only Portland cement cracked after a longer period of drying – five and a half day with step wise relief of the strain. This indicates that mortars containing SCMs as a binder exhibit higher risk to cracking while drying.

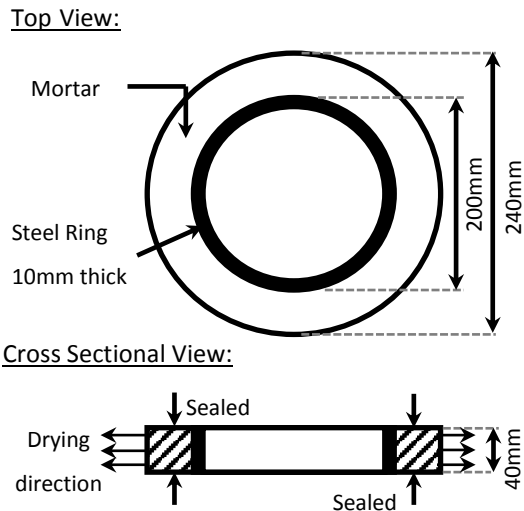


Figure 4-3 Ring test – mortar samples. (ASTM C1581/C1581M)

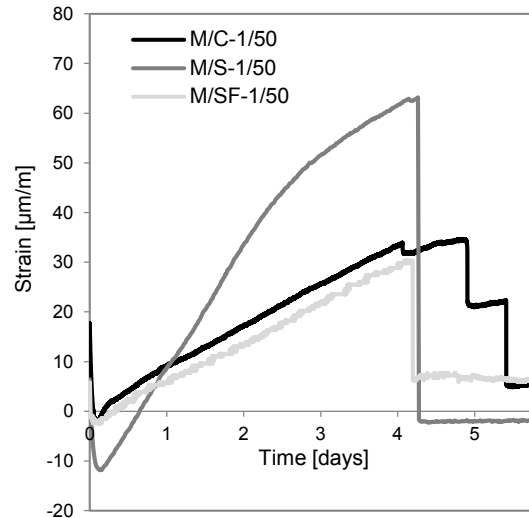


Figure 4-4 Strain development in mortar samples (M/C-1/50, M/S-1/50, M/SF-1/50) exposed to drying in the restrained ring test.

D) Sealed curing

Concrete samples were prepared using CEM I 52.5R with 9% silica fume at low water to binder ratio of 0.25. Workability of the mix was controlled by reducing total aggregate fraction to 60% and by adding 1% superplasticiser (Sika ViscoCrete® 20 HE) by mass of total binder. The mix was cast into a cylindrical plastic container (Ø95 mm, 65 mm height) and compacted in three layers on a vibrating table. The container was sealed with a lid and wrapped in many layers of cling film to prevent any moisture exchange with the environment. The sealed sample (C/SF-14/SC) was cured in room temperature until the age of 14 days. Moreover, the same concrete mix was cast into three cylindrical tubes (Ø75 mm, 300 mm height) for linear deformation measurement. Each end of the concrete cylinder was embedded with a steel stud for length change measurements. Details of this procedure and calculations are presented in Section 3.2. Measurement began after initial set, which was approximately 6 hours after casting and the results are plotted in Figure 4-5. Since the sample was sealed cured, it can be assumed that the observed deformation is associated with autogenous shrinkage. The highest shrinkage increment was observed in the first two weeks after casting, reaching a value of 322 µ-strain. Afterwards, the rate of the shrinkage decreased. Such levels of shrinkage in early age concrete is expected to produce microcracking.

E) Freezing-thawing (-20/+20°C) for 42, 56 and 70 cycles

Concrete disc samples (C/C-14/FT) of diameter 100 mm and thickness 50 mm were prepared and cured for 14 days in water at 20°C. The samples were then subjected to freezing and thawing according to the procedure described in Standards of European Committee for Standardization (CEN/TR 15177:2006). The samples were exposed to increasing number of freeze-thaw cycles, where each cycle consists of 8 hours of freezing at -20°C and 4 hours of thawing at +20°C with weight measurement every 14 cycles. The results presented in Figure 4-6 indicate that mass loss increased with number of freeze-thaw cycles up to 56 cycles and then the mass loss

stabilized. This is associated with frost attack and scaling of the concrete surface. The samples were removed after 42, 56 and 70 cycles of freeze-thaw for microcrack characterisation.

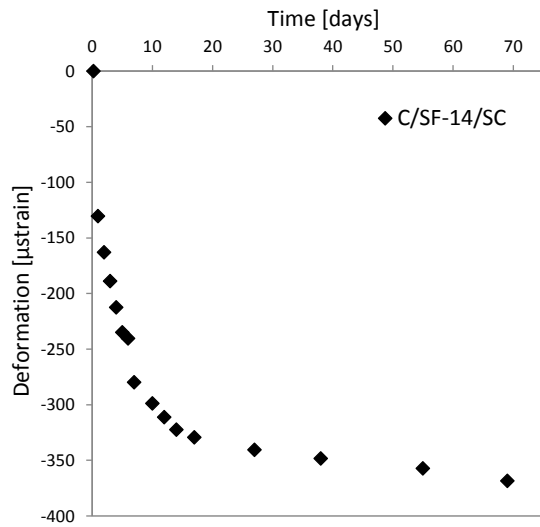


Figure 4-5 Linear deformation of sealed-cured concrete sample (C/SF-14/SC).

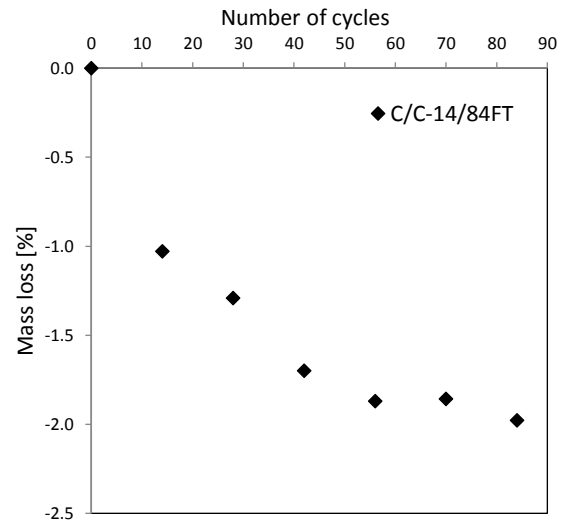


Figure 4-6 Mass loss of concrete sample subjected to 84 cycles of freeze-thaw (C/C-14/84FT).

4.2.3 Observation of microcracks

Fluorescence microscopy and image analysis were used to observe and measure the microcracks induced by the different conditioning regimes. Each disc sample was pressure impregnated at 0.7MPa above atmospheric pressure with low viscosity fluorescent dyed epoxy resin. The resin penetrates the sample via microcracks and pores and fills all of the connected empty spaces. The impregnated sample was then cured at room temperature for 3 days to allow proper hardening of the resin. When the epoxy has hardened, a 10 mm thick slice was extracted from the centre of each sample (cross-sectioned) and the slice was ground using silicon carbide paper of P120, P240 and P500 grit sizes to obtain a flat surface for imaging. The cross-section was then imaged with a petrographic microscope and SLR camera using UV illumination. The epoxy penetration depth, microcrack pattern and other crack characteristics were characterised using image analysis.

A) Drying shrinkage microcracking (internal restraint)

Example images taken with the DSLR camera for cement paste (CP/C-7/30 and CP/C-7/105) and mortar (M/C-7/30 and M/C-7/105) are shown in Figure 4-7, where the epoxy penetration depth and microcrack pattern can be observed. The images clearly show that increasing the severity of drying induces more microcracking and increases impregnation depth, which is expected. 2D image analysis on micrographs taken by the petrographic microscope demonstrated that the microcracks formed approximately perpendicular to the drying surface, with a penetration depth of less than 10 mm. The detectable microcracks had widths ranging from 1 to 60μm, however more than 80% of them had widths and lengths of <10 μm and <100 μm. Despite being subjected to drying at 105°C, which is much higher than what most structures are exposed to, the microcracks were rather isolated with little tendency for branching and had very low density (approximately 1

microcrack per mm²). More information on the 2D characteristics of this type of microcracking can be found in a PhD study of Zhigen Wu (Wu, 2014).

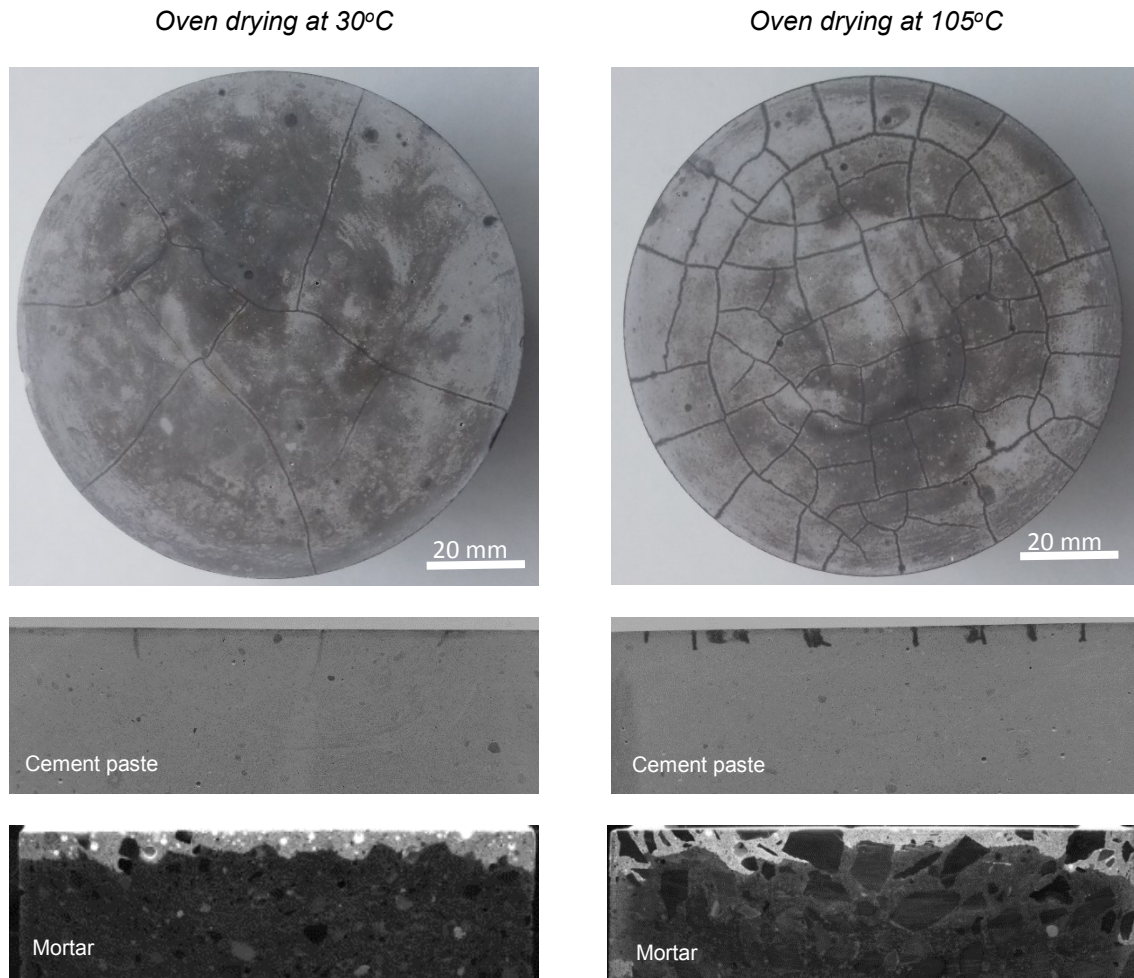


Figure 4-7 Top and side view of cement paste (CP/C-7/30 and CP/C-7/105) and side view of mortar (M/C-7/30 and M/C-7/105) samples impregnated with resin after drying at 30°C and 105°C.

B) Drying shrinkage microcracking (external restraint)

Substantial amount of cracks were visible on the circumferential surface of cement paste rings. These are the 1, 3 and 7 days old cement paste samples (CP/C, CP/S, CP/SF) that were externally restrained and dried in various relative humidity (35%, 50%, 65% and 80%). The bar charts presented in Figure 4-8 show the average number of cracks formed after 1, 5 and 7 days of drying measured on three replicate samples each. It can be seen that the number of cracks increases with drying time and with decrease in relative humidity. It can also be observed that well hydrated samples and therefore denser systems cracked more easily than younger samples. Pastes containing silica fume were the least resistant to cracking. However, these cracks were large enough to be visible to the naked eye. These are macrocracks rather than microcracks and so they will not be further considered in this project.

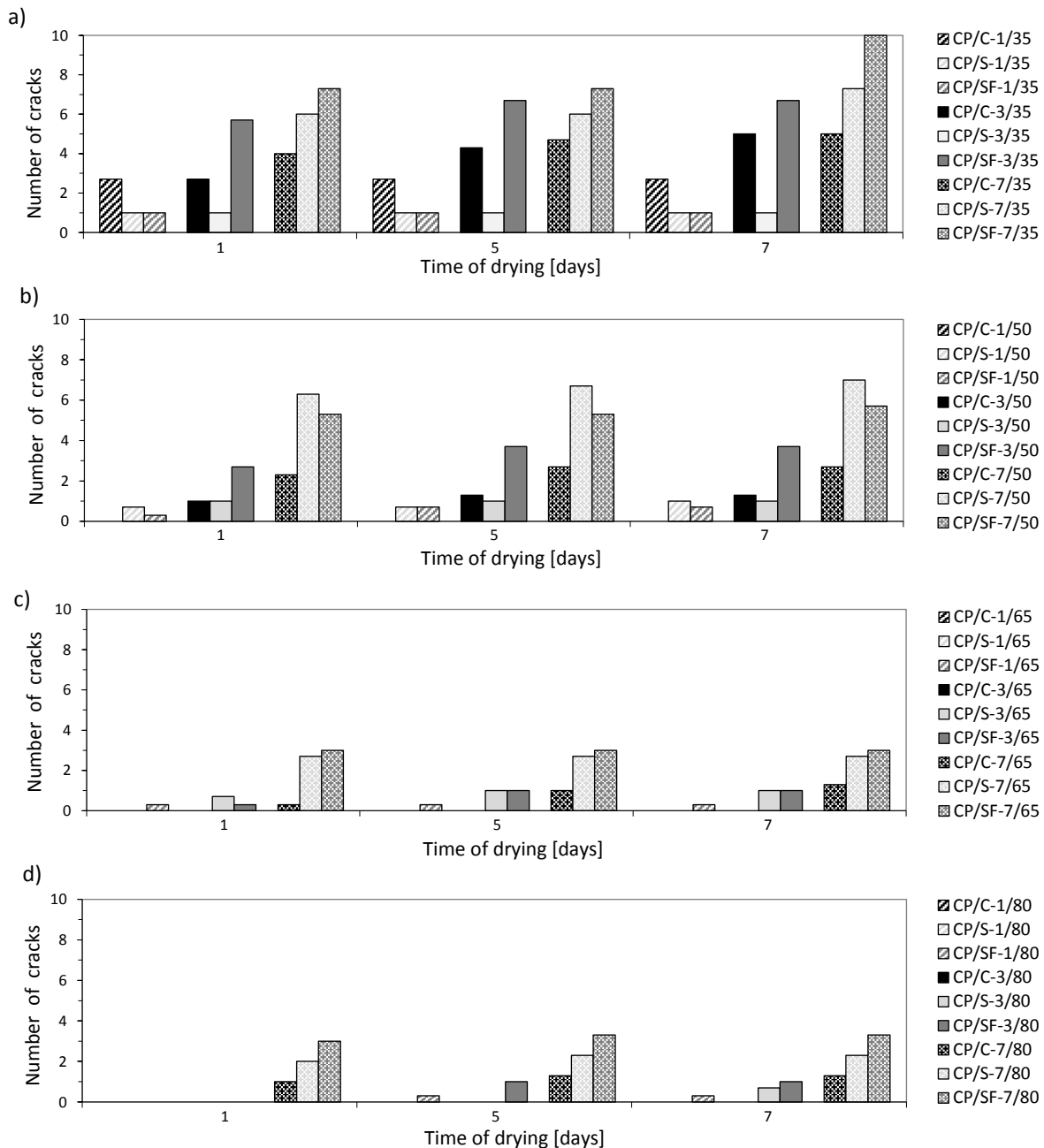


Figure 4-8 Cracking of restrained cement paste rings after drying at a) 35%, b) 50%, c) 65% and d) 80% RH.

C) Autogenous shrinkage microcracking

Severe internal microcracking was observed in the concrete sample (C/SF-14/SC, w/b 0.25) that was sealed cured to induce autogenous shrinkage. Images of the impregnated sample are shown in Figure 4-9. The microcrack pattern can be clearly observed as the resin penetrated the samples via connected network of the cracks. The formed microcracks are uniformly and densely distributed throughout the whole area of the cross-section taken from the middle of the sample. The crack width range from a few μm to few hundreds of μm , however more than 80% of the cracks had widths of $< 50 \mu\text{m}$.



Figure 4-9 Microcrack pattern of concrete sample (C/SF-14/SC) subjected to autogenous shrinkage.

D) Freeze-thaw microcracking

Severe cracking was also observed in concrete samples (C/FT) subjected to 42, 56 and 70 cycles of freezing and thawing. The degree of microcracking varied depending on the number of the freeze-thaw cycles. Images of the impregnated samples are shown in Figure 4-10. 2D image analysis of cross sections imaged with fluorescence microscope show that increasing freeze-thaw cycles produced wider cracks with denser distribution, which facilitated the resin to penetrate deeper into the sample. An average impregnation depth measured on the cross sections were 11, 16 and 19 mm for samples exposed to 42, 56 and 70 cycles respectively. This clearly demonstrates that the degree of damage can be controlled by varying the number of freeze-thaw cycles. Moreover, the induced crack width ranged from several μm to mm. These cracks appear densely distributed and well-connected.

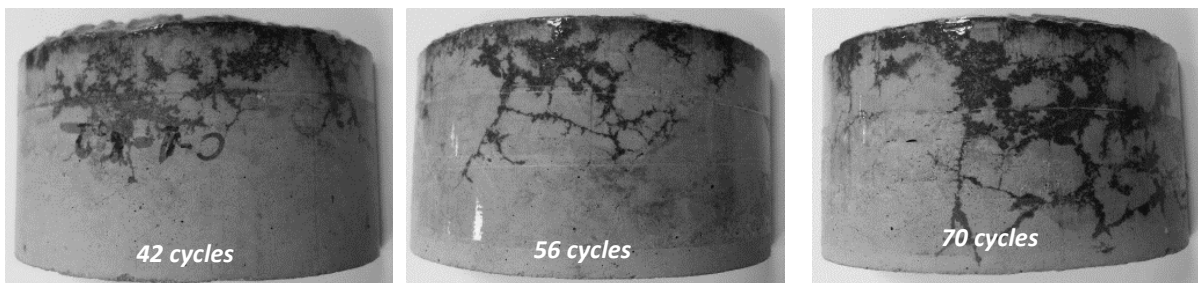


Figure 4-10 Concrete samples impregnated with fluorescent resin after 42, 56 and 70 freeze-thaw cycles (C/FT/42, C/FT/56 and C/FT/70).

4.3 Focused ion beam nanotomography (FIB-nt)

FIB-nt allows the reconstruction of a three-dimensional structure from images acquired by serial sectioning via a focused stream of high-energy ionized Ga⁺ and imaging the successively exposed surfaces by either secondary or backscattered electron microscopy. An evaluation of the potential of FIB-nt to detect and image microcracks in 3D was carried out on a Zeiss Neon 40 with cross beam FIB-SEM at an angle of 54° and SmartSEM V05.04 operating software. This facility, shown in Figure 4-11, is located at the Centre for Research in Nano-Engineering at UPC in Barcelona.

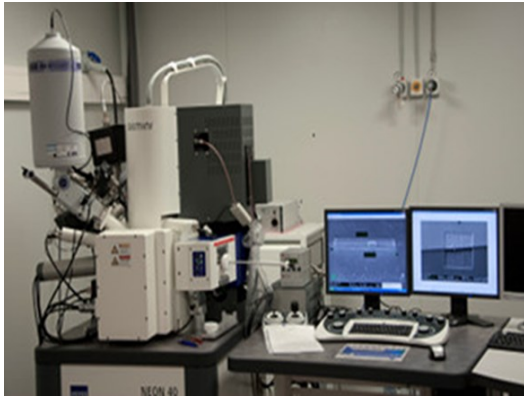


Figure 4-11 Zeiss Neon 40 FIB-SEM workstation at UPC – CRnE, Barcelona, Spain.

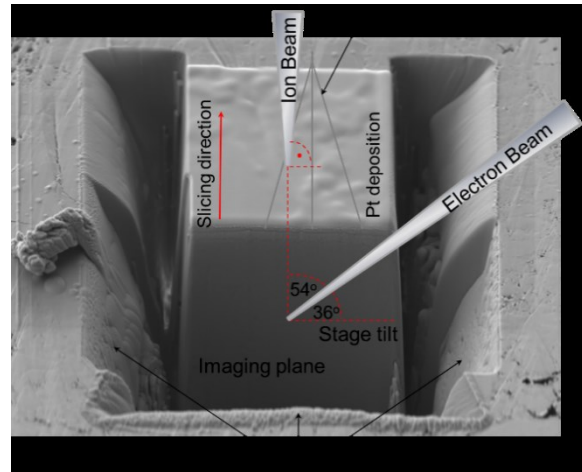


Figure 4-12 Sample positioning and cube preparation for FIB-nt.

4.3.1 Samples

Cement paste (CP/C-7/30) and mortar (M/C-7/30) were prepared and oven dried at 30°C until constant mass. Dried samples were vacuum impregnated with low viscosity epoxy resin and then ground with silicon carbide papers (P120, P240, P500, P1200) and polished on cloths with diamond pastes (9, 6, 3 and 1 μm) in order to achieve a flat surface. Following that, the samples were placed on metal stubs with conductive adhesive tape and coated with carbon to minimize charging during image acquisition.

4.3.2 Imaging procedure

The sample was transferred to the microscope chamber and placed on the sample stage. Because of the oblique geometry of the SEM-FIB column, the stage has to be tilted to an angle of 36° during sectioning and imaging as shown in Figure 4-12. The sample surface is perpendicular to the ion beam, but images are taken by the electron beam at a 54° angle. Thus, the images has to be corrected for distortion. This is done via the SmartSEM software by recalculating the y dimension of each pixel according to the equation: $y' = y \times \sin(54^\circ)$. Serial sectioning is preceded by preparation of an imaging cube of the required size. A square region of interest (ROI) was selected and deposited with a thin platinum layer using the gas injection system. The area of the Pt deposition is slightly bigger than the size of the prepared cube to protect the surface from undesirable ion-induced erosion. Then, three trenches were eroded around the Pt layer using a 30 nA milling current to expose

the required cube size, which was $20 \times 20 \times 20 \mu\text{m}^3$ and $30 \times 30 \times 30 \mu\text{m}^3$ for CP/30 and M/30 samples respectively. The two parallel trenches allow for re-deposition of milled material during serial sectioning and prevent shadow-effects, while the third trench exposes the imaging plane as shown in the Figure 4-12.

Additionally, reference marks for precise overlay of acquired images were produced by eroding three lines on top of the cube. This alignment is essential because any movements of the imaging plane during milling will produce drift artefacts. The reference marks consist of one parallel to the slicing direction line and one additional line at 25° angle to the first line. The reference lines are approximately 1 to 2 μm deep and were produced using a 1 nA milling current for approximately 10 sec. These lines are visible on the images as three reference spots and the distance between them decrease on subsequent slices which allows precise alignment.

Automated serial sectioning was carried out by cyclical milling and imaging until the required thickness was obtained. Low milling current of 1 nA was applied to achieve uniform milling with slicing distance of 40 and 60 nm for cement paste and mortar samples respectively. The microscope was operated in the secondary electron (SE) mode at 2 kV accelerating voltage and 5.1 mm working distance. Images were collected at $14650 \times$ (CP/C-7/30) and $960 \times$ (M/C-7/30) magnification with brightness and contrast set at 50% and 35% respectively. Images were digitized to 1024×768 pixels, which correspond to voxel size of $20 \times 20 \times 40$ nm for CP/C-7/30 and $30 \times 30 \times 60$ nm for M/C-7/30. Approximately 800 images were acquired for each stack and these were saved as tiff files. The whole process took around 15 to 20 hours for each sample.

4.3.3 Results

The reconstructed image volumes for the cement paste (CP/C-7/30) and mortar (M/C-7/30) samples are shown in orthogonal views and 3D renderings in Figure 4-15 and 4-16 respectively. Image alignment according to the reference marks was carried out in Fiji/ ImageJ with Template Matching plugin (Template Matching, Fiji/ ImageJ) for image registration. A landmark (reference mark) was first defined on the first image and the software then finds this landmark on subsequent images throughout the whole image stack. The images are then translated and aligned so that the landmark pattern stayed in the same position. Figure 4-13 shows a top view of one of the imaged cube before and after alignment as an example. Following that, a sub-volume cube of $15 \times 12 \times 10 \mu\text{m}^3$ (cement paste) and $25 \times 23 \times 20 \mu\text{m}^3$ (mortar) was cropped to exclude superfluous regions containing the references marks, Pt layer, etc.

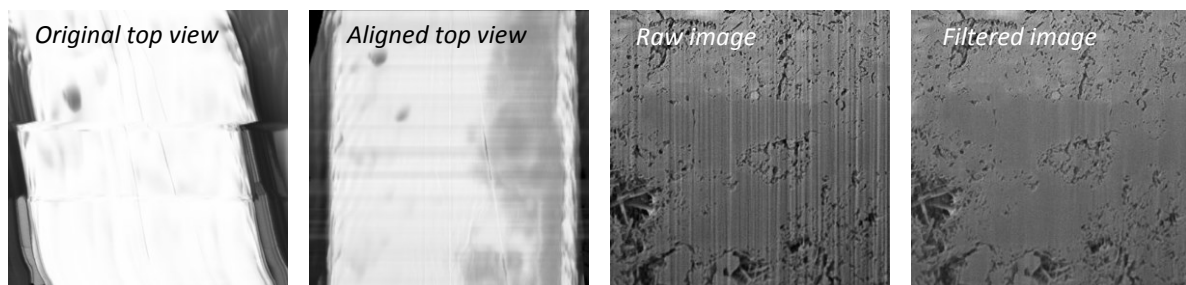


Figure 4-13 Original and aligned images. Alignment according to the reference lines on the top of the sectioned cube.

Figure 4-14 Raw and wavelet-FFT filtered image of cement paste (CP/C-7/30) captured by FIB-nt.

Additionally, a wavelet-FFT filter was applied to the images to remove vertical stripes known as ‘waterfall effect’. This is an artefact of FIB-nt that is particularly severe for samples having phases that exhibit variable resistance to ion milling. The Matlab algorithm proposed by Münch et al. (2009) was adopted for the wavelet-FFT filter. An example of raw and filtered images are shown in Figure 4-14.

On grey scale (8 bit) images, dark areas correspond to voids spaces i.e. microcracks and pores, whereas brighter areas are solids such as cement grains, hydration products and aggregate particles. The 3D image of cement paste sample (Fig. 4.15) clearly shows radial and bond cracks around unreacted cement particles. This is a typical example of cracking induced by the presence of an internal restraint (stiff particle) in a shrinking matrix. The 3D image of the mortar sample (Fig. 4.16) shows the presence of microcracks perpendicular to the dried surface caused by moisture gradient that develops during drying. The widths of the detected cracks are between 50 nm to 1.5 μm .

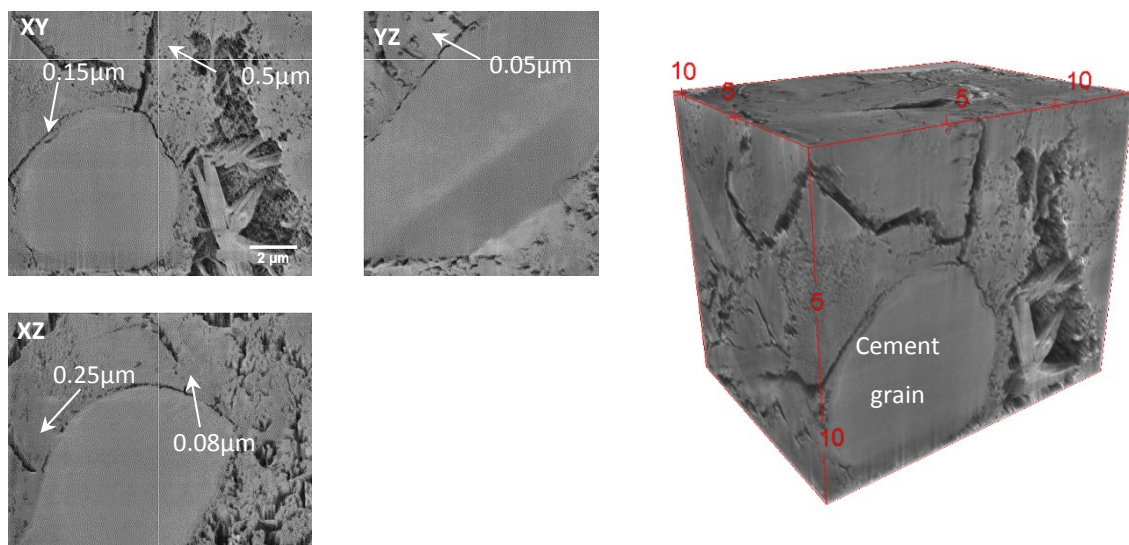


Figure 4-15 Orthogonal views and 3D rendering of cement paste (CP/C-7/30) acquired using FIB-nt showing bond microcracks around unreacted cement grain.

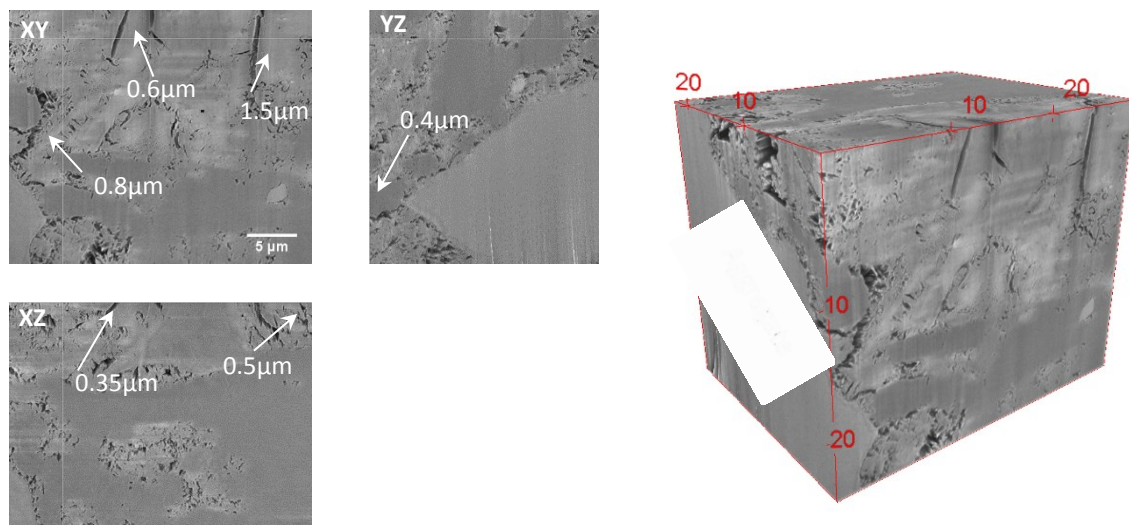


Figure 4-16 Orthogonal views and 3D rendering of mortar (M/C-7/30) acquired using FIB-nt showing matrix and bond cracks.

4.4 Broad ion beam (BIB) serial sectioning combined with SEM imaging

Broad ion beam is a technique for producing highly polished cross-sections of delicate composite materials for SEM investigations. The combination of BIB irradiation and high resolution imaging of successive layers provides another approach for 3D imaging that bears similarities to that of FIB-nt (Desbois et al, 2010). To assess the feasibility of this method for 3D imaging of microcracks, an argon ion beam cross-section polisher JEOL SM-09010 (Figure 4-17) and Zeiss Supra 55 scanning electron microscope were utilized. Both devices are located at the Department of Structural Geology, Tectonics and Geomechanics in RWTH Aachen University, Aachen, Germany.



Figure 4-17 JEOL SM-09010 Ar-BIB cross-section polisher at RWTH Aachen University, Germany.

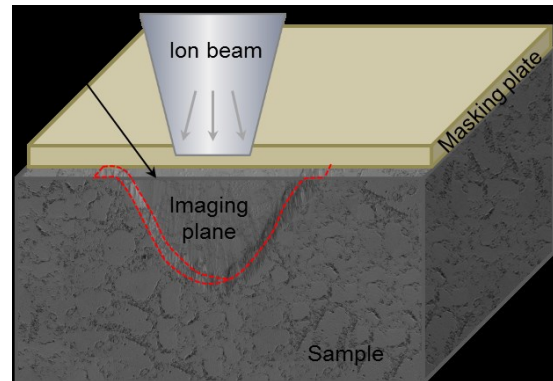


Figure 4-18 Schematic of Ar-BIB cross-sectioning.

4.4.1 Samples

A mortar sample (M/C-7/30) was prepared, cured and then dried at 30°C until constant mass. The dried sample was vacuum impregnated with low viscosity fluorescent epoxy resin and then sectioned to produce a block of dimension 10×10×5 mm³. The imaging surface was sputter coated with gold after each preparation of polished cross-section in order to minimize charging effects during SEM imaging.

4.4.2 Imaging procedure

The sample was placed on the specimen stage in the cross-section polisher. An optical microscope was used for specimen positioning in the chamber. To produce a cross-section, a masking plate was placed across the selected region and this was irradiated with a broad argon ion beam (about 500 μm in diameter) at 6 kV accelerating voltage and high milling current of 150 nA. The masking plate is a platinum bar which guides the ion beam vertically to the top surface of the sample to create a polished surface beneath as shown in Figure 4-18. With these parameters, a cross-section with imaging surface of about 2 mm² was achievable in 8 hours. After each sectioning, the sample was coated with gold and then imaged in tiles with 10% overlapping using BSE and SE detectors. The microscope was operated at 25 kV accelerating voltage and 4.6 mm working distance. Images were collected at 1000× and 14000× magnification, and digitized to 1024 × 768 pixels at a pixel size of 0.24 μm and 0.02 μm respectively.

4.4.3 Results

The sectioning and imaging procedure was repeated for five times for the same selected region in order to image the microstructure in 3D. Figure 4-19 presents the five successively polished cross-sections, the BSE and SE images stitched in Fiji/ ImageJ with Grid/Collection Stitching plugin (Grid/Collection Stitching, Fiji/ ImageJ). Thickness of each removed layer was obtained based on the distance between the first and successive cutting marks, which was measured on the acquired images. The measured thickness between each successive layer were 11, 19, 20 and 11 μm respectively. Unfortunately, the repeatability of the slice thickness was poor, and this was probably due to the manual operation of the cross-section polisher.

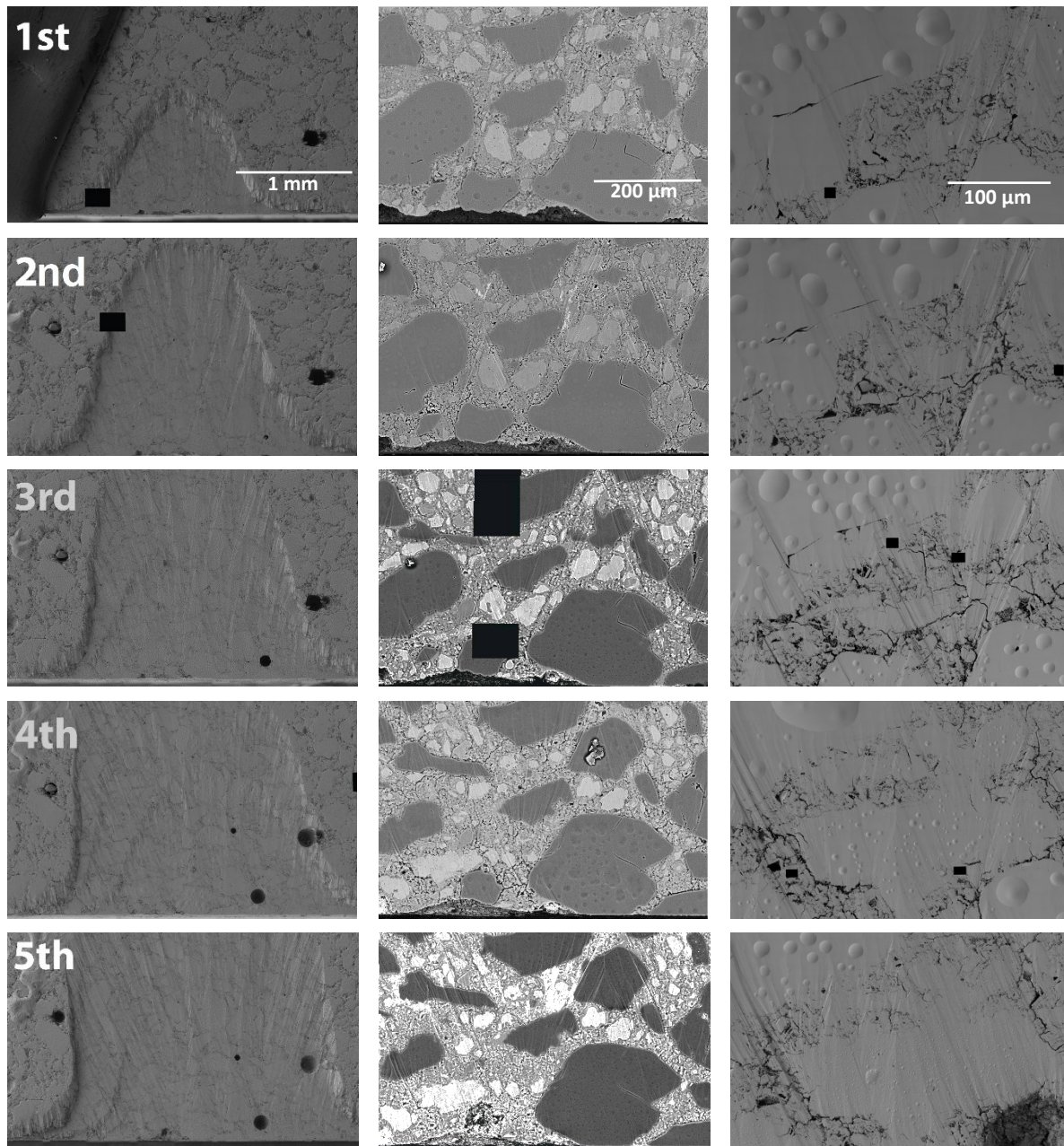


Figure 4-19 Five successively polished cross sections (left row), stitched BSE image (middle row) and SE image (right row) of M/C-7/30. Images collected at 500 \times , 1000 \times and 14000 \times magnification respectively.

The stitched BSE and SE images were aligned, cropped and reconstructed. The reconstructed image volumes of the mortar (M/C-7/30) are shown in orthogonal views and 3D renderings in Figure 4-20 and 4-21 for BSE and SE images respectively. On the XY plane, many small bond and matrix microcracks of widths ranging from 0.5 to 2.5 μm were detectable. This shows that the images are of very high resolution in the XY plane. However, the resolution in the YZ and XZ planes were very poor. It appears that significant amount of information were lost between slices and that this affected the accuracy of the image alignment. Most importantly, this makes it very difficult to link microcracks detected on the first cross-section with the microcracks on the following cross-sections.

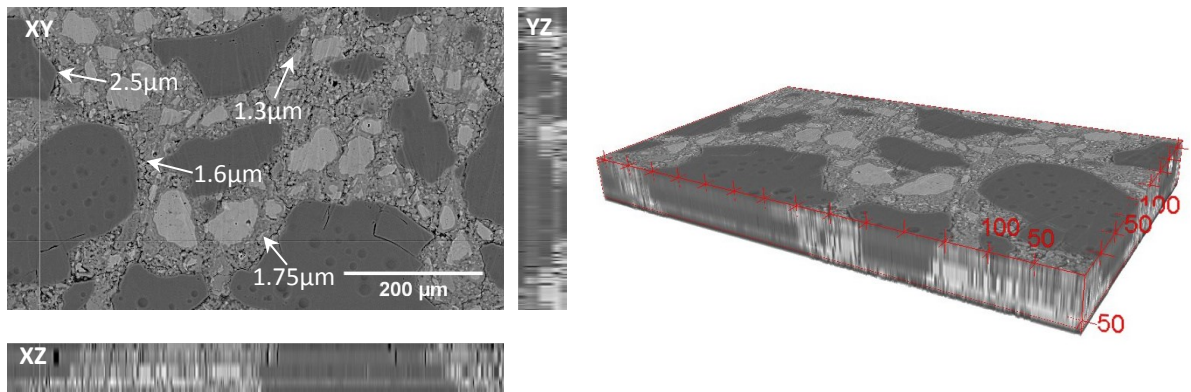


Figure 4-20 Orthogonal views and 3D rendering of mortar (M/C-7/30) obtained from BIB serial sectioning combined with SEM-BSE imaging. XZ and YZ planes show very poor resolution of the technique.

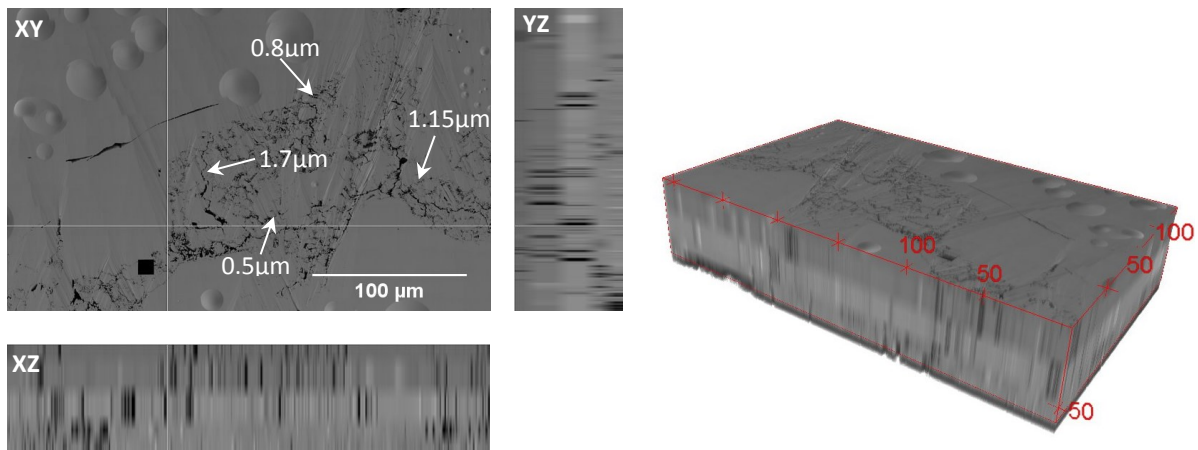


Figure 4-21 Orthogonal views and 3D rendering of mortar (M/C-7/30) obtained from BIB serial sectioning combined with SEM-SE imaging. XZ and YZ planes show very poor resolution of the technique.

4.5 Laser scanning confocal microscopy (LSCM)

Laser scanning confocal microscopy is a widely used technique in biological research. It is able to acquire images from within the sample and reconstruct these to generate a 3D image. A major advantage of this technique is that the 3D imaging is carried out via an optical sectioning process that is direct and non-destructive. Experiments were carried out to evaluate the possibility of using this technique for imaging microcracks in 3D using a Leica TCS SP5 laser scanning confocal microscope (Figure 4-22). This microscope is supported by the LAS AF Lite software and belongs to the Concrete Durability Group at Imperial College London.

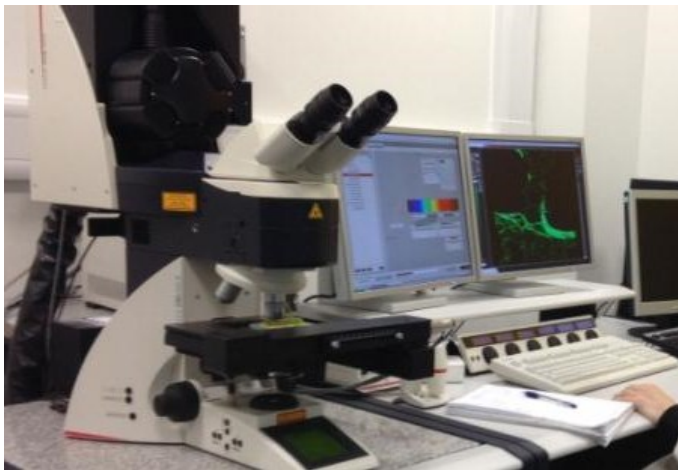


Figure 4-22 Leica TCS SP5 laser scanning confocal microscope at Civil and Environmental Engineering Department, Imperial College.

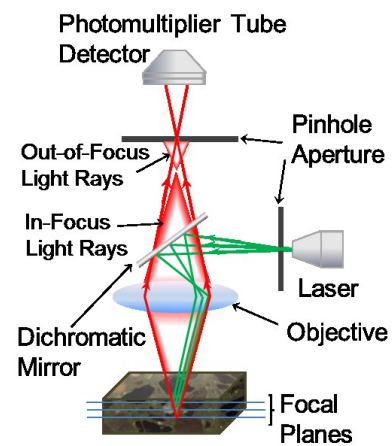


Figure 4-23 Confocal microscopy

4.5.1 Samples

Concrete (C/C-14/56FT) was prepared and water cured at 20°C until the age of 14 days. Then, the sample was exposed to 56 cycles of freeze-thaw action according to CEN/TR 15177:2006, where each cycle consisted of 8 h freezing at -20°C and 4 h of thawing at +20°C. Following that, the sample was gently dried in a step-wise manner at 30°C, 40°C and 50°C to prevent additional cracking. Then, the sample was impregnated with low viscosity fluorescent dyed epoxy resin and sectioned into a rectangular block (40×20×8 mm). Finally, the sample was ground at successively finer grit sizes (P120, P240, P500, P1200) and polished with diamond pastes of 9, 6, 3 and 1 μm fineness.

4.5.2 Imaging procedure

The polished sample was placed on the motorized scanning stage of the microscope, which has a Z-stepping distance of 0.025 μm. The microscope uses a focused laser beam as the light source and a pinhole to remove out-of-focused light emanating from below and above the focal plane. The principles of the technique is schematically presented in Figure 4-23. The laser passes through a pinhole aperture that is in a conjugate plane

with a scanning point on the sample and a second pinhole aperture in front of the PMT detector (photomultiplier tube). As the laser is scanned across the sample in a defined focal plane, secondary fluorescence emitted from the sample is passed back through the dichromatic mirror and focused as a confocal point at the detector pinhole aperture. However, some amount of fluorescence occurs at points above and below the focal plane that are not confocal with the pinhole and forms extended Airy disks in the aperture plane. These out-of-focus fluorescence are blocked by the pinhole aperture and do not contribute to the resulting image. Refocusing the objective shifts the excitation and emission points on a sample to a new plane that becomes confocal with the pinhole apertures of the light source and detector.

An argon laser line of 488 nm was used to excite the fluorophores in the polished sample and the beam splitter was configured to 500-600 nm range to allow the emitted fluorescence to be collected by the PMT. The laser intensity was set to 15% while the sensitivity of the PMT was adjusted correspondingly to prevent oversaturation. The pinhole aperture was maintained at 1 Airy unit and a zoom factor of 1× was adopted. The microscope is equipped with four objective lens: two oil immersion at 63× and 40× and two dry lenses at 20× and 5× magnification. Figure 4-24 and Table 4-3 show respectively examples of confocal images of concrete sample (C/C-14/56FT), the theoretical resolution and size of the FOV for each of the objective lens. The images were digitised to 1024 × 1024 pixels at a pixel spacing of 3.027, 0.757, 0.378 and 0.240 μm for 5×, 20×, 40× and 63× objective lens respectively. All images were converted to grey scale and inverted to highlight the features of interest. The fluorescent epoxy filled microcracks and pores are visible as dark features on the images whereas the bright areas correspond to solids. Additionally, a median filter of 1×1×1 was applied to remove noise.

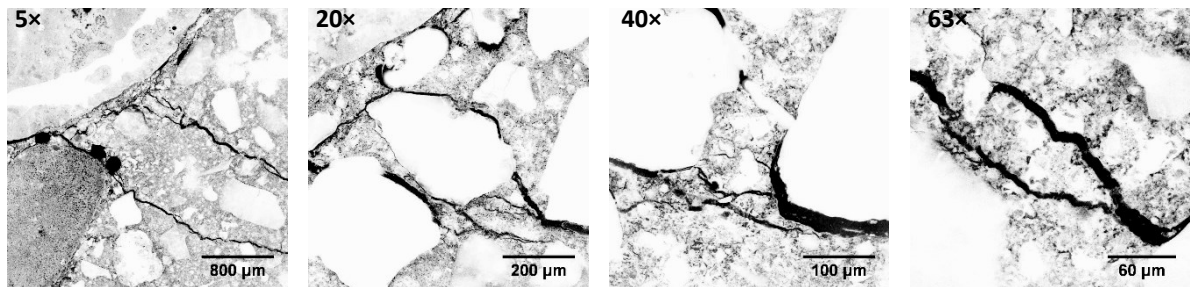


Figure 4-24 2D confocal images of concrete after 84 cycles of freeze-thaw (C/C-14/56FT) captured using the 5×, 20×, 40× and 63× objective lens.

Objective lens	Resolution X-Y [μm]	Resolution Z [μm] (for 1AU)	FOV [mm]
5×	1.30	43.20	3.10×3.10
20×	0.40	3.90	0.75×0.75
40×	0.15	0.95	0.35×0.35
63×	0.14	0.55	0.20×0.20

Table 4-3 FOV and resolution for each objective lens.

4.5.3 Results

Figure 4-25 and Figure 4-26 show respectively examples of 2D images from a recorded image stack and the 3D reconstructed image in orthogonal views with the 3D rendering. Cracks of width larger than $1\ \mu\text{m}$ can be detected in images acquired by the $20\times$ objective lens. Smaller sub-micron microcracks can be observed in images acquired at higher magnifications ($40\times$, $63\times$ objective). However, a disadvantage of this technique is that it has a limited imaging depth. It can be seen that the first several images nearest to the surface are clear and sharp, but subsequent images become gradually blurrier and out-of-focus. The imaging depth of LSCM is strongly dependent on the type of material imaged. Non-transparent materials such as cement-based materials can only be imaged to several micrometers deep because of the loss of signal with depth. To overcome this limitation, a new imaging approach was proposed and developed in collaboration with Marcus Yio (Yio et al., 2015). This approach combines sequential imaging with serial sectioning and reconstruction, and will be described in detail in Chapter 5.

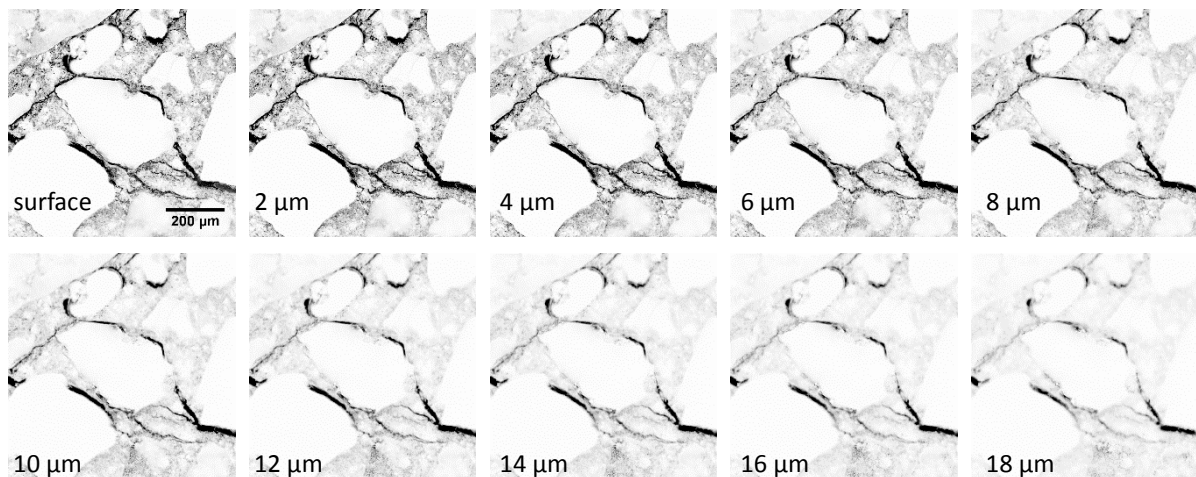


Figure 4-25 Confocal image stack of a concrete (C/C-14/56FT) collected up to an imaging depth of $18\ \mu\text{m}$ ($20\times$ objective lens, FOV $0.75\times 0.75\ \text{mm}$).

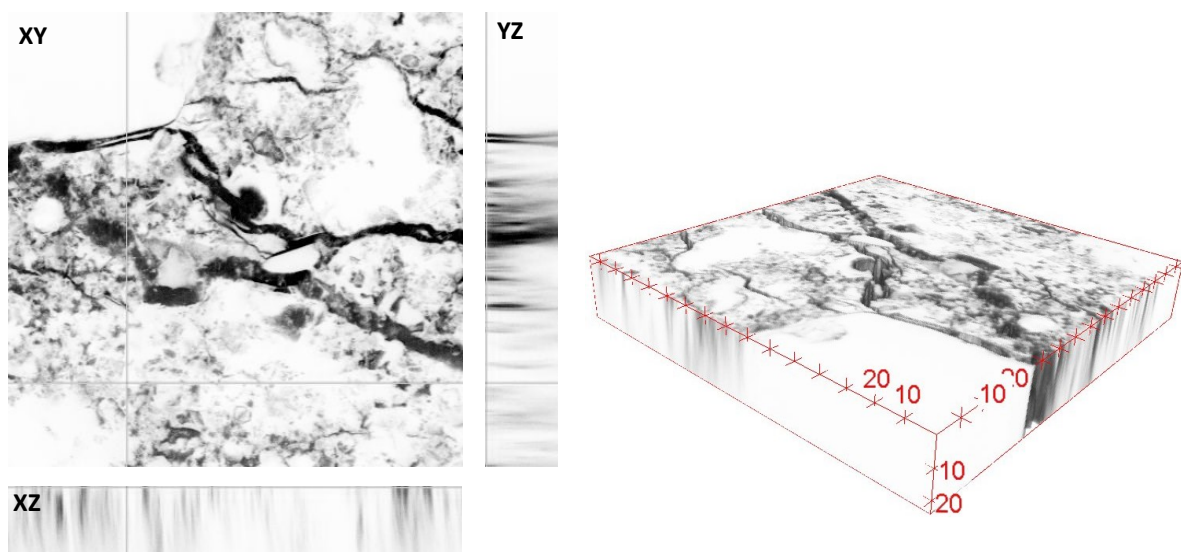


Figure 4-26 Orthogonal views and 3D rendering of concrete (C/C-14/56FT) obtained from LSCM with $40\times$ objective lens. XZ and YZ planes show loss of signal with depth.

4.6 X-ray microtomography

X-ray micro-computed tomography (μ -CT) is a non-destructive 3D imaging technique. This method works by collecting hundreds of 2D radiograph projections at a predefined angle step while the sample is rotated. Subsequently, the radiographs are mathematically reconstructed to produce a 3D image of the sample. Spatial resolution of this technique strongly depends on sample size and CT scanner characteristics. For this reason, two CT scanners will be evaluated. The first is Xradia MicroXCT-400 scanner equipped with 6 objective lenses: 0.39 \times (Macro), 1 \times , 4 \times , 10 \times , 20 \times and 40 \times (Figure 4-29) and several software packages to control the imaging process (XMController, XMReconstructor and XM3DViewer). The second is Metris X-Tek HMX ST 225 (Figure 4-27) with CT PRO Metris X-Tek software. These CT scanners are located in Slovenian National Building and Civil Engineering Institute (ZAG) in Ljubljana, Slovenia and in the Natural History Museum in London respectively.



Figure 4-27 Metris X-Tek HMX ST 225 CT scanner in the Natural History Museum, London.

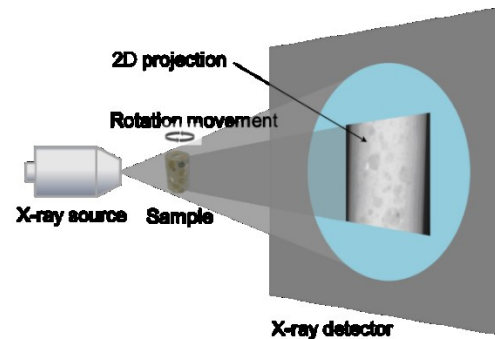


Figure 4-28 Principles of the X-ray microtomography.

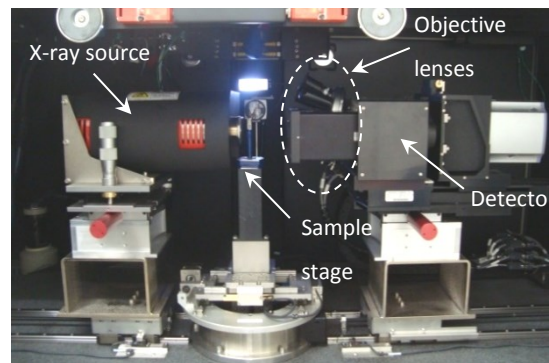


Figure 4-29 MicroXCT-400 Xradia CT scanner in ZAG, Ljubljana, Slovenia.

4.6.1 Samples

Two concrete samples were prepared and subjected to drying shrinkage (C/C-7/105) and autogenous shrinkage (C/SF-14/SC). Cylindrical samples were extracted by drilling cores from a larger sample. Three cores with diameter of 4 mm, 9 mm and 30 mm were obtained from C/C-7/105 sample and a 30 mm core was obtained from the C/SF-14/SC sample. X-ray microtomography does not require any additional sample preparation.

4.6.2 Imaging procedure

The cylindrical sample was mounted on a sample holder and placed on the sample stage between the X-ray source and the detector in a way to achieve maximum geometrical magnification and at the same time to allow an optimal fitting of the sample into the field of view of the detector. Figure 4-28 illustrates the principles of this technique. Different scanning set-up parameters were employed for the two CT scanners.

The X-ray source of the Metris X-Tek HMX ST 225 scanner was operated at 220 kV and 200 μ A current. Additionally, a 5 mm thick copper filter was selected to remove low-energy X-rays that do not provide useful information to improve image quality. The rotation step was set at 0.1146°, therefore 3142 projections were acquired with exposure time of 1.25 seconds per frame. The imaging process was completed within 40 min and following that, automated reconstruction was carried using the PRO Metris X-Tek software.

The Xradia MicroXCT-400 scanner was operated at 100 kV and 10 W power. Objective lenses used were the 4 \times and 0.39 \times magnification to match the samples size. Low energy X-ray filters were selected to improve image quality. The rotation step was set at 0.09°, therefore 4000 projections were acquired with exposure time of 0.3 frame per second. The imaging process was carried out automatically and required up to 4 hours. Following that, 3D volume reconstruction of the collected 2D projections was carried out using the XMReconstructor software.

Subsequently, corrections for centre shift (offset of the axis of rotation) and beam hardening (an increase in mean energy of the X-ray beam as it passes through the scanned object) were applied and the 2D reconstructed slices were saved as 16 bit tiff files. Examples of the 2D slices from each sample, scan settings and achieved voxel size resolution are presented in Figure 4-30.

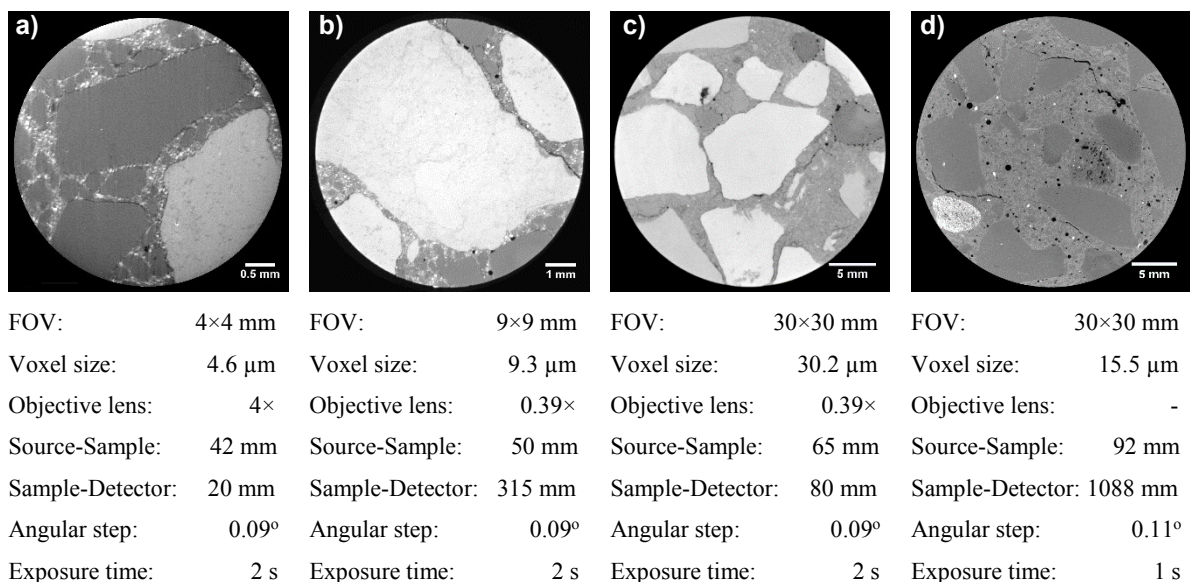


Figure 4-30 2D reconstructed slices of concrete (C/C-7/105 and C/SF-14/SC) from X-ray microtomography and scan settings. Images (a) to (c) obtained with X-Radia 400 CT scanner and image (d) with Metris X-Tek HMX ST 225.

4.6.3 Results

The reconstructed image volumes of the Ø4 mm, Ø9 mm and Ø30 mm cores from concrete C/C-4/105 imaged by XRadia 400 CT scanner and Ø30 mm core from concrete C/SF-14/SC imaged by Metris X-Tek HMX ST 225 CT scanner are shown in Figure 4-31. A median filter of $0.5 \times 0.5 \times 0.5$ was applied to all images to remove noise and sub-volume cubes of 3.1^3 mm^3 , 5.8^3 mm^3 , 20.2^3 mm^3 and 20.8^3 mm^3 were cropped out of the whole image from the respective cores.

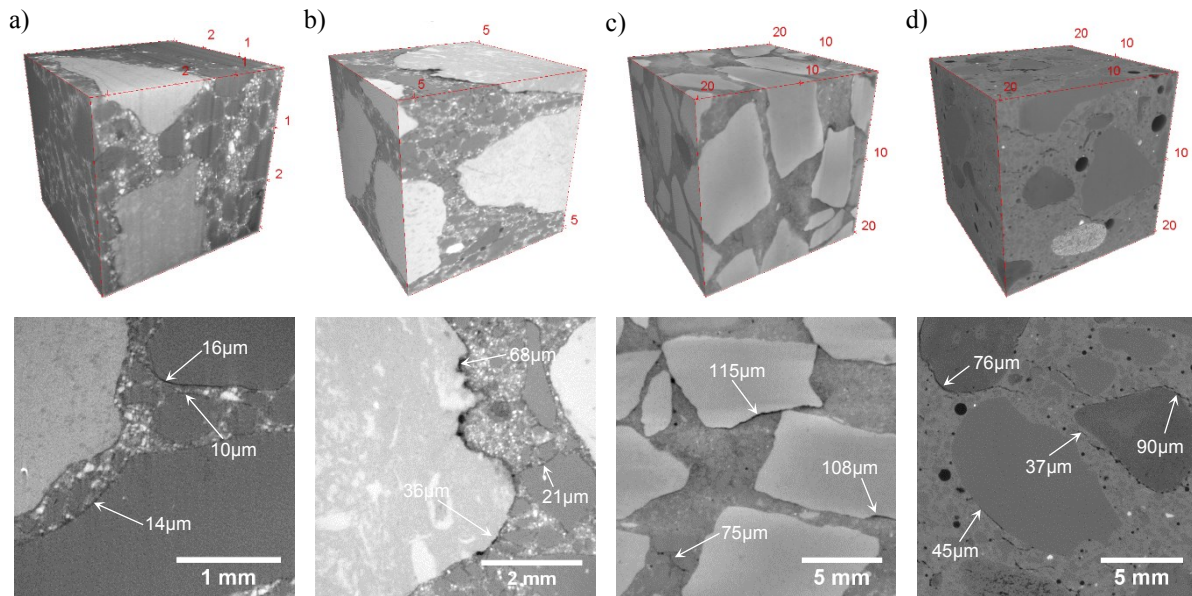


Figure 4-31 3D rendering of concrete cores of a) Ø4 mm, b) Ø9 mm and c) Ø30 mm (C/C-4/105) imaged with X-Radia 400 CT scanner and d) Ø30mm (C/SF-14/SC) imaged with Metris X-Tek HMX ST 225 CT scanner with corresponding 2D slices showing example microcracks.

Results confirm that the achieved voxel size resolution strongly depends on sample size. For cores scanned with the XRadia 400 CT scanner, this is typically 1/1000 of the sample diameter. For example, a voxel size resolution of $4.6 \mu\text{m}$ was achieved in the Ø4 mm core and this decreased to $30.2 \mu\text{m}$ for the Ø30 mm core. Such a huge voxel size will affect the ability to detect small microcracks in a representative volume of material. It is recommended that a feature should be represented by a minimum of two or three voxels to be resolved. Therefore, only microcracks above $10 \mu\text{m}$, $20 \mu\text{m}$ and $60 \mu\text{m}$ in width can be detected on the Ø4 mm, Ø9 mm and Ø30 mm cores respectively. This is consistent with the measurements shown in Figure 4-31. In comparison, the Ø30 mm core scanned with Metris X-Tek HMX ST 225 achieved a somewhat higher voxel size resolution of $15.5 \mu\text{m}$ and therefore it allowed detection of microcracks above $30 \mu\text{m}$ in width as presented in Figure 4-31 d).

4.7 Comparison of imaging techniques for microcrack detection

Comparison of four different imaging techniques (SEM, LSCM, OM and $\mu\text{-CT}$) for microcracks detection was performed on fluorescent epoxy impregnated mortar subjected to drying shrinkage (M/C-7/105). First a 9 mm diameter core was drilled out of the sample and scanned with xRadia 400 CT scanner at a voxel

resolution of 8.26 μm . Then, the core was sectioned with a diamond saw to extract a slice from the middle which was ground and polished at successively finer grit sizes to a 1 μm fineness. Following that, the slice was imaged with an optical microscope (fluorescence mode), confocal microscope and scanning electron microscope in backscattered electron mode after carbon coating. In order to facilitate comparison, the images were captured at the same magnification (50 \times) which corresponds to pixel size of 0.922 μm (SEM), 0.605 μm (LSCM) and 0.86 μm (OM) and stitched together using Microsoft ICE software. A 2D reconstructed slice was selected from the μ -CT data that matched the images obtained by the SEM, LSCM and OM techniques. The same field of view ($2.5 \times 2.5 \text{ mm}^2$) was cropped from the four images and thresholded by means of manual tracing to expose only the visible cracks. Figure 4-32 shows the original and binary images of the selected region obtained by the four imaging techniques. The results clearly show that SEM detected the highest amount of microcracks, followed by LSCM and OM. The μ -CT detected the least amount of microcracks.

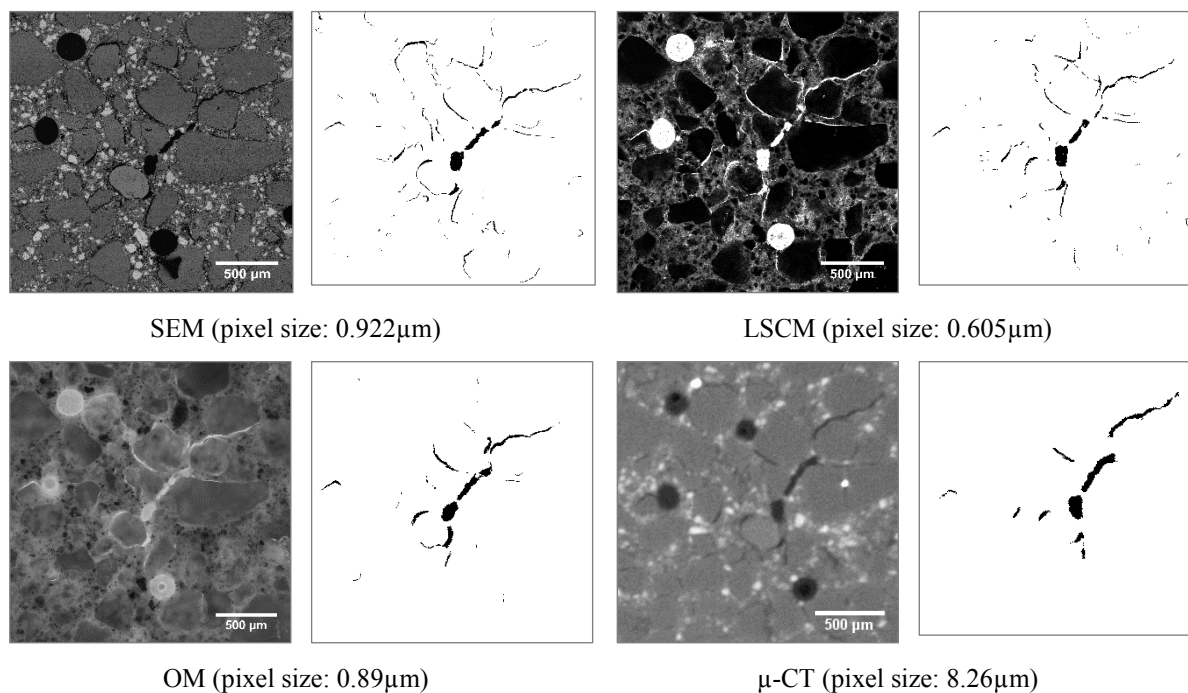


Figure 4-32 Area-matching micrographs obtained using four different imaging techniques. The sample is mortar M/C-7/105.

Image analysis was carried out to measure the characteristics of the detectable microcracks: crack density, areal fraction, distribution of crack width and average crack width. The details of the image analysis are presented in Section 3.3. Results from the analysis are plotted in Figure 4-33 and Figure 4-34. The results show a significant variation in the measured microcrack density. The highest crack density of 1.59 mm/mm^2 was measured on the image acquired by SEM, followed by LSCM (0.99 mm/mm^2) and OM (0.58 mm/mm^2). The lowest crack density of 0.34 mm/mm^2 was obtained from the μ -CT image. On the contrary, the area fraction of the microcracks did not vary significantly between the four images. This suggests that the largest microcracks, which were detected by all techniques, had the greatest contribution to the total area fraction. The smaller cracks that cannot be resolved by the lower resolution techniques had a minor contribution to the total area fraction.

The size (width) distribution of the cracks are presented in Figure 4-34. The SEM technique was able to detect microcracks above 1 μm in width and 80% of the detectable microcracks had widths below 10 μm . The SEM has the highest resolution of the four techniques evaluated and therefore is expected to capture all of the microcracks present. Both LSCM and OM were able to detect cracks wider than 2 μm . However, LSCM has the higher resolution, producing sharper images and stronger contrast between crack and non-crack areas. 80% of cracks detected by LSCM had widths below 15 μm , while the equivalent value for OM was only 45%. $\mu\text{-CT}$ had the lowest resolution and was only able to resolve microcracks wider than 9 μm . The average crack width obtained from SEM, LSCM, OM and $\mu\text{-CT}$ was 10.8 μm , 13.7 μm , 22.9 μm and 36.3 μm respectively. Obviously, this value increases with decrease in the achievable resolution of the technique.

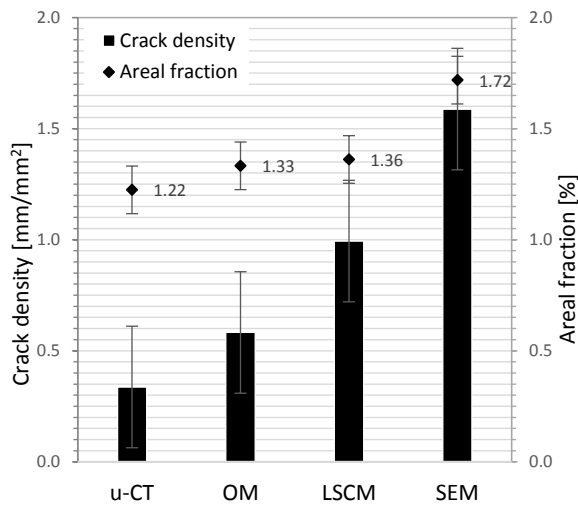


Figure 4-33 Microcrack density and areal fraction as measured by four imaging techniques.

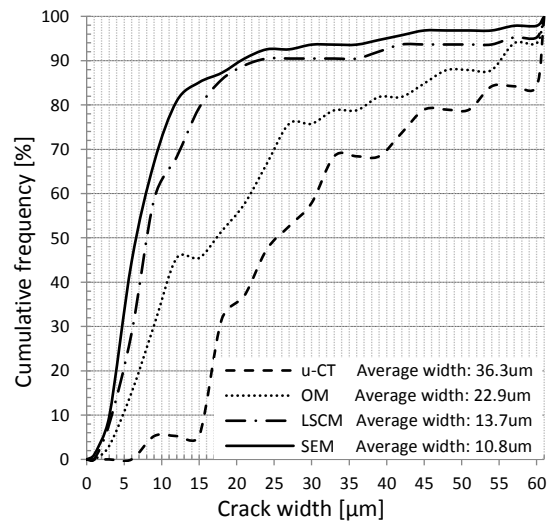


Figure 4-34 Microcrack width distribution and average crack width as measured by four imaging techniques.

4.8 Summary

Preparing samples and inducing microcracks in the laboratory environment turned out to be a difficult task. The challenge is to design the experiment in which microcracks will form in a way that is similar to those in real structures, where usually several deterioration processes occur simultaneously. In this Chapter, four strategies to generate microcracks in cement-based materials were attempted. These were used to study the characteristics of microcracks and to ascertain if it is possible to image the microcracks with available 3D microscopy techniques. An overview of the induced microcracking is schematically illustrated in Figure 4-35.

Uni-directional drying at 30°C and 105°C generated different amounts of drying shrinkage and microcracking. However, the microcracks formed were perpendicular to the drying surface and are rather isolated with little tendency for branching. These microcracks also had very low density (approximately 1 microcrack/mm²) and small widths (<10 μm). Detecting such microcracks will require a technique that is able to image a large sample volume at very high resolution. This is a very ambitious task since the available 3D imaging techniques either lack the required resolution or cannot image large enough volume. It is also

questionable if such characteristics are useful as findings from the PhD study of Zhigen Wu (2014) showed that such drying-induced microcracks probably have little impact on the durability of real concrete structures.

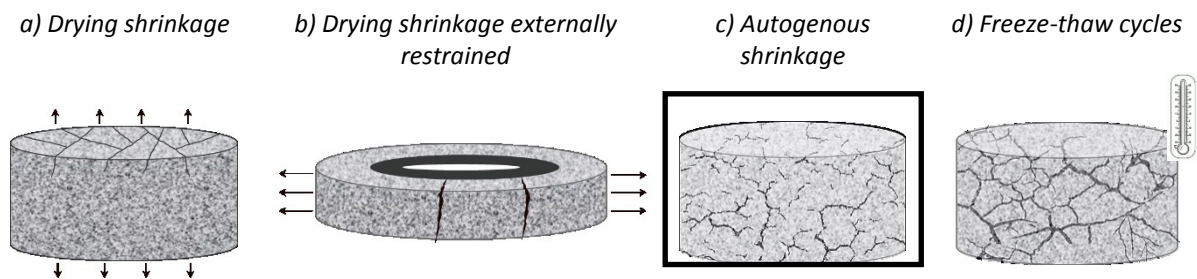


Figure 4-35 Schematic presentation of microcracking caused by different mechanisms.

Another method to produce cracks was by adopting the standardised ring test (ASTM-C1581/C1581M). This procedure can determine the time at which the samples crack when drying shrinkage is restrained both internally (by aggregates) or externally (by steel ring). Unfortunately, these conditions generated only a few very large cracks that were visible to the naked eye. Furthermore, the induced crack widths are strongly dependent on the geometry of the sample and steel ring, i.e. size and thickness. Hence, this method is not of interest for the scope of this project.

A feasible and ‘realistic’ approach to generate microcracks is to subject samples to autogenous shrinkage by sealed curing. Autogenous shrinkage is an important component of volume change besides drying shrinkage and temperature deformation, and it may lead to severe microcracking depending on the magnitude of shrinkage (Bisschop et al., 2002; Lura et al., 2003 & 2009). Autogenous shrinkage is caused by self-dessiccation of concrete due to reduction in internal relative humidity as the water is consumed during cement hydration. Therefore, low w/b ratio high performance concretes (HPC), which in recent years has become increasingly used, are more prone to autogenous shrinkage induced microcracking. The formed microcracks are uniformly and densely distributed, with widths ranging from several μm to hundreds of μm . Their detection with available 3D microscopy techniques is possible and so this type of microcracking will be the focus of the work presented in Chapter 7. To date, no attempts have yet been made on direct characterisation of autogenous shrinkage-induced microcracking in 3D.

Another alternative to generate microcracking is to expose saturated concrete to freeze-thaw cycles. It was observed that the degree of damage increased with increase in number of freeze-thaw cycles. The induced crack widths were in the μm to mm range. The cracks were found to be isotropic, well-distributed and well-connected, as reported by Promentilla and Sugiyama (2010). Unfortunately, these microcracks are probably not very realistic of frost damage that occur in practice. This is because factors such as degree of saturation, loading, salt scaling and freezing/thawing rate are important to frost damage, but these are not adequately captured in the simulated exposure. Therefore, the characteristics of microcracks in real concrete structures exposed to frost are expected to be different to those in lab prepared samples.

Imaging microcracks in cement-based materials in 3D is a challenging task. This is because the widths of the induced microcracks are in a range of 1 to 100 μm and their density vary depending on the damage mechanisms. Given that the size of aggregate particles in concrete are typically up to 10 or 20 mm, the employed technique must be capable of 3D imaging at cm-scale field of view with a resolution of around 1 μm . Such a technique does not yet exist. The 3D imaging techniques explored cover a wide range of FOV and resolution. This is summarised in Figure 4-36 that plots the imaged sample size versus obtained resolution in the Z direction. Note that the resolution in the XY plane for all techniques is much greater than the XZ and YZ planes. Therefore the critical assessment is in the Z direction. Results from this chapter show that currently available 3D imaging techniques are not capable of providing a full characterisation of microcracks in a representative volume of sample.

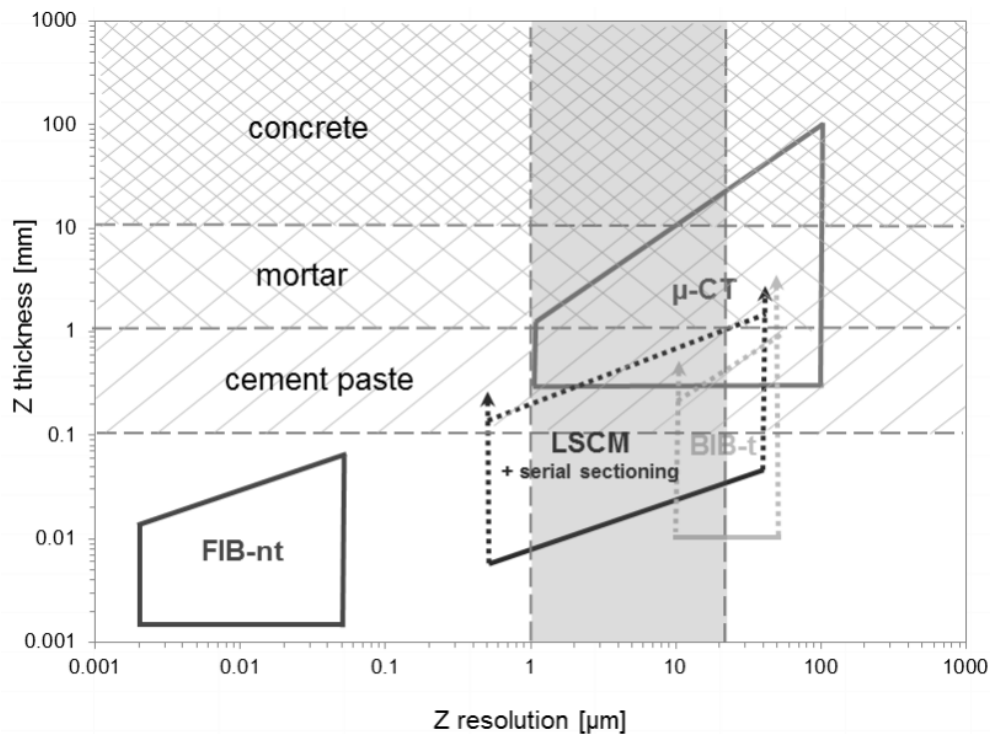


Figure 4-36 Overview of the 3D imaging methods examined showing the achievable image thickness and resolution in the Z direction.

FIB-nt is limited in terms of the extremely small imaged volume and the very long and expensive sectioning process by ion milling. Therefore, only localised single crack can be imaged and this excludes the technique as a method for characterising microcracks in concrete. The broad ion beam combined with SEM imaging approach extends the imaged volume, but its Z-resolution is limited to 10-20 μm because of the slicing depth. Furthermore, each slice requires 6-8 hours of polishing and another 2 hours of SEM imaging at high magnification. LSCM has good spatial resolution, but limited imaging depth. A promising approach is to combine LSCM with serial sectioning. This new approach was developed in collaboration with Marcus Yio, another PhD student in the group, will be discussed in Chapter 5.

X-ray microtomography is able to scan large sample volumes from mm to cm scale non-destructively. However, its resolution decreases with increase in sample size. Its resolution is also dependent on the spot size of the X-ray source. The X-Radia 400 CT scanner tested in this study was able to achieve voxel size resolution of 1/1000 of sample size while the Metris X-Tek HMX ST 225 CT scanner achieved a voxel size resolution of 1/2000 of sample size. At current capabilities, only the larger microcracks are detectable. Nevertheless, μ CT manufacturers are continuously working on developing systems with very small spot sizes and with improved resolution.

Overall, all of the existing imaging methods have their limitations when used for 3D characterization of microcracks in concrete. A way forward is to combine several imaging methods to characterise the microcracks at different length scales, but the challenge will be in the integration and interpretation of the obtained information. Another approach is to design the experiments (sample type, method for inducing cracks) to match the capability of the existing imaging technique.

Chapter 5

Extending imaging depth of LSCM with serial sectioning

The aim of this Chapter is to present a new method that enhances the ability of LSCM to image large 3D volumes of porous materials at sub-micron resolutions. This work was carried out in collaboration with Marcus Yio, a PhD student in the group and it was published in *Journal of Microscopy* (Yio et al., 2015). The method proposed by us combines LSCM with mechanical serial sectioning to produce a series of overlapping confocal z-stacks which are subsequently aligned and stitched based on phase correlation to progressively form a large 3D image. The 3D image can also be extended in the XY direction to further increase the overall image volume. We have trialled the method on different cementitious materials (fly ash, cement paste and concrete samples). Here only results of microcracked concrete are presented as it is the subject of this thesis. Other potential applications are briefly indicated and the advantages and limitations of the proposed method are also discussed.

5.1 Background

Laser scanning confocal microscopy (LSCM) is an extension of 2D optical microscopy. This technique is capable of non-destructive 3D imaging of a thick specimen and for decades has been widely used in numerous biological science disciplines. It enables the reconstruction of three-dimensional structures from sets of 2D images obtained at different depths within a thick object by scanning the light source across the sample and by displacing the focal plane in the Z-axis – a process known as optical sectioning.

The main reason why this technique became popular in biological research is that the high-resolution of the reconstructed image volume obtained from soft and transparent specimens is relatively unaffected by sample thickness (imaging depth). However, for other non-transparent or opaque materials, the intensity of detected signal drops dramatically with depth and this degrades the resolution at larger imaging depths. This is the most problematic aspect of the technique, but it is not the only one. The resolution of confocal microscopy is also affected by several different factors, such as the properties of the objective lens and wavelength of the light source.

These factors limit the use of LSCM for three-dimensional characterisation of cement-based materials. The main application of this technique to such materials has been the characterisation of their surface roughness using the reflected mode of LSCM, as reported by several authors (Ficker et al., 2010, Lange et al., 1993, Kurtis et al., 2003). Also, the fluorescence mode of LSCM has been used by Head and co-authors (Head and Buenfeld, 2006, Head et al., 2006, Head et al., 2008) to produce 3D images of capillary pores, ‘Hadley’ grains and

microcracks in concrete at sub-micron resolution. Such high resolution of around 0.2 μm and 0.3 μm in the XY and Z planes respectively, can be achieved by using high numerical aperture objectives and by minimising the pinhole size (Pawley, 1995). However, the imaging depth of LSCM for non-transparent materials remains extremely small. A maximum imaging depth of 10 μm for concrete at 0.2 μm Z resolution was achieved by Head and Buenfeld (2006) in their experiment, while Petford et al. (2001) reported an imaging depth of ~ 90 μm for sandstone at 2 μm Z resolution and Mauko et al. (2009) – of ~ 100 μm for marble at 1.7 μm Z resolution. This limitation is a huge challenge for 3D imaging of non-transparent materials with LSCM. Hence, the proposed method overcomes the problem of resolution degradation of the reconstructed image volume with increase in sample size.

5.2 Principles of LSCM

Laser scanning confocal microscopy (LSCM) is an extension of 2D optical microscopy. It is capable of collecting serial optical sections from a thick specimen to produce a 3D image. The principle of LSCM is explained in detail in (Head and Buenfeld, 2006, Pawley, 1995). Essentially, a highly-focused laser beam is used as a light source and a pinhole is employed to remove out-of-focus light emanating from below and above the focal plane so as to give a very small focal volume. By scanning the light source across the sample and by displacing the focal plane in the Z-axis (by raising or lowering the microscope stage or the objective lens), a high-resolution 3D image can be built up from a series of two-dimensional images (known as a z-stack) obtained at various depths within the sample. Such procedure classify LSCM as a non-invasive technique for 3D imaging by means of serial optical sectioning.

Diffraction of light occurs when the laser beam passes through the sample and optics in the system; as a consequence, the image formed is a spread Airy disk with a series of concentric rings around a central spot of high intensity. The resolution of LSCM is therefore diffraction limited. The degree of spreading is termed as the point spread function (PSF). Due to the elongated shape of the PSF along the optical axis, the Z resolution is usually 2 or 3 times worse than the XY resolution. The XY resolution, according to the Rayleigh criterion, is the distance between two points at one-half the Airy disk diameter (Pawley, 1993). The Airy disk diameter depends on the excitation wavelength (λ) and the numerical aperture (NA) of the objective lens. The Z resolution, which is also the optical section thickness, is also dependent on the refractive index of immersion oil (n_1) and the pinhole aperture size (P). The excitation wavelength is predetermined by the fluorophores used, while the numerical aperture and immersion oil are fixed to the objective used. The Z resolution can be significantly improved by reducing the pinhole size. For high power objectives, such as 40 \times , 63 \times and 100 \times oil immersion objectives with NA > 1.0, the XY and Z resolution can be ≤ 0.2 μm and ≤ 0.5 μm respectively when the pinhole aperture is reduced to around 0.3 Airy unit. One Airy unit defines the diameter of the first concentric ring in the Airy disk (Pawley, 1993). There are many formulae in the literature for calculating the XY and Z resolutions of LSCM and different manufacturers use slightly different approaches to define the resolutions of their systems. The following two expressions are given by Leica Microsystems Inc. for the system used in this study:

$$\text{XY resolution} = 0.4 \frac{\lambda}{NA} \quad \text{Eq. (5-1),}$$

$$\text{Z resolution} = \sqrt{\left[\left(\frac{\lambda n_1}{NA^2} \right)^2 + \left(\frac{1.22\sqrt{2P}n_1\lambda}{NA^2} \right)^2 \right]} \quad \text{Eq. (5-2).}$$

Pores and microcracks in hardened cement-based materials can only be imaged if they contain fluorophores, this is achieved by vacuum-impregnating the sample with a fluorescent dyed epoxy resin (Head and Buenfeld, 2006, Wong et al., 2006). It is noted that vacuum impregnation is able to fill very fine pores with epoxy resin for BSE imaging, which has a greater resolving power than LSCM and so this does not pose a limitation. Fluorophores have their corresponding maximum absorption and emission wavelengths; therefore, it is crucial to ensure that the correct laser wavelength and beam splitter are used for imaging. It has been demonstrated in (Head and Buenfeld, 2006, Head et al., 2006) that LSCM images of capillary pores in the XY plane are comparable to those obtained using BSE. However, cement-based materials contain various translucent and opaque components such as hydration products, anhydrous cement grains and aggregates. This limits the laser penetration depth and the ability of LSCM to image a representative volume.

5.3 Trials to increase imaging depth in conventional imaging

Various methods were tested to optimise and enhance the imaging depth of conventional fluorescence LSCM. Samples used for this investigation were cement paste obtained from Wong and Buenfeld (2006) and 7 days old sample of cement paste (CEM I 52.5R, water with fluorescent dye Struers EpoDye) mixed with crushed glass. All the pursued trials are very briefly discussed in the following sections.

5.3.1 Fluorophore concentration

Optimisation of fluorophore concentration is important to prevent self-quenching of fluorophores which can result in reduced fluorescence intensities. The fluorophore used in this thesis was Struers EpoDye (C.I. Solvent Yellow 43). It has a maximum absorption wavelength of 490 nm and a maximum emission wavelength of 520 nm at pH 8 (Bartlett et al., 2008), see Figure 5-1-a.

These are similar to those of fluorescein. To establish the optimum concentration of fluorophore, epoxy mixtures containing 0.001% to 5% by mass fluorophore were prepared and mixed with a magnetic stirrer for 24 h to ensure that the fluorophores were evenly dispersed in the resin. Droplets of the epoxy were then excited using a 488 nm laser at intensities of 1%, 4% and 15% (i.e. the default setting for fluorescein). The PMT was set at a constant 625 V. The results (Figure 5-1-b) show that a low fluorophore concentration (0.05 %) was sufficient to give the maximum fluorescence intensity under normal operating laser intensity of 15%. Varying the fluorophore concentration did not produce a significant improvement in imaging depth.

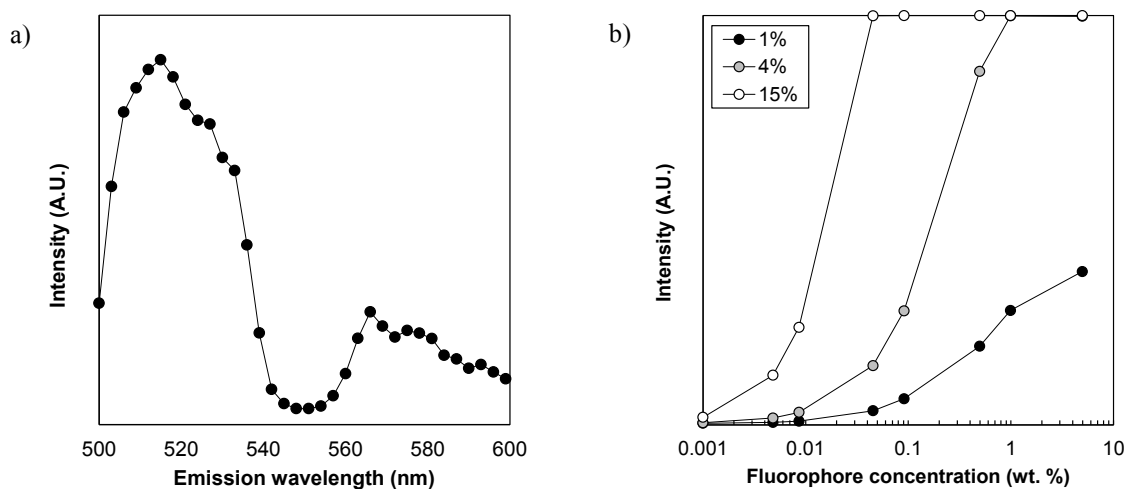


Figure 5-1 a) Emission profile of EpoDye; b) Plot showing fluorescence intensity versus concentration of Struers EpoDye (excited by a 488 nm laser at intensities of 1%, 4% and 15%) (Yio et al., 2015).

5.3.2 Theoretical Z resolution

Optimisation of the theoretical Z resolution for the confocal system was carried out by reducing the pinhole size from 1 AU to 0 AU. In calculating the Z resolution for each objective lens using Eq. (5-2), the light wavelength was taken as 488 nm (λ) to match the maximum absorption wavelength of Struers EpoDye, and the refractive index of immersion medium (n_1) for the 5 \times and 20 \times objective lens was taken as the refractive index of air, i.e. 1 whereas for the 40 \times and 63 \times objective lenses, n_1 was taken as the refractive index of the immersion oil used, i.e. 1.518 (supplied by Leica Microsystems). The pinhole size was varied from 0 to 1 AU to investigate its effects on the Z resolution. Results are shown in Figure 5-2 for each objective lens. In all cases, the Z resolution improves by around 2 times as the pinhole reduces from 1 to 0 AU. In reality, it is not possible to reduce the pinhole size down to 0 AU as this would mean that the pinhole is fully closed and no light can be detected. The minimum achievable pinhole size on Leica TCS SP5 is 0.28 AU. Moreover, reducing the pinhole size limits the amount of detectable signals and as a result, images may appear dark with poor signal-to-noise ratios (SNR). Unfortunately, in all cases an improvement of the z-resolution, did not increase imaging depth.

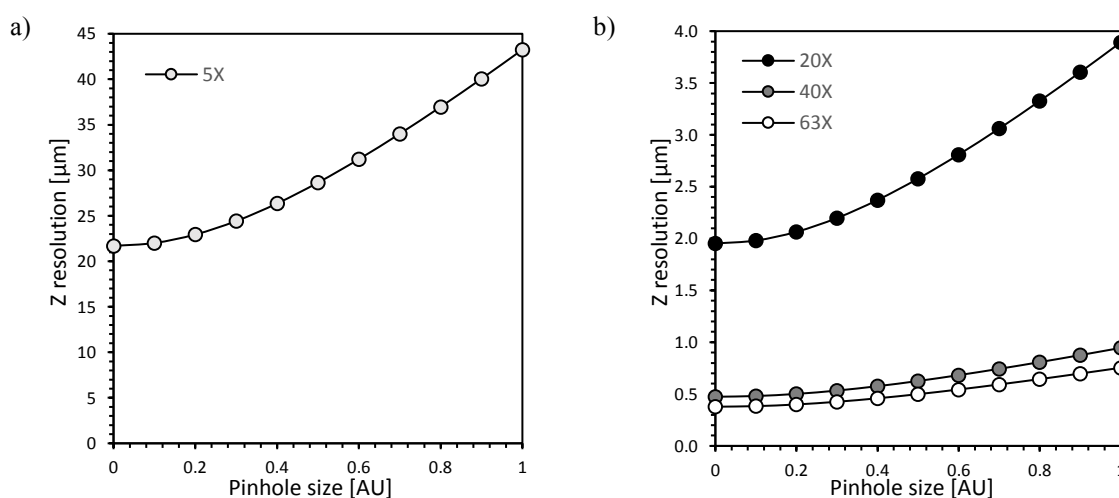


Figure 5-2 Influence of pinhole size on the Z resolutions of a) 5 \times and b) 20 \times , 40 \times and 60 \times objective lenses.

5.3.3 Light compensation

Another potential method to increase imaging depth is light compensation that is by increasing the sensitivity of photomultiplier tube (PMT) or increasing laser intensity with imaging depth. Figure 5-3 illustrates the compensation effects: a) shows an XY image of cement paste near to the sample surface ($\sim 2 \mu\text{m}$ below surface), which is clear and sharp and b) shows an image captured at the same spot but further below the sample surface ($\sim 7 \mu\text{m}$), which appears relatively dark and out of focus, while c-e) show compensated images of b) by adjusting PMT, laser intensity, and laser intensity with PMT, respectively. The results show that these compensations can improve mainly the brightness and signal-to-noise ratio of the images. However, the ability to image at larger depths was only improved by a marginal fraction.

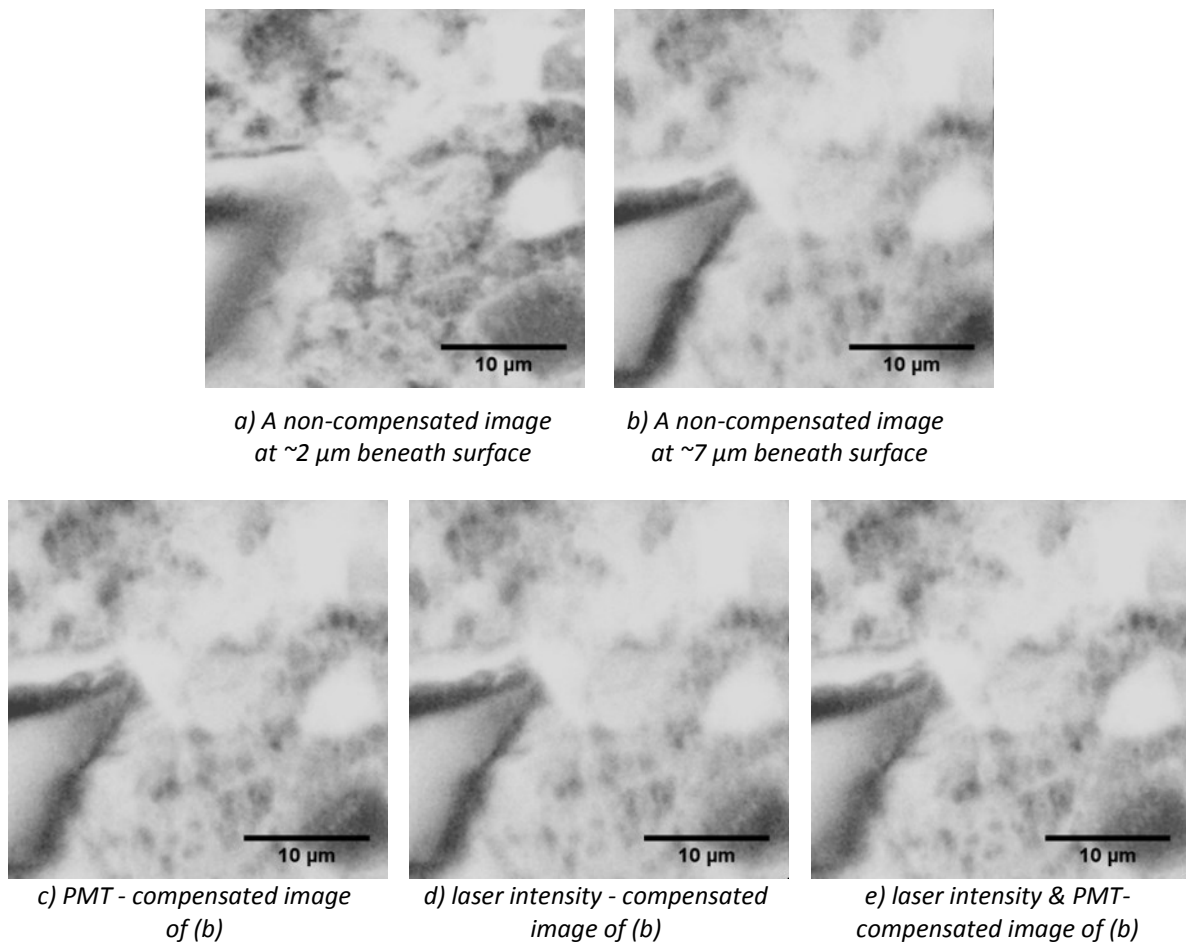


Figure 5-3 Comparison between raw and processed images using light compensation by photomultiplier tube (PMT) or laser intensity. Images are of hardened cement paste.

5.3.4 Image processing methods

Histogram matching and deconvolution are another two image processing methods tested. Histogram matching (performed with Fiji/ ImageJ) modifies the histograms of successive image slices from deeper sections to match that of the first surface image (Castleman, 1996). This equalises image intensities throughout the stack, but the clarity and sharpness of images remain unchanged and degrade with depth. Deconvolution (performed with AutoDeblur – Media Cybernetics) improves the resolution of optical images by removing out-of-focus

light caused by the point-spread function (PSF) (Pawley, 1995). There are two types of deconvolution: non-blind deconvolution based on a theoretically generated or measured PSF and blind deconvolution that estimates the PSF from the image itself. Figure 5-4 illustrates results of image processing applied to the non-compensated image stack from Section 5.3.3: a) shows a raw image (the same as Figure 5-3b), b-e) show processed images of a) using histogram matching and different deconvolution. It was observed that the image enhancement by histogram matching increases image brightness without affecting clarity and sharpness; while deconvolution improves resolution without affecting image brightness and contrast. However, both methods have limited ability to increase the imaging depth of LSCM image stacks because they are insufficient to fully compensate the degradation in signal with depth. The quality of images from deeper sections remains relatively poor.

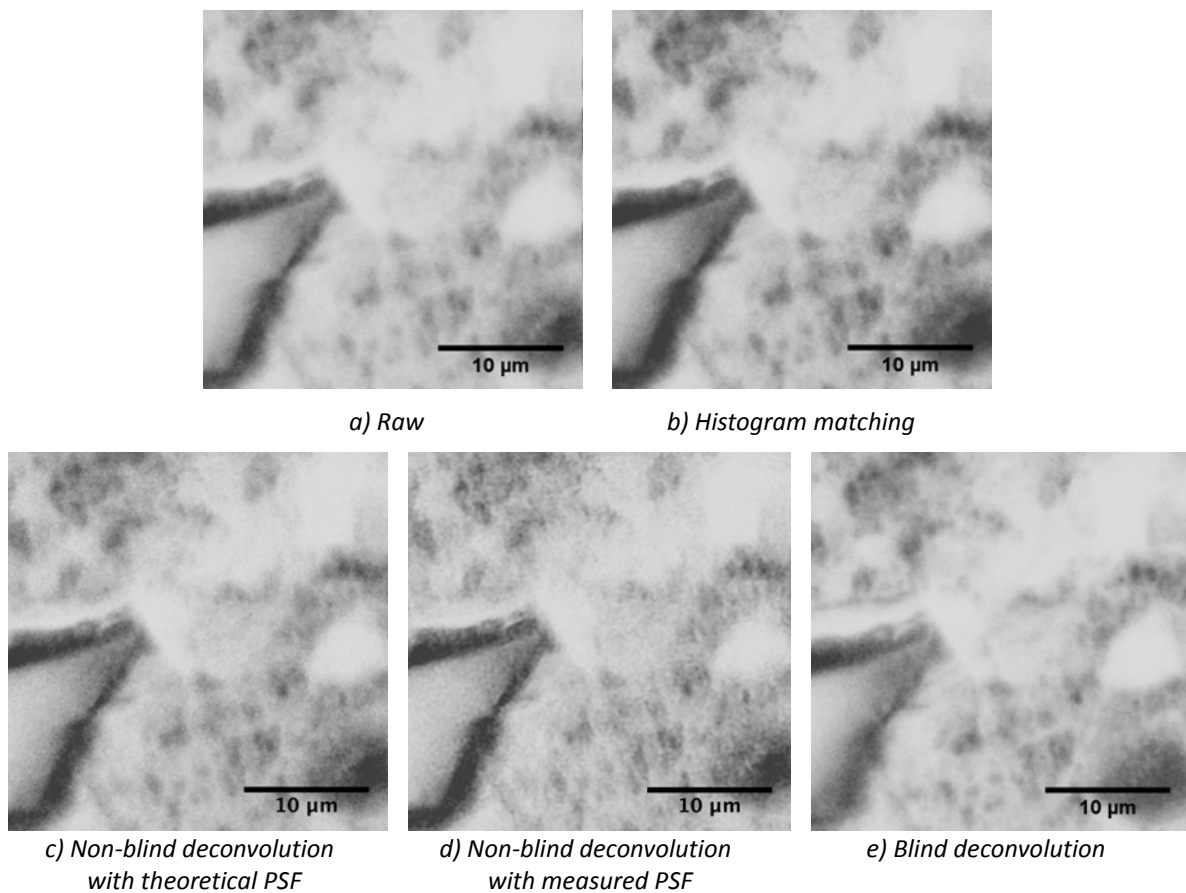


Figure 5-4 Comparison between raw and processed images using histogram matching and deconvolution.

5.3.5 Two-photon microscopy

Two-photon microscopy uses a pulsed laser of longer wavelength photons to reduce light scattering. It also requires no pinhole aperture and this minimises signal loss. Theoretically, it can achieve a deeper imaging depth (Pawley, 1995). Therefore, a feasibility study to verify the capability of two-photon microscopy for imaging cement-based materials was performed.

This investigation was carried out with a cement paste sample and a two-photon microscope Leica SP5 MP at the Facility for Imaging by Light Microscopy, Imperial College London. Figure 5-5 compares the image

captured by two-photon microscopy with the same spot acquired by confocal microscopy. The objective lens used was a 63× water immersion and a 63× oil immersion and the laser wavelength was set at 930 nm and 488 nm for two-photon microscopy and LSCM, respectively. Results show that the resolution of the two-photon microscopy is slightly better, however the achievable imaging depth was similar to that of LSCM as no significant improvement was observed.

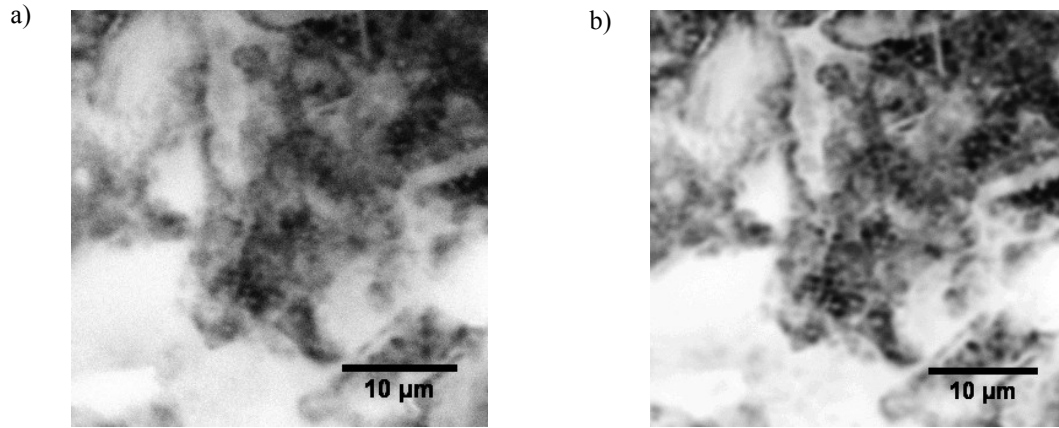


Figure 5-5 Comparison between a) confocal; and b) two-photon microscopy images acquired using a 63× water and 63× oil immersion objective lens with 488 nm and 930 nm laser, respectively.

5.3.6 Transparent aggregates

The idea of using transparent aggregates instead of natural, opaque aggregates came from the discussion of Head and Buenfeld (2006). They remarked that natural aggregates containing transparent or semi-transparent minerals in greater proportions than opaque or light absorbing minerals should facilitate the imaging with the confocal technique. Hence, an experiment was designed to examine whether the use of such aggregates increase the imaging depth. Figure 5-6 presents images of cement paste with glass ‘aggregates’ acquired with lower magnification objective lens of 5×, zoom 2× to show larger FOV (1.55 × 1.55 mm²).

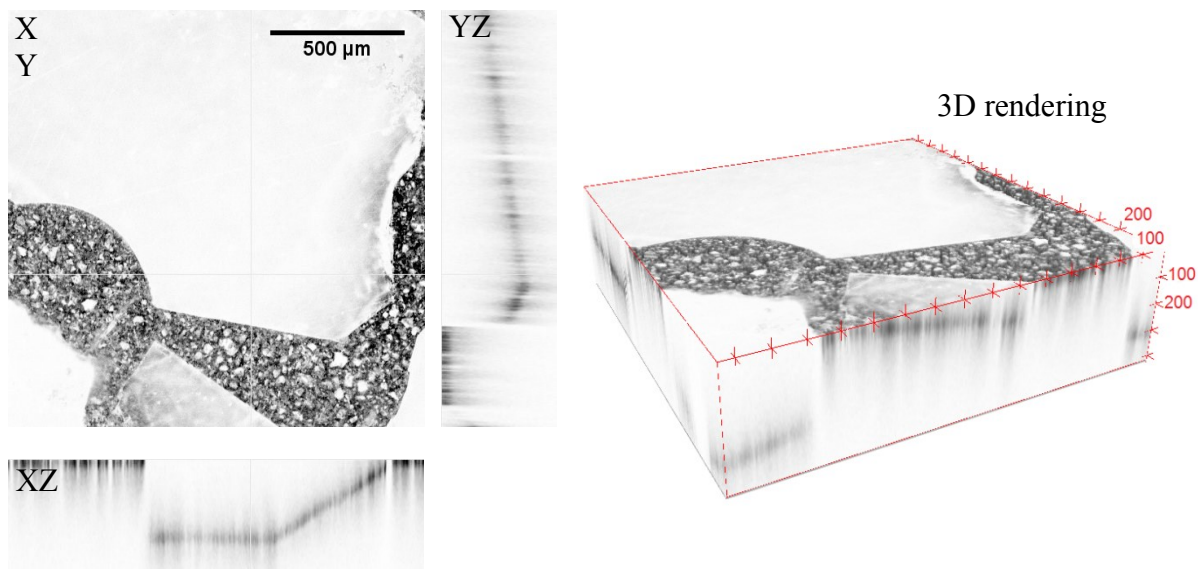


Figure 5-6 Orthogonal view and 3D rendering of cement paste with glass ‘aggregates’ acquired by LSCM with 5× objective lens. XZ and YZ planes show loss of signal with depth underneath glass ‘aggregates’.

Both XZ, YZ planes and 3D rendered images show that despite undisturbed signal penetration through glass ‘aggregates’ which increases imaging depth, there are still regions where non-transparent cement paste around these aggregates blocks the light and limits imaging depth underneath glass ‘aggregates’. Overall, the use of transparent aggregates does not eliminate the problem.

5.4 Proposed method

Given that none of the methods explored in Section 5.3 were successful, we developed a new method to obtain large 3D volumes of hardened cement-based materials by serial sectioning, sequential imaging and volume reconstruction. This method is described in detail in the following sections.

5.4.1 Extending imaging depth (in Z direction) of LSCM

Prior to application of the proposed method, samples must be impregnated with fluorescent epoxy resin (see Section 5.5.1) to preserve the microstructure and more importantly to ensure the visibility of interconnected void space (cracks, pores, etc.). The method consists of five main steps as follows:

1) Serial sectioning

This is done by mechanical grinding and polishing to expose new surfaces for imaging. Cement-based materials are highly heterogeneous and contain phases of varying hardness, so the time and grinding media required to remove a certain amount of material may vary from sample to sample. Hence, an initial process of trial and error is required to estimate these. This is crucial because the success of the method relies on the ability to control the amount of material removed and to ensure that the z-stack from each serial section shares overlapping regions with the subsequent section for stitching using 3D image reconstruction tools. Generally, polycrystalline diamonds of 15 μm can be used but the grinding time should be limited to a few seconds per direction (see Section 5.5.2). The force exerted on the sample and the rotation frequency of the plate should be kept moderately low (e.g. 7 N and 50 RPM) to prevent over grinding. It should be stressed that these are not definitive. Slight adjustments may be required to accommodate variations in hardness of the sample along the sectioning depth.

2) Image acquisition

Following each cycle of sectioning, a high-power objective lens with sub-micron resolution is used to acquire a z-stack from a plane slightly above the sample surface to a plane well below it. The thickness of the stack depends on the type of material imaged and the objective used. For hardened concrete and cement pastes imaged with a 40 \times or 63 \times objectives, z-stacks of approximately 10 μm thick should be acquired, while for 5 \times or 20 \times objectives, z-stacks up to 100 μm thick ensure that each z-stack contains a sufficient number of well-focused optical slices that can be used for 3D reconstruction. The intensity profile provides a good indication of where the image acquisition should begin and end because image intensity is high near the surface and gradually fades away from the surface (see Figure 5-7). If a larger area is required, mosaic of image tiles can be acquired (see Section 5.4.2 for more details).

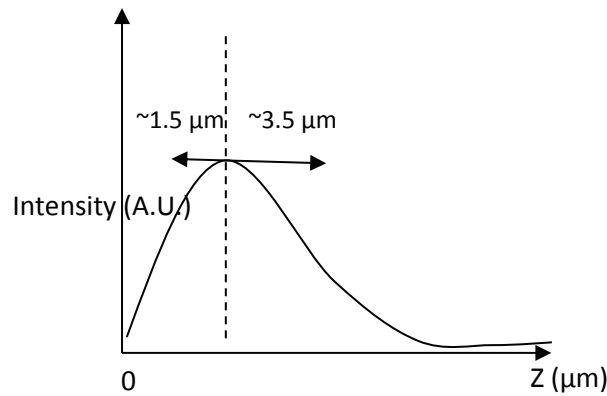


Figure 5-7 Intensity profile of images from a single z-stack showing signal degradation with increase in depth below sample surface. Well-focused images are selected for subsequent stitching.

3) Image selection

Well-focused images with high signal to noise ratio are selected from each stack for stitching. This is done based on the intensity profiles of each stack (Figure 5-7), which always show a peak corresponding to some point below the sample surface. Usually images within 1 to 2 μm above and 3 to 4 μm below the peak intensity can be selected depending on the sample and the imaging settings used. The number of images selected from each stack is kept constant.

4) Alignment

The selected images are then aligned using image registration. Here, we use StackReg (Thévenaz et al., 1998) in Fiji/ ImageJ which is based on an automatic sub-pixel registration algorithm that minimises the mean square difference of intensities between a reference and a test data set. It uses each slice as a template with respect to which the next slice is aligned, so that the alignment proceeds by propagation. Since the sample is well-preserved with epoxy resin, deformation does not occur during serial sectioning. Hence, the alignment process is entirely based on rigid transformation that involves only translation and rotation of images.

5) Stitching

Finally, the aligned z-stacks are stitched. Stitching is done in pairs between consecutive stacks (e.g. stack 1 with stack 2, etc.) using the Pairwise stitching plugin (Preibisch et al., 2009), which calculates the translational shifts in the X, Y and Z directions between two overlapping z-stacks based on Fourier transform-based phase correlation. Note that rotational shift has been accounted for during the image alignment process (see step 4). Once the translational shifts are determined, the two z-stacks are fused together based on non-linear blending that minimises the brightness difference across the boundary. All the z-stacks stitched in pairs are then progressively stitched together based on the computed translational shifts to reconstruct a final 3D image. Figure 5-8 shows a schematic illustration of the stitching process.

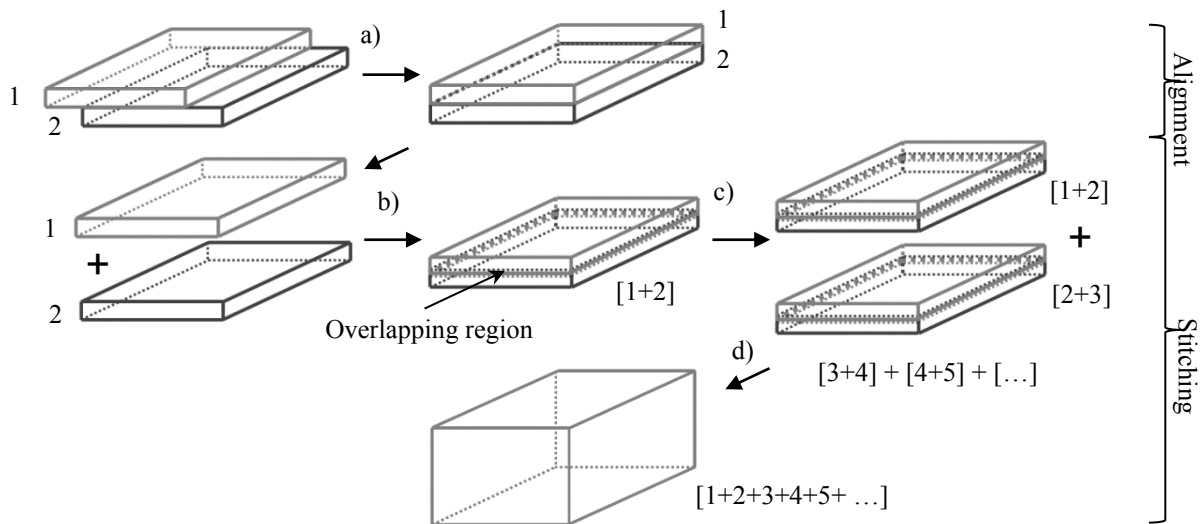


Figure 5-8 Schematic diagram of the stitching process. Selected images from each z-stack are aligned a), stitched in pairs b), and then progressively combined (i.e. $[1+2] + [2+3] + [3+4] + [4+5] + [\dots]$) by stitching the overlapping regions c) to reconstruct an image volume d), (Yio, et al. 2015).

Figure 5-9 shows an actual demonstration of the process on an air void (white) in cement paste filled with epoxy (please note there is another air bubble captured in the resin inside the air void, that is black). The images are cropped to highlight a small region of interest in the XZ plane. The first column shows two stacks, each stack is about $5\ \mu\text{m}$ thick and consists of 30 images, before and after alignment. As can be seen the air voids appear slightly ovate due to presence of overlapping regions. The second column shows a close-up of the stitching outcome between z-stack number 1 and 2. The overlapping region between the two stacks is marked yellow. The displacement between the two stacks in Z, termed as axial shift (ΔZ), is also annotated. ΔZ provides an indication of the thickness of materials removed by sectioning. The third column shows the reconstructed image where the stacks (9 in total) are stitched at the overlapping regions. The image clearly shows circular air voids, however an uneven brightness may occur as a result of slight variations in the imaging conditions, sample characteristics and/or photo-bleaching. This can be corrected by histogram matching.

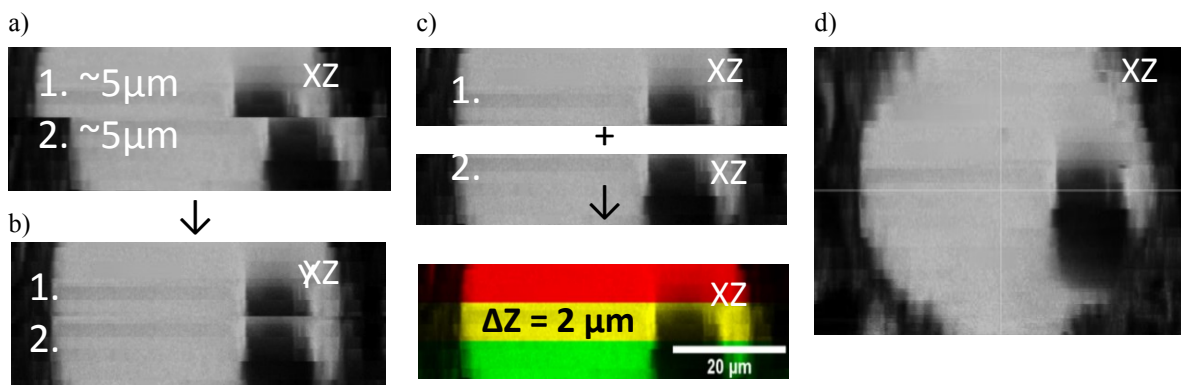


Figure 5-9 Demonstration of the stitching process on an air void filled with resin: a) selected images from two serial section z-stacks, b) alignment of the image stacks, c) close-up of the stitching outcome between z-stack number 1 and 2, and d) stitching of the overlapping regions.

5.4.2 Extending imaging volume in XY plane

The field of view of each image stack is fixed according to the magnification of the objective lens (e.g. 5× objective lens: $3.10 \times 3.10 \text{ mm}^2$, 20× objective lens: $0.75 \times 0.75 \text{ mm}^2$, 40× objective lens: $0.35 \times 0.35 \text{ mm}^2$, 63× objective lens: $0.20 \times 0.20 \text{ mm}^2$). However, it is possible to enlarge this substantially by imaging in tiles and overlapping neighbouring tiles to form a large mosaic. Figure 5-10 shows an example of a 2×2 ‘snake by rows’ mosaic that is made by overlapping 4 image tiles (A, B, C and D). The mosaic tiles are stitched in XY using the Grid/Collection stitching plugin in Fiji/ ImageJ (Preibisch et al., 2009). The stitching processes are automated, and able to compute the translational shifts at sub-pixel precision. Accuracy is expressed in terms of correlation coefficient, R ($0 \leq R \leq 1$) where $R = 1$ indicates that the overlapping regions from mosaic tiles are perfectly identical and hence are highly correlated.

If imaging larger volume in both XY and Z directions are acquired, mosaic tiles should be stitched in the XY prior to the stitching in the Z direction. The stitched mosaic is taken as a single z-stack and its intensity profile is used for selection of high quality images to follow the next steps of the stitching process in Z direction, i.e. alignment and pairwise stitching of the consecutive z-stacks (consecutive mosaics). Figure 5-11 shows a schematic illustration of the image tiles stitching. It is recommended that the overlapping region is between 10 to 20% of the image.

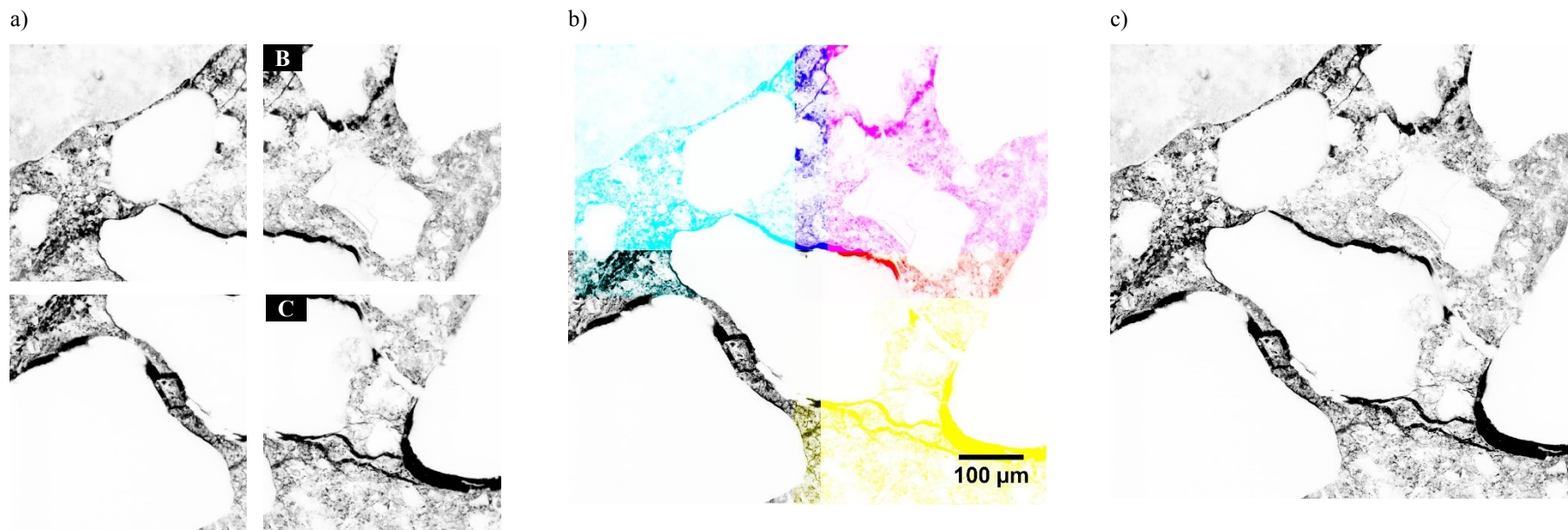


Figure 5- 10 Stitching 2 × 2 mosaic: a) A, B, C and D image tiles of a mosaic, b) stitched image tiles with overlapping region, c) reconstructed large image ABCD-mosaic.

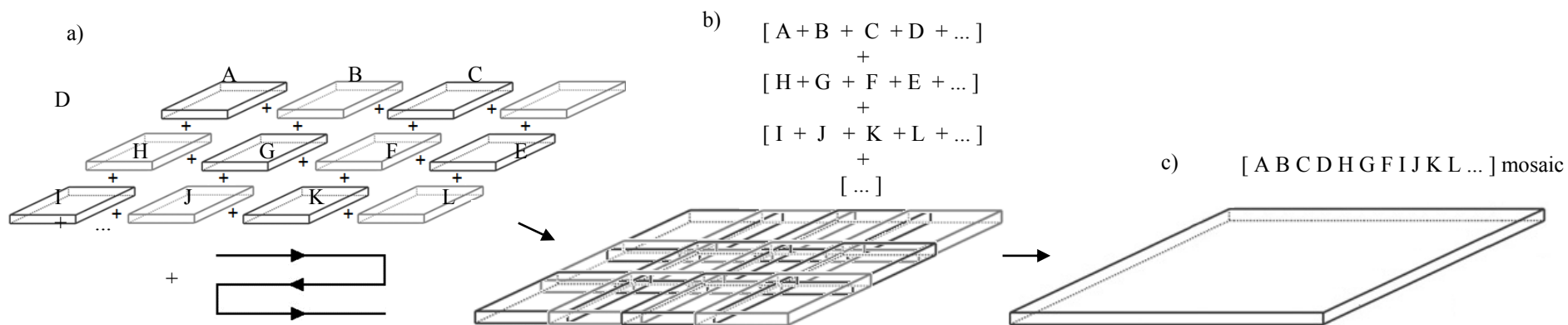


Figure 5- 11 Schematic diagram of the stitching process: a) imaged z-stack tiles of a mosaic ‘snake by rows’, b) stitched z-stack tiles with overlapping region of ~20%, and c) reconstructed thin image volume, used as a single z-stack for stitching in Z direction.

5.5 Application of the proposed method for imaging microcracks

The proposed method was validated by comparison between reconstructed and reference image volumes of spherical fly ash particles embedded in fluorescent resin. In general, a reference image volume of approximately 15 μm thick was acquired from the fly ash sample prior to the start of the sectioning process for comparison with the reconstructed image volume. This validation is explained in detail in our paper (Yio, et al., 2015). Overall, the results obtained show that the serial sectioning and reconstruction process did not distort the reconstructed image and therefore the method is reliable. Here, it was applied to image microcracks in a concrete sample exposed to freeze-thaw action.

5.5.1 Sample preparation

Concrete (C/C-14/56FT) was prepared and cured under water at 20°C until the age of 14 days. Then, the sample was exposed to 56 cycles of freeze-thaw action according to Standards (CEN/TR 15177:2006), where each cycle consists of 8 h freezing phase at -20°C and 4 h of thawing phase at +20°C. Following that, the sample was gently dried prior impregnation. Step-wise oven drying at the temperature of 30°C, 40°C and 50°C was employed to prevent additional cracking. Finally, the sample was impregnated with low viscosity fluorescent dyed epoxy resin under 7 bar pressure, cut into a rectangular block (40 \times 20 \times 8 mm) and ground at successively finer grit sizes (P120, P240, P500, P1200) on diamond disc Struers MD –Piano and polished with diamond pastes of 9, 6, 3 and 1 μm fineness on polishing cloths. Please note, that this is the same sample used in Chapter 4 and details of the materials, mix proportion and conditioning can be found in Section 4.2.1 and 4.2.2 – E.

5.5.2 Imaging

A Leica TCS SP5 laser scanning confocal microscope was used for imaging. The microscope is equipped with a motorised scanning stage Märzhäuser that has a resolution (stepping distance) of 0.025 μm and a repeatability of $\pm 0.75 \mu\text{m}$. An argon laser line of 488 nm was used to excite the fluorophores and the beam splitter was configured to range from 500 nm to 600 nm to allow the emitted fluorescence to be collected by the PMT. A 40 \times (NA 1.25) oil immersion objective with a spatial XY resolution of 0.156 μm , spatial Z resolution of 0.945 (for 1 AU) and a field of view of 350 \times 350 μm^2 was used.

The impregnated flat polished sample was placed on the stage of the microscope and the laser intensity was set to 15% while the sensitivity of the PMT was adjusted correspondingly to prevent under-saturation or over-saturation of the brightness intensity. The pinhole aperture was maintained at 1 Airy unit and a zoom factor of 1 \times was adopted while images were digitised to 1024 \times 1024 pixels to give a pixel spacing of 0.378 μm . This is the default imaging setting used in this thesis to enable a large volume of the sample to be imaged at a sufficient resolution to capture the microcracks. Images were captured from well above and well below the sample surface to achieved about 10 μm thick z-stack each time.

The concrete sample was also imaged in a 2 \times 2 mosaic to increase the image volume further in the XY plane (see Section 5.5.5).

5.5.3 Serial sectioning

Serial sectioning was performed by grinding using a resin bonded diamond disc at 1200 grit / 15 μm fineness (Struers MD-Piano on a LaboPol-5 machine). The force exerted on the samples was maintained at 7 N and the rotation frequency of the plate was maintained at 50 RPM. Grinding was carried out for a very short period to control the amount of material removed between each section. The optimum grinding time were determined to be 2 to 3 s per direction. This removed approximately 3 μm thick of material from the sample. Following this, the sample was polished using diamond at successively finer sizes of 9, 6, 3 and 1 μm fineness (3 to 4 minutes per direction) for imaging.

5.5.4 Reconstructed image volume – single FOV

Serial sectioning and imaging were repeated 50 times in total. The 50 collected image stacks from concrete sample (C/C-14/56FT) were processed following steps no 3, 4 and 5 of the proposed method (Section 5.4.1). The details of the reconstructed image volumes are summarised in Table 5-1. The number of images selected per stack was 35 images, which correspond to a thickness of 5.2 μm . After alignment, the image z-stacks were stitched in pairs and the correlation coefficients (R) was calculated for each pairwise stitching. The ratio between the average ΔZ and the selected stack thickness was 0.63. In other words, the average overlapping region between stacks was at least 37%, which is relatively high. The average correlation coefficients (R) was > 0.9. This shows that the overlapping regions between stacks are nearly identical, highlighting the accuracy of the serial sectioning, stitching and reconstruction.

No. of z-stacks	No. of images selected per stack	Thickness of each stack (μm)	ΔZ (μm)		Overlapping region (%)		R (-)		Reconstructed image thickness (μm)
			Average	Std. dev.	Average	Std. dev.	Average	Std. dev.	
50	35	5.2	3.296	1.228	36.6	23.6	0.922	0.040	166.93

Table 5-1 Summary of reconstruction results.

Figure 5-12 shows a plot of the computed ΔZ and R versus the cumulative reconstructed image thickness. Hypothetically, the relationship between ΔZ , R and the sectioning process is as follows: ΔZ (equivalent to the thickness of material removed) is dependent on grit size, time and pressure applied during the grinding process. A larger ΔZ would result if a thicker layer is removed under a larger grit size, higher grinding pressure or a longer grinding time. Consequently, the overlapping region between stacks would reduce and become less correlated (R). Although it was attempted to use the same sectioning process throughout this study, the values of ΔZ and R varied slightly between consecutive stacks. This could be due to the fact that the serial sectioning process was semi-automated and that there is a variation in the sample hardness. However, the minimum R values in all cases were no less than 0.8, meaning that all consecutive stacks contained overlapping

regions that correlated fairly well. It was noted that larger ΔZ tended to give poorer R, but this relationship was not absolute (see Figure 5-12). While the method can be inconsistent, it is worth pointing out that it is not necessary to have uniform thickness of materials removed each time as long as all the z-stacks have overlapping regions for stitching.

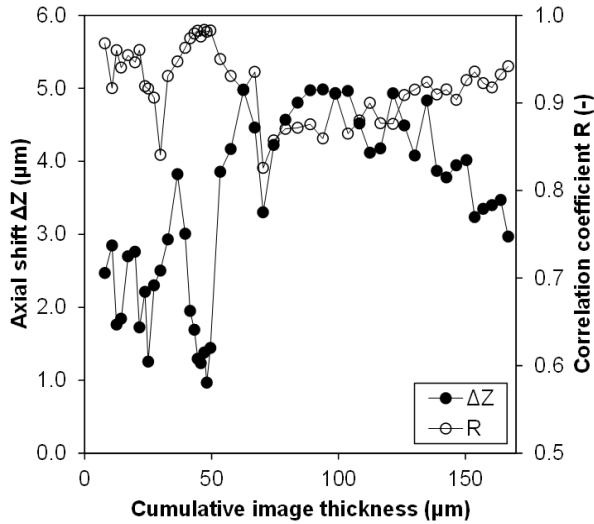


Figure 5-12 Plot of axial shift and correlation coefficient as a function of cumulative image thickness, (Yio, et al., 2015)

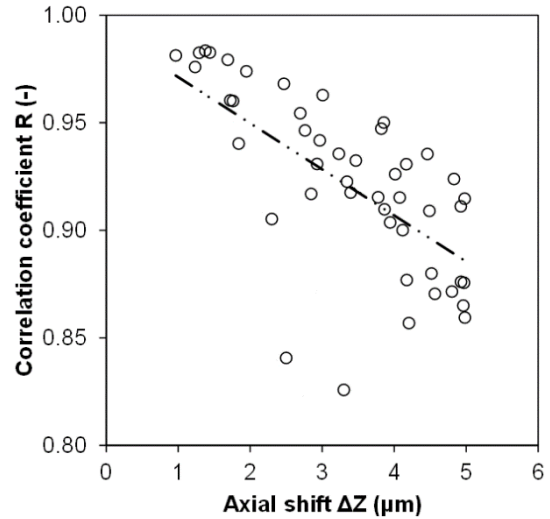


Figure 5-13 Plot showing R versus ΔZ for all samples, (Yio, et al., 2015)

The reconstructed image volumes for the concrete sample is shown in orthogonal views in Figure 5-14. All images are converted to a grey scale and inverted to highlight the features of interest. Dark areas are the fluorescent epoxy-filled void spaces (microcracks and capillary pores) whereas bright areas correspond to solids. A median filter of $1 \times 1 \times 1$ was applied to the images to remove noise.

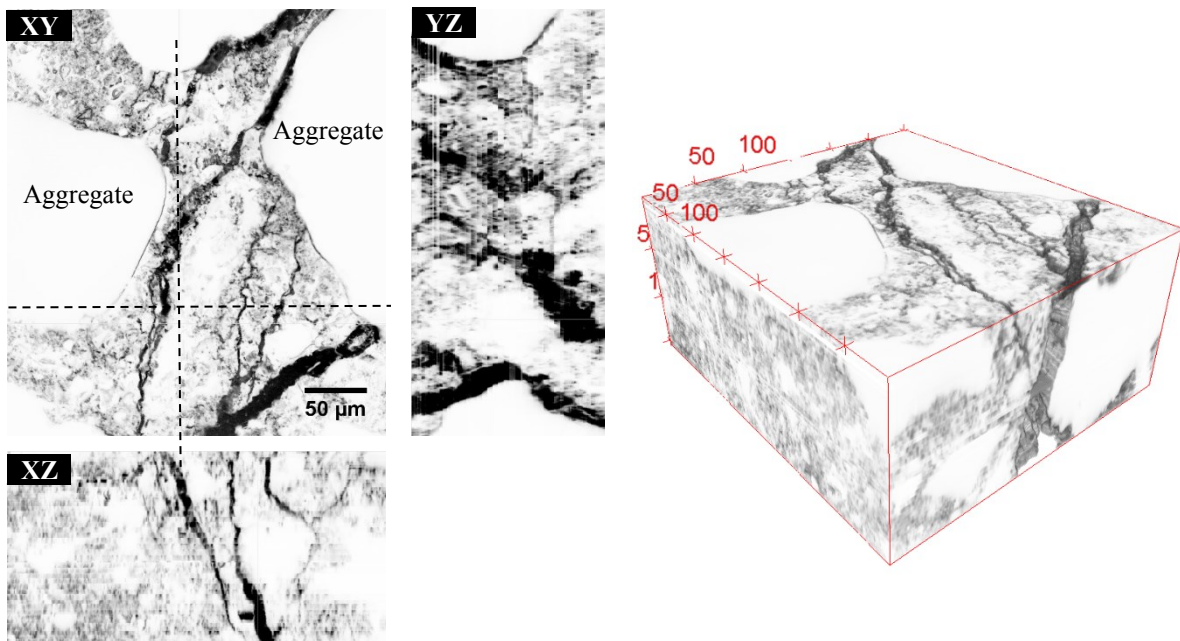


Figure 5- 14 Orthogonal views of reconstructed image of concrete (C/C-14/56FT) with 3D rendering.

The reconstructed image volume of the concrete sample (C/C-14/56FT) shows substantial amounts of microcracking induced by cyclic freeze-thaw. Bond cracks at the interface between aggregates and cement paste, and matrix cracks that propagate through the cement paste are clearly visible. The smallest microcrack detected was around 0.8 μm and the largest observed was about 50 μm wide. The 3D morphology of the microcracks are clearly visible in the orthogonal views as well as in the 3D rendering.

5.5.5 Reconstructed image volume – mosaic 2×2

Any imaging technique is inherently limited in the size of the largest sample that it can image and its ability to resolve the smallest features present in it. The proposed method has been shown to be able to reconstruct thick volumes of cement-based materials from series of fluorescence LSCM z-stacks at sub-micron resolutions with good accuracy. The method can also be extended by stitching in the XY plane to further increase the field of view and hence the overall image volume without loss of resolution. Figure 5-15 shows an example of this where the concrete sample (C/C-14/56FT) was imaged as four (2×2) overlapping mosaic tiles and subsequently reconstructed. The overlapping regions between the mosaic tiles were around 20%. Here, several aggregates are fully captured and the propagation of the microcracks can be better defined compared to that shown in Figure 5-14.

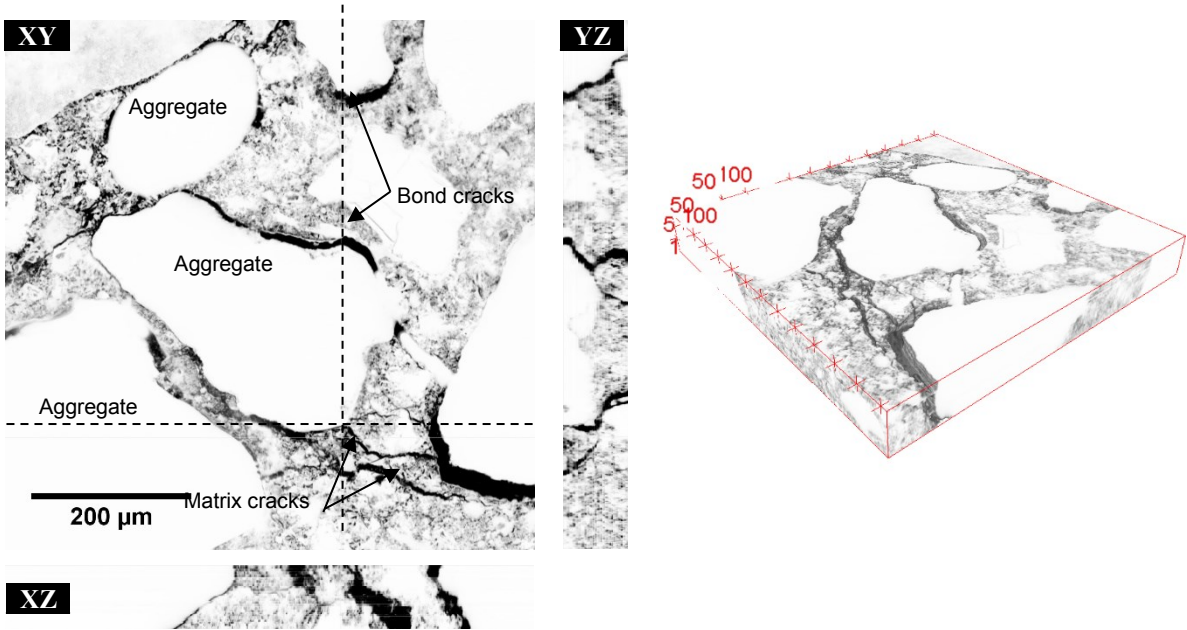


Figure 5- 15 Orthogonal views of the image volume reconstructed from the mosaic 2×2 . Total area in XY is $700 \times 700 \mu\text{m}^2$.

A potential problem in fluorescence microscopy is uneven illumination (sometimes called ‘shadow effects’) in the XY plane, especially when a large area is imaged and the sample is not perfectly flat and horizontal. In such instance, the image can be corrected prior to alignment by means of pseudo flat-field correction. This is carried out by dividing the raw image by a flat-field image generated by mean-filtering the raw image using a large kernel size. An example of this is shown in Figure 5-16. Uneven brightness may also occur along the depth of reconstructed image volumes due to factors such as varying imaging conditions after

each cycle of sectioning, inherent inconsistencies or heterogeneities in the sample and/or photo bleaching of the fluorophores due to pro-longed exposure to laser. This can be rectified using histogram matching (Camp, et al., 1997, Castleman, 1996) that matches the histograms of successive image slices to that of the first image of the reconstructed image volume to give uniform intensity along the depth.

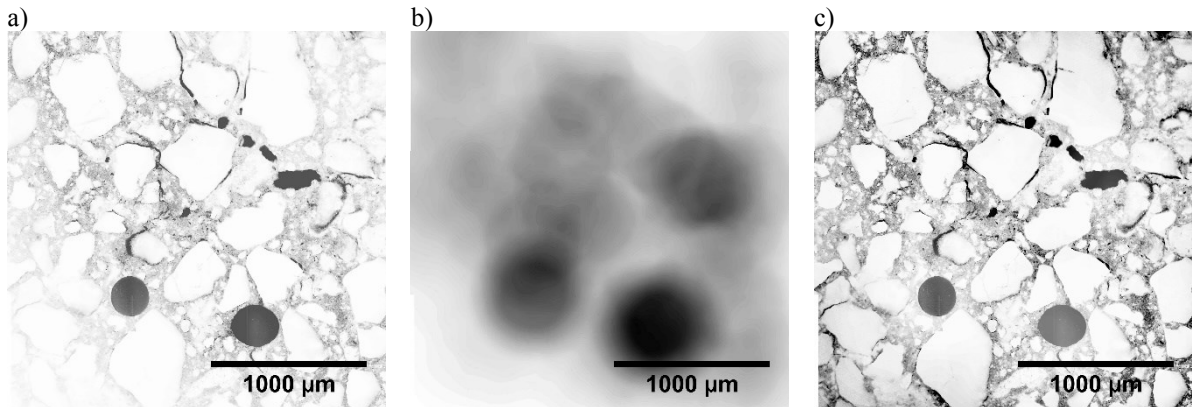


Figure 5-16 Correction of uneven brightness in the XY plane of a large LSCM image: a) raw image b) flat field image generated by mean filtering of a) with a kernel size of 350 pixels, and c) corrected image. This image was captured with 20× objective lens as a 3 × 3 mosaic, with a stitched area of 2.43 × 2.43 mm².

5.6 Summary

A major limitation of laser scanning confocal microscopy (LSCM) when used for three-dimensional characterisation of non-transparent porous materials such as cement-based materials is its shallow imaging depth. This chapter presents several attempts to overcome this limitation. Unfortunately, most of them, (apart from serial sectioning), failed. Fluorophore concentration did not play a major role in the imaging depth because a small amount of fluorophores was sufficient to give maximum fluorescence intensity under normal operating laser intensity. Light compensation by adjustment of PMT and laser with depth, and histogram matching improved mainly the image brightness; their contribution to increasing imaging depth was insignificant. Blind deconvolution was able to improve overall image quality but it was not effective on images from deeper sections. In the case of two-photon microscopy, the imaging depth was similar to that in conventional LSCM and no significant improvement was observed. Use of transparent aggregates improved the imaging depth only locally, because underneath the aggregates the problem reappears.

A new method that overcomes the imaging depth limitation by combining fluorescence LSCM with serial sectioning was developed. The proposed method has been shown to be able to reconstruct thick volumes of cement-based materials from series of fluorescence LSCM z-stacks at sub-micron resolutions with good accuracy. The method can also be extended by stitching in the XY plane to further increase the field of view and hence the overall image volume without loss of resolution.

Theoretically, the image volumes can be extended infinitely in both the XY and Z planes. However, in practice there are several factors that could limit this. For example, it is difficult to ensure that the sample is perfectly flat and equal thickness throughout, particularly for a large sample. Therefore, it may not be possible to capture mosaic tiles that cover the entire sample at the same focal plane. The sectioning method (i.e. mechanical grinding) also causes the edges of the sample to be worn more easily than the centre. The height of the stage can

be adjusted to accommodate this to a certain degree, but reconstruction could become problematic if there is a large discrepancy in the focus depth of the images in each tile.

Serial sectioning is intrusive, meaning that the sample cannot be revisited once sectioned. Moreover, if too thick layer is removed during grinding, it may not be able to stitch with the following z-stack, as the method requires each z-stack to have overlapping regions with neighbouring stacks. In such case, information between stacks are lost and the whole procedure should be started again. This is very risky as the depth of sample that can be imaged is limited by the impregnation depth of the fluorescent resin since imaging is done in the fluorescence mode. The impregnation depth is dependent on the method of impregnation, viscosity of resin and the pore structure of the sample. However, if imaging a thicker section is required, the sample can be re-impregnated with resin. In this study, the impregnation depth of fluorescent resin for concrete was > 3 cm.

Another disadvantage of LSCM is that it cannot distinguish solid phases of different compositions. It can only image void spaces that contain fluorescent epoxy. Voids that are isolated are not 'seen' as these would not be impregnated with the fluorescent epoxy. On the other hand, the technique lends itself very well for the purpose of characterising interconnected pores and cracks that influence mass transport properties. This can be an advantage of the technique for characterisation of microcracks in cement-based materials induced either by autogenous shrinkage, drying shrinkage, thermal effects, mechanical loading or any deleterious mechanisms, as microcracks are expected to have a significant effect on transport properties.

The proposed method can image a representative volume of concrete in 3D at sufficiently high resolution to capture the microcracks and capillary porosity, which any of the existing techniques are able to do. More importantly, the obtained characteristics could be correlate to transport properties e.g. by isolating the influence of microcracks from other factors such as pore structure and degree of saturation.

However, the main drawback of the proposed method is that the process of serial sectioning, imaging and reconstruction may be very laborious and time consuming especially for imaging large volume at high resolution. For example, the average time required to serial section and image one $5.2 \mu\text{m}$ thick stack at $0.945 \mu\text{m}$ Z resolution from a concrete sample is approximately 45 minutes using our current facilities. We believe, that this can be improved by automating the process, but even then, it is not practical to image sample volumes up to a few cm or even a few mm thick. Such thicknesses are required for imaging representative volume of mortar and concrete in order to characterise developed microcracking. Consequently, the proposed method will not be used further for the purpose of this thesis. However, it is envisaged to have other applications where a smaller image volume is required, for example in characterising 3D particle shape of cements, supplementary cementitious materials and fillers. Existing imaging techniques such as FIB-nt and synchrotron μCT are able to cover only particles in the range between 0.4 to $2.0 \mu\text{m}$ and 20 to $60 \mu\text{m}$, respectively (Holzer, et al., 2010). The proposed method can be used to image a wider range of particle size that bridges the gap between these two techniques. The proposed method was used to image pore structure of cement paste with different binders (Yio, et al., 2017). Other materials that can be characterised include various permeable rocks that are of importance to the oil industry such as carbonates and limestone (e.g. Ketton and Estailades) containing highly connected micropores that cannot be captured by X-ray μCT (Blunt, et al., 2013). Bioceramics that are used in medical applications as bone substitutes are another example. These materials contain micropores of less than $10 \mu\text{m}$ (Dorozhkin, 2010).

Chapter 6

Three-dimensional image analysis of microcracks

3D image analysis is very challenging especially when the features of interest are difficult to segment. Microcracks fall in this category because they tend to share the same brightness value in the image histogram as pores or air voids since all of these features are either empty, water saturated or impregnated with the same resin. Therefore, the aim of this Chapter is to develop an algorithm to separate microcracks from pores, and to extract quantitative data of microcracks such as crack density, orientation degree, distribution of width and length, connectivity and tortuosity. The entire image processing algorithm will consist of the following steps: image pre-processing, segmentation and binarisation, separation of microcracks from other porous features and finally quantification. A 3D image of concrete (C/SF-14/SC) obtained using Metris X-Tek HMX ST 225 CT scanner was used to demonstrate the proposed algorithm in this Chapter. Details of the sample are presented in Section 4.2.2 and 4.6. The 3D image was processed in Avizo Fire 7.1 and Fiji/ ImageJ software.

6.1 Background

Qualitative analysis is often used in cement and concrete research, for example to assess composition, to investigate the influence of various environmental conditions on concrete durability and to study mechanical properties related to failure processes. Qualitative analysis of microstructure can provide useful insights into various concrete properties. However, quantitative analysis is essential for a more fundamental study, for example in statistical analyses, theoretical modelling and validation. Recent developments in computer-based image analysis techniques provide powerful tools that can be adapted towards quantitative microstructural investigation of concrete, including characterisation of microcracks and air voids.

Image processing involves the manipulation of images in order to extract useful information without altering the data present in the original images. The aim is to obtain quantitative information from the extracted features of interest (Marion, 1991). Various operations can be applied to the original images to remove noise and enhance contrast between features of interest (microcracks and voids) and the background. This can be achieved by application of filters such as mean, median or edge detection filters (Efford, 2000, Marion, 1991). Quantitative image analysis requires segmentation to transform the original image into a binary image where the features of interest are separated from the background. Segmentation is usually performed on the basis of thresholding the image histogram. Many different thresholding methods have been developed and adapted to facilitate this process.

A key challenge in segmentation is the separation of features of interest from other features that share similar intensity values in the histogram. This step typically involves morphological and arithmetical operations such as dilation, erosion, closing, opening and hole filling (Efford, 2000, Soille, 2004). Figure 6-1 illustrates the effect of each of these operators. Morphological operators process the binary image based on characteristics of its shape, which are encoded in the structuring element. The selection of appropriate operations and a reasonable number of iterations help to enhance the effectiveness of phase separation.

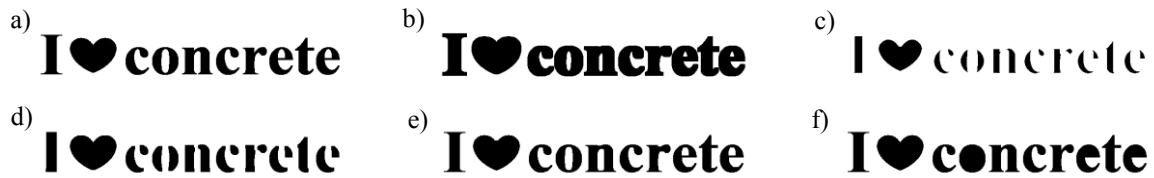


Figure 6-1 Examples of morphological operations: a) original image, b) dilation, c) erosion, d) opening, e) closing, f) holes filling.

The oldest method to analyse microcracks in concrete involves mapping and manual measurements, while more recent methods include automatic quantification (Ammouche, et al., 2000, Ringot and Bascoul, 2001, Soroushiana, et al., 2003). An automatic analysis is facilitated by a large number of algorithms and commercial image analysis software designed with the aim to extract quantitative information from images without needing user intervention. Most of the quantification tools implement stereological techniques to quantify parameters such as degree of anisotropy, orientation, surface area and density or size distribution (Ringot, 1988).

6.2 Image pre-processing and segmentation

Acquiring good quality images is of foremost importance in image analysis. Even so, it is common to apply some pre-processing operations such as filtering to enhance image quality. They can be used to reduce noise, enhance features or define image volumes to be analysed. These are explained in the following sections.

6.2.1 Raw data

The raw data obtained from X-ray microtomography is a stack of approximately two thousand reconstructed slices (in the XY plane) saved as 16-bit tiff images. Figure 6-2-I shows an example of one of the 2D reconstructed slices, which is slice number 1590 from sample C/SF-14/SC. Note that for the remainder of this Chapter, all image processing procedures will be demonstrated on this particular slice. The whole 3D image is digitised to 2011×2011×2011 voxels at a voxel size of 15.5 μm and its total file size is 15.2 GB. Image analysis of such a huge file requires very high computing power and is time consuming. Additionally, many image processing commands and plugins (in Fiji/ ImageJ or Avizo Fire) are written for 8-bit images. For these reasons, all 16-bit images are converted to 8-bit images. This means that every pixel can be assigned with $2^8=256$ different grayscale values ranging from 0 to 255. The size of the converted 3D image is then decreased to

half of the original image because half as many bits are needed for each pixel/voxel in the 8-bit image compared to the 16-bit image. This facilitates image analysis and increases processing speed.

6.2.2 Cropping-out

Prior to any processing, a sub-volume of the whole image needs to be defined and cropped. This will exclude the edges of the sample from further analysis that tend to contain anomalies. For example, samples that are obtained by drilling or coring tend to be affected by fracturing at the cutting edges or aggregate particle pull-outs. Also, image contrast at the edge of the sample is always lower due to beam hardening effects and therefore it is advisable to crop out this part of the image prior to analysis. Figure 6-2-I and Figure 6-2-II show selected image area for cropping and the cropped image in a format of 1320×1320 pixels respectively.

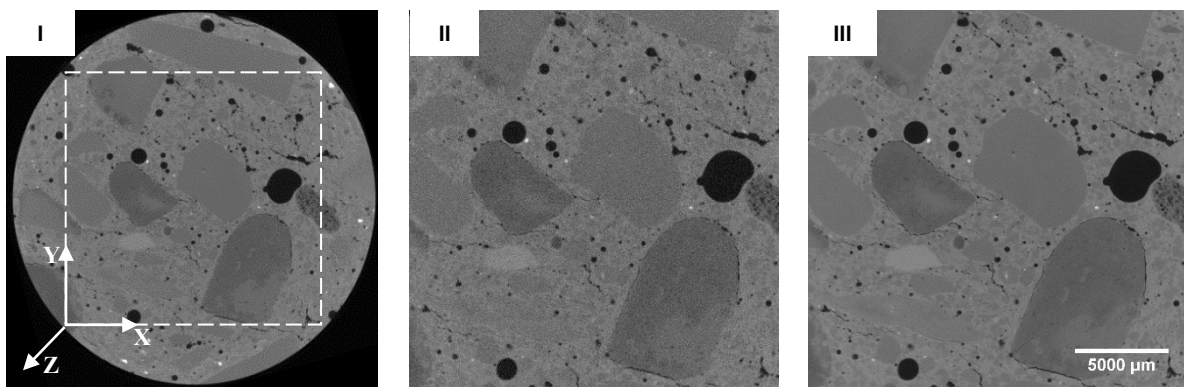


Figure 6-2 Cropping out: I) raw image 2011 × 2011 pixels with selected area for cropping; II) cropped image of 1320 × 1320 pixels; III) 3D median filter of radius 1 applied to reduce noise.

6.2.3 Median filter

Noise reduction was performed by applying a 3D median filter that processes the entire image as a whole. The median filter is a non-linear digital filtering technique, often used to preserve edges while removing noise. Such noise reduction is a typical pre-processing step to improve the results of later processing such as segmentation. The grey levels of all voxels within a defined neighbourhood are sorted from the smallest value to the largest. The central voxel in the sort is the median value and each voxel from the neighbourhood is assigned with this new value.

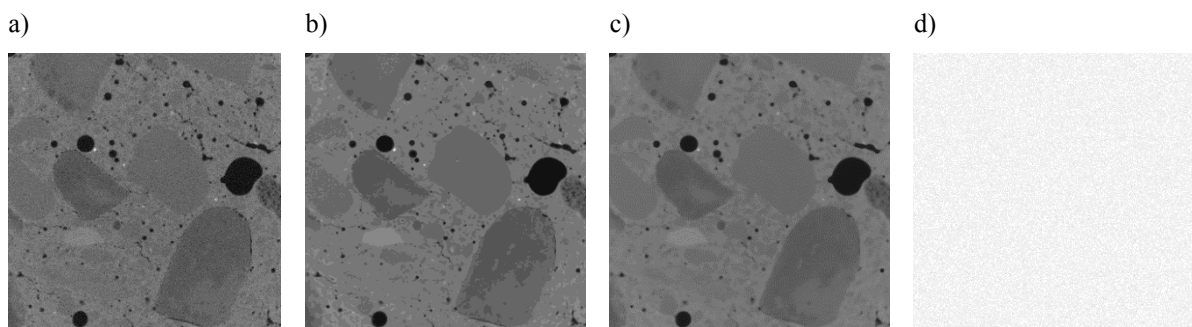


Figure 6-3 Demonstration of noise reduction using median filter with different radii: a) original image; b) filtered with radius 2; c) filtered with radius 4; d) noise (a)-(b).

The median filter in Fiji/ ImageJ uses circular neighbourhoods with determined radius values. An example of filtered image with radius of 2 and 4 are presented in Figure 6-3. Figure 6-3-d shows the noise removed from the original image by subtracting the filtered image (b) from the original image (a). It shows that the noise consists of small positive and negative values, mostly lacking in interesting structure. However, if a very high radius value is applied, then the filtered image can become excessively smoothed or blurred, such as in the case shown in Figure 6-3-c. Consequently, a small radius value of 1 was selected to maintain image quality (see Figure 6-2-III). This radius will be applied to all images collected with X-ray μ -CT in Chapter 8.

6.2.4 Segmentation

Quantitative image analysis requires the feature of interest (microcracks) to be selected and extracted from other phases in the image. This process is called segmentation and the result is a binary image, in which each pixel is assigned either a value of one or zero to indicate whether it belongs to the feature of interest or not. A binary image is usually generated by thresholding, which is the process of selecting the range of greyscale values in the image histogram that represents the particular phase of interest. Several histogram-based thresholding methods exist in the literature where the threshold value is applied globally to the whole image or locally where different threshold values are applied to different parts of the image.

Figure 6-4 shows examples of three different global thresholding methods applied to the same image to segment pores and cracks. These are automated threshold determination methods available in Fiji/ ImageJ : a) the Mean method (Glasbey, 1993) uses the mean grey levels as threshold (Figure 6-4-a); b) the Moments method (Tsai, 1985) attempts to preserve the moments of the original image in the resultant binary image (Figure 6-4-b) and c) the Intermodes method (Prewitt & Mendelsohn, 1966)) assumes a bimodal histogram that is iteratively smoothed using a running average of size 3 until only two local maxima remains (j and k) and the threshold is computed as $(j+k)/2$ (Figure 6-4-c). This example shows that the final result is very sensitive to the chosen threshold. A high threshold value detects more structures, making them bigger until they merge as shown in Figure 6-4-a, while a low threshold value can prevent merging, but does not fully detect the structures as shown in Figure 6-4-c.

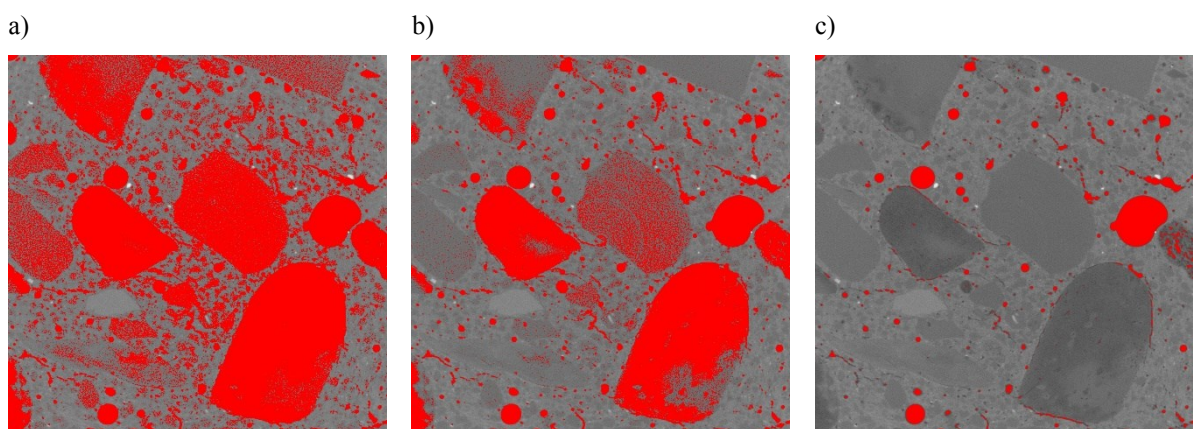


Figure 6-4 Demonstration of various thresholding methods: a) Mean, b) Moments, c) Intermodes.

Having tried a number of thresholding methods, it was found that the most suitable and reliable method for this study is the overflow method proposed by Wong and Buenfeld (2006). This method was also chosen by other authors for their X-ray tomography images, for example by Promentilla and Sugiyama (2010). The overflow method was originally developed for segmenting pores and cracks from greyscale images of cement-based materials captured using backscattered electron microscopy. Therefore, it would be interesting to see the differences between images acquired by the SEM-BSE and the μ -CT. For this reason, the scanned core from sample C/SF-14/SC was sliced, impregnated and polished prior to imaging with SEM-BSE. The images were taken at low magnification of $19\times$ to achieved similar pixel size of $13,3\ \mu\text{m}$ to the voxel size of the μ -CT image. Figure 6-5-a shows the images from both techniques. Note that it is very difficult to find the exact 2D slice from the 3D image, especially because it is not possible to ensure parallel cutting of the core to the 2D slicing of the reconstructed μ -CT image.

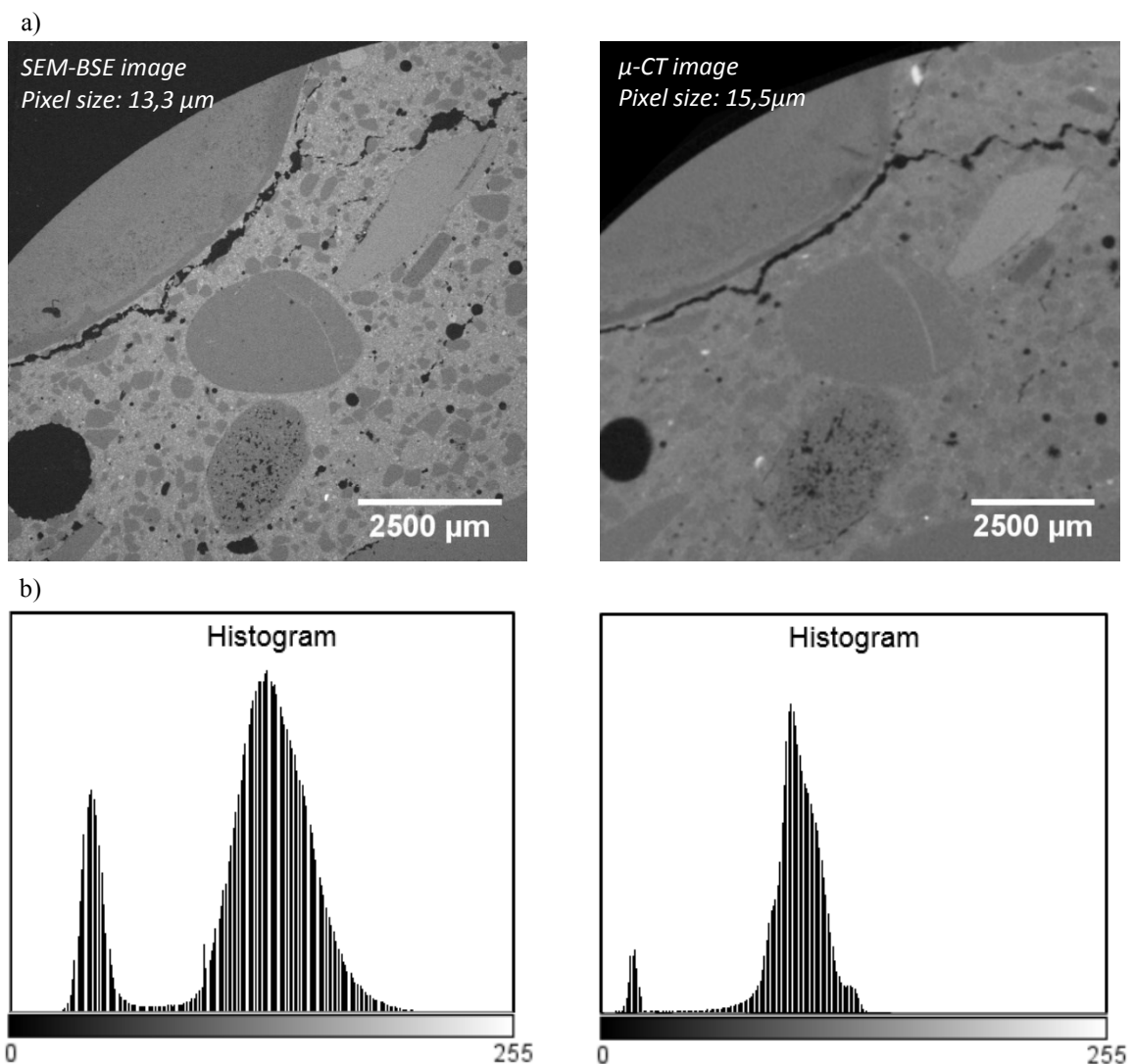


Figure 6-5 Comparison of images acquired by SEM-BSE and μ -CT (a) with their histograms (b).

The first impression is that the SEM-BSE image is much sharper and clearer than the μ -CT image despite their similar pixel/voxel size. This is due to the advantage of the higher spatial resolution of SEM imaging over X-Ray tomography. More detailed comparison between these techniques, especially in terms of

microcracks detection can be found in Section 4-7. Apart from resolution the images show identical features; with similar brightness and contrast and similar range of values on the greyscale histograms (Figure 6-5-b). This suggests that the overflow method developed for SEM-BSE images will work as well for μ -CT images. This comparison also shows that the additional sample preparation required for SEM-BSE does not induce any further changes or damage to the sample microstructure.

The overflow method was recently tested and validated using 3D monte-carlo simulations (Yio et al., 2016). Application of this method for microcrack and pore segmentation is demonstrated in Figures 6-6, 6-7 and 6-10. According to this method, the overflow point corresponds to the inflection of the cumulative grey scale histogram. This inflection can be estimated from the intersection between the two linear segments as shown in the Figure 6-7. The grey value at this intersection can be used as the upper threshold for microcracks and pores.

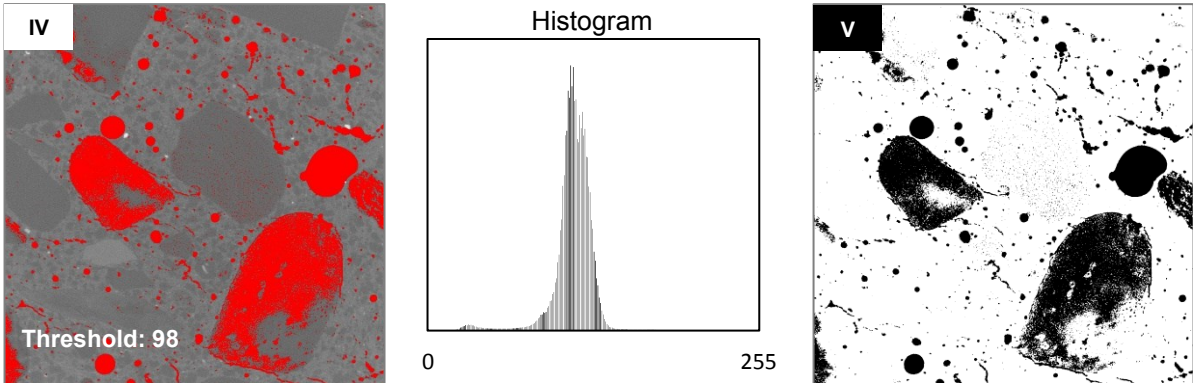


Figure 6-6 Segmentation: IV) thresholding with overflow method (Wong et al., 2006) and grey scale histogram of the stack; V) binary image after segmentation.

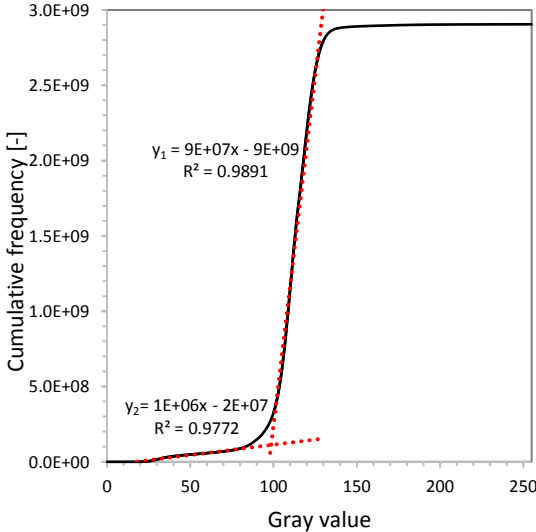


Figure 6-7 Cumulative grey scale histogram of image III The grey value x at the intersection between y_1 and y_2 is used as the threshold according to the overflow method (Wong et al., 2006). Here $x = 98$ for $y_1 = y_2$.

6.3 Separation algorithm

Image analysis of microcracks is very challenging because the microcracks are always segmented together with pores since they share similar grey value in the histogram. Therefore, an algorithm was developed to separate microcracks from other pores such as air voids and pores in aggregates. The entire separation process is summarised on a flow chart shown in Figure 6-8. In this diagram, Arabic numerals are used to represent a particular image processing operation while Roman numerals correspond to the processed images that are presented in Figures 6-2, 6-6, 6-9, 6-10, 6-12 to 6-25 of this Chapter. All steps of the separation algorithm are explained in the following paragraphs.

6.3.1 Separation of pores in coarse aggregates

The aggregates used for preparing concrete samples in this thesis are Thames Valley sand and gravel, which are alluvial deposits. The gravel fraction consists limestones, ironstone, flint, quartzite, quartz and some shells and coral fragments (Robson, 1975), which have different characteristic, especially density. Thus, they would appear in variable pixel intensity values on the reconstructed μ -CT slices. Additionally, some coarse aggregates are very porous while others do not contain any pores. These make the image analysis more difficult and involve additional steps, i.e. separation of pores within aggregate particles.

This section explains the separation and removal of pores in coarse aggregates from the binary image (V). The first step is to detect edges of porous features by applying a morphological gradient filter to the greyscale image (III). Morphological gradient emphasises the object edges using a combination of a greyscale image dilation and erosion. The dilation computes, for each pixel/voxel, the maximum value of its neighbouring pixels/voxels, while the erosion computes the minimum value. Dilation and erosion act as local maximum and minimum operators respectively. The neighbourhood is defined by a structuring element e.g. a ball (sphere in the case of 3D image) with a relevant half-kernel size. Soille (2004) discusses three types of morphological gradients: basic morphological gradient, half-gradient by erosion (internal gradient) and half-gradient by dilation (external gradient). Basic morphological gradient filter (MG) for a grayscale image (A) by using a structural element (B) is defined by Equation 6-1, where \oplus and \ominus denotes dilation and erosion respectively:

$$MG(A) = (A \oplus B) - (A \ominus B) \quad (\text{Eq. 6-1})$$

The external and internal gradients are given by Equations 6-2 and 6.3 respectively:

$$MG_e(A) = (A \oplus B) - A \quad (\text{Eq. 6-2})$$

$$MG_i(A) = A - (A \ominus B) \quad (\text{Eq. 6-3})$$

The external gradient enhances external boundaries of objects brighter than their background and internal boundaries of objects darker than their background, while the internal gradient works in the opposite way.

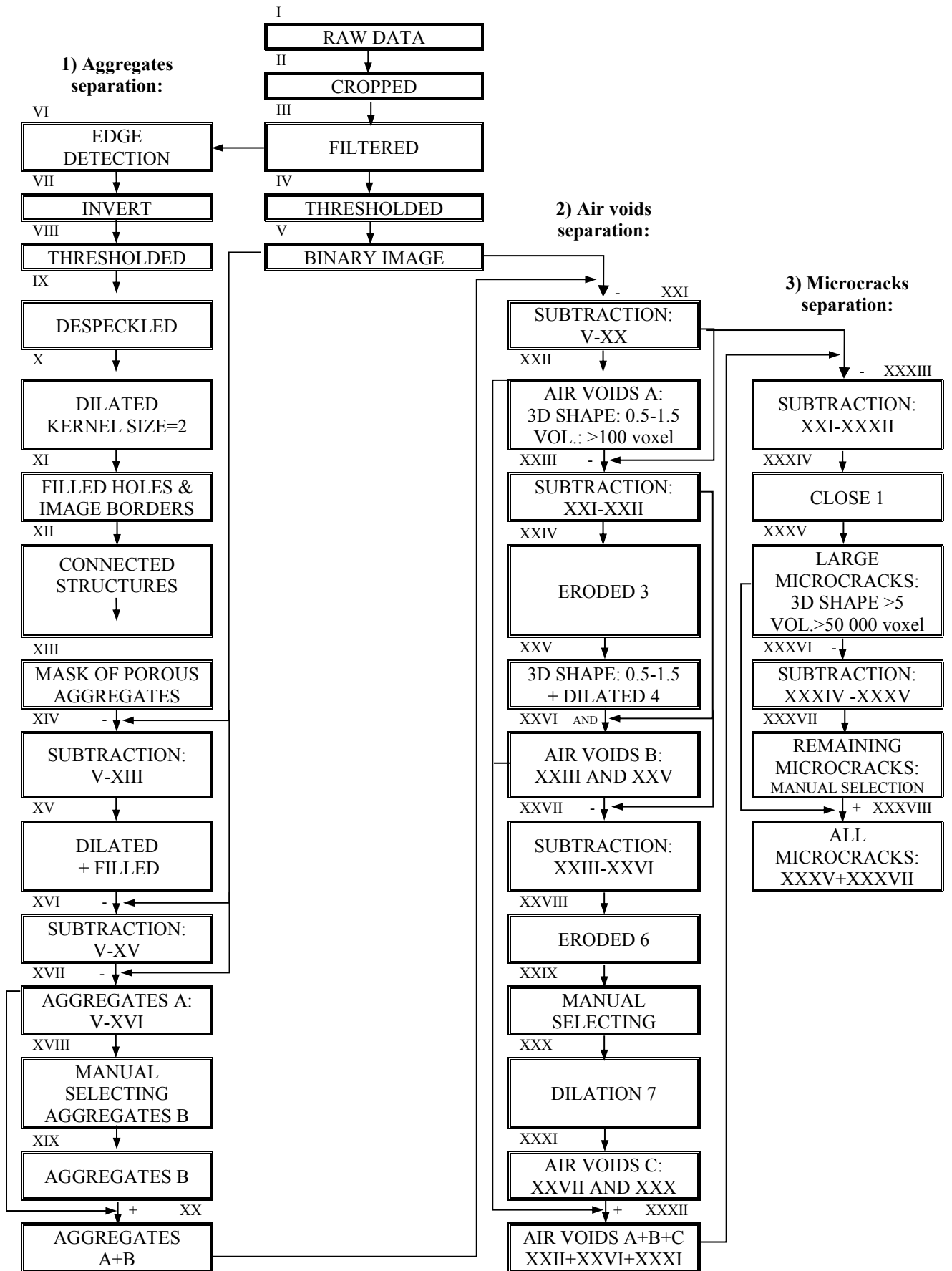


Figure 6-8 Algorithm to separate microcracks from pores in aggregates and air voids.

Here, the external gradient was selected to completely preserve pore edges. Figure 6-9-VI shows the result where a ball (sphere) was used as a structural element with half-kernel size of 3 voxels. The filtered image was then converted to a binary image by applying inversion (VII) and thresholding (VIII). The overflow method (Wong et al., 2006) was again adopted to estimate the threshold from the cumulative histogram presented in Figure 6-10.

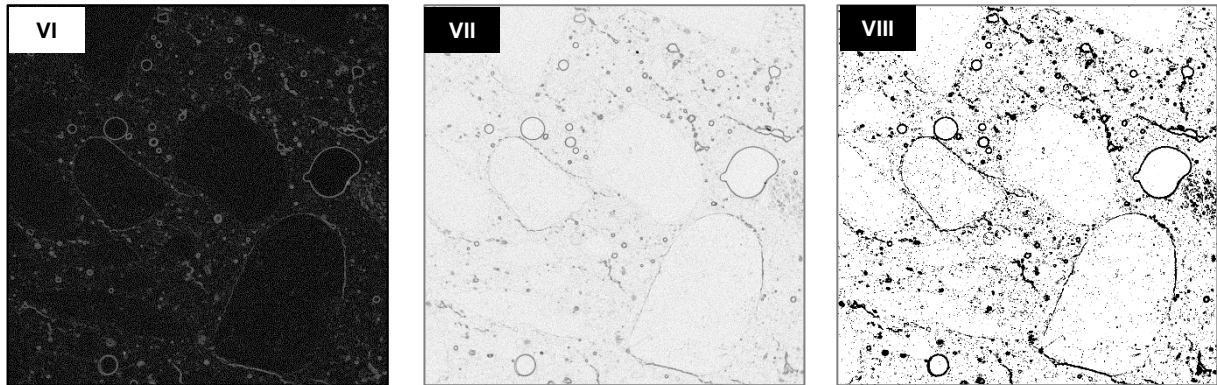


Figure 6-9 Edge detection: VI) detected edges by external morphological gradient with a 3 voxel half-kernel size ball as structuring element; VII) inverted image of VI; VIII) thresholded (binary) image of VII with overflow method (Wong et al., 2006) using threshold value 237.

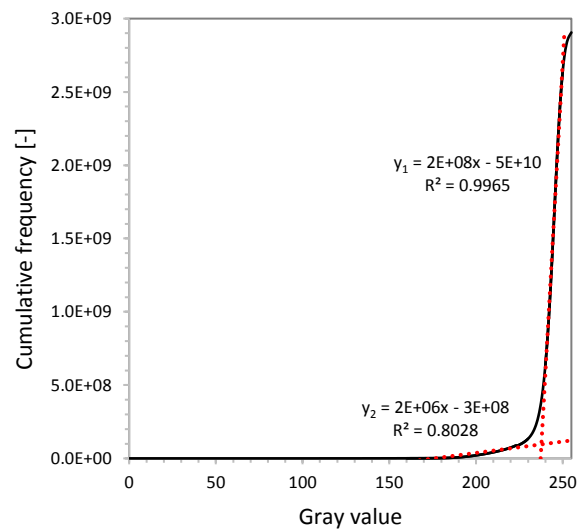


Figure 6-10 Cumulative grey scale histogram of image V The grey value x at the intersection between y_1 and y_2 is used as the threshold according to the overflow method (Wong et al., 2006). Here $x = 237$ for $y_1 = y_2$.

It can be seen that the binary image (VIII) contains many small particles or specks that are noise. These can be removed by using a despeckle operation that searches the image for clusters of pixels/voxels up to the specified size and removing such objects. Figure 6-11-IX shows the cleaned image after despeckling at 3 voxels.

The next step is to process the cleaned image (IX) in order to separate pores in aggregates. This include binary dilation followed by fill holes and fill image borders operations.

Binary dilation (Efford, 2000) is a mathematical morphology operation that uses a structuring element for expanding regions in an image. The structuring element is a small matrix of pixels/voxels, each with a value of zero or one. The matrix dimensions specify the size of the structuring element and the pattern of ones and zeros specifies its shape e.g. cube, disc (in 2D) or ball (in 3D). Morphological techniques probe an image with a structuring element. The structuring element is positioned at all possible locations in the image and compared with the corresponding image pixels/voxels. For binary dilation it is a test of whether the structuring element "hits" (intersects) the neighbourhood. As a result, it creates a new binary image in which the pixel/voxel has a non-zero value only if the test is successful at that location in the input image.

The fill holes operation changes background pixels/voxels (zeros) to foreground pixels/voxels (ones), stopping when it reaches object boundaries. In other words, it closes the object. The fill image borders operation applies the fill holes operation at the six exterior faces of the 3D image. The boundary of the fill operation is determined from the specified neighbourhood connectivity. For example, 6-connectivity for voxels with a common face connected, 18-connectivity for voxels with at least one common edge connected and 26-connectivity for voxels with at least one common vertex connected.

The effect of binary dilation using a ball as a structuring element with half-kernel size of 2 voxels is shown in Figure 6-11-X. The image (X) is clearly enlarged and smoothed. A layer of voxel was added to both the inner and outer boundaries of the foreground, therefore small intrusions into boundaries of the region are filled and gaps between different regions become smaller. Additionally, all holes were enclosed within isolated regions after performing fill image borders and fill holes operations, both set to 26- connectivity. These filled most of the air voids (see Figure 6-11-XI).

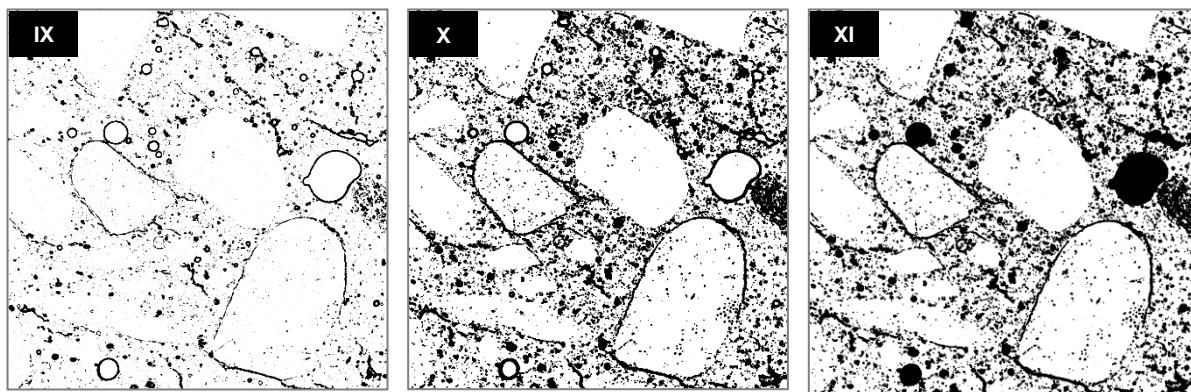


Figure 6-11 Despeckling, dilation and hole filling: IX) removing small particles from image VIII with despeckle filter at 3 voxels; X) image after binary dilation using a ball structuring element with half-kernel size of 2 voxels; XI) image after filling image borders and holes specified at 26-connectivity.

The operations described above are aimed at enlarging all objects and connecting structures, especially cracks and air voids into one (or few) 3D cluster(s) of voxels, which is shown in Figure 6-12-XIII. This selection was made with a segmentation tool (Pick & Move) in Avizo Fire. It allows the selection of the entire connected region (purple on image XII) by clicking on one of its voxels. All voxels belonging to the same phase will be selected in the whole 3D image. Thus, pores in aggregates which are isolated and disconnected to the selected

cluster(s) (grey colour on the image XIII) are separated from the image as shown in Figure 6-12-XIV. In this image, all pore features are preserved except those in the aggregate.

Then, image XIV was subtracted from the original thresholded image V to obtain an image of pores in aggregates only (Figure 6-13-XV). The subtraction operation takes the two images as input and produces a third image whose pixel/voxel values are simply those of the first image minus the corresponding pixel/voxel values from the second image (Marion, 1991).

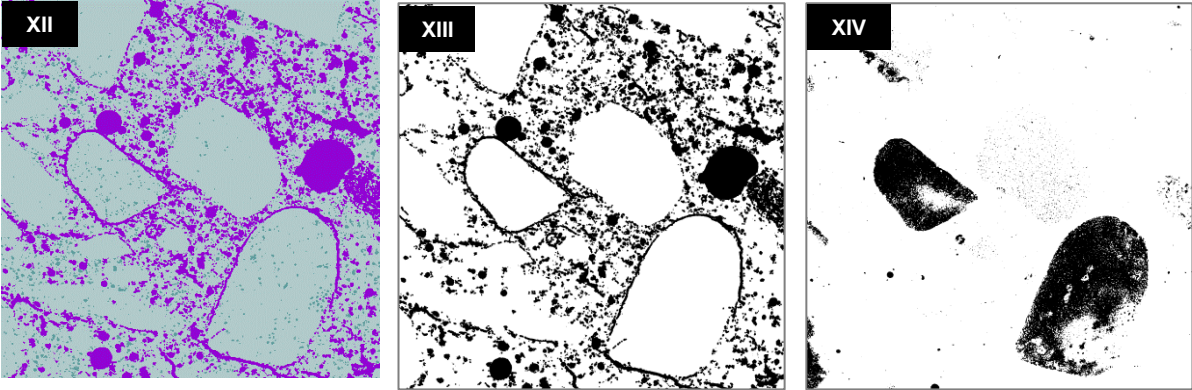


Figure 6-12 Image processing: XII) Manual selection of connected structures (cracks and air voids); XIII) Segmented image with removed pores in aggregates, XIV) Result of subtraction (Image V - Image XIII).

To ensure that pores in aggregates are fully preserved, image XIV is dilated using a ball structuring element with half-kernel size of 2 voxels and holes are closed by applying fill holes and fill image borders operations at 26-connectivity (Figure 6-13-XV). Processed image is saturated with black pixels/voxels to keep the overall shape and outline of image XIV. The size of half-kernel in dilation of image XIV was set to 2 voxels, which is consistent with image X to ensure that every pixel/voxel belonging to cracks around aggregates are unaffected. The new image XV was then subtracted from the original image V to separate more pores within the aggregates. The newly created image XVI was also subtracted from the original image V giving as a result an image of pores in aggregates, labelled here as part A (image XVII).

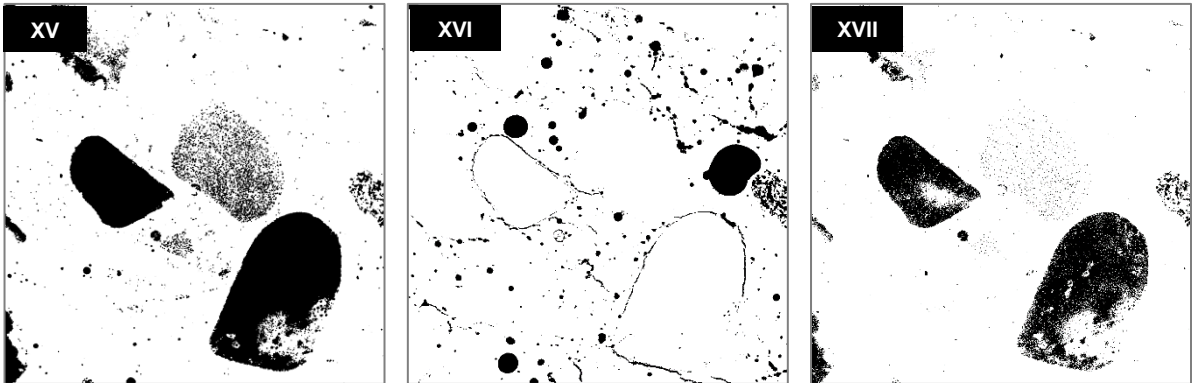


Figure 6-13 Image processing: XV) Image after dilation, fill holes and fill image borders at 26-connectivity; XVI) Result of subtraction: (Image V) - (Image XV); XVII) Result of subtraction: (Image V) - (Image XVI) showing pores in aggregates, part A.

Unfortunately, there might be some non-separated pores remaining that these need to be removed manually. These generally occur in highly porous aggregates and are preserved as a part of the 3D cluster(s) in the Figure XIII. Their separation was made with the segmentation tool (Pick & Move or/and Brush) in Avizo Fire (purple colour on the image XVIII). The manually selected region was then thresholded and used together with image V for logical operation AND (display of only shared pixels/voxels) to create an image of remaining pores in aggregates, labelled as part B (see Figure 6-14-XIX).

The final step was to combine the pores from part A and B into one image by implementing mathematical operation ADD, which simply adds up the values of the corresponding pixel/voxel from the two images. The result is presented in Figure 6-14-XX. When overlaid onto the original image (III), it can be seen in Figure 6-21-a) that the selected objects (highlighted in red) correspond well to the pores in aggregates.

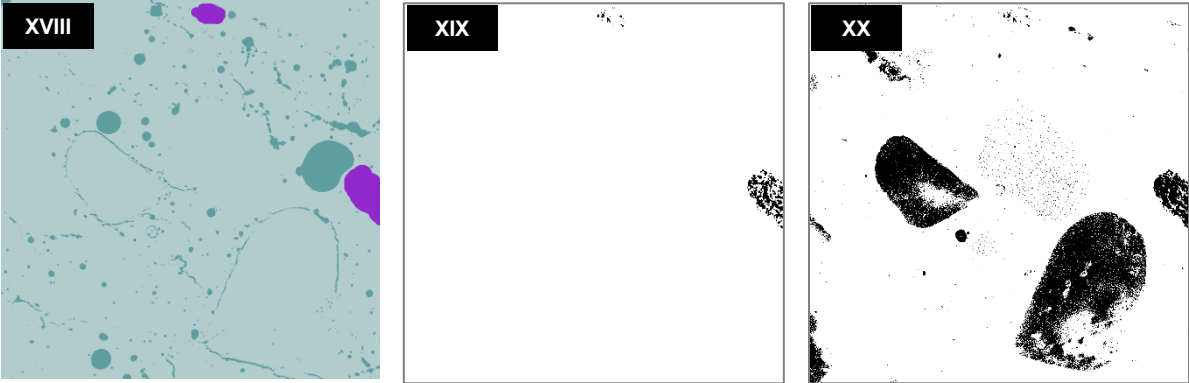


Figure 6-14 Image processing: XVIII) Manual selection of remaining porous aggregates, XIX) porous aggregates - part B, XX) Separated porous aggregates (sum of part A and B).

6.3.2 Separation of air voids

Figure 6-15-XXI shows the result of subtracting image XX from image V to produce a binary image that contains only air voids, capillary pores, and microcracks.

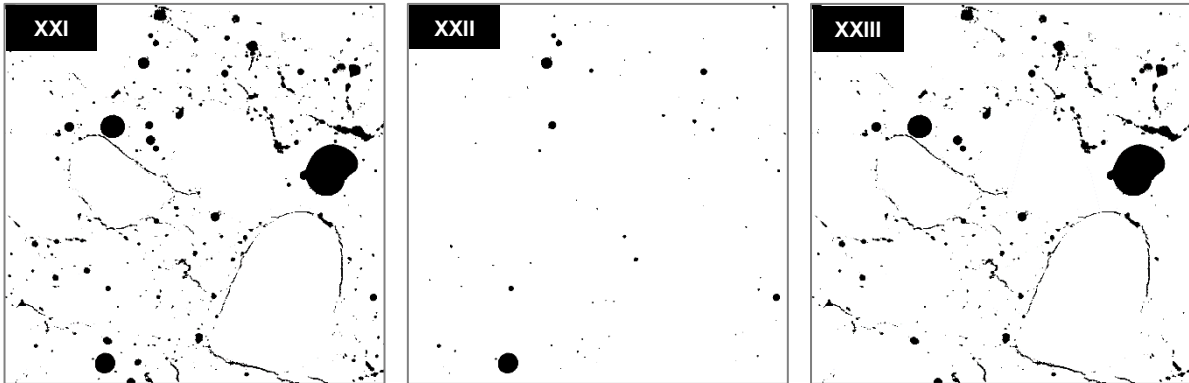


Figure 6-15 Separation of air voids: XXI) Image without porous aggregates obtained by subtraction (Image V - Image XX); XXII) Air voids separated remained after sieve analysis of image XXI (Air voids part A); XXIII) Result of subtraction: (Image XXI - Image XXII).

The next step is to isolate and remove the air voids. In general, air voids are relatively easy to separate because of their spherical shape. Many of these features can be removed by applying sieve analysis, for example by filtering objects having 3D shape factors in the range between 0.5 and 1.5, and with volumes above 100 voxels. These was achieved in Avizo Fire, image XXII shows the sieved air voids (part A). However, this operation alone is not capable of separating all of the air voids effectively. This is because some of the air voids are not perfect spheres, may coalesce with other voids, or connect with other features such as microcracks. Examples of such non-spherical air voids are shown in Figure 6-15-XXIII, which is obtained by subtracting image XXII from image XXI.

In order to separate these air voids, additional image involving binary erosion and dilation is required. The effect of erosion on a binary image is to gradually reduce the foreground by removing a layer of pixels/voxels at a time, while dilation works in the opposite sense. Figure 6-16-XXIV shows the effect of erosion of binary image XXIII using a ball (sphere) structuring element with half-kernel size of 3 voxels. This disconnects air voids from microcracks.

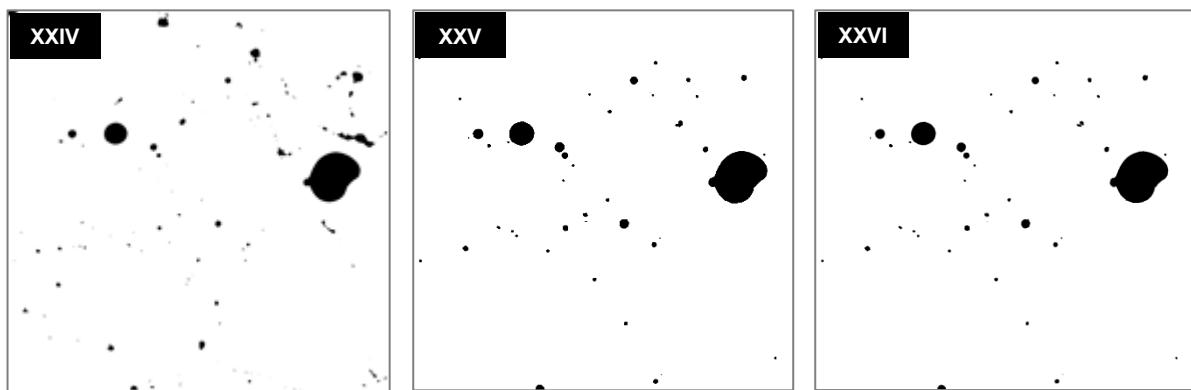


Figure 6-16 Image processing: XXIV) Image after binary erosion using a ball structuring element with half-kernel size of 3 voxels; XXV) Remaining air voids after sieve analysis of image XXIV with 3D shape factor between 0.5 and 1.5, binary dilated using ball structuring element with half-kernel size of 4 voxels; XXVI) Result of logical AND operation: (Image XXIII) AND (Image XXV), air voids part B.

The eroded image XXIV is then subjected to a sieve analysis to separate objects with 3D shape factor between 0.5 and 1.5. The result of this is then dilated using a ball (sphere) structuring element with half-kernel size of 4 voxels (Figure 6-16-XXV). The dilation is performed with bigger kernel (by one voxel) to ensure that all common air voids are separated in the next step, which is the logical AND operation between image XXIII and dilated image XXV. The result of this is presented in Figure 6-16-XXVI. In this way the next large portion of air voids was isolated (part B).

This step usually removes all of the air voids depending on the complexity of the microstructure. However, the presented sample is one of the more complex cases and a small amount of air voids remained (see Fig. 6-17-XXVII) because the applied erosion with half- kernel size of 3 voxels was not sufficient to disconnect them from microcracks. Therefore, erosion was repeated at larger half- kernel size to remove a thicker layer of pixels/voxels from the object in order to disconnect the remaining air voids from microcracks. Figure 6-17-XXVIII presents the result of eroding image XXVII using a ball (sphere) structuring element with half-kernel size of 6 voxels. Then, the remaining air voids are selected manually using the Pick & Move tool in Avizo Fire

as presented in Figure 6-17-XXIX. This is a simple and quick process because there are only a few air voids to select. Additionally, it is more accurate than sieve analysis based on 3D shape factor because such severe erosion can significantly alter the spherical shape of the air voids.



Figure 6-17 Image processing: XXVII) Result of subtraction: (Image XXIII) - (Image XXVI); XXVIII) Image after binary erosion using a ball as a structuring element with half-kernel size of 6; XXIX) Manual selection of remaining air voids.

The selected air voids are then dilated using a ball structuring element with half-kernel size of 7 voxels (Image XXX). As before, the dilation is performed with a slightly larger kernel size (bv one voxel) compared to erosion to allow accurate separation of the remaining air voids (part C) in the next step, which is the logical AND operation between image XXVII and image XXXI. This ultimately separates all the air voids shown in Fig. 6-18-XXXII, which is the sum of three images containing air voids from parts A, B and C.

To verify that the separation is complete and accurate, visual inspection is carried out on each XY slice of the air voids binary image (Image XXXII) and compared with corresponding XY slice of the raw data (Image III). An example of such visual inspection is shown in Figure 6-21-b), where it can be seen that the red labelled air voids from image XXXII perfectly match with the black air voids in the original grey scale image.

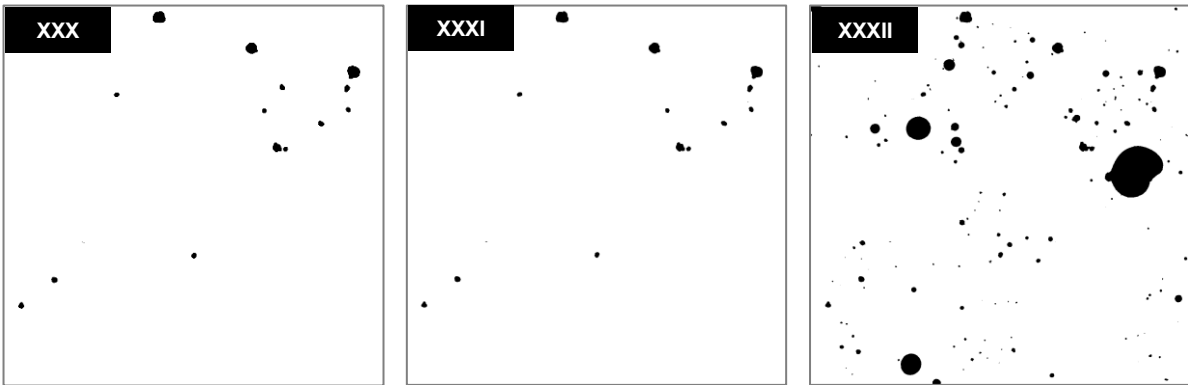


Figure 6-18 Image processing: XXX) Image after binary dilation using a ball as a structuring element with half-kernel size of 7; XXXI) Result of logical AND operation: (Image XXVII) AND (Image XXX), air voids part C; XXXI) All air voids: part A+B+C, result of addition: (Image XXII) + (Image XXVI) + (Image XXXI).

6.3.3 Separation of microcracks

The last step in the separation algorithm is to extract microcracks, which are the main feature of interest in this work. This will be carried out using a semi-automatic procedure to ensure all microcracks are detected. Figure 6-19-XXXIII shows the binary image without porous aggregates and air voids (removed by subtracting image XXXII from image XXI). It can be seen that the microcracks are well preserved, but some small amount of noise still remained. In order to remove this noise, the image is processed with a closing operation followed by sieve analysis. The closing of an image A with a structuring element B, denoted as $A \bullet B$, is defined as a dilation followed by an erosion using the same structuring element (Efford, 2000), producing a new binary image C:

$$C(A) = A \bullet B = (A \oplus B) \ominus B \quad (\text{Eq. 6-5}).$$

This operation is called closing because it fills holes without affecting the other features of interest. It is similar to dilation, but less destructive and therefore well suited for eliminating noise such as small holes in cracks or to join disconnected cracks without affecting their original shape. Figure 6-19-XXXIV shows the result of closing image XXXIII using a ball (sphere) structuring element with half-kernel size of 1 voxel.

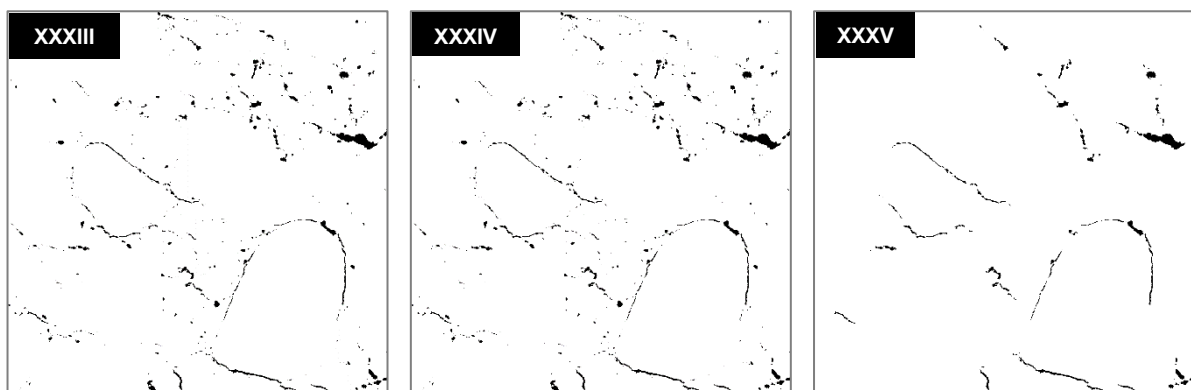


Figure 6-19 Image processing: XXXIII) Image without porous aggregates and air voids (Image XXI - Image XXXII); XXXIV) After binary closing using a ball structuring element with half-kernel size of 1 voxel to remove noise; XXXV) Large microcracks that remained after sieve analysis of XXXIV with 3D shape factor > 5 and size $< 50,000$ voxels.

Then, the objects in image XXXIV are labelled and analysed with sieve analysis (Section 6.4) to obtain their 3D shape factors and volumes. Those with shape factors below 5 and volumes smaller than 50,000 voxels are filtered to remove remaining noise. This procedure will preserve most of the microcracks as shown in Figure 6-19-XXXV. However, some very small microcracks are occasionally removed along with the noise. To improve this, manual selection of the remaining microcracks is needed. This is the most tedious part of the separation process. However, it is essential to achieve an accurate quantitative analysis.

The remaining microcracks are detected by subtracting image XXXV of the large microcracks only from image XXXIV. This produces image XXXVI which is then overlaid on to the original greyscale image. At first sight, visual identification of the microcracks appears to be difficult because of their small size and they resemble noise. However, it turns out to be a simpler task when each XY slice of the separated 3D image is compared with the corresponding XY slice of the raw data (after cropping and filtering). The remaining

microcracks are selected by the Pick & Move tool in Avizo Fire and highlighted in purple (see Figure 6-20-XXXVII). The selected microcracks are added to image XXXV (large microcracks) to produce the final image of all the microcracks (Figure 6-20-XXXVIII).

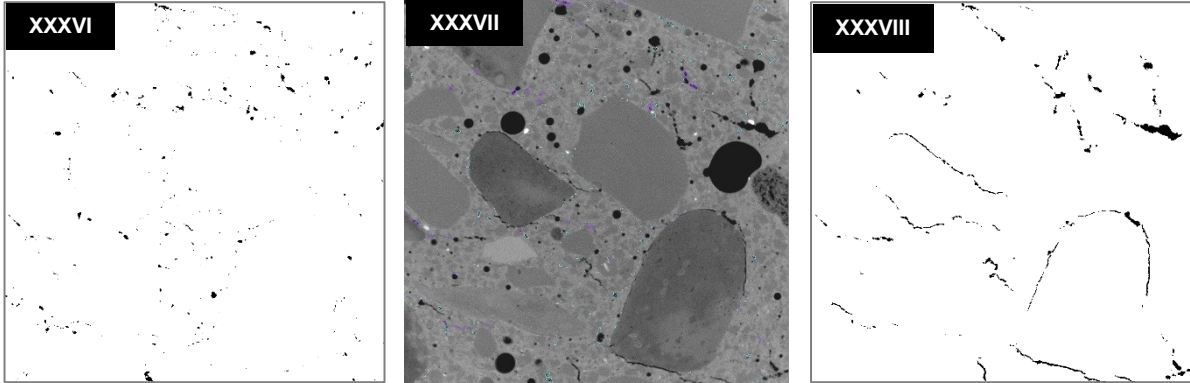


Figure 6-20 Image processing: XXXVI) Remaining features after subtraction (Image XXXIV - Image XXXV); XXXVII) Manual selection of remaining microcracks; XXXVIII) Result of addition (Image XXXV/large microcracks/ + Image XXXVII /selected remaining microcracks/) to produce the final image containing all microcracks.

The overlaid image of the selected microcracks (highlighted in red) on to the original image (III) can be seen in Figure 6-21-c). The segmented objects correspond well to the microcracks.

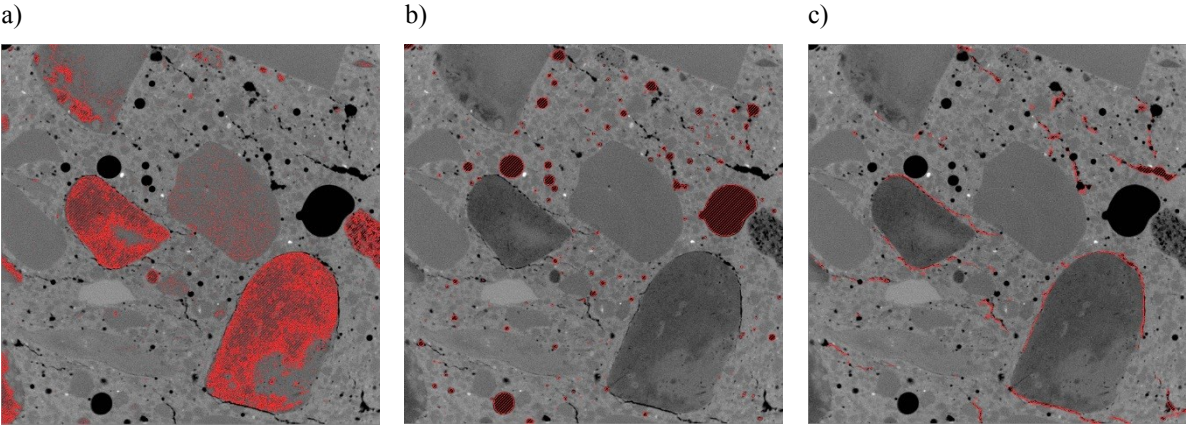


Figure 6-21 Overlaid image of selected a) pores in aggregates, b) air voids and c) microcracks (highlighted in red) on to the original image (III).

6.4 Quantitative measurement

Quantitative measurements can be carried out after separating the microcracks from other pores in the 3D image via the proposed algorithm described in this section. Depending on the type of crack parameter to be measured, the segmented image can be used as is or it has to undergo additional processes such as labelling and skeletonisation. Figure 6-22 shows an example 3D image of microcracks that have been segmented (a), labelled (b) and skeletonised (c). The segmented image is used for global analysis such as total volume, specific surface

area and degree of anisotropy. The labelled image allows measurements to be made on each microcrack separately while the skeletonised image allows topological parameters such as tortuosity to be measured.

Labelling is a process where every pixel/voxel of the same microcrack is assigned a unique value starting from 1. The assigned value depends on the location of the microcrack in the image, the largest value gives the total number of microcracks. To do so, the image is scanned thrice from top to bottom and from left to right. The first scan detects the start of each microcrack. The second scan gives the same grey level to all the pixels/voxels belonging to the same microcrack. The third scan checks that all microcracks have consecutive indices (i.e. there is no missing number). An important consideration in labelling is the definition and the type of connectivity. For 3D images, this can be either 6, 18 or 26, i.e. features are considered connected if they share at least one common face, edge or vertex respectively.

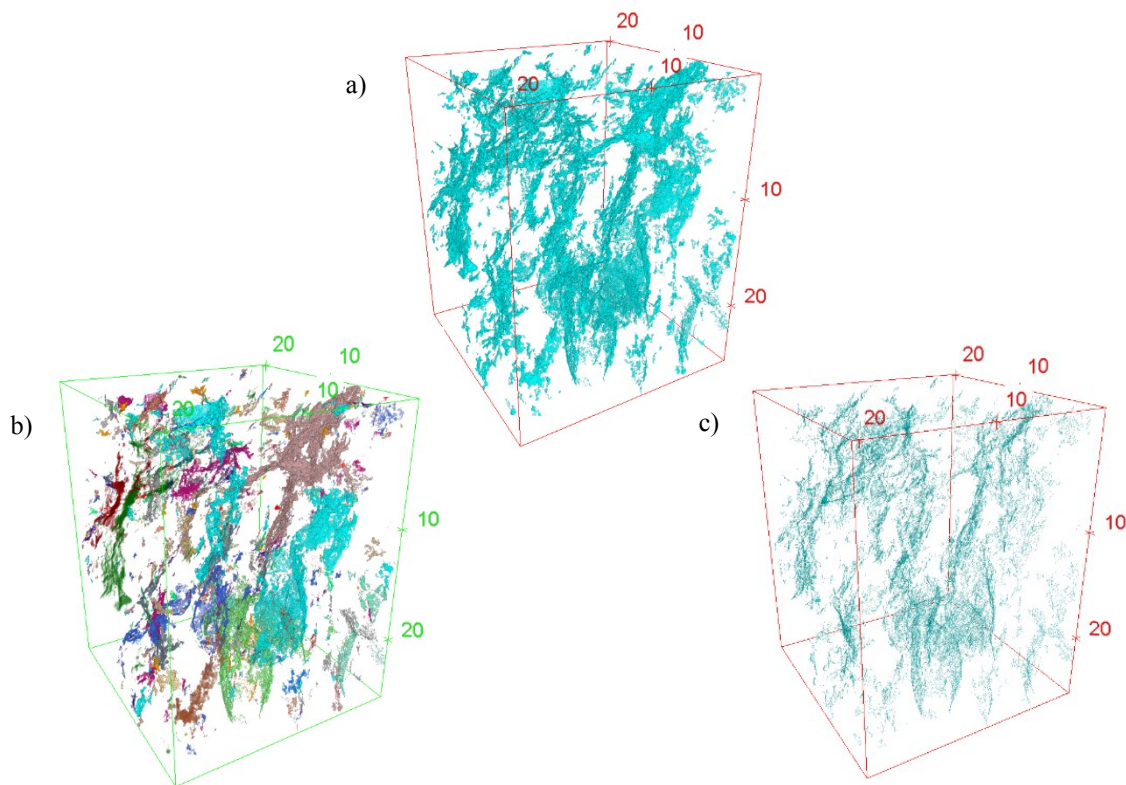


Figure 6-22 a) Segmented, b) labelled and c) skeletonised image of microcracks.

Skeletonisation is the process of reducing the size of an object in a binary image to a skeleton that preserves the general shape and connectivity of that object. There are three major skeletonization techniques. These are based on geometric continuities (via Voronoi diagrams generated by the boundary points), object reduction (layer by layer erosion called thinning) and curve propagation (detection of ridges in a distance map of boundary points) (Sangeetha et al., 2015). The method used in this work is an implementation by Ignacio Arganda-Carreras of the 3D thinning algorithm from Lee, (Lee et al., 1994). It is available as a plugin called Skeletonise 3D in BoneJ version 1.4.1 (Doube et al., 2010). BoneJ is a plugin in Fiji/ ImageJ that was originally designed for analysing bone structure. Nevertheless, it is used here for microcracks as it works well with any 3D structure regardless of the origin. The Skeletonise 3D plugin finds the skeleton of the microcracks using a

topology-maintaining medial axis thinning algorithm. Basically, it erodes the surface of the microcracks iteratively until only the skeleton remains. Erosion is performed symmetrically in order to guarantee medial position of the skeleton lines such that the connectedness of the object is preserved and any holes or cavities are created.

Properties such as volume, area, width, length etc are measured for each microcrack and the results are used to calculate various parameters such as total crack volume and volume fraction, dendritic and numerical density, specific surface area, average width and length of microcrack and their distribution, degree of anisotropy, connectivity and tortuosity. These are discussed in Section 6.4.1. Additionally, the air voids that are segmented as part of the algorithm to isolate microcracks from other features are also quantitatively characterised. This will be explained in Section 6.4.2.

6.4.1 Microcrack characteristics

a) Volume fraction

Volume fraction (V_V) is the total volume of microcracks (V_{crack}) i.e. the sum of the volume of each labelled microcrack, divided by the entire volume of the sample (V_{image}). In the case of 2D image analysis, the area fraction (A_A) is obtained from the ratio between total area of the microcracks (A_{crack}) to the total area of the image (A_{image}). These are defined in Eq. 6-6 and 6-7 respectively:

$$V_V = \frac{V_{crack}}{V_{image}} \quad (\text{Eq. 6-6})$$

$$A_A = \frac{A_{crack}}{A_{image}} \quad (\text{Eq. 6-7})$$

b) Specific surface area and surface density

Surface area (SA) of microcracks can be measured by determining the total area of exposed crack voxel faces. However, this method tends to over-estimate the true surface area because of the jagged voxel representation of smooth surfaces. Another approach is to reconstruct a polygonal mesh of iso-surface of the three-dimensional structure and then sum up the area of polygons in the mesh. One variant of this method is the marching cubes algorithm that extracts iso-surfaces using a triangular surface mesh (Lorenson and Cline, 1987), which is implemented as Isosurface plugin in BoneJ (Doube et al., 2010). The main disadvantage of estimating the surface area of 3D objects via reconstruction is the relatively high computational complexity. An alternative is the stereological approach using line intercept count method (LICM) (Huang and Klette, 2004), which is applicable for 2D and 3D analysis. It involves four steps: generate a line probe, search for an object boundary, count object-probe intercepts and finally apply stereological formulas to obtain estimation of perimeter (for 2D analysis) and surface area (for 3D analysis).

From the measured surface area, two other parameters can be calculated: specific surface area and surface density. Specific surface area (SSA) is the ratio of the surface area (SA) to the total volume of

microcracks (V_{crack}). For 2D analysis, the total perimeter (SA_{2D}) and area of the microcracks (A_{crack}) are used instead, as shown in Equations 6-12 and 6-13:

$$SSA = \frac{SA}{V_{crack}} \quad (\text{Eq. 6-12})$$

$$SSA_{(2D)} = \frac{SA_{2D}}{A_{crack}} \quad (\text{Eq. 6-13})$$

Surface density (SD) is the ratio of the surface area of the microcracks (SA) to the image volume (V_{image}), or the ratio of the perimeter of the microcracks (SA_{2D}) to the image area (A_{image}) for 2D analysis:

$$SD = \frac{SA}{V_{image}} \quad (\text{Eq. 6-14})$$

$$SD_{(2D)} = \frac{SA_{2D}}{A_{image}} \quad (\text{Eq. 6-15})$$

c) Width

Microcrack width distribution can be estimated from local thickness measurements. This can be implemented using a Thickness plugin (Dougherty and Kunzelmann, 2007, Hildebrand and Rüegsegger, 1997) in BoneJ (Doubé et al., 2010). The method estimates a volume-based local thickness by fitting maximal spheres to every point in the feature of interest. From these local thicknesses a volume-weighted mean thickness and the thickness distribution are calculated. Average width of microcracks can be also calculated with cylinder rod model, which assumes that all microcracks are rod-like and its thickness is defined as:

$$W_{mean} = \frac{4}{SA/V_{crack}} \quad (\text{Eq. 6-16})$$

Where SA/V_{crack} is a ratio of the surface area to the volume of microcracks. Similarly, for 2D images the average microcrack width can be expressed as:

$$W_{mean\ 2D} = \frac{4}{SA_{2D}/A_{crack}} \quad (\text{Eq. 6-17})$$

Where SA_{2D}/A_{crack} is a ratio of the surface area (perimeter) to the area of microcracks.

d) Length

Length of microcracks (L) is expressed as dendritic length of the skeletonized microcracks. This is calculated as the volume of the individual microcrack ($V_{ind.\ crack}$) divided by the voxel face area. For 2D analysis, this would be the microcrack area ($A_{ind.\ crack}$) divided by the pixel side length in accordance with the following:

$$L = \frac{V_{ind.\ crack}}{\text{voxel face area}} \quad (\text{Eq. 6-18})$$

$$L_{2D} = \frac{A_{ind.\ crack}}{\text{pixel side length}} \quad (\text{Eq. 6-19})$$

Distribution of microcrack length is the percentage of microcracks within a given length range and this is usually plotted in a bar chart or as a cumulative graph. Total length of microcracks is the sum of each

individual microcrack length. This can also be obtained from the total crack volume (V_{crack}) or total crack area (A_{crack}) for 2D analysis, as shown below:

$$L_{total} = \frac{V_{crack}}{\text{voxel face area}} \quad (\text{Eq. 6-20})$$

$$L_{total\ 2D} = \frac{A_{crack}}{\text{pixel side length}} \quad (\text{Eq. 6-21})$$

The average crack length is the total microcrack length divided by the total number of microcracks, according to:

$$L_{mean} = \frac{L_{total}}{N_{crack}} \quad (\text{Eq. 6-22})$$

$$L_{mean\ 2D} = \frac{L_{total\ 2D}}{N_{crack\ 2D}} \quad (\text{Eq. 6-23})$$

e) Density

Density of the microcracks can be expressed as numerical density (D_N) or as dendritic density (D_D). Numerical density (D_N) is the number of microcracks (N_{crack}) per image volume (V_{image}). Dendritic density (D_D) is the total dendritic length of the microcracks (L_{total}) per image volume (V_{image}). The dendritic length of the microcracks is the length of the skeletonized microcracks. For 2D image analysis, the microcrack density can be obtained from the number of microcracks ($N_{crack\ 2D}$), total length of microcracks ($L_{total\ 2D}$) and image area (A_{image}) as shown in Eq. 6-8 to 6-11.

$$D_N = \frac{N_{crack}}{V_{image}} \quad (\text{Eq.6-8})$$

$$D_{N(2D)} = \frac{N_{crack\ 2D}}{A_{image}} \quad (\text{Eq. 6-9})$$

$$D_D = \frac{L_{total\ 2D}}{V_{image}} \quad (\text{Eq. 6-10})$$

$$D_{D(2D)} = \frac{L_{total}}{A_{image}} \quad (\text{Eq. 6-11})$$

f) Orientation and degree of anisotropy

Degree of anisotropy (DA) is a parameter that describes the level of orientation of microcracks within a volume. Anisotropy is the property of being directionally dependent. This implies that the microcracks have different properties in different directions, as opposed to isotropy. The orientation of microcracks is determined by the intercept method and presented in the form of rose of intercepts (Launeau and Robin, 1996). This method is based on counting intercepts between the microcracks and a set of test lines drawn through the image. The test lines are drawn at angles of 0° , 45° , 90° and 135° . The 3D image is then analysed slice by slice in XY, XZ and YZ directions. The number of intersections is counted and the total for each angle is then divided by the total length of the test line. The result is an intercept density plotted as a rose diagram.

Degree of anisotropy of the microcracks in 3D is calculated using the mean intercept length (MIL) and eigenvalue analysis. This method is implemented using the Anisotropy plugin (Odgaard, 1997, Harrigan and Mann, 1984) in BoneJ (Doube et al., 2010). It works by applying a large number equal length oriented vectors from a random point through the 3D image volume. For each vector, the number of intercepts between microcracks and image background is counted. The mean intercept length for each vector is calculated as the vector length divided by number of intercepts. Subsequently, a cloud of values is built up where each value represents a vector times its mean intercept length. A classical eigenvalue analysis of this cloud is then rendered, which involves fitting an ellipsoid to the cloud, construction of a material anisotropy tensor and subsequent eigen decomposition results in eigenvalues and eigenvectors. This analysis extracts a minimal and maximal eigenvalue from which the degree of anisotropy is calculated as:

$$DA = \left(1 - \frac{[\min \text{ eigen value}]}{[\max \text{ eigen value}]} \right) \quad (\text{Eq. 6-24})$$

If the maximum and minimum eigenvalues are equal, then $DA = 0$ and this means that there is no privileged structural direction (total isotropy). The degree of anisotropy increases with increase in the difference between eigenvalues.

g) Connectivity

Connectivity is an important parameter that describes the topology of a porous medium. The connectivity of each microcrack ($C_{ind.}$) can be expressed as the ratio between the volume of a connected microcrack ($V_{ind. crack}$) and the total volume of all microcracks (V_{crack}):

$$C_{ind.} = \frac{V_{ind. crack}}{V_{crack}} \quad (\text{Eq.6-25})$$

Therefore, if all microcracks are interconnected, $C_{ind.}$ would be equal to 1. This is unlikely to occur in real samples, so the connectivity of the largest microcrack (C_1) can be used to represent the overall connectivity of microcracks in the sample. Another way to assess connectivity is by counting the number of connections (CN), i.e. the number of junctions in a network of skeletonised microcracks. The ratio of the connections number to the image volume provides the density of connections (D_{CN}):

$$D_{CN} = \frac{CN}{V_{crack}} \quad (\text{Eq. 6-26})$$

h) Tortuosity

Tortuosity is a parameter that characterizes the convoluted pathways through porous media that influences mass transport properties. Several definitions for tortuosity exist in the literature such as geometric, hydraulic, electrical and diffusive tortuosity (Ghanbarian, et al., 2013). In this study, we will only consider geometric tortuosity because this parameter decouples the geometric characteristics of microcracks from the influence of mass transport properties, which we wish to characterise separately. Geometric tortuosity is defined as the ratio of the actual flow path lengths to the shortest (straight) length across the porous medium. Therefore,

geometric tortuosity of microcracks (τ_g) can be expressed as the ratio of the total length (L_{total}) of the microcracks to the sum of Euclidean distance ($L_{distance}$) of all skeletonised microcrack branches:

$$\tau_g = \frac{L_{total}}{\sum L_{distance}} \quad (\text{Eq. 6-27})$$

Where Euclidean distance is the straight-line distance between the ends of the skeletonised microcrack.

Another approach to estimate microcrack tortuosity is via its centroid path, which is the path formed by centroids of each XY plane of a binary 3D image along the z-axis. The centroid path tortuosity (τ_{CP}) of microcracks is the ratio of the length of a curve (l) to the distance between its ends along the z-axis. In this case, the distance between the ends of the curve is given by the number of planes along the z-axis (h):

$$\tau_{CP} = \frac{\sum l}{h} \quad (\text{Eq. 6-28})$$

This method first computes the centroid of the microcrack on each image plane. Then it computes the path length through the centroids and divides this by the number of planes along the z-axis. When the 3D image is flipped in the YZ and XZ directions, the centroid path tortuosity can also be calculated also along the x- and y-axes.

6.4.2 Air voids characteristics

The segmented air voids were quantified using a global analysis to measure parameters such as total volume, volume fraction, surface area, specific surface area and surface density, and degree of anisotropy. In addition, labelling was carried out for parameters that describe size and shape since these are usually expressed in the form of frequency distribution or histogram. Projection of the histogram data into the 3D image can be additionally made using sieve analysis in Avizo Fire. This generates a new labelled image that classifies air voids into groups within a specified range of the measured parameter. The number of groups and their respective ranges can set by the operator. Figure 6-23 shows examples of the segmented, labelled and classified air voids into eight categories. The following section explains the parameters describing air voids and the results from air void analysis of concrete sample C/SF-14/SC will be presented in Section 6.5.2.

a) Volume fraction

Volume fraction of air voids (V_{av}) is the ratio between the total volume of air voids ($V_{air\ voids}$) to the entire image volume (V_{image}):

$$V_{av} = \frac{V_{air\ voids}}{V_{image}} \quad (\text{Eq. 6-29})$$

c) Density

Density of air voids (D_{Nav}) is the number of air voids ($N_{air\ voids}$) per image volume (V_{image}):

$$D_{Nav} = \frac{N_{air\ voids}}{V_{image}} \quad (\text{Eq.6-30})$$

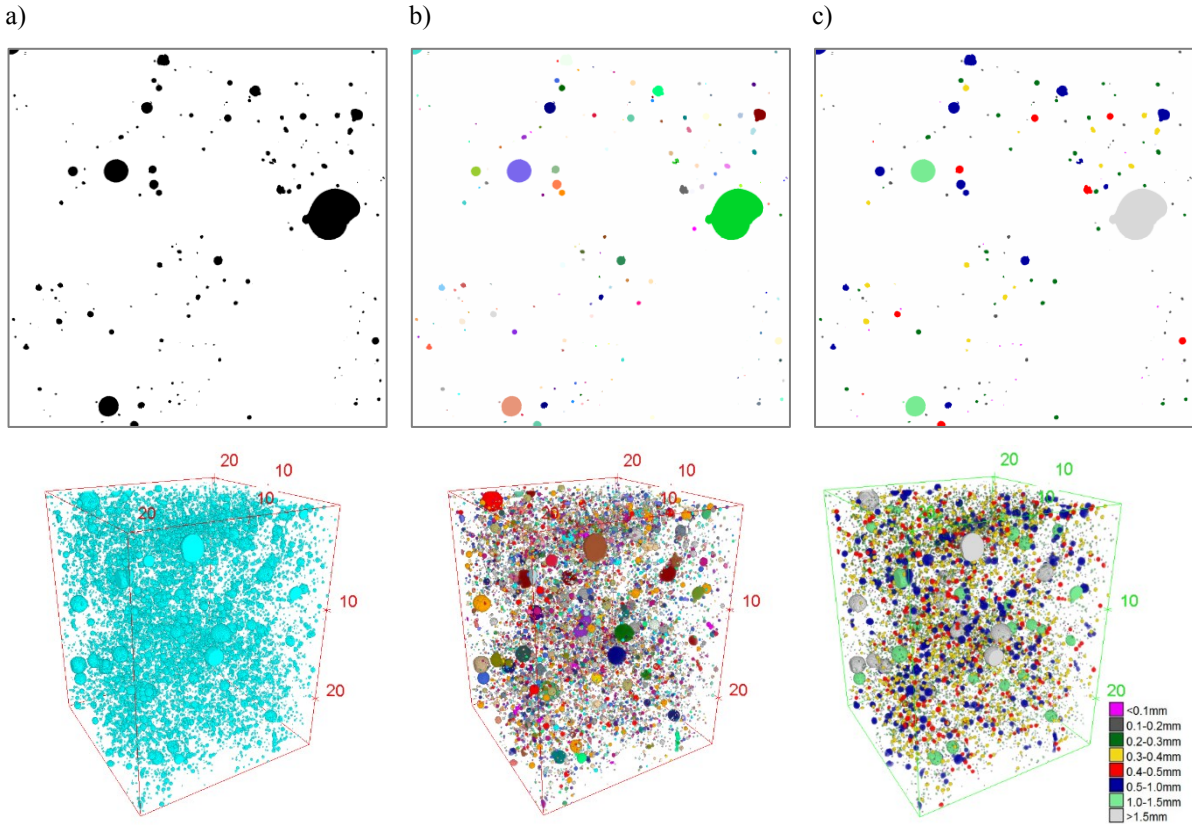


Figure 6-23 Labelling of air voids: a) segmented image, b) labelled air voids, c) labelled air voids into eight categories according to their size distribution (equivalent spherical diameter). The upper and lower images show the 2D slices and the 3D volume respectively.

c) Specific surface area and surface density

Surface area of air voids can be measured using similar methods to that of microcracks as described in Section 6.4.2. Specific surface area (SSA_{av}) is the ratio of the air void surface area (SA_{av}) to the total volume of air voids ($V_{air\ voids}$):

$$SSA_{av} = \frac{SA_{av}}{V_{air\ voids}} \quad (\text{Eq.6-31})$$

Surface density (SD_{av}) is the ratio of the air void surface area (SA_{av}) to the image volume (V_{image}):

$$SD_{av} = \frac{SA_{av}}{V_{image}} \quad (\text{Eq. 6-32})$$

d) Size

Width (W_{av}) and length (L_{av}) of air voids can be estimated from Feret diameter measurements, which is defined as the distance between the two parallel planes that restrict the object perpendicular to the planes. The Feret diameter of an air void is therefore a measure of each air voids size along a specified direction and therefore relies on sampling distribution in different directions. The number of directions is set by default to 31 for 3D image analysis. The shortest and longest Feret diameter of an air void in orthogonal directions are

identified as its width and length respectively. Since air voids are approximately spherical, their diameter can be expressed as the equivalent spherical diameter:

$$\phi_{eq} = \sqrt[3]{\frac{6 \times V_{air\ void}}{\pi}} \quad (\text{Eq. 6-33})$$

e) Shape

A commonly used shape factor is the aspect ratio (AR), defined as the ratio between length (L_{av}) and width (W_{av}) of air voids. Aspect ratio would vary from near zero for a very elongated particle to one for an equidimensional particle:

$$AR = \frac{L_{av}}{W_{av}} \quad (\text{Eq. 6-34})$$

Sphericity is a measure of how round an object is and is therefore a relevant parameter for characterising air voids. Sphericity (Ψ_{av}) is defined as the ratio of the surface area of a sphere (with the same volume as the given particle) to the surface area of the particle (Wadell, 1935). Therefore, sphericity of an air void can be calculated as:

$$\Psi = \frac{\pi^{\frac{1}{3}} \times (6 \times V_{air\ void})^{\frac{2}{3}}}{A_{air\ void}} \quad (\text{Eq. 6-35})$$

where $V_{air\ void}$ and $A_{air\ void}$ are volume and surface area of the air void respectively. The sphericity of a sphere is 1 by definition.

Elongation (E) is a parameter that indicates how slender an object is. Objects that are symmetrical about all axes such as spheres or cubes would have an elongation value of 0 whereas objects with large aspect ratios would have an elongation value closer to 1. For air voids, the elongation factor can be defined as the ratio of the medium ($\phi_{med\ av}$) and the largest Feret diameter i.e. air void length (L_{av}):

$$E = \frac{\phi_{med\ av}}{L_{av}} \quad (\text{Eq. 6-36})$$

f) Spacing factor

Powers (1949) defined an air void spacing factor \bar{L} as the distance between the surface of a bubble and its sphere of influence, such that

$$\bar{L} = \begin{cases} \frac{3}{\alpha} \left[1.4 \left(\frac{p}{A} + 1 \right)^{\frac{1}{3}} - 1 \right] & \frac{p}{A} \geq 4.33 \\ \frac{p}{\alpha A} & \frac{p}{A} < 4.33 \end{cases} \quad (\text{Eq. 6-37})$$

where α is the specific surface, defined as the ratio of the average void surface area to the average void volume, and p/A is the volumetric paste to air ratio, where p is the volume fraction of cement, water, and supplementary cementitious materials (if any).

g) Anisotropy

Degree of anisotropy of air voids (DA_{av}) describes the level of orientation of air voids within the sample volume. It is calculated using the same approach as the degree of anisotropy for microcracks (see Section 6.4.1). Orientation of air voids can be also determined using the intercept method (Launeau and Robin, 1996) and presented by means of a rose of intercepts in XY, XZ and YZ directions.

6.5 Results from image analyses

6.5.1 Comparison of microcrack characteristics from 3D and 2D image analysis

This section compares results of microcrack characteristics obtained from 3D image analysis to those of 2D analysis for the same crack network. In order to obtain meaningful comparisons, we will analyse the microcrack characteristics using 3D and 2D interpretations applied to the same image of concrete C/SF-14/SC obtained with the Metris X-Tek HMX ST 225 CT scanner. The image has a volume of 10858 mm^3 and area of 699701.15 mm^2 (sum of all slices for 2D image analysis). The sample is a concrete with CEM I + 9% of silica fume and 60% of aggregates with maximum aggregate size of 10 mm, at low water to binder ratio of 0.25. Such composition together with sealed curing would generate large autogenous shrinkage and consequently cracking.

The 3D image of microcracks is first analysed in its entirety and then as a series of individual 2D images. All measurements and calculations will be carried out in accordance to the rules of 3D and 2D quantitative image analysis described in the preceding sections. The labelling and skeletonization of the microcracks are also performed in 3D and 2D (slice by slice) accordingly. Figure 6-24 presents an example of segmented microcracks and the results of labelling carried out in 3D and 2D. As expected, the number of microcracks labelled in 2D is much higher than that in 3D. The 3D labelling assigns each three-dimensional microcrack as one object while in 2D the same microcrack is divided and labelled into many objects. This is because the 2D labelling is performed separately on each 2D slice of the reconstructed image. Similar observation can be made from Figure 6-25, which shows the skeletonised microcracks in 3D and 2D. The skeleton of the 3D image is hardly visible because the thinning process produces one voxel width skeleton of the three dimensional microcracks while for the 2D approach it is a one pixel skeleton of the two dimensional microcracks on each XY plane individually.

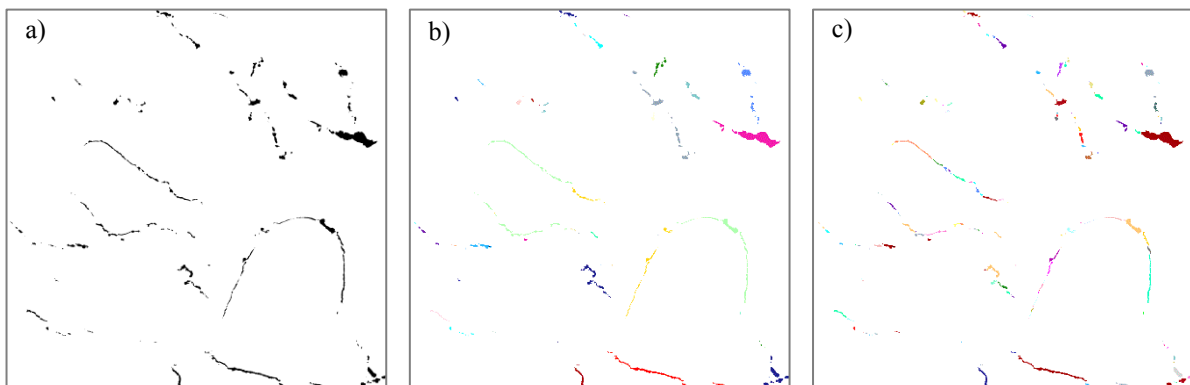


Figure 6-24 Labelling of microcracks: a) Segmented binary image; b) labelled microcracks with 3D interpretation; c) labelled microcracks with 2D interpretation.

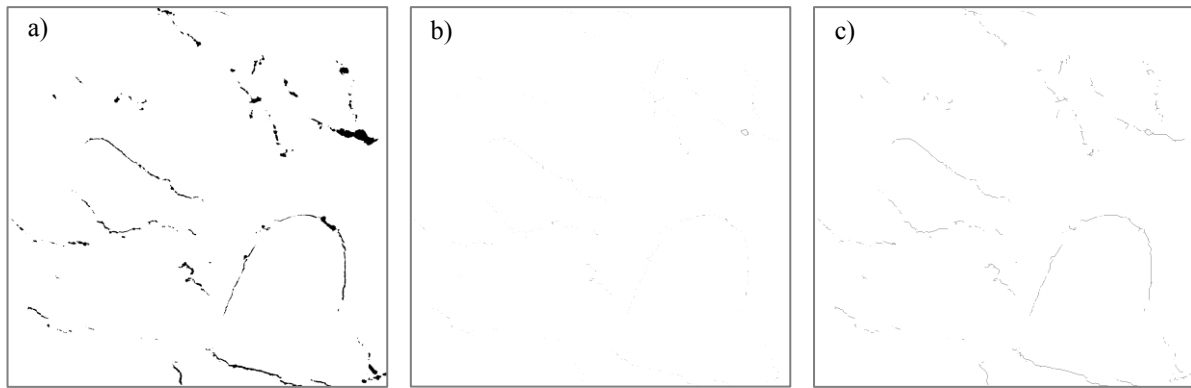


Figure 6-25 Skeletonisation of microcracks: a) Segmented binary image, b) skeleton of microcracks with 3D interpretation and c) skeleton of microcracks with 2D interpretation.

Results from the 3D and 2D image analysis are presented in Table 6-1 and Figures 6-26 – 6-33. The total number of microcracks (N_{crack}) contained in the sample was 1338 (3D) and 281749 (2D), which gives a microcrack density (D_N) of 0.12 crack/mm³ and 0.41 crack/mm² respectively. The difference is to be expected because of the way in which microcracks are labelled in 3D and 2D analyses. As explained earlier, a single three-dimensional microcrack is labelled as many separated microcracks in 2D analysis.

Nomenclature:	Parameter:	Measured value in 3D:	Measured value in 2D:
$V_{\text{image}} / A_{\text{image}}$	Image volume / area	10858.40 mm ³	699701.15 mm ²
N_{crack}	Total number of cracks	1338	281749
D_N	Numerical crack density	0.12 crack/mm ³	0.41 crack/mm ²
D_D	Dendritic crack density	1.13 mm/mm ³	0.11 mm/mm ²
$V_{\text{crack}} / A_{\text{crack}}$	Total volume / area of cracks	115.26 mm ³	7427.39 mm ²
V_V / A_A	Volume / area fraction	1.06%	1.06%
SA	Surface area/ perimeter	5762* 4070** 3713*** mm ²	217374*** mm
SSA	Specific surface area	49.99* 35.31** 32.21*** mm ⁻¹	29.27*** mm ⁻¹
SD	Surface density	0.53* 0.37** 0.34*** mm ⁻¹	0.31*** mm ⁻¹
L_{total}	Total length of cracks	12306.67 mm	77366.36 mm
L_{mean}	Average length of cracks	8.452 mm	0.275 mm
W_{mean}	Average width of cracks	0.159•, 0.124•• mm	0.167•, 0.137•• mm
W/L	Average width to length ratio	0.02•	0.61•
DA	Degree of anisotropy	0.56	0.21 XY, 0.34 XZ, 0.15 YZ
C_1, C_{10}	Connectivity†	0.18, 0.63	N/A
CN	Connections number	56635	N/A
D_{CN}	Density of connections	5.22	N/A
τ_g	Tortuosity	1.27	N/A
τ_{CP}	Centroid path tortuosity	6.71 x-, 6.12 y-, 8.89 z-axes	N/A

Table 6-1 List of measured parameters of microcracks in sample C/SF-14/SC.

Note: *Voxel face area, **Iso-surface, ***LICM, •Local thickness, ••Rod model thickness, †Connectivity of the largest microcrack (C1) and connectivity if the 10 largest microcracks (C10).

The alternative, dendritic density of the microcracks is instead 1.13 mm/mm^3 (for 3D) and 0.11 mm/mm^2 (for 2D). The total dendritic length of the microcracks (D_D), which is used to calculate the density is either the length of the 3D skeleton of microcracks ($L_{\text{total}}=12306.67 \text{ mm}$) or the length of skeletonised microcracks slice by slice ($L_{\text{total}}=77366.36 \text{ mm}$), divided by image volume and image area respectively, and that leads to such distinct results. Nevertheless, the total volume fraction of microcracks V_V is exactly identical to the area fraction of microcracks A_A ($= 1.06\%$). Thus, the area fraction from 2D analysis can be used as a good estimate for volume fraction, as would be expected from stereology.

The surface area of microcracks (SA) in 3D was estimated via voxel face area, iso-surface and line intercept count method (LICM). Surface area of microcracks in 2D was estimated using the LICM only since the other two methods are not applicable. Specific surface area (SSA) and surface density (SD) were calculated from these and the result are presented in the Figure 6-26. It is clearly visible that the iso-surface and LICM methods gave similar and confirmatory results. However, the voxel face area method over-estimates the measured properties and is therefore not recommended for 3D surface area estimation. The 2D results from LICM are also consistent with 3D measurements provided by the same method. This confirms the stereological assumption that SSA and SD from 2D analysis are comparable with results from 3D analysis.

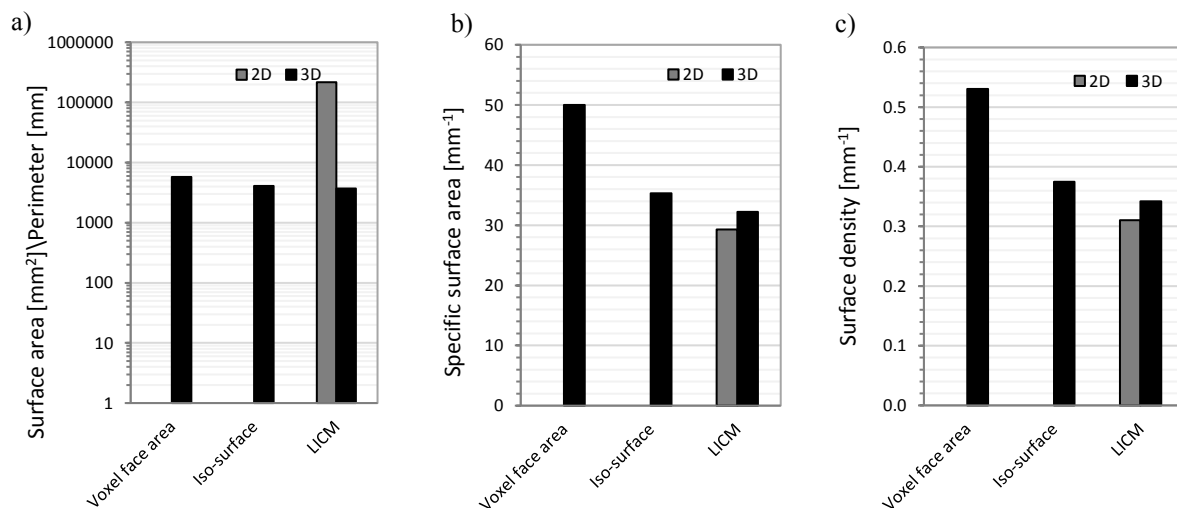


Figure 6-26 Estimation of a) surface area, b) specific surface area and c) surface density of microcracks by voxel face area, Iso-surface (triangular surface mesh) and LICM (line intercept count method) in 3D and 2D analysis.

The width of microcracks (W) was estimated by local thickness measurements in BoneJ (Dougherty and Kunzelmann, 2007, Hildebrand and Rüegsegger, 1997). This was carried out on the whole 3D image and on each separate slice from the 2D stack. Figure 6-27 shows that the results from both analyses, plotted as a cumulative frequency versus width, are overlapping. This shows that there is no significant difference between 2D and 3D measurement of microcracks width. Approximately 80% of the microcracks has width below $200 \mu\text{m}$, which is indicated by purple colour in the 3D image presented in Figure 6-28. The average width (W_{mean}) based on the local thickness method is $159 \mu\text{m}$ and $167 \mu\text{m}$ for 3D and 2D analysis respectively. In contrast, the rod model gives a much lower average crack width of $124 \mu\text{m}$ (for 3D) and $137 \mu\text{m}$ (for 2D). This can be expected since the rod model makes a simplistic assumption that all microcracks are rod-like and their width is calculated based on their surface areas and volumes in accordance with Eq. 6-12.

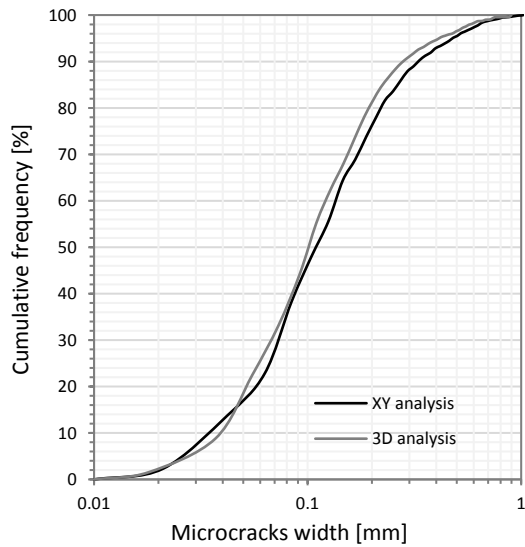


Figure 6-27 Cumulative width distribution of microcracks from 2D (XY) and 3D image analyses.

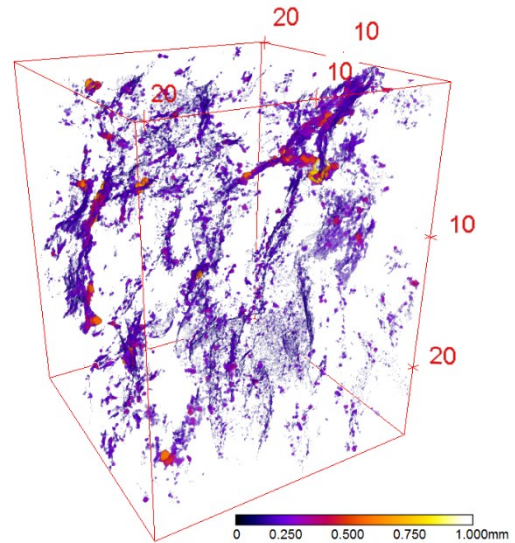


Figure 6-28 Microcracks width distribution based on local thickness measurements in BoneJ. Colours indicate microcrack width range.

The length of microcracks (L) was measured from the skeletonised 3D image and 2D slices. Figure 6-29 presents the results plotted as cumulative distribution and it shows very clearly that the interpretation of microcrack length is very different in 3D compared to 2D analysis. The average microcrack length (L_{mean}) is 8.452 mm and 0.275 mm for 3D and 2D analysis respectively. About 80% of microcracks from 3D analysis has lengths smaller than 3 mm, while the same percentage of microcracks from 2D analysis has lengths below 300 μm . Such distinct findings are expected since the 2D approach divides each microcrack into many disconnected microcracks in each slice and therefore under-estimates the microcrack lengths significantly. Figure 6-30 shows labelled microcracks in accordance to length range.

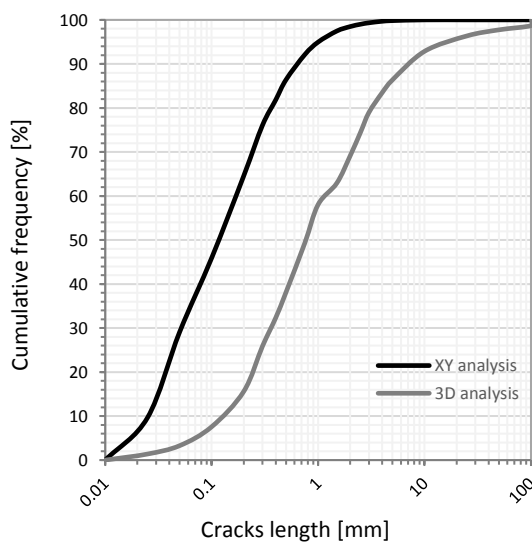


Figure 6-29 Cumulative length distribution of microcracks from 2D and 3D image analyses.

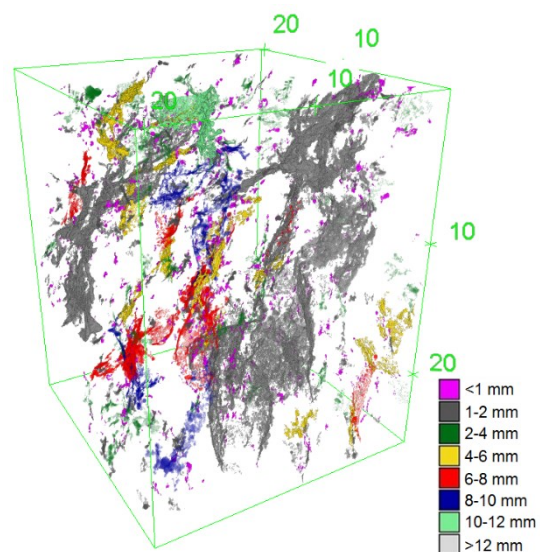


Figure 6-30 Microcracks length distribution based on the dendritic length of microcracks 3D skeleton.

Degree of anisotropy of microcracks (DA) was measured in 3D by the mean intercept length method (MIL). In addition, the 2D intercept method was applied to calculate the intercept density at 0°, 45°, 90° and 135° in each XY, XZ and YZ directions. Figure 6-31 shows the results from 2D analysis plotted as rose diagrams (black lines) and the 3D visualisation of the MIL vector cloud in XY, XZ and YZ orthogonal views; both methods gave very consistent results.

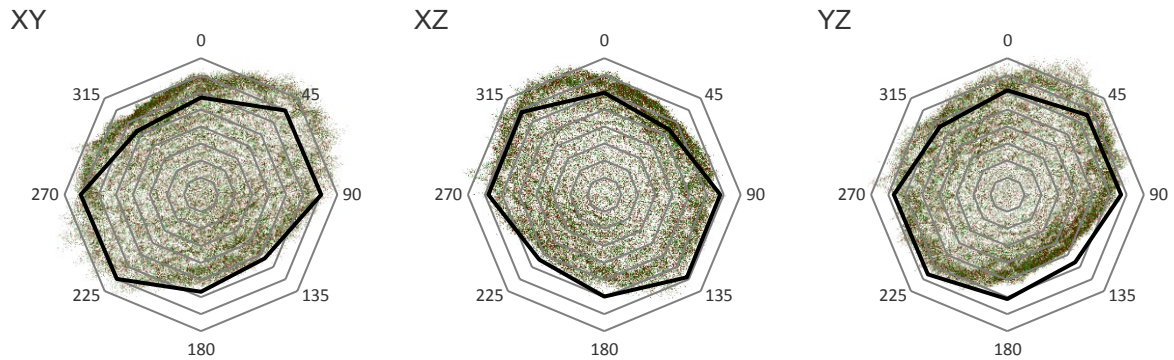


Figure 6-31 Orientation of microcracks presented in 2D by means of rose of intercepts at 0°, 45° 90° and 135° angle (black lines) and with 3D visualisation of the MIL vector cloud in XY, XZ, YZ directions.

The microcracks have preferential orientation within the volume, i.e. the diagonal directions of XY, YZ (45-90° – 225-270°) and XZ (90-150° – 270-315°) planes. Note, that the orientation at YZ plane is slightly less strong. This can be further explained by referring to the size and shape of the large sample from which the core was extracted for imaging. The prepared sample was cast into a disc-shaped mould of 95 mm in diameter and 65 mm in height. Such sample geometry is expected to influence the stress development during sealed curing.

The overall degree of anisotropy from the 3D analysis is about 0.56, which indicates that the microcracks are oriented within the volume, while the estimation of the degree of anisotropy in 2D analysis (that is the intercept density) is far smaller and varies for different directions, of 0.21 in XY, 0.34 in XZ and 0.15 in YZ. This indicates an important issue related to the estimation of the degree of anisotropy in 2D analysis compared to 3D analysis. It might happen that the 2D slice taken for analysis will be cut in the direction where microcracks exhibit the lowest DA e.g. in XY plane (DA=0.15), which may lead to wrong interpretation that microcracks have an isotropic orientation. These findings confirm the advantage of 3D analysis over 2D analysis.

The connectivity of the largest microcrack (C_1) is 0.18, which is a low value and indicates that these features are rather isolated. However, the 10 largest microcracks occupy about 63% of the total volume of microcracks. Furthermore, the connections number (CN) of the 3D microcrack skeleton is high, at about 56635 junctions in a network of skeletonised microcracks. This gives a density of connections (D_{CN}) of 5.22 junction/mm³.

The microcrack geometric tortuosity (τ_g) measured in the sample is relatively low at 1.27, which means that the Euclidean distance and the actual branch lengths are similar. This also suggests that the microcracks are simple, straight and non-tortuous features. In contrary, the centroid path tortuosity (τ_{CP}) calculations gives higher values of 6.71, 6.12 and 8.89 when measured along x-, y- and z- axes respectively. This is a completely

different approach that calculates tortuosity as the ratio of the path formed by centroids of each 2D slice along one axis to the number of the 2D slices along that axis. The higher value for z- axis may be related to the higher number of 2D slices along z-axis.

6.5.2 Comparison of air voids characteristics from 3D and 2D image analysis

Characteristics of air voids obtained from 3D and 2D image analysis are compared in this section. The same image of concrete C/SF-14/SC captured with the Metris X-Tek HMX ST 225 CT scanner was used for quantitative analysis. The applied image pre-processing is described in Section 6.2 (segmentation) and Section 6.3.2 (separation algorithm). The 3D image of air voids with a volume of 10858 mm³ was analysed in accordance to the rules of 3D image analysis described in Section 6.4.2. Following that, the image was analysed as a series of individual 2D images with an area of 699701mm². Results from the 3D and 2D image analysis are presented in Table 6-2 and Figures 6-33 – 6-36.

Nomenclature:	Parameter:	Measured value in 3D:	Measured value in 2D:
$V_{\text{image}} / A_{\text{image}}$	Image volume / area	10858.40 mm ³	699701.15 mm ²
N_{av}	Total number of air voids	14300 air voids	352143 air voids
D_{Nav}	Numerical air voids density	1.32 air voids/mm ³	0.50 air voids/mm ²
$V_{\text{av}} / A_{\text{av}}$	Total volume / area of air voids	224.95 mm ³	14483.81 mm ²
$V_{\text{Vav}} / A_{\text{Aav}}$	Volume / area fraction	2.07%	2.07%
SA_{av}	Surface area / perimeter	4727.98*3360.47** 3135.92*** mm ²	214452.05 mm
SSA_{av}	Specific surface area	21.02* 14.94** 13.94*** mm ⁻¹	14.20 mm ⁻¹
SD_{av}	Surface density	0.44* 0.31** 0.29*** mm ⁻¹	0.31 mm ⁻¹
$L_{\text{av mean}}$	Average length of air voids	289 μm	194 μm
$W_{\text{av mean}}$	Average width of air voids	219 μm	155 μm
$\emptyset_{\text{eq mean}}$	Average equivalent diameter of air voids	220 μm	162 μm
AR_{mean}	Average aspect ratio	0.78	0.76
Ψ_{mean}	Average sphericity of air voids	0.93	0.98
E_{mean}	Average elongation factor of air voids	0.21	0.24
\bar{L}	Spacing factor	0.56	0.59
DA_{av}	Degree of anisotropy	0.14(3D)	0.01(XY), 0.03(XZ), 0.06(YZ)

Table 6-2 List of measured parameters of air voids in sample (C/SF-14/SC) from 3D and 2D analysis.
Note: *Voxel face area, **Iso-surface, ***LICM.

The total number of air voids (N_{av}) contained in the sample was 14300 (3D) and 352143 (2D), which gives an air voids density (D_{Nav}) of 1.32 air void/mm³ and 0.50 air void/mm² respectively. Total volume of air voids ($V_{air\ voids}$) is equal to 224.95 mm³ and thus they occupy 2.07% of the total image volume (V_{Vav}). A well compacted concrete is expected to have an entrapped air content of 1% or lower. Therefore, the measured air content for this sample is relatively high. This is probably due to the fact that the concrete has a high binder content (488 kg/m³ of CEM I and 49 kg/m³ of silica fume) and very low water to binder ratio of 0.25. This would have caused difficulties in achieving a full compaction. The total volume fraction of air voids V_{Vav} is identical as the area fraction of the air voids A_{Aav} in 2D analysis. Thus, the area fraction from 2D analysis can be used as a good estimation for volume fraction, which is similar to microcracks.

Figure 6.32 shows the measured surface area (SA_{av}), specific surface area (SSA_{av}) and surface density (SD_{av}) of air voids using three different methods in 3D (voxel face area, iso-surface and the line intercept count method - LICM). In 2D, only LICM was used as the other two methods are not applicable. It can be seen that the method based on voxel face area tends to overestimate surface area, specific surface area and surface density, which was expected. The method based on iso-surface and line intercept count gave comparable results. The 2D results are consistent with 3D measurements provided by the same method, which confirms the general agreement of the stereological assumption between 2D and 3D measurements. This is also consistent with the results from the microcrack analysis (Figure 6-26).

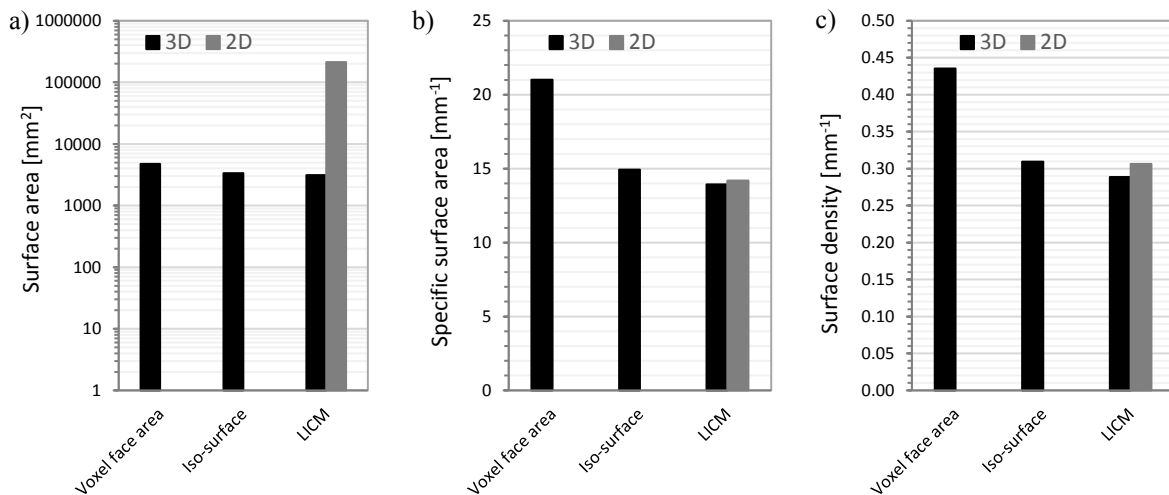


Figure 6-32 Estimation of a) surface area, b) specific surface area and c) surface density of air voids by three methods: voxel face area, Iso-surface (triangular surface mesh) and LICM (line intercept count method).

Size of the air voids was characterised via equivalent spherical diameter (\varnothing_{eq}), Feret length (L_{av}) and Feret width (W_{av}). Results from the 3D analysis are presented in a form of frequency histogram in Figure 6-33. Figure 6-23 c) shows an image with the air voids labelled into 8 categories according to their size range. It can be seen that the biggest population of air voids are in a range of 100-300 μ m in diameter, which corresponds to the expected size of entrapped air. Results from the Feret width and the equivalent spherical diameter measurements are almost identical, with an average value of 219 μ m and 220 μ m respectively. In contrast, the Feret length histogram is shifted slightly towards larger values and this indicates that the air voids may be slightly elongated. However, 2D analysis of air void size gave much smaller values for all three parameters (see

Table 6-2). This is again due to the approach used in 2D analysis that divides each air void into many air voids in each slice that are measured and averaged. Consequently, this under-estimates the actual air voids sizes significantly.

Shape of the air voids was characterised via aspect ratio (AR), sphericity (Ψ) and elongation (E), and the 3D results are presented in Figure 6-34. The mean values for these parameters are 0.78, 0.93 and 0.21 respectively, which indicate the air voids are approximately spherical. 83% of the air voids has sphericity above 0.9. However, the aspect ratio and elongation parameters suggest that the air voids are slightly elongated. This may be due to the effect of casting concrete in layers and the upward movement of air voids during compaction. Nevertheless, 80% of air voids has elongation factor lower than 0.3 and aspect ratio factor higher than 0.7, which suggest that the effect is small. Almost identical results were obtained for these parameters in 2D analysis (see Table 6-2), thus the stereological assumption might be easily adopted for shape parameters of air voids. The same applies to spacing factor that shows comparable results in 3D and 2D.

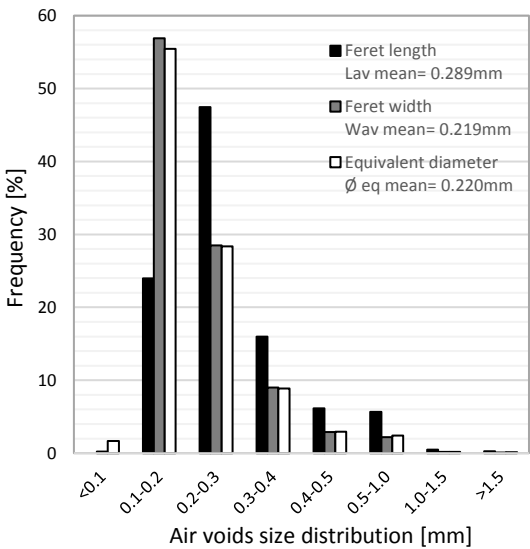


Figure 6-33 Air voids size distribution according to equivalent diameter, Feret width and length (3D).

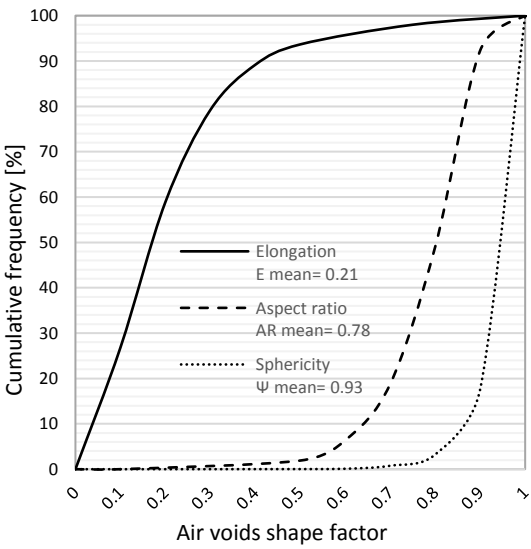


Figure 6-34 Air voids shape factors: aspect ratio, sphericity and elongation (3D).

Degree of anisotropy of air voids (DA_{av}) measured in 3D by the mean intercept length method (MIL) produced a small value of 0.14 and this indicates that the air voids are practically isotropic. This finding is supported by the 2D intercept method, which shows that the intercept density is approximately the same at all angles as can be seen in the rose diagrams (black lines) plotted in Figure 6-35. Additionally, the 3D visualisation of the MIL vector cloud demonstrates consistency of the results. This is in contrary to microcracks, which display a stronger anisotropic characteristic as seen in Figure 6-31.

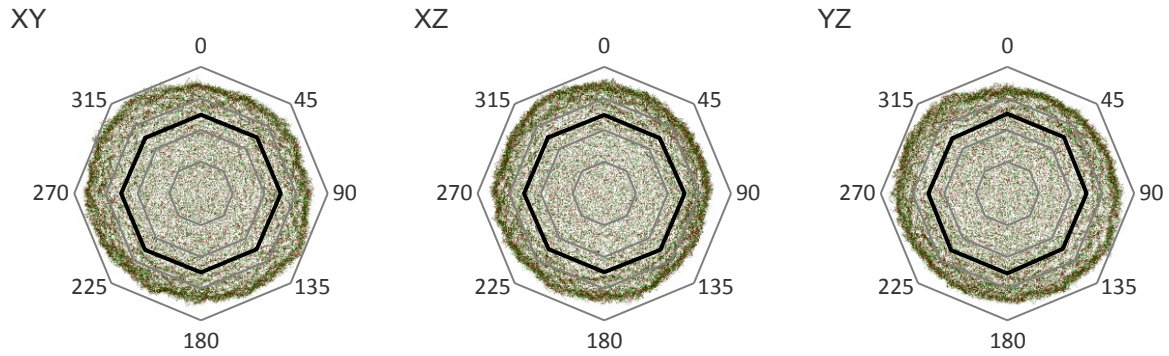


Figure 6-35 Orientation of air voids presented by means of rose of intercepts at 0o, 45o 90o and 135o angle (black lines) with 3D visualisation of the MIL vector cloud in XY, XZ, YZ directions.

6.6 Representative sample volume

It is always questionable in image analysis whether the analysed volume over which a measurement is made, will yield a value representative of the whole material. The choice of representative volume for composite materials, i.e. the representative elementary volume (REV) can be a complicated process. The REV should be large enough to represent the microstructure without introducing non-existing macroscopic properties and at the same time should be small enough to be analysed analytically. In order to establish the REV of a given material for an individual parameter, it is essential to measure that parameter within various volumes of the material. If the volume is too small, then the readings will tend to oscillate. If the analysed volume is increased, the oscillations will dampen out and eventually become stable for a sufficiently large sample size, as illustrated in Figure 6-36. This sample size is referred to as the representative elementary volume.

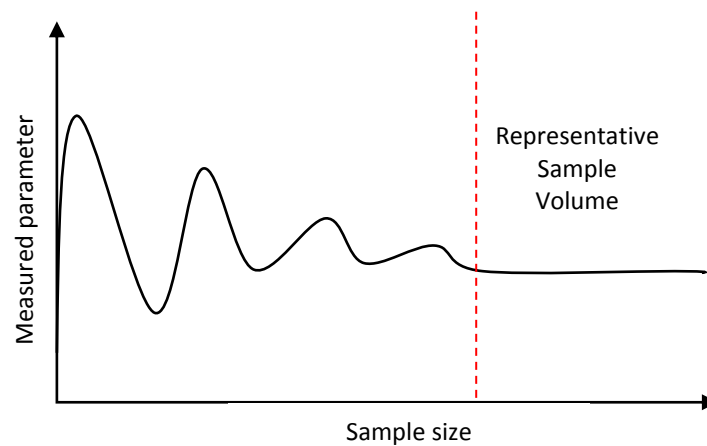


Figure 6-36 Oscillation of measured parameters versus sample size.

The 3D reconstructed and segmented image of sample C/SF-14/SC was used to determine the representative sample volume for characterising microcracks and air voids. From the 3D image, ten sub-volumes were cropped out, each being 10% smaller than from the previously cropped sample. The sub-volumes ranged from $1300 \times 1300 \times 1600 \text{ voxel}^3$ to $130 \times 130 \times 160 \text{ voxel}^3$, as illustrated in Figure 6-37.

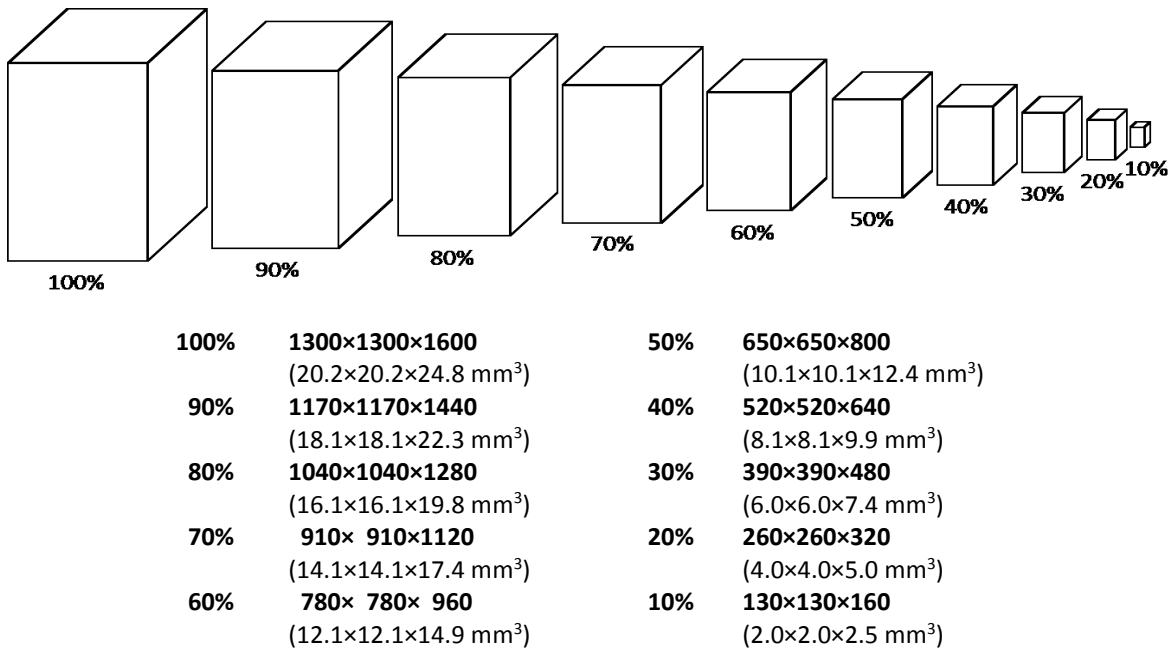


Figure 6-37 Determination of a representative sample volume for characterising microcracks and air voids.

Each cropped image was analysed separately to obtain characteristic parameters of microcracks and air voids. Results from the quantitative image analysis are shown in the following charts (Figure 6-38 – Figure 6-46). The results show that measurements of volume fraction (Figure 6-38) and density of microcracks and air voids (Figure 6-39) oscillate substantially for small samples up to the size of 780x780x960 voxel3, that is 60% of the volume analysed in Section 6-5. The measurements become stable for larger samples. This indicates that for both parameters (volume fraction and density) obtained from 70% to 100% of the analysed volume should give representative results from the microcracked concrete. Similar trends can be observed for other parameters such as specific surface area and surface density presented in Figure 6-40 and Figure 6-41. Here measurements start to stabilize even for smaller sample size of 40-50% of the original volume. This confirms the representativeness of the measured values for the whole material. The same applies to parameters such as connectivity and tortuosity of microcracks (see Figure 6-42).

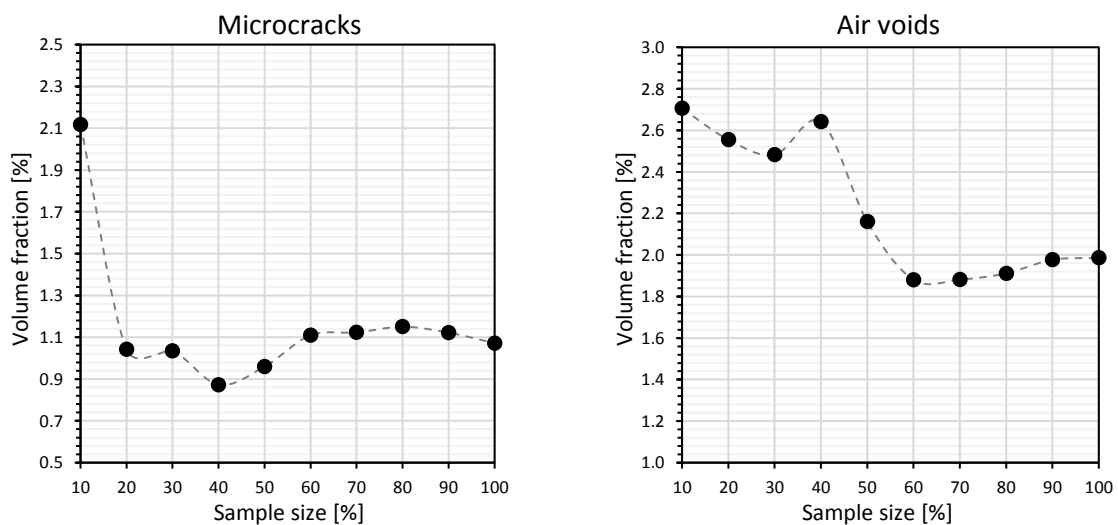


Figure 6-38 Effect of sample size on the measured volume fraction of microcracks and air voids.

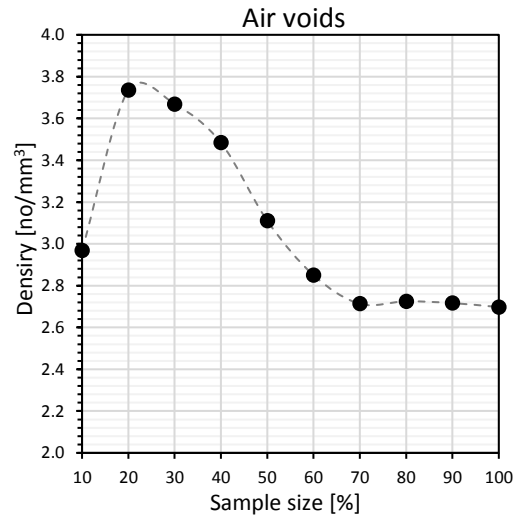
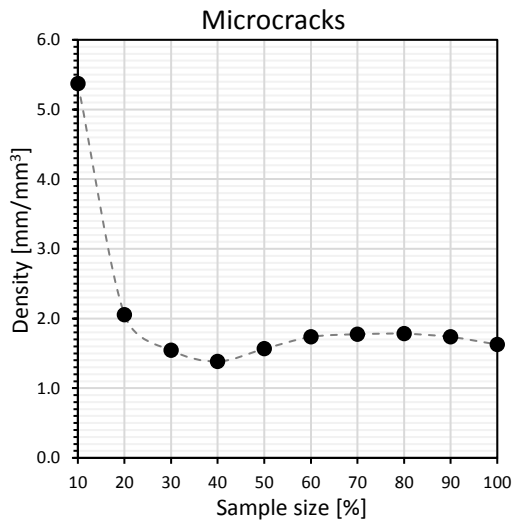


Figure 6-39 Effect of sample size on the measured density of microcracks and air voids.

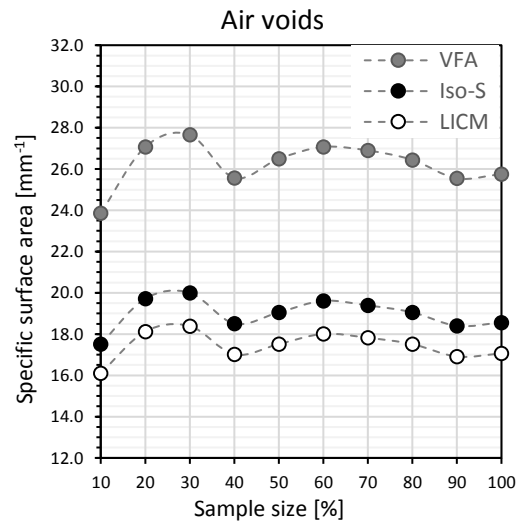
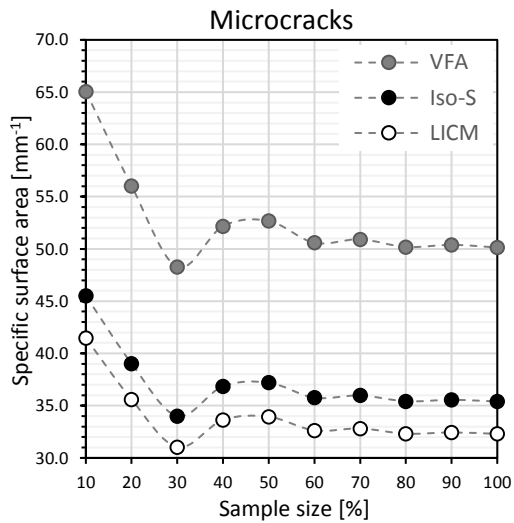


Figure 6-40 Effect of sample size on the measured specific surface area of microcracks and air voids.

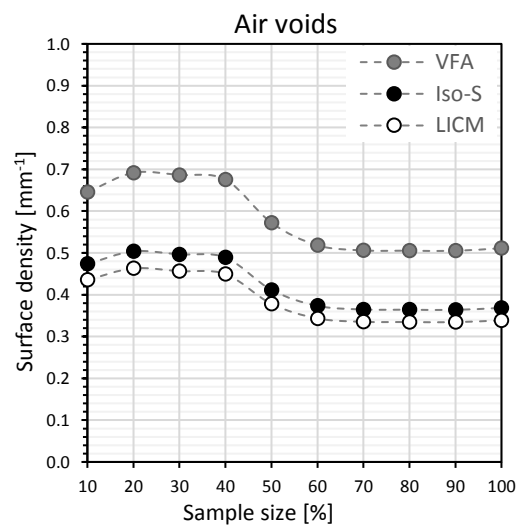
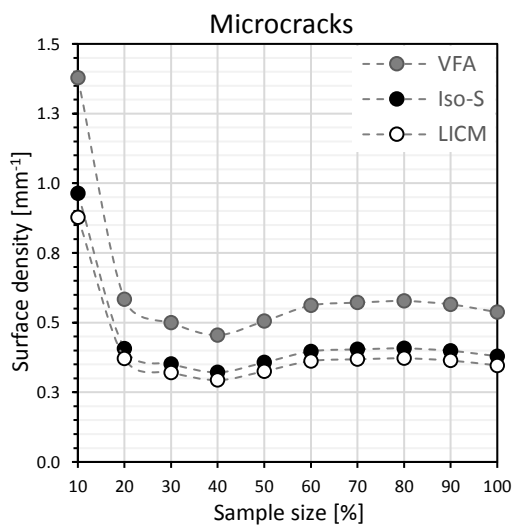


Figure 6-41 Effect of sample size on the measured surface density of microcracks and air voids.

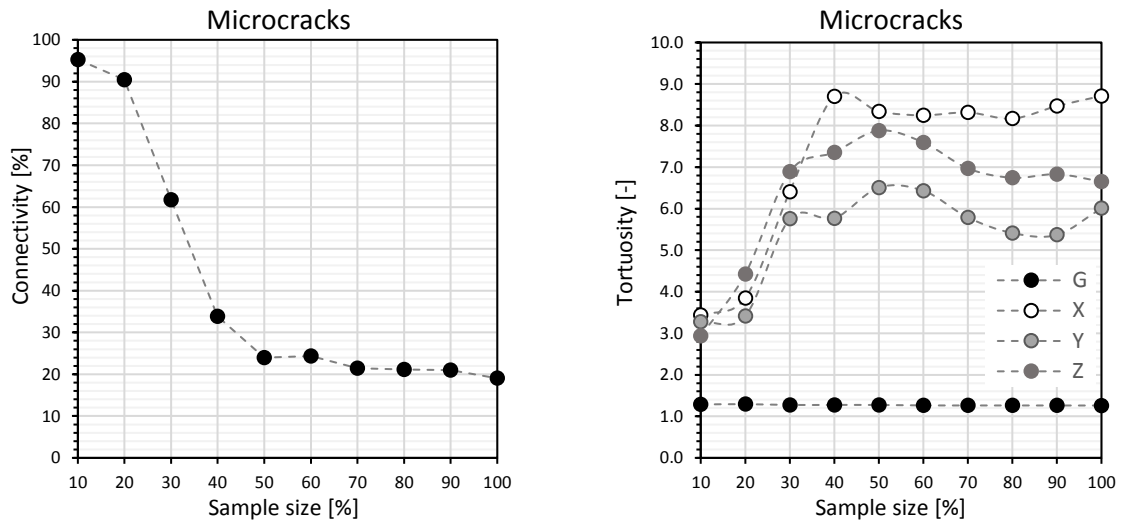


Figure 6-42 Effect of sample size on measured connectivity and tortuosity of microcracks.

However, the measured degree of anisotropy of microcracks and air voids continue to fluctuate over the range of analysed sample sizes as shown in Figure 6-43. A similar behaviour is observed for the average microcrack width and length analysed within various volumes (Figure 6-44). The last three to four readings (from sample size of 70%, 80%, 90% and 100% of the original volume) have reduced the oscillations. However, this is not a sufficient evidence to declare with confidence that representative results have been obtained for the whole material. For these parameters, a larger sample should be analysed and compared.

Figure 6-45 shows that other parameters describing size and shape of air voids such as width, length, equivalent diameter, sphericity, elongation and aspect ratio, remain stable for all sample sizes (excluding the smallest volume, i.e. the 10% of the original volume). This shows that the sample sizes over which these measurements are made have little influence on the results. However, this does not apply to spacing factor (Figure 6-46) that fails to reach a stable value at the largest sample size. Thus, a larger volume should be analysed for this parameter.

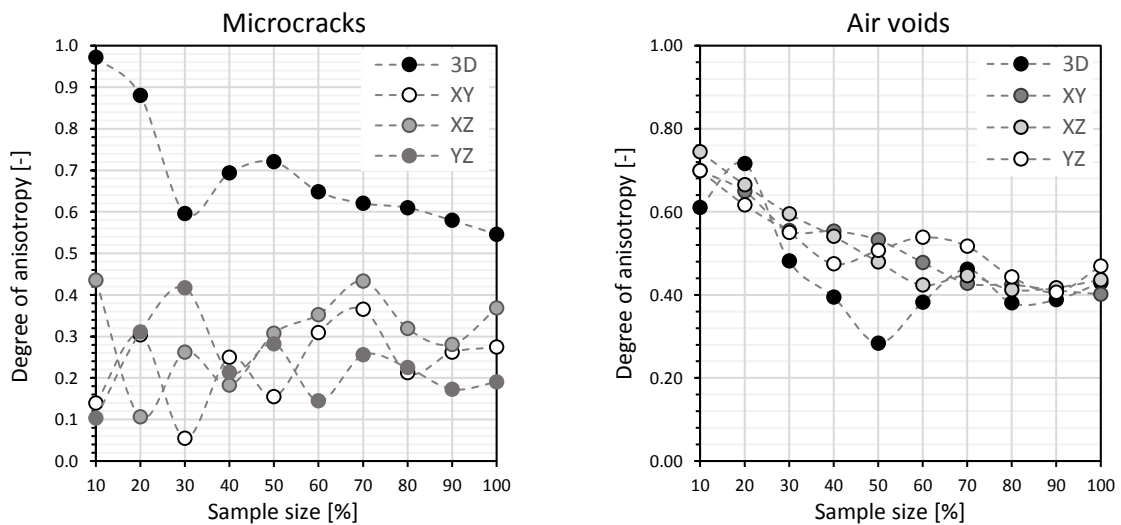


Figure 6-43 Effect of sample size on the degree of anisotropy of microcracks and air voids.

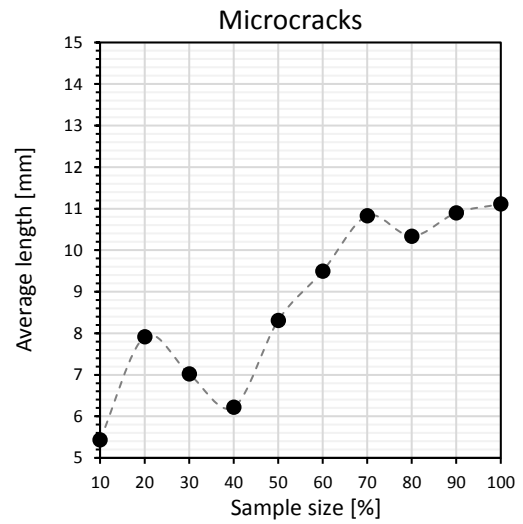
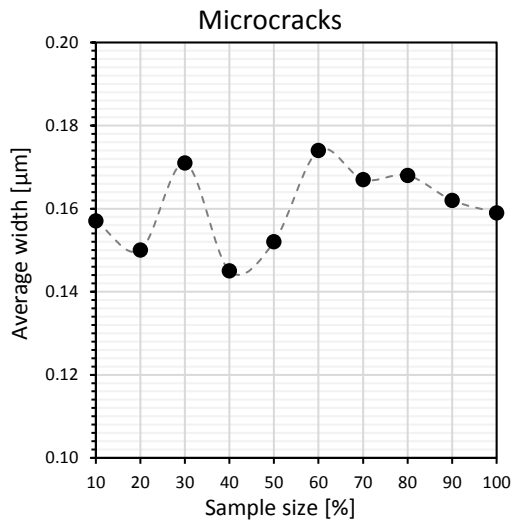


Figure 6-44 Effect of sample size on the measured microcrack width and length.

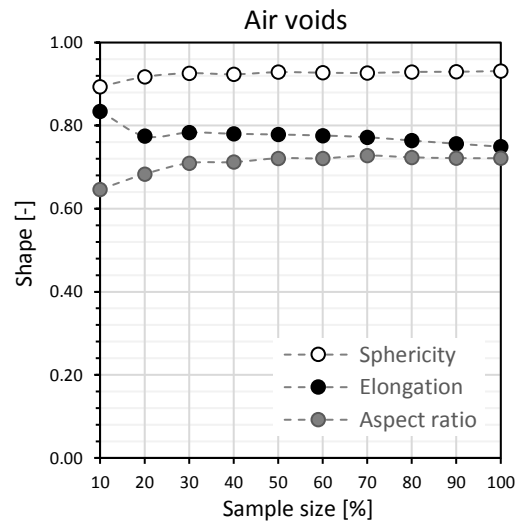
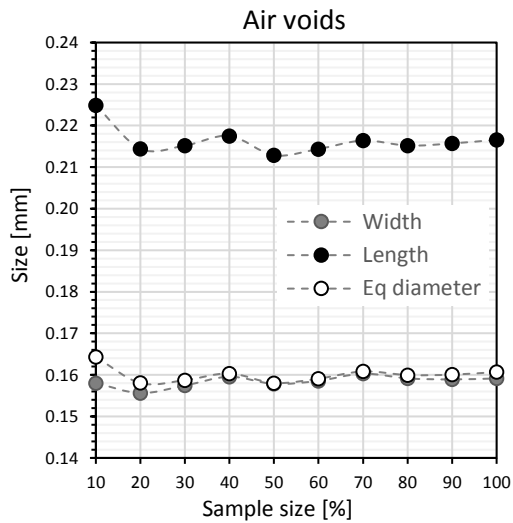


Figure 6-45 Effect of sample size on the measured air void size and shape.

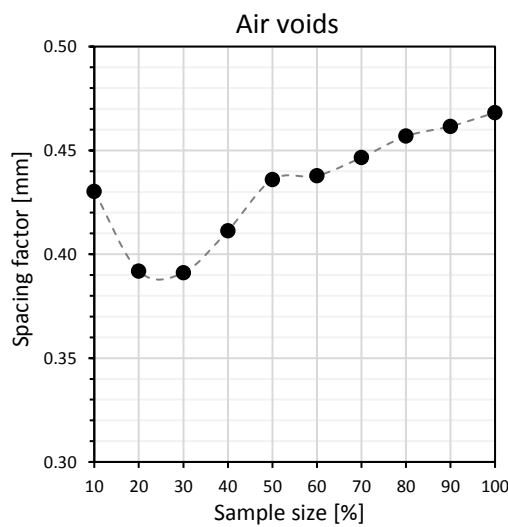


Figure 6-46 Effect of sample size on measured air void spacing factor.

6.7 Conclusion

3D image analysis of the microstructure of concrete is challenging especially when the features of interest are difficult to segment. Microcracks fall in this category because they share similar range of brightness values in the greyscale histogram to pores or air voids. The microcracks, pores and air voids are either empty, water saturated or impregnated with the same resin. Therefore, the primary objective of this chapter was to develop an algorithm to separate microcracks from other pore features.

The proposed algorithm consists of image pre-processing, segmentation (binarisation) and separation of features of interest. The separation is divided into three stages: separation of pores within porous aggregates, separation of air voids from the cement paste and finally extraction of microcracks. These stages are illustrated in Figure 6-47. The whole process can take several hours depending on the computing power (RAM memory, processor speed, etc.), because of the large image file size of several gigabytes that is processed at each step. Nevertheless, the whole process can be completely automated by writing simple macros, in which the following operations are repeated on all images that needs to be analysed and the results are saved as new images. The new images can then be processed with the subsequent operations and so forth. Macros can be recorded for example in ImageJ/ Fiji (from menu: Plugins/ Macros/ Record). The recorded Macros can be run overnight, which significantly shortens the time of the analysis.

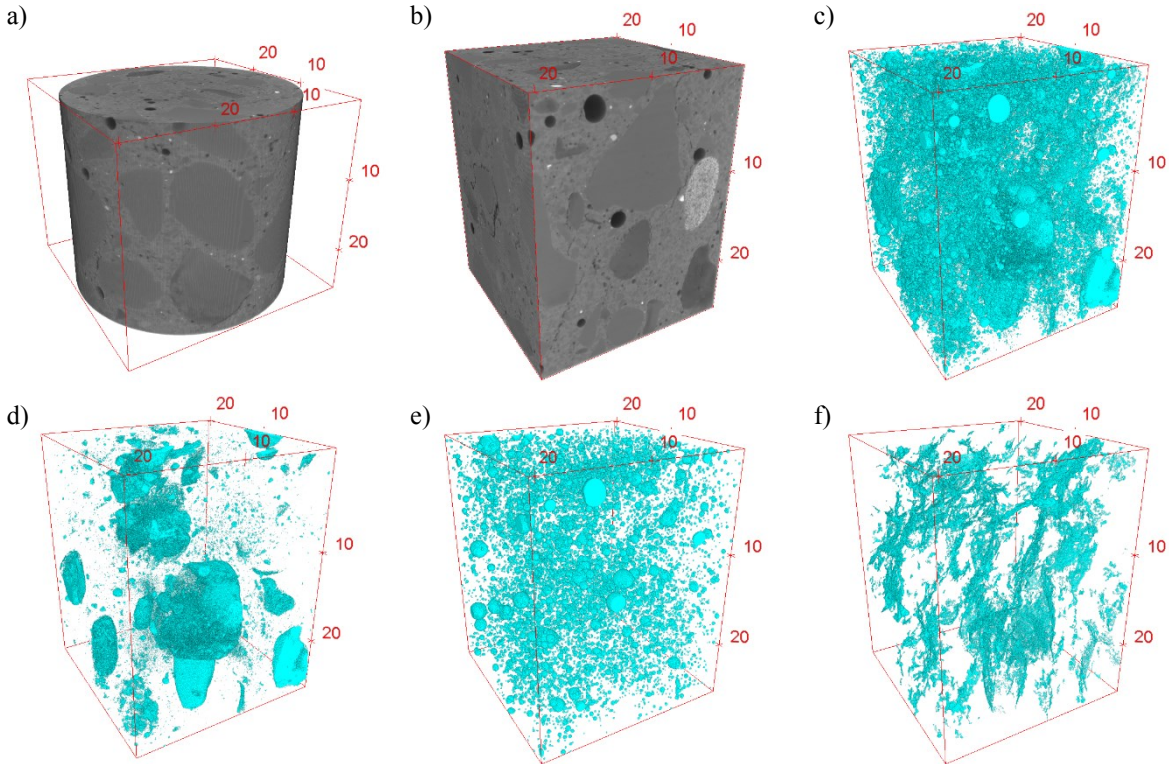


Figure 6-47 Steps in the separation algorithm: a) raw data, b) cropped image, c) binary image, d) pores in porous aggregates, e) air voids f) microcracks.

The accuracy of the segmentation of the proposed algorithm is reliable when applied to images of concrete from X-ray microtomography. It is also plausible that the algorithm would be applicable to 3D images

obtained from other microscopy techniques. The only questionable issue is related to the sensitivity of the results to the applied thresholds. Changing the selected threshold will give different results and this is an inevitable characteristic of image analysis. Therefore, it is important to select one method of thresholding and apply this consistently to the entire dataset. This will ensure that comparison of measured parameters between images is consistent, meaningful and reliable. Moreover, the overflow method (Wong et al., 2006) that was used in this study is well established and has been verified using Monte-Carlo simulations for cementitious materials (Yio et al., 2016).

Image processing and quantitative analysis were carried out using Fiji/ ImageJ and Avizo Fire software packages. Several methods were employed to measure a range of 3D parameters such as surface area via iso-surface triangular meshing or microcrack width from local thickness measurement. These methods are implemented in BoneJ plugin (Doube et al., 2010) and although originally designed for bone analysis, they have been found to be applicable for quantitative characterisation of microcracks and air voids in concrete. Other parameters such as volume and volume fraction, density, length, Feret diameters and sphericity of air voids were carried out using Avizo Fire.

2D analysis of concrete cross-section images obtained with fluorescence microscopy and scanning electron microscopy has been widely used in studying the microstructure of cement-based materials for the past several decades. Very often, these measurements are converted to their equivalent three-dimensional property by means of stereological formulations or other corrections. However, the reliability of such 2D to 3D conversions depends on a number of assumptions that are not always valid. This study showed that 3D characterisation of microcracks and air voids can produce very different results compared to 2D analysis, even when both are performed on the same sample. Only two sets of parameters are interchangeable, volume - area fraction and width - thickness measurements for microcracks and volume - areal fraction and shape measurements of air voids produced the same outcome, while results from other parameters vary to a significant extent. The largest disparity occurred for measurements that relate to microcrack length and density and air voids size. Other parameters such as connectivity and tortuosity are only measurable via 3D image analysis. It is also advantageous to apply 3D analysis especially when characterising orientation and degree of anisotropy of microcracks since they can appear to be aligned in one direction, but isotropic in other directions.

The issue with representative sample volume is also questionable, especially when dealing with an imaging technique where the spatial resolution is strongly dependent on sample size, such as X-ray tomography. A smaller sample size allows for higher resolution to be achieved and more detailed analysis can be performed, but the obtained results may not be sufficiently representative of the entire sample. The analysis provided in Section 6.6 shows that the sample size chosen in this study for X-ray tomography should be representative for characterising air voids and microcracks induced by autogenous shrinkage. The majority of the measured parameters achieved stable values except for a few parameters, e.g. width and length of microcracks and spacing factor of air voids, where further study using a larger sample size would be required.

The proposed separation algorithm and image analysis procedures described in this chapter will be applied in subsequent chapters for the quantification of microcracks in concretes subjected to autogenous shrinkage.

Chapter 7

Influence of various parameters on autogenous shrinkage-induced microcracking in concrete

The focus of this Chapter is on microcracking induced by autogenous shrinkage phenomenon. The main objective here is to determine the magnitude of autogenous shrinkage (by linear deformation measurements) and to understand its effect on the microstructure of concrete, in particular the formation of microcracking (by imaging and image analysis). To that end, a range of samples (30 different concrete mixes) were prepared to investigate influences of different parameters, such as the water to binder ratio, cement type, curing age, aggregate size and content and sample size.

7.1 Background

Autogenous shrinkage is an important component of volume change besides drying shrinkage and temperature deformation, which may lead to microcracking (Bisschop et al., 2002, Lura et al., 2003, Lura et al., 2009). This is especially the case for concretes containing supplementary cementitious materials (SCMs) with low water to binder ratio such as high-performance concrete (HPC), which in recent years, has become increasingly used in civil engineering because of its excellent performance such as high workability, high strength and low permeability.

Autogenous shrinkage is caused by self-desiccation of concrete due to reduction in internal relative humidity as the water is consumed during cement hydration. If the autogenous shrinkage is restrained either internally by rigid aggregate particles or externally by neighbouring structural members, internal tensile stresses will be produced, which may consequently exceed the tensile strength of the concrete and lead to cracking.

Numerous studies have been performed to study the nature of autogenous shrinkage, to measure its magnitude (Igarashi et al. 2000, Lura et al., 2003, Lura, 2003) and to propose mitigating strategies to minimise internal microcracking (Huo and Wong, 2006, Jiang et al., 2014). Several shrinkage-counteracting techniques have been suggested to reduce shrinkage and cracking sensitivity of concrete such as shrinkage reducing admixtures (SRA) and internal curing (IC) using water saturated lightweight aggregates (LWA) (Lura, 2003, Zhutovsky and Kovler, 2012, Zhutovsky et al., 2013) and super-absorbent polymers (SAP) (Craeye et al., 2011). However, these techniques also affect the mechanical properties and durability of concrete, and additionally raise the total cost of concrete production.

Despite the growing interest in autogenous shrinkage, no attempts have yet been made on direct characterisation of the microcracks developed due to this phenomenon. Such information would be helpful to

further understand the effects of autogenous shrinkage and could be used to develop models for predicting transport properties from microstructure. This is crucial because the transport of ions, gas or water through the porous microstructure of concrete is responsible for many deterioration mechanisms affecting concrete structures. Microcracks are much larger than the capillary pores and so may accelerate transport processes and consequently the ultimate failure of concrete structures.

7.2 Samples for shrinkage measurement and 2D microcrack analysis

All samples prepared for this chapter are subjected to autogenous shrinkage. Two groups of samples were prepared, for linear shrinkage measurement and 2D imaging and image analysis of microcracks respectively. Details of the prepared samples are shown in Table 7-1:

Influencing parameters:	Changing variables:					
	Binder	w/b	Age [days]	MSA [mm]	Agg. % vol.	Sample size [mm]
Water to binder ratio	CEM I 52,5R (C)	0.45				
	CEM I 52,5R + 9% silica fume (SF)	0.40				
	CEM I 52,5R + 9% silica fume (SF)	0.35	14	10	68	Ø95, H65
	CEM III/B42,5N (S)	0.30				
		0.25				
		0.20				
Age	CEM I 52,5R (C)		1			
	CEM I 52,5R (C)		3			
	CEM I 52,5R + 9% silica fume (SF)	0.30	7	10	68	Ø95, H65
	CEM III/B 42,5N (S)		14			
			28			
Maximum size of aggregate	CEM I 52,5R (C)			5		
	CEM I 52,5R + 9% silica fume (SF)	0.30	14	10	68	Ø95, H65
	CEM III/B 42,5N (S)			20		
Aggregate volume fraction	CEM I 52,5R (C)				50	
	CEM I 52,5R + 9% silica fume (SF)	0.30	14	10	60	Ø95, H65
	CEM III/B 42,5N (S)				68	
Sample size (diameter)	CEM I 52,5R (C)					Ø25
	CEM I 52,5R + 9% silica fume (SF)	0.30	14	10	68	Ø50
	CEM III/B 42,5N (S)					Ø95

Table 7-1 Samples for linear shrinkage deformation measurements and 2D analysis of microcracks imaged with LSCM.

Samples for linear shrinkage deformation measurement were cast in cylindrical moulds of 78 mm in diameter and 300 mm high. Three replicate samples were prepared for each mix and the results i.e. deformation over time were plotted as an average of three measurements taken from each replica. Details of the linear shrinkage measurement method can be found in Section 3.2. Samples for 2D analysis of microcracks were prepared as disc samples of 95 mm in diameter and 65 mm high. A cross-section was extracted from the middle of each disc, then epoxy impregnated and imaged with LSCM. Finally, the results are analysed by means of image analysis. Details of the sample preparation and image analysis are given in Chapter 3 Methodology.

7.3 Autogenous shrinkage

Measurement of autogenous deformation of cement paste and concrete may bring tremendously varied results between different authors (Hammer et al. 2002). This is due to the different techniques used in individual studies and associated with them difficulties in interpretation such results.

The linear measurement method adopted in this work is considered to be a reliable technique. It takes into account factors such as bleeding and thermal action, according to Hu et al (2013). The measured linear deformation is associated with the development of autogenous shrinkage, because all samples were sealed-cured to avoid drying or any moisture exchange to the environment throughout the experiment. This is supported by parallel measurements of sample mass that showed negligible change. For example, at the age of 70 days only approximately 3g/kg of mass loss occurred for most of the samples. Such minor decrease in mass can be due to a slight leakage during sealed curing and/or measurement errors associated to the scale accuracy. However, it should be noted that with this method, the earliest measurement can only be taken after final setting (approximately 6-9 hours after casting), while for different techniques such as volumetric method (see Section 2.2) the autogenous deformation can be recorded from the time of mixing dry ingredients with water. In this case the volumetric method may give 3-5 times higher results than the linear technique (Barcelo et al. 1999), depending on the type of cement paste and on the experimental conditions.

The results of linear deformation measurements over time for concrete mixes with ordinary Portland cement CEM I 52.5 R (C), CEM I 52.5R with 9% replacement of silica fume (SF), and pre-blended CEM III/B 42.5N consists of 70% of GGBS i.e. ground granulated blast furnace slag (S) as binders are plotted in Figures 7-1, 7-2 and 7-3 for various water to binder ratios, maximum aggregate sizes and aggregate volume fractions, respectively. Overall, the results obtained in this work are consistent with previous studies which state that autogenous shrinkage is greater in concrete mixes with supplementary cementitious materials (SCM) such as GGBS and silica fume (Lura, 2003, Tazawa, 1999). This is due to the rapid absorption of water in the hydration process with SCMs at the early ages. Application of SCMs create finer pore structures, which results in a lower RH and produce higher chemical shrinkage (0.26 ml/g (Bentz, 2007), 0.22 ml/g (Jensen & Hansen, 1996) and only 0.06 ml/g (Bentz, 2007) for GGBS, silica fume and Portland cement respectively) and above that lead to removal of calcium hydroxide that would restrain the shrinkage.

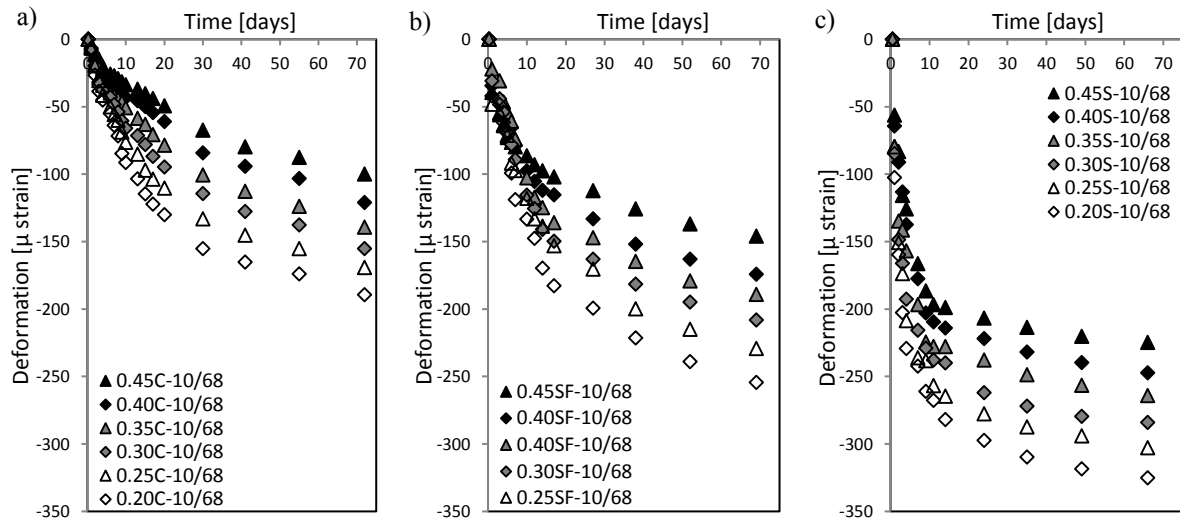


Figure 7-1 Linear deformation measurement of concrete mixes with different binders: a) Portland cement (C), b) silica fume (SF) and c) GGBS (S) and water to binder ratios of 0.20, 0.25, 0.30, 0.35, 0.40 and 0.45.

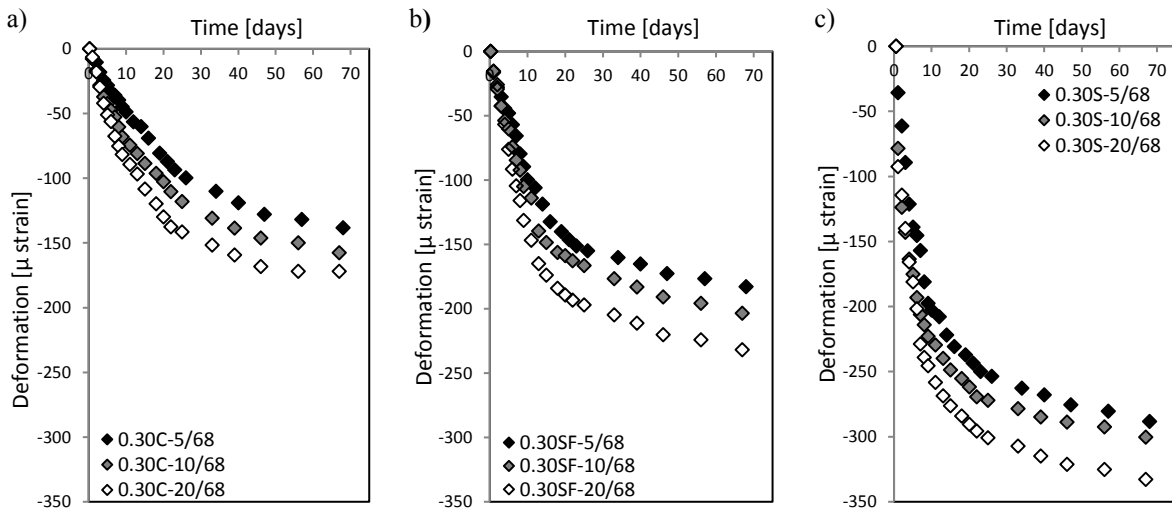


Figure 7-2 Linear deformation measurement of concrete mixes with different binders: a) Portland cement (C), b) silica fume (SF) and c) GGBS (S) and maximum aggregate sizes of 5 mm, 10 mm and 20 mm.

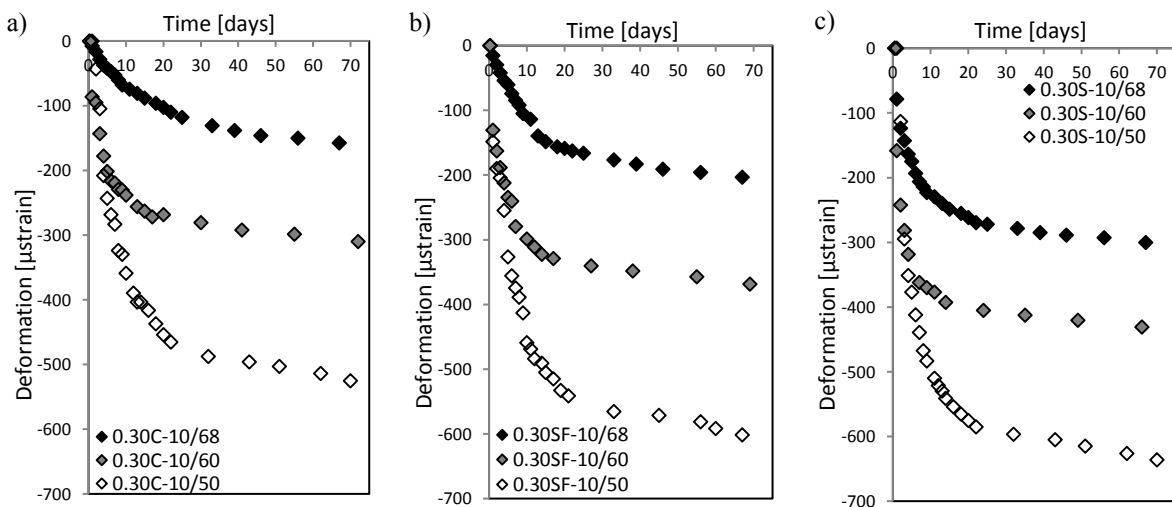


Figure 7-3 Linear deformation measurement of concrete mixes with different binders: a) Portland cement (C), b) silica fume (SF) and c) GGBS (S) and aggregate contents of 50%, 60% and 68%.

Additionally, greater shrinkage for concrete with GGBS was observed compared to silica fume concretes. This can be explained by the fact, that for all samples the length measurement was started after the same period (time zero) and that Portland-GGBS cement reacts more slowly (the Portland cement components begins to hydrate first, which is followed by the reaction of the GGBS with calcium hydroxide released by Portland cement), and this is what probably caused the autogenous deformation of GGBS samples to be recorded at an earlier stage than the silica fume samples.

The water to binder ratio is another parameter that significantly influences the magnitude of autogenous shrinkage. Concrete mixes with w/b ratio of 0.45, maximum size of aggregate (MSA) of 10 mm and aggregate volume of 68% shrank up to 100, 150 and 225 μ -strain for samples with neat Portland cement (C), 9% of silica fume (SF) and GGBS (S) respectively at the end of the experiment (after 70 days). Similar mixes at lower w/b ratio of 0.20 achieved higher shrinkage of 190, 250 and 325 μ -strain respectively. These results are comparable with previous studies. For example, Igarashi et al. (2000) reported that Portland cement concrete and silica fume concrete (10% addition) can produced shrinkage of 100 and 220 μ -strain for mixes with w/b ratio of 0.33 and 350 and 500 μ -strain for mixes with w/b ratio of 0.25. Similarly, Lura (2003) and Jiang et al. (2014) reported that GGBS concretes with w/b ratio of 0.37 and 0.20 can reach shrinkage values of 200 and 700 μ -strain respectively. Additionally, Jiang et al. (2014) investigated the effect of w/b ratio of Portland cement concrete. They reported deformation of 400, 500 and 750 μ -strain for concretes with w/b ratio of 0.40, 0.30 and 0.20 respectively.

Aggregate size and volume fraction can also have an impact on the measured shrinkage. Increasing aggregate size produced a slight increase in shrinkage of approximately 20 to 30 μ -strain between samples with MSA of 5 mm and 10 mm. A similar difference was observed between samples with MSA of 10 mm and 20 mm, regardless of binder type. This is related to enlargement of the specific surface area of aggregates with smaller MSA, which produces a larger restraint to shrinkage.

The results also show that decreasing aggregate volume fraction increases measured shrinkage significantly. Samples with 60% and 50% of total volume of aggregate produced two and three times higher shrinkage respectively in comparison to the concrete mixes with 68% of aggregate content. These results are expected since the total volume of cement paste that undergoes shrinkage increases.

The highest shrinkage increment, for all samples, was observed in the first two weeks from casting. Subsequently, the rate of the shrinkage progressively decreased. Such a large development of shrinkage during the early ages of concrete while the microstructure is still developing may lead to undesirable microcracking.

7.4 Two-dimensional characterisation of microcracks

The characteristics of microcracks in samples having a range of w/b ratio, age, sample size, volume fraction and maximum size of aggregates were measured according to the procedures described in Section 3.4.1. On the cross-section, the microcracks show a typical morphology that is influenced by the presence of aggregate particles, see Figure 7-4. The cracks occur either at the aggregate-paste interface (bond cracks) or through the cement paste (matrix cracks), propagating from the surface of one aggregate particle to the surface of a neighbouring aggregate particle. The crack is either arrested at the aggregate particle or travels around the aggregate particle. It may also propagate through the aggregate, although this is rare. The microcracks propagate

also from one to another air voids if such features are encountered on their path. The detectable microcracks occur evenly on the whole cross-section. Moreover, the tendency for branching and connecting microcracks, especially in samples with severe microcracking, is clearly visible.

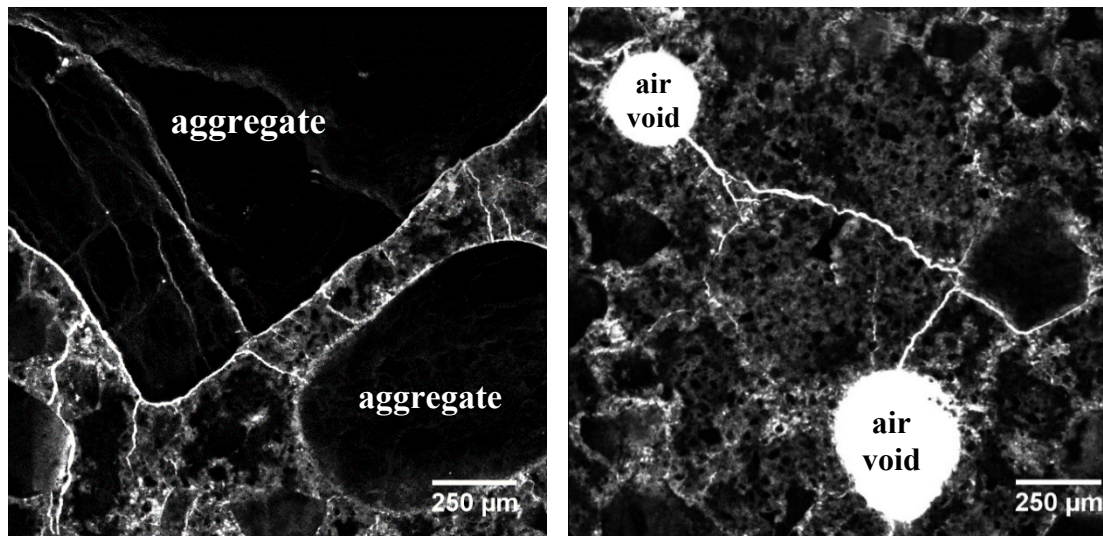


Figure 7-4 Typical microcrack morphology in a concrete sample subjected to autogenous shrinkage showing bond and matrix microcracks at the aggregate – cement paste – air voids interfaces.

The observed microcracks are mainly inherent, i.e. induced by autogenous shrinkage rather than other factors such as drying. It could be argued that some of the cracks might have occurred during the first steps of sample preparation i.e. cutting and freeze drying. Subsequent sample preparation that consists of grinding and polishing should not introduce any new visible damage due to the epoxy impregnation that preceded these procedures. Any new microcracks that form after impregnation are not visible because these would not be epoxy-filled and consequently not imaged with fluorescence microscopy.

The concern about microcracks induced by initial sample preparation was minimised by testing performed on references i.e. “crack free” samples as presented in Section 3.3.1. The reference testing showed insignificant evidence of damage caused by cutting or freeze drying. The small number microcracks detected were short and occupied only 0.07% of the imaged area, which is much less significant compared to the microcracks seen in the actual samples that were subjected to autogenous shrinkage. Furthermore, all samples were prepared in exactly the same way, which enabled us to make a fair comparison of microcracks between these samples.

Autogenous shrinkage induced microcracks were characterised by the following parameters:

- area fraction,
- specific surface area
- percentile distribution of microcrack width and average crack width,
- percentile distribution of microcrack length and average crack length,
- microcrack dendritic density,

- degree of anisotropy/ orientation of microcracks shown by means of rose of intercepts at 0°, 45°, 90° and 135°.

The measured values of these parameters are presented and discussed in Sections 7.4.1 to 7.4.6.

7.4.1 Area fraction

The data obtain from the analysis of cross-sections of concretes prepared with three binders (neat Portland cement, Portland cement with silica fume and GGBS) are shown in Figure 7-5 a), b), c), d) and e) for samples with different w/b ratio, age, aggregate maximum size, aggregate fraction and sample size respectively.

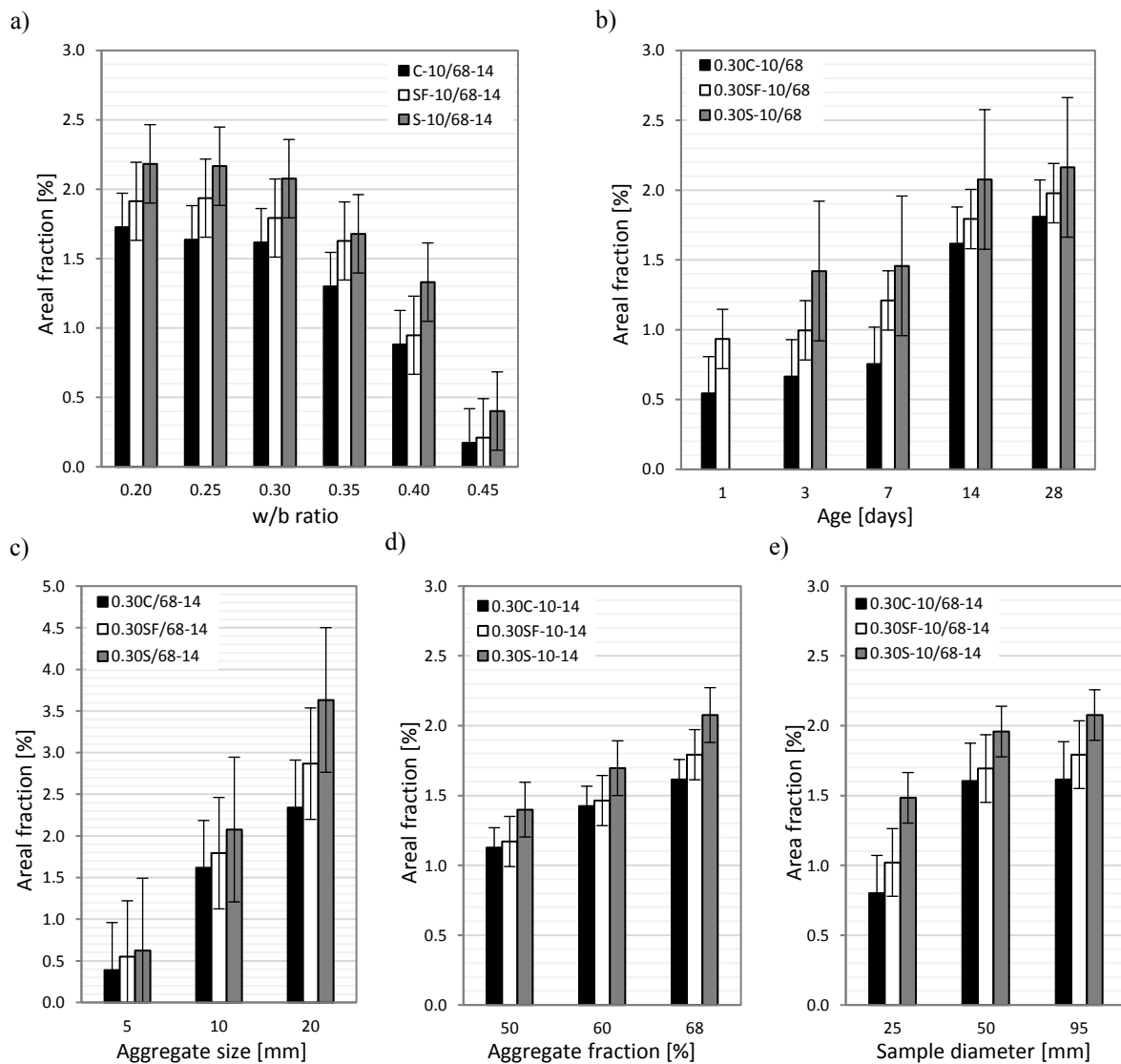


Figure 7-5 Area fraction of microcracks measured in samples with different a) w/b ratio, b) age, c) maximum aggregate size, d) aggregate fraction and e) sample size.

As mentioned earlier, binder type is an important parameter influencing autogenous shrinkage induced microcracking. Generally, the use of SCMs increases the area fraction of microcracks in comparison to neat Portland cement (C) concretes (Figure 7-5 a). The results also show that samples containing GGBS (S)

experienced greater amount of microcracking compared to samples with silica fume (SF). The microcrack area fraction is inversely proportional to the crack density (see Figure 7-16). This indicates that the microcracks formed in Portland cement concretes must be narrow and long, while those in concretes containing SCMs particularly GGBS are wider and larger. Further detailed analysis of microcrack width and length confirmed this statement.

Area fraction of microcracks is also influenced by the water to binder ratio. Samples with low w/b ratios such as w/b = 0.20, w/b = 0.25 and w/b = 0.30 had very similar results of $A_A = 1.6\%$, $A_A = 1.9\%$ and $A_A = 2.1\%$ in C, SF and S samples respectively. While, an increase of the w/b from 0.35 to 0.45 results in a decrease of area fraction of about 0.5% for an increase of 0.05 in w/b.

The results in Figure 7-5 b provide evidence that most of the microcracks are formed during the first two weeks, while in the next two weeks the propagation of microcracks is substantially inhibited. This is also supported by the results from shrinkage measurements. Moreover, the data show that approximately 30% of the microcracks for neat Portland cement concrete (C) and 50% of the microcracks for concrete with silica fume (SF) formed in the first 24 hours after casting. Note that no data for the GGBS concrete (S) is provided because this particular sample was not hard enough for cutting at this early stage. The large amount of microcracking that formed in the first 24 hours does not seem to correlate well with the amount of measured shrinkage. However, it must be remembered that the adopted procedure is only able to measure shrinkage after initial setting. Due to this delay, it is not possible to record the complete deformation that occurs from the first moment when water and binder(s) come in contact.

The area fraction of the microcracks is strongly affected by maximum aggregate size. Figure 7-5 c shows that there is a near linear increase in area fraction with increase in aggregate size from 5 mm to 10 mm and 20 mm. The area fraction increased from 0.4%, 0.5% and 0.6% for MSA of 5 mm, to 1.6%, 1.8% and 2.0% for MSA of 10 mm and to 2.3%, 2.9% and 3.6% for MSA of 20 mm for concretes with neat Portland cement (C), Portland cement with silica fume (SF) and GGBS (S) samples, respectively.

Similarly, the microcrack area fraction increased with increasing aggregate fraction from 50% to 68% as shown in Figure 7-5 d, which is quite contradictory, since an increase of aggregate fraction results in reduction of cement paste and consequently diminishing the shrinkage. However, higher aggregate fraction may influence the morphology of microcracks, particularly their width and length. Microcracks in concretes with higher aggregate fraction were shorter but wider (see Section 7.4.3 and 7.4.4.), which increased their area fraction and decreased the density. On the contrary to thinner but longer microcracks in concretes with lower aggregate fraction, resulting in a decrease of the area fraction and an increase of the density.

Figure 7-5 e shows, that samples with diameter of 50 mm and 95 mm have very similar microcrack area fractions, but samples with diameter of 25 mm had about 25 – 50% lower results, depending on the type of the binder used. This may lead to questioning whether sample size influences microcrack characteristics. It seems that, concretes prepared in mould with diameter of 50 mm are of a neuralgic size below which microcracks tend to exhibit different characteristics in comparison to characteristics obtained from larger samples. However, it is important to point out that the imaged and analysed area of Ø25mm samples was four and two times smaller than Ø95mm and Ø50mm samples respectively, which may affect the results.

7.4.2 Surface area

Surface area of the microcracks (SA_{2D}) was estimated using the line intercept count method (in Avizo Fire). Based on the obtained results, two parameters were estimated: specific surface area (SSA_{2D}), i.e. the ratio of surface area to total area of microcracks and surface density (SD_{2D}) i.e. the ratio of surface area to analysed image area. The results are tabulated in Table 7-2.

Sample	SSA_{2D} [mm^{-1}]/ SD_{2D} [mm^{-1}]		
	C	SF	S
0.20 -10/68-14	10.329/ 0.178	9.235/ 0.177	8.058/ 0.176
0.25 -10/68-14	9.973/ 0.163	8.673/ 0.168	7.946/ 0.172
0.30 -10/68-14*	9.270/ 0.150	8.848/ 0.159	7.878/ 0.164
0.35 -10/68-14	9.569/ 0.124	9.015/ 0.147	6.875/ 0.115
0.40 -10/68-14	10.164/ 0.090	8.697/ 0.082	6.334/ 0.084
0.45 -10/68-14	11.674/ 0.020	9.186/ 0.019	7.054/ 0.028
0.30-10/68- 1	13.329/ 0.073	11.835/ 0.111	-
0.30-10/68- 3	12.673/ 0.084	11.673/ 0.116	9.546/ 0.136
0.30-10/68- 7	12.433/ 0.094	10.116/ 0.122	9.136/ 0.133
0.30-10/68- 14 *	9.270/ 0.150	8.848/ 0.159	7.878/ 0.164
0.30-10/68- 28	9.064/ 0.164	8.647/ 0.171	7.734/ 0.167
0.30-10/ 50 -14	29.146/ 0.329	25.106/ 0.294	23.123/ 0.324
0.30-10/ 60 -14	18.547/ 0.264	16.742/ 0.246	15.154/ 0.257
0.30-10/ 68 -14*	9.270/ 0.150	8.848/ 0.159	7.878/ 0.164
0.30- 5 /68-14	12.846/ 0.050	12.106/ 0.067	11.123/ 0.069
0.30- 10 /68-14*	9.270/ 0.150	8.848/ 0.159	7.878/ 0.164
0.30- 20 /68-14	7.041/ 0.165	6.278/ 0.180	5.572/ 0.202
0.30-10/68-14/ 25mm	8.924/ 0.072	7.492/ 0.076	6.764/ 0.100
0.30-10/68-14/ 50mm	9.185/ 0.147	9.129/ 0.155	8.124/ 0.159
0.30-10/68-14/ 95mm *	9.270/ 0.150	8.848/ 0.159	7.878/ 0.164

Table 7-2 Specific surface area and surface density of microcracks.

Note: * the same sample are listed several times to facilitate comparison between different groups of samples.

The control concretes with neat Portland cement showed microcracks having higher SSA and slightly lower SD values compared to samples that contained SCMs, especially GGBS. The difference is mainly due to the larger crack area fraction in concretes with SCMs. Moreover, the differences in concrete microstructure caused by use of SCMs, may affect the surface area. Finer pore structure of cement paste contained silica fume or GGBS in concrete contributes to refining sharpened edges of microcracks, which influences both parameters describing microcracks: decreases the specific surface area and increases the surface density of microcracks.

Increasing curing age, aggregate volume fraction or aggregate size decreases microcrack SSA, but increases SD. These correlations related to the area fraction and density of microcracks. Samples measured at

later age have denser microstructure and the propagating and widening microcracks become smoother. In concretes with different MSA, the size and smoothness of microcracks significantly increases in concretes with larger aggregates, affecting the specific surface area and surface density of microcracks. Similar, even stronger impact on these parameters were encountered in concrete with different aggregate volume fractions, where the amount of microcracks increases and their size and smoothness decrease with an increase of cement paste volume.

Interestingly, the specific surface area of microcracks was not much influenced by w/b ratio or sample size. The measured SSA values for samples prepared with various w/b ratio were relatively consistent, ranging from 9-10 mm⁻¹, 8-9 mm⁻¹ and 6-7 mm⁻¹ for neat OPC, OPC with silica fume and GGBS respectively. However, the surface density of microcracks decreased significantly with higher w/b ratios. This is expected since the amount of microcracking and hence the total surface area of microcracks decreased at higher w/b ratio (Figure 7-4a) while the imaged area remains the same for each sample.

7.4.3 Width

Microcrack widths were measured as local thickness with Thickness plugin in BoneJ (Dougherty et al., 2007, Hildebrand and Rüegsegger, 1997). The local thicknesses were measured at every pixel in the structure of microcracks and the data were then used to calculate an area-weighted mean width ($W_{\text{mean 2D}}$) and width distribution. Table 7-3 presents the mean width values for all samples. Figures in Appendix I (Figures I-1, I-2, I-3, I-4 and I-5) plot the distribution curves of microcrack widths for samples with different w/b ratio, binder type, age, aggregate maximum size, aggregate fraction and sample size respectively. The smallest detectable crack width using fluorescence imaging is 1.5 µm and this is sufficient for the purpose of this study. Microcracks finer than 1.5 µm can be seen using BSE imaging at very high magnifications, but these are relatively few, and tend to be short and isolated. Overall, a large portion of the detectable microcracks (70-80% of the population) have crack widths in a range between 10 µm and 100 µm.

Simple comparison of an average microcrack width (see Table 7-3) shows some evident tendencies between different concrete mixes. The results very clearly shows that the microcracks in concretes containing SCMs were wider than in neat Portland cement concretes. For example, at 14 days, MSA of 10 mm and aggregate volume fraction of 68%, the average crack widths were 38 µm, 50 µm and 70 µm for samples prepared with neat Portland cement (C), 9% replacement of silica fume (SF) and 70% of GGBS (S), respectively. The average crack widths also increased with curing age. Typically, the mean width of microcracks at 28-day was 10 – 20 µm larger than that at 1-day. Additionally, the results confirmed the significant increase of microcracks width with an increase in MSA, which has been already observed e.g. by Wu et al., (2015). The average crack width in samples with MSA of 10 mm and 20 mm was respectively two and three times bigger than in samples with MSA of 5 mm. Moreover, samples with higher aggregate fraction of 60% and 68% contained microcracks of mean crack widths approximately two and three times greater than samples with aggregate fraction of 50% only. Besides, the mean crack widths increased by a factor of 2 – 3 in samples prepared in moulds of Ø50 mm and Ø95 mm in comparison to samples cast in moulds of Ø25 mm. The relevancy of this finding may be vital in respect to the sampling representativeness.

Sample	$W_{\text{mean 2D}} [\mu\text{m}]$		
	C	SF	S
0.20 -10/68-14	35.48 (0.68)	48.95 (0.98)	71.58 (1.46)
0.25 -10/68-14	37.70 (0.71)	48.52 (0.94)	65.61 (1.84)
0.30 -10/68-14*	38.23 (0.77)	50.30 (1.04)	69.61 (1.30)
0.35 -10/68-14	42.54 (0.92)	62.36 (1.25)	77.43 (1.63)
0.40 -10/68-14	41.80 (0.89)	63.32 (1.34)	75.24 (1.57)
0.45 -10/68-14	17.49 (0.19)	54.20 (1.01)	52.82 (0.91)
0.30-10/68- 1	18.78 (0.22)	40.52 (0.62)	-
0.30-10/68- 3	20.27 (0.62)	34.91 (0.71)	57.03 (1.09)
0.30-10/68- 7	20.09 (0.71)	38.26 (1.18)	53.52 (0.72)
0.30-10/68- 14 *	38.23 (0.77)	50.30 (1.04)	69.61 (1.30)
0.30-10/68- 28	41.61 (0.87)	54.85 (1.02)	68.11 (2.28)
0.30-10/ 50 -14	16.34 (0.88)	17.56 (0.60)	25.34 (0.78)
0.30-10/ 60 -14	30.28 (1.58)	33.78 (0.87)	41.13 (1.94)
0.30-10/ 68 -14*	38.23 (0.77)	50.30 (1.04)	69.61 (1.30)
0.30- 5 /68-14	14.69 (0.67)	23.27 (0.69)	32.41 (0.49)
0.30- 10 /68-14*	38.23 (0.77)	50.30 (1.04)	69.61 (1.30)
0.30- 20 /68-14	45.48 (1.14)	71.78 (1.49)	102.33 (3.01)
0.30-10/68-14/ 25mm	13.25 (0.52)	18.52 (0.93)	29.43 (1.78)
0.30-10/68-14/ 50mm	35.83 (0.96)	43.72 (1.10)	67.59 (3.38)
0.30-10/68-14/ 95mm *	38.23 (0.77)	50.30 (1.04)	69.61 (1.30)

Table 7-3 Average microcrack widths in μm with standard errors in brackets.
Note: * same sample listed to facilitate comparison between different groups of samples.

The trends described above are supported by the width distribution curves (Figures 7-6 – 7-10). The width distribution curves for concretes with SCMs are shifted towards larger values. For example, microcracks having widths $< 50 \mu\text{m}$ (14-day, 10 mm MSA and 68% aggregate volume fraction) represent 87%, 84% and 79% of the population in samples with Portland cement (C), silica fume (SF) and GGBS (S), respectively. While, microcracks having widths $> 100 \mu\text{m}$ represent 4%, 7%, and 12% of the population in Portland cement (C), silica fume (SF) and GGBS (S) samples, respectively. Similar trends can be seen in the width distribution curves for samples analysed at different ages, MSA and aggregate volume fractions. The results clearly show that an increase in curing age, aggregate size or content shifts the curves to higher crack widths. The differences are most visible in the range between $30 \mu\text{m}$ and $200 \mu\text{m}$.

In contrast, the average widths of microcracks showed no consistent or significant correlation with w/b ratio. An average crack width ranged between $35\text{-}42 \mu\text{m}$ for neat Portland cement concretes (C), $48\text{-}63 \mu\text{m}$ for concretes with silica fume (SF) and $65\text{-}77 \mu\text{m}$ for concretes with GGBS (S) with slightly lower values recorded for w/b ratio of 0.45 but these samples were the least cracked. Essentially, the cumulative width distribution curves of microcracks with different w/b ratio overlap each other. These suggest that w/b ratio has an

insignificant effect on microcrack widths. Only samples at w/b ratio of 0.40 and 0.45 showed a slight divergence, probably because they experienced the least shrinkage and consequently the least microcracking. Also, there is no major differences in the width distribution between the 50 mm and 95 mm diameter samples, while samples from the 25mm diameter cylinders showed distribution curves shifted to much lower values.

7.4.4 Length

Length of the microcracks (L) was measured as dendritic length of the skeletonised microcracks and the measured values were used to calculate a mean length (L_{2Dmean}) and to produce a cumulative length distribution for each sample. Table 7-4 shows the mean values. Figures in Appendix II (Figures II-1, II-2, II-3, II-4 and II-5) present the distribution curves for samples with different w/b ratio, binder type, age, aggregate maximum size, aggregate fraction and sample size.

Sample	$L_{mean\ 2D}$ [mm]		
	C	SF	S
0.20 -10/68-14	0.194 (0.012)	0.204 (0.007)	0.184 (0.006)
0.25 -10/68-14	0.183 (0.013)	0.192 (0.008)	0.179 (0.004)
0.30 -10/68-14*	0.161 (0.006)	0.194 (0.009)	0.174 (0.011)
0.35 -10/68-14	0.149 (0.005)	0.182 (0.007)	0.154 (0.006)
0.40 -10/68-14	0.136 (0.006)	0.167 (0.006)	0.102 (0.005)
0.45 -10/68-14	0.094 (0.003)	0.135 (0.006)	0.092 (0.006)
0.30-10/68- 1	0.104 (0.002)	0.185 (0.012)	-
0.30-10/68- 3	0.135 (0.006)	0.189 (0.008)	0.157 (0.011)
0.30-10/68- 7	0.129 (0.004)	0.189 (0.005)	0.169 (0.009)
0.30-10/68- 14 *	0.161 (0.006)	0.194 (0.009)	0.174 (0.011)
0.30-10/68- 28	0.182 (0.013)	0.203 (0.007)	0.177 (0.017)
0.30-10/ 50 -14	0.231 (0.005)	0.243 (0.008)	0.193 (0.008)
0.30-10/ 60 -14	0.186 (0.006)	0.217 (0.002)	0.182 (0.008)
0.30-10/ 68 -14*	0.161 (0.006)	0.194 (0.009)	0.174 (0.011)
0.30- 5 /68-14	0.095 (0.003)	0.103 (0.004)	0.113 (0.003)
0.30- 10 /68-14*	0.161 (0.006)	0.194 (0.009)	0.174 (0.011)
0.30- 20 /68-14	0.239 (0.013)	0.214 (0.012)	0.250 (0.015)
0.30-10/68-14/ 25mm	0.137 (0.005)	0.131 (0.008)	0.138 (0.010)
0.30-10/68-14/ 50mm	0.178 (0.007)	0.152 (0.006)	0.155 (0.009)
0.30-10/68-14/ 95mm *	0.161 (0.006)	0.194 (0.009)	0.174 (0.011)

Table 7-4 Average microcrack lengths in mm with standard errors in brackets.

The analysed microcracks in all samples are relatively short, with most having lengths smaller than 1 mm. The average length ranged between 0.1 to 0.2 mm for majority of the samples. Despite this consistency, some relevant tendencies can be remarked. For example, concretes with SCMs, especially silica fume (SF), tend

to show slightly longer microcracks compared to those in neat Portland cement samples (C). Another clear trend is that concretes with low w/b ratio show longer crack lengths. For example, the average crack length for concretes at w/b ratio of 0.20 is twice that of those at w/b of 0.45. Increasing curing age produced a slight increase in microcrack length, which indicates that microcracks propagate with time and connect with neighbouring cracks. This applies especially to the period within the first two weeks of casting.

Decreasing aggregate volume fraction from 68% to 60% and 50% produced more visible increases in microcrack length of about 5-20% (between 68% and 60% aggregate fraction) and 10-30% (between 68% and 50% aggregate fraction). However, the larger increase in crack length was observed in increasing the MSA, from about 55-90% and 110-150% 5 mm between 5 mm – 10 mm and 5 mm – 20 mm, respectively. The least influencing crack length was sample sizes.

7.4.5 Density

Figure 7-6 shows the crack density measured in concretes with different binder type, w/b ratio, age, aggregate maximum size, aggregate fraction and sample size.

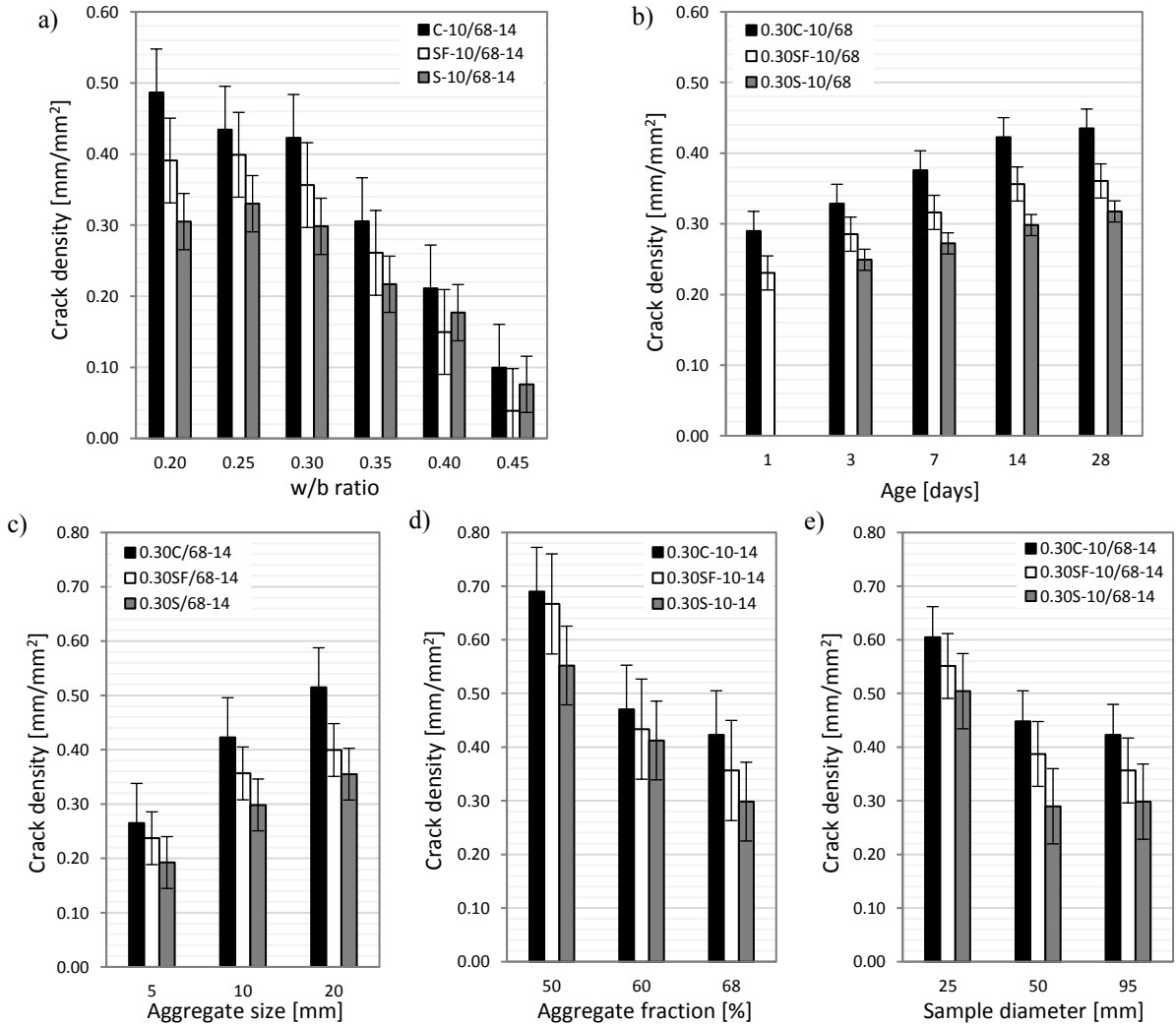


Figure 7-6 Microcrack density measured in samples with different a) w/b ratio, b) age, c) maximum aggregate size, d) aggregate fraction and e) sample size.

The analysis indicates that the type of binder has great impact on the characteristics of the microcracks. The highest density was measured in samples with neat Portland cement while replacement of the binder with silica fume or GGBS significantly lowers the density of microcracks by up to 20% to 30%.

The results show that the factor of w/b ratio higher than 0.30 significantly decrease the density of microcracks (approximately four times between w/b=0.30 and w/b=0.45) while for lower w/b ratio than 0.30 is much less influencing. Therefore, the w/b ratio of 0.30 seems to be the critical value, below which there is no significant differences in characteristics of microcracks. This is also confirmed by analysis of other parameters.

For all binder types, the density of the microcracks increased significantly with increase in age, particularly during the 14 days. Beyond that, no significant changes were observed. This demonstrates that the development of microcracking occurs mainly during the early ages, which is consistent with the results obtained from autogenous shrinkage measurements (Section 7.3).

Aggregate size and content also influence the characteristics of microcracks. Figure 7-6 c, d show that crack density increased with increase in maximum aggregate size or decrease in aggregate fraction. This is to be expected since the distance between individual aggregate particles increases in both cases. A larger separation between aggregate particles provide more space for propagation of microcracks through the weaker cement paste.

Figure 7-6-e shows no significant difference in crack density between samples of 50 mm and 95 mm in diameter. On the contrary, the crack density of the 25 mm diameter samples was evidently higher. However, this may be due to the fact, that the imaged and analysed area of Ø25 mm samples (cross-section of $25 \times 65 \text{ mm}^2$) is three times smaller than that of Ø95 mm samples, and therefore is not representative. For the future it is recommended to conduct the analysis of smaller samples on more than one cross-section in order to improve the reproducibility and accuracy of the measurement.

7.4.6 Degree of anisotropy

Degree of anisotropy of microcracks (DA_{2D}) was measured by the mean intercept length method (MIL) (see Section 6.4.1). The results presented in Table 7-5. indicate that the microcracks are nearly isotropic due to the very small values of degree of anisotropy measured. For most samples, this parameter was in a range between 0.10 – 0.35. However, it must be pointed out that the measurements were performed in two-dimensions, i.e. only in one direction that is perpendicular to the direction of casting fresh mixes.

The orientation of microcracks is presented in rose diagrams of intercept densities at 0° , 45° , 90° , 135° angles. Results are shown in Appendix III, for samples with different binder type, w/b ratio, age, aggregate fraction, maximum size of aggregate and sample size. The rose diagrams are consistent with the measured values of the degree of anisotropy, indicating isotropic orientations. As can be seen in the diagrams, the intercept densities (black lines) are at approximately similar distance from the centre for the samples at all orientation angles. Only a small number of samples showed a slight elongation across the 0-180° axis. This may be related to the shape and orientation of aggregates or might be recognised as an issue of compaction of fresh mixes.

Sample	DA _{2D} [-]		
	C	SF	S
0.20 -10/68-14	0.142	0.340	0.357
0.25 -10/68-14	0.308	0.290	0.268
0.30 -10/68-14*	0.342	0.367	0.360
0.35 -10/68-14	0.221	0.284	0.297
0.40 -10/68-14	0.171	0.074	0.164
0.45 -10/68-14	0.108	0.153	0.159
0.30-10/68- 1	0.306	0.195	-
0.30-10/68- 3	0.092	0.238	0.351
0.30-10/68- 7	0.102	0.069	0.219
0.30-10/68- 14 *	0.342	0.367	0.360
0.30-10/68- 28	0.343	0.268	0.286
0.30-10/ 50 -14	0.116	0.034	0.176
0.30-10/ 60 -14	0.263	0.257	0.289
0.30-10/ 68 -14*	0.342	0.367	0.360
0.30- 5 /68-14	0.266	0.234	0.269
0.30- 10 /68-14*	0.342	0.367	0.360
0.30- 20 /68-14	0.261	0.248	0.491
0.30-10/68-14/ 25mm	0.037	0.304	0.280
0.30-10/68-14/ 50mm	0.297	0.110	0.295
0.30-10/68-14/ 95mm *	0.342	0.367	0.360

Table 7-5 Degree of anisotropy of microcracks induced by autogenous shrinkage.

7.5 Summary

Results obtained from measurements of autogenous shrinkage linear deformation are consistent with 2D image analysis. The greater the development of autogenous shrinkage, the higher the degree of microcracking. Table 7-6 summarises the overall trends of the measured parameters indicated by a colour code (red – increase, green – decrease, yellow – no change).

The most significant parameter influencing the autogenous shrinkage and induced by this phenomenon microcracking is water to binder ratio. More severe microcracking and higher shrinkage were observed in concretes with lower water to binder ratio. The w/b ratio of 0.35 seems to be the critical value below which concrete is seriously damaged. Higher w/b ratio, especially w/b=0.40 and w/b=0.45 do not cause a high risk of severe microcracking.

The use of SCMs such as silica fume and especially GGBS also significantly increases autogenous shrinkage and consequently the risk of microcracking. The microcracks formed in concretes containing these binders were wider, longer and had greater area fraction, while their density and specific surface area decreased.

In contrast, the control Portland cement concretes showed the least amount of autogenous shrinkage and microcracking. The highest growth of autogenous shrinkage occurred within the first two weeks after mixing and this corresponds to the development of microcracking observed on the 2D images. After 14 days, the samples continue to undergo autogenous shrinkage, but at a much reduced rate. Consequently, the microcrack characteristics of the 14 and 28 day old samples are relatively similar.

	Binder type	w/c ratio	Age [days]	MSA [mm]	Aggregate % vol.	Sample size [mm]
	C»SF»S	0.20»0.25»0.30»0.35»0.40»0.45	1»3»7»14»28	5»10»20	68»60»50	25»50»95
AS						-
A _A						
W						
SSA						
SD						
D _D						
L						
DA						

Table 7-6 Overall trends of the measured parameters indicated by colour codes.

AS – autogenous shrinkage, A_A – area fraction of microcracks, W – crack width, SSA – specific surface area, SD – surface density, D_D = dendritic density, L – crack length, DA – degree of anisotropy.

Colour code: increase, decrease, no change.

Increasing MSA (at equal aggregate volume fraction) lowers surface area of aggregate particles to bond with the cement paste. This produces higher stress concentrations at the aggregate-cement paste interface and more microcracking compared to concretes with smaller aggregate particles. Furthermore, microcracks in samples with larger MSA are wider and longer due to the higher shrinkage and fewer obstructing aggregate particles per unit volume of concrete to arrest the cracks. Conversely, decreasing aggregate volume fraction (at constant MSA) increases autogenous shrinkage significantly because of the higher volume fraction of the shrinking matrix and lower percentage of the restraining aggregate particles. The microcracks formed in concretes with low aggregate volume fraction are narrower and has lower area fraction, but they are longer and have higher density and connectivity. Many studies have been dedicated to understand the effect of aggregates on drying-induced microcracking, both experimentally and theoretically. For instance, Idiart et al. (2011, 2012) studied the effect of aggregate size and volume fraction on drying induced microcracking, and qualitatively compared their numerical simulation with experimental results. Their hygro-mechanical model showed larger degrees of internal microcracking for higher levels of drying as well as for increasing aggregate volume fraction and size. Grassl et al. (2010) studied internal microcracking by means of a lattice model on 2D composites with

circular aggregates. They found that the average crack width increased with increasing aggregate size and decreased with increasing aggregate volume fraction, whereas the crack density showed opposite trends. Findings from this work are consistent with their results.

To verify the influence of sample size, de facto, the effect of MSA to sample diameter ratio, concrete mix with MSA of 10 mm was cast into three containers with diameter of 25, 50 and 95mm, which correspond to MSA/sample diameter ratio of 2.5, 5 and 9.5. Obtained results demonstrate that microcrack characteristics' dependency on sample size does not exist for higher MSA/sample diameter ratio (>5), while lowering this ratio (e.g. to 2.5) may significantly affect the results. This is related to the aspect of the representative sampling volume.

Chapter 8

3D characterisation of autogenous shrinkage-induced microcracks

The aim of this Chapter is to demonstrate the application of 3D imaging and image analysis on a range of samples in order to better understand the characteristics of microcracks induced by autogenous shrinkage. As demonstrated in Chapter 4, X-ray microtomography is one of the most suitable techniques for detecting microcracks in three-dimensions. This technique is employed in this Chapter to image the microstructure of selected concrete samples from Chapter 7. The data are processed using the image analysis algorithm proposed in Chapter 6 and the results correlated to parallel measurements from Chapter 7. 2D and 3D image analyses are compared, and their advantages and limitations are discussed.

8.1 Background

The nature of microcracks induced by autogenous shrinkage in concrete containing supplementary cementitious materials is not well understood. One reason for this is the lack of suitable techniques to detect and characterise the microcracks. Conventional methods include imaging polished cross sections with scanning electron microscopy and optical microscopy. However, these techniques only provide a two-dimensional representation of a three-dimensional structure. Parameters such as connectivity and tortuosity of microcracks which are critical with respect to understanding transport phenomena are completely unattainable with these methods. Also, indirect methods such as ultrasonic and acoustic emission, which work by detecting the sound waves produced by crack nucleation and propagation in real time, provide very limited information about size, position and geometry of the developed crack pattern. This is a major limitation and significantly reduces the insights that can be gained from such analyses.

Another reason is that the contribution of autogenous shrinkage in typical concrete mixes has been previously neglected due to the dominant role of drying shrinkage. Nonetheless, the increasing use of high strength concretes that are of low water/binder ratio, containing complex mix of cementitious materials and chemical admixtures in recent years has highlighted the problem of autogenous shrinkage in these concretes.

In the past few decades, three-dimensional imaging methods such as computed tomography based on conventional X-ray or synchrotron radiation have gained wide applications in cement and concrete materials science. These techniques can image the true nature of the analysed structure in 3D rather than its 2D projection. However, the resolution of these techniques is limited and decreases with increase in sample size. Conventional μ -CT scanners are capable of achieving a spatial resolution of $>1 \mu\text{m}$. This has been applied in cement and concrete research in a number of applications for imaging large scale features, e.g. freeze-thaw induced

microcracking (Promentilla et al., 2008), quantitative measurements of crack growth under loading (Landis et al., 2006), in situ observation of cracking and fracture behaviour under progressive uniaxial compressive loading (Yang et al., 2017) and characterization of deterioration caused by sulphate attack (Naik et al., 2006, Stock et al., 2002), carbonation (Han et al., 2012) and leaching (Burlion et al., 2006). Synchrotron μ -CT with slightly higher resolution of between 0.7 to 1.0 μm has been used to image pores in hardened cement paste (Gallucci et al., 2007) and anhydrous cement particles (Garboczi and Bullard, 2004). As far as I am aware, there have been no attempts on direct 3D characterisation and understanding of the microcracks caused by autogenous shrinkage using CT techniques.

8.2 Samples for analysis of microcracks in 3D

Samples for analysis of microcracks in 3D were selected based on the results obtained from the 2D analysis of microcracks (Chapter 7). The shortlisted samples differed with respect to:

- Type of binder: Portland cement CEM I 52.5 R (C), CEM I 52.5R with 9% replacement of silica fume (SF), and pre-blended CEM III/B 42.5N with 70% ground granulated blast furnace slag (S) – 3 samples;
- Water to binder ratio: 0.20, 0.25, 0.30, 0.35, 0.40, 0.45 – 6 samples;
- Curing age: 1, 3, 7, 14 and 28 days – 1 sample scanned 5 times at different ages.

For each of these, a cylindrical sample ($\text{Ø}30$ mm, H65 mm) was prepared for imaging with X-ray microtomography. Samples with various binders and w/b ratios were cored from a larger volume of concrete (disc $\text{Ø}95$ mm, H65 mm). Note that one mix (0.30SF-10/68-14) was prepared in two replicate samples and imaged twice for statistical purposes. Additionally, the same mix (0.30SF-10/68-14) was chosen for the experiment at different ages, where one sample (cylinder $\text{Ø}30$ mm, H65 mm) was prepared and imaged at the required age to investigating the development of microcracking over time. The sample was sealed in a tight-fitting plastic container to ensure sealed curing during the experimentation. This is one of the great advantages of X-ray microtomography, where the same sample can be non-destructively scanned as many times as requested. Detailed information of the prepared samples is shown in Table 8-1.

Influencing parameters:	Variables:					
	Binder	w/b	Age [days]	MSA [mm]	Agg. % vol.	Sample size [mm]
Binder	C SF* (binder) S	0.30	14	10	68	30 (cored)
Water to binder ratio	SF	0.45 0.40 0.35 0.30* (w/b) 0.25 0.20	14	10	68	30 (cored)
Age	SF	0.30	1 3 7 14* (age) 28	10	68	30 (cast)

Table 8-1 Samples for 3D analysis of microcracks with X-ray microtomography. * - replicates.

8.3 Three-dimensional characterisation of microcracks

The prepared cylindrical samples were imaged using Metris X-Tek HMX ST 225 CT scanner with setting up parameters the same as described in Section 3.3.3. The acquired fourteen 3D images were afterwards subjected to the proposed algorithms for segmentation and separation of microcracks developed in Chapter 6. Then the separated microcracks from these images were characterised by the following parameters:

- volume fraction,
- specific surface area and area density,
- average crack width and the percentile distribution of microcrack widths,
- average crack length and the percentile distribution of microcrack lengths,
- microcrack dendritic density,
- degree of anisotropy/ orientation of microcracks,
- connectivity,
- tortuosity.

Detail information of these parameters are described in Section 6.4.1 and the measured values are presented and discussed in the following Sections (8.3.1 – 8.3.8).

8.3.1 Volume fraction

The segmented 3D images of microcracks are presented in Figures 8-1, 8-2 and 8-3. A straightforward visual inspection indicates that the binder type and water to binder ratio have the greatest impact on microcracking, while the effect of concrete age is unnoticeable to the naked eye. However, this is only a visual impression because detailed quantitative analysis (discussed later) demonstrates some important differences between images acquired at different ages.

Results from the measurement of volume fraction of microcracks are presented in Figures 8-4 a), b) and c) for concretes with different binder, w/b ratio and age respectively. The results show similar trends to findings from density measurements. The highest microcrack volume fraction of 3.28% was registered for concrete with GGBS. The microcrack volume fraction decreased by at least 50% in concrete with silica fume (1.67%) and in neat Portland cement concrete (0.28%). This indicates that the density and size of microcracks increased in concretes with SCMs, especially with GGBS.

Figure 8.4 b) shows that the volume fractions of microcracks in concretes with very low w/b ratio were quite similar. For example, concretes with w/b ratio of 0.20 to 0.30 showed 1.56 to 1.64% vol. microcracks. In contrast, for concretes with higher w/b ratio, this parameter progressively decreased to 0.89%, 0.83% and 0.39% for w/b ratios of 0.35, 0.40 and 0.45 respectively. This suggests that w/b ratio of 0.30 is a critical value and that above this value microcracking occurs much less severely.

Figure 8-4 c) shows that the microcrack volume fractions in samples imaged at different ages increased with time. This can be interpreted as growth and widening of the earlier formed microcracks. The volume fraction at age of 1, 3, 7, 14 and 28 days was 0.98%, 0.99%, 1.11%, 1.26% and 1.37%, respectively. This shows that approximately 70% of microcracking occurs in the first 24 hours. Therefore, this is a crucial stage because the risk of failure when exposed to stress is the highest for such a fragile and young microstructure.

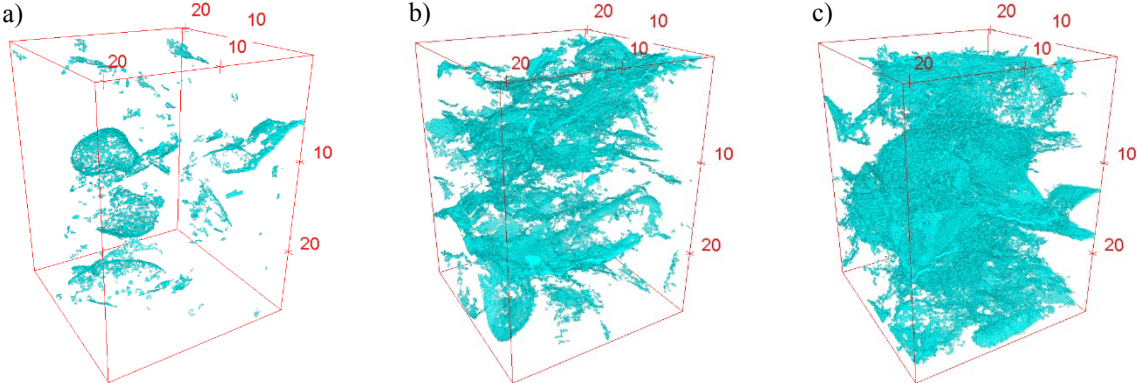


Figure 8-1 Segmented microcracks in concretes with different binders a) 0.30C-10/68-14, b) 0.30SF-10/68-14-(w/b replica), c) 0.30S-10/68-14. (Scale in mm).

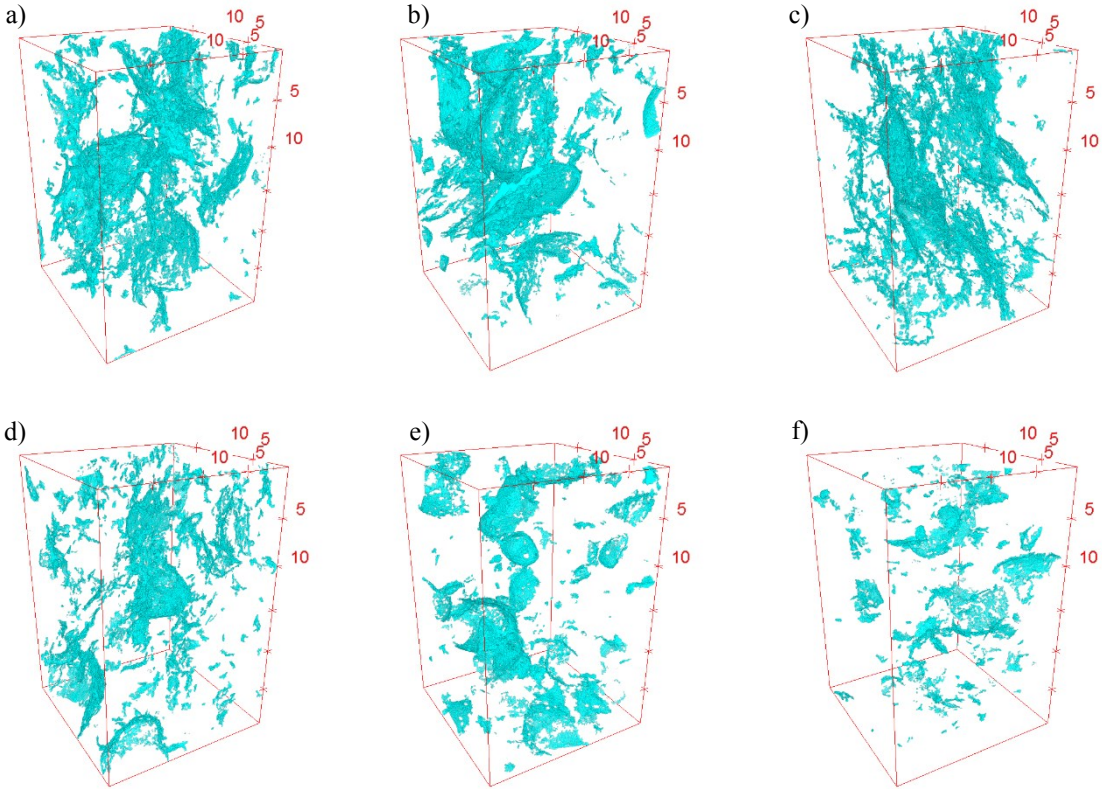


Figure 8-2 Segmented microcracks in concretes with different water to binder ratio: a) 0.20SF-10/68-14, b) 0.25SF-10/68-14, c) 0.30SF-10/68-14-(w/c replica), d) 0.35SF-10/68-14, e) 0.40SF-10/68-14, f) 0.45SF-10/68-14. (Scale in mm).

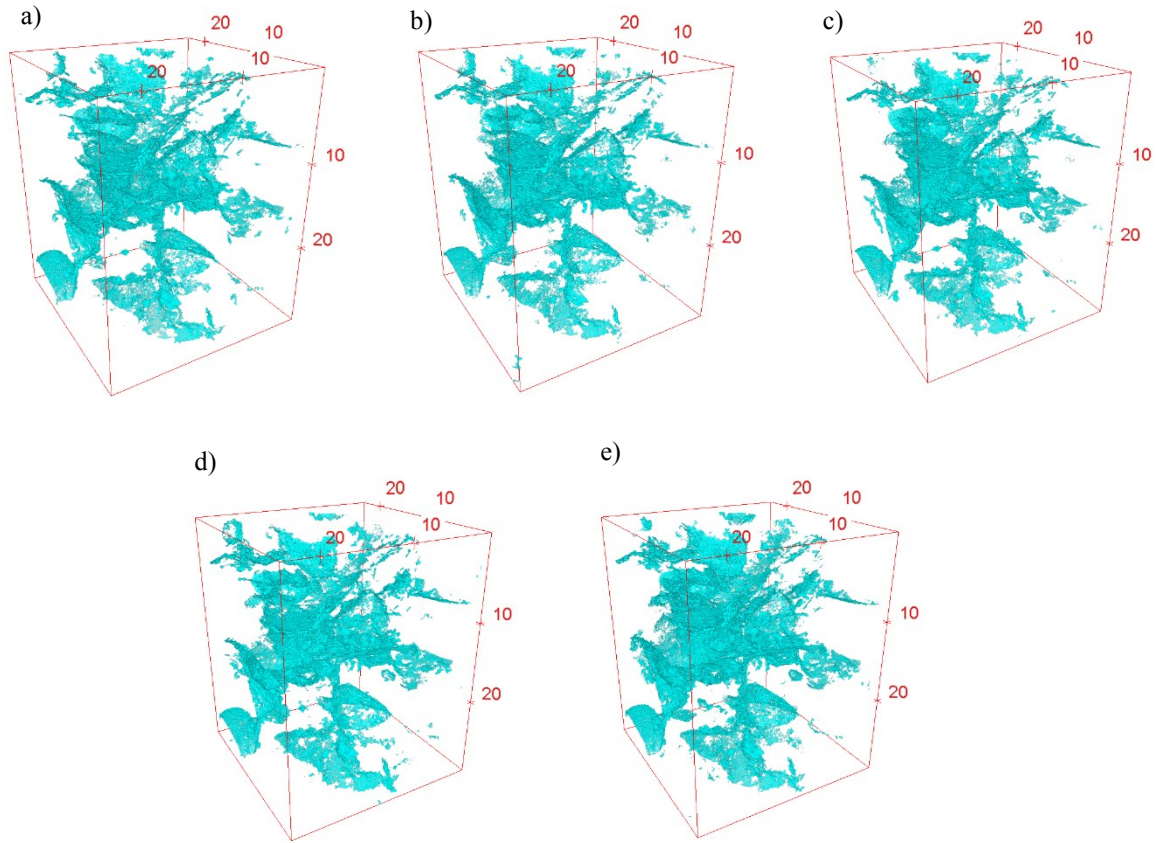


Figure 8-3 Segmented microcracks in concretes at different age: a) 0.30SF-10/68-1, b) 0.30SF-10/68-3, c) 0.30SF-10/68-7, d) 0.30SF-10/68-14- (age replica), e) 0.30SF-10/68-28. (Scale in mm).

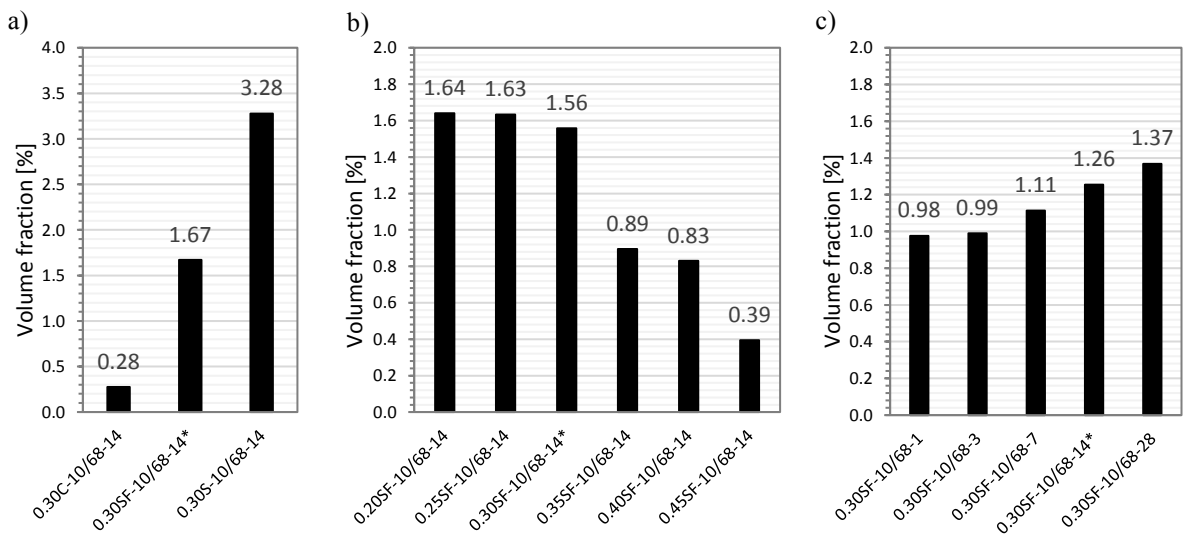


Figure 8-4 Volume fraction of microcracks in concretes with a) different binders, b) different water to binder ratio and c) at different age. (* - refers to relevant replicas).

8.3.2 Surface area

Surface area of microcracks was measured by three different methods: voxel face area, iso-surface mesh (in BoneJ) and line intercept count method (in Avizo Fire) as explained in Section 6.4.1. The obtained results were then used to calculate two parameters i.e. specific surface area (SSA), which describe smoothness of surface and surface density (SD).

Figures 8-5, 8-6 and 8-7 present the surface data for different binders, w/b ratios and ages, respectively. It can be seen, that the iso-surface mesh method and LICM produced similar results, while the voxel face area method gave slightly higher values. Specific surface area was quite uniform for all samples containing silica fume, regardless of w/b ratio and curing age, an average value of 24 mm⁻¹ and 22 mm⁻¹ was obtained with iso-surface mesh method and LICM respectively. Whereas, the SSA of microcracks from samples with different type of binders were varied; microcracks in OPC concrete had SSA of almost 30 mm⁻¹ and 27 mm⁻¹, respectively for iso-surface mesh method and LICM, and microcracks in GGBS concrete had much smaller SSA, respectively 20 mm⁻¹ and 18mm⁻¹ for each method. This can be associated with differences in microstructure of neat Portland cement concrete and SCMs concretes.

In contrast, the measured microcrack surface density exhibits various trends not only between concretes with different type of binder, but also between w/b ratio and age. These results are analogous to volume fraction of microcracks (shown in Section 8.3.1) since the SD of microcracks is defined as total surface area divided by sample volume (image volume). Surface density of microcracks in concretes with GGBS and silica fume is five and eight times higher than in neat OPC concrete (Figure 8-5b). Concretes with w/b ratio of 0.30 and lower had similar SD, while for concretes with w/b ratio greater than 0.30 showed decreasing SD to approximately 0.1 mm⁻¹ (Figure 8-6b). Figure 8-7c shows that microcrack SD increases with age.

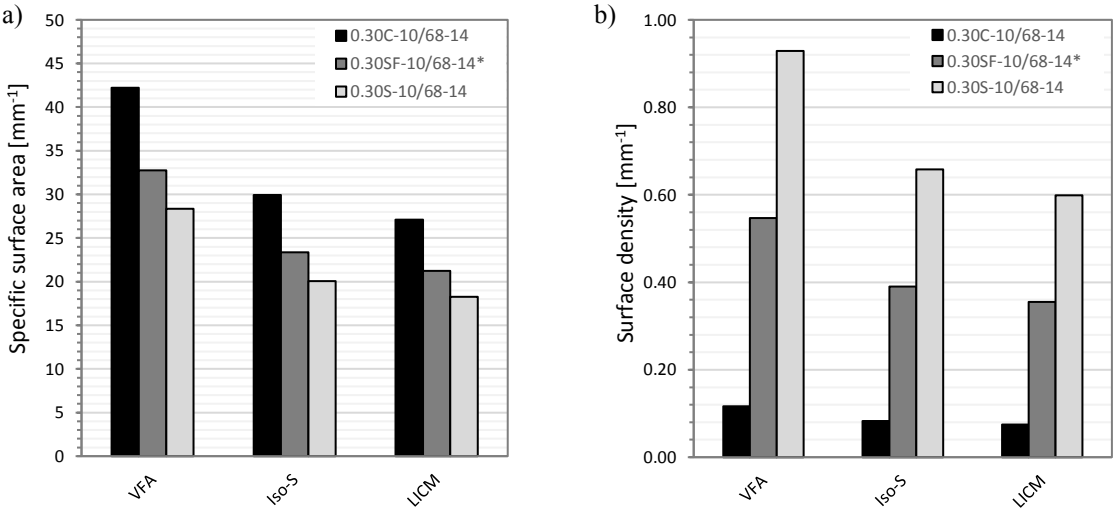


Figure 8-5 a) Specific surface area and b) surface density of microcracks in concrete with different binders obtained via voxel face area (VFA), triangular surface mesh (Iso-S) and line intercept count method (LICM). (* - refers to binder replica).

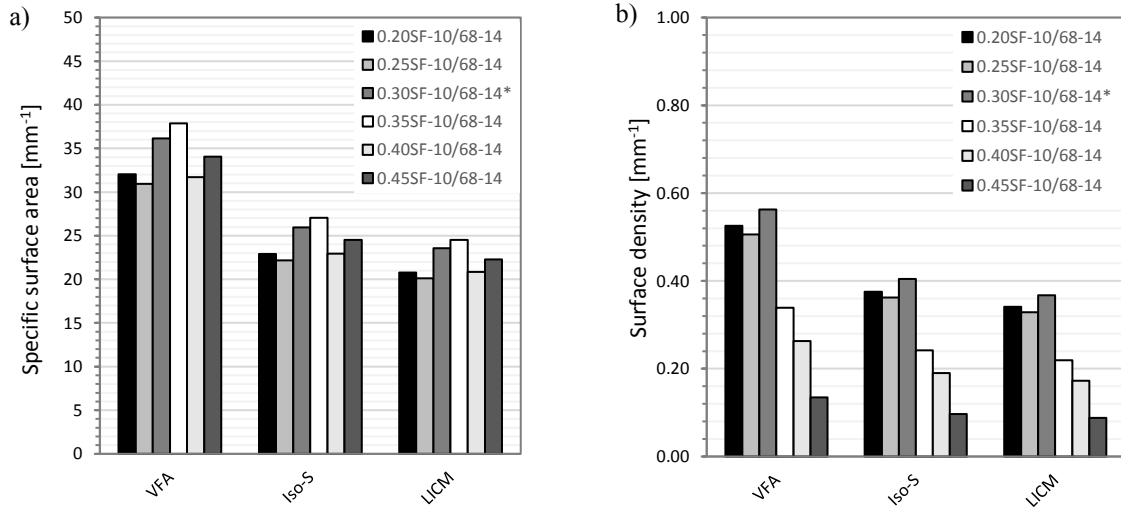


Figure 8-6 a) Specific surface area and b) surface density of microcracks in concrete with different water to binder ratio via voxel face area (VFA), triangular surface mesh (Iso-S) and line intercept count method (LICM). (* - refers to w/b ratio replica).

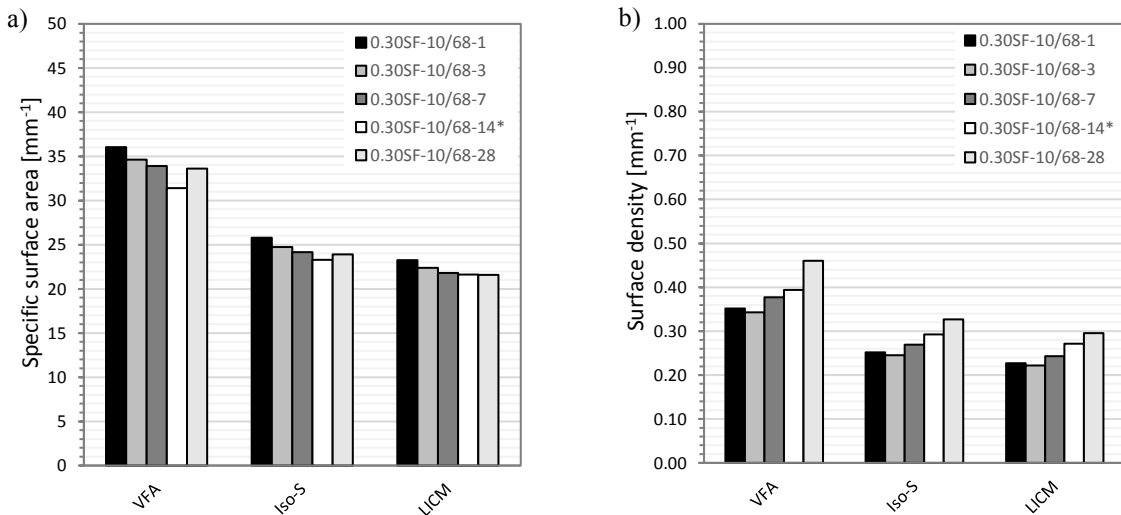


Figure 8-7 Estimation of a) specific surface area and b) surface density of microcracks in concrete at different age via voxel face area (VFA), triangular surface mesh (Iso-S) and line intercept count method (LICM). (* - refers to age replica).

8.3.3 Width

Width of microcracks was measured using BoneJ – Thickness plugin (Dougherty and Kunzelmann, 2007, Hildebrand and Rügsegger, 1997) as volume-based local thickness. This method defines the thickness at every point in the structure as the diameter of the largest sphere that fits within the structure in each point. Graphical results of this analysis are presented in Figures 8-8, 8-9 and 8-10 for samples with different types of binders, w/b ratios and ages respectively. These are 3D colour images of thickness map, in which the colour value of each pixel representing the microcrack thickness at that point. Visual assessment of the images suggests

that most of the microcracks in all samples have width (thickness) in a range between 100 μm and 200 μm , as indicated by the dominance of purple colour that corresponds to these values.

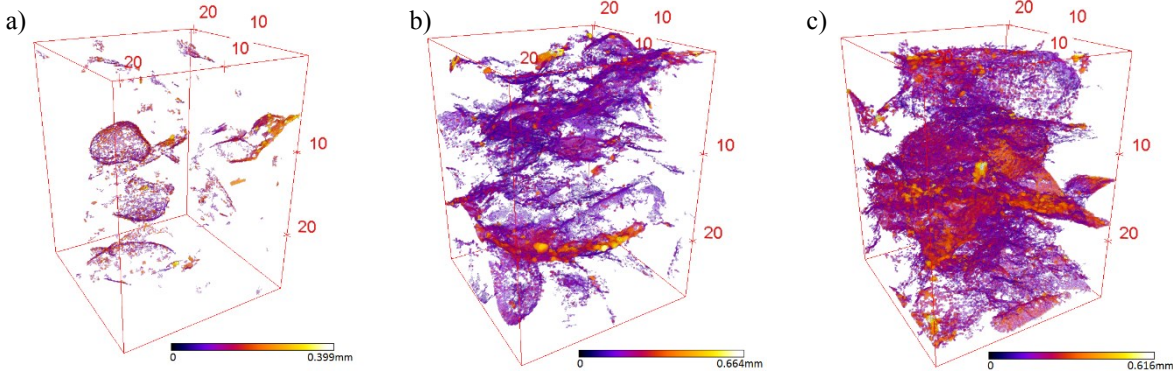


Figure 8-8 Microcrack width distribution in concretes with different binders: a) 0.30C-10/68-14, b) 0.30SF-10/68-14- (binder replica), c) 0.30S-10/68-14 based on local thickness measurements in BoneJ. Colour indicates microcrack width range.

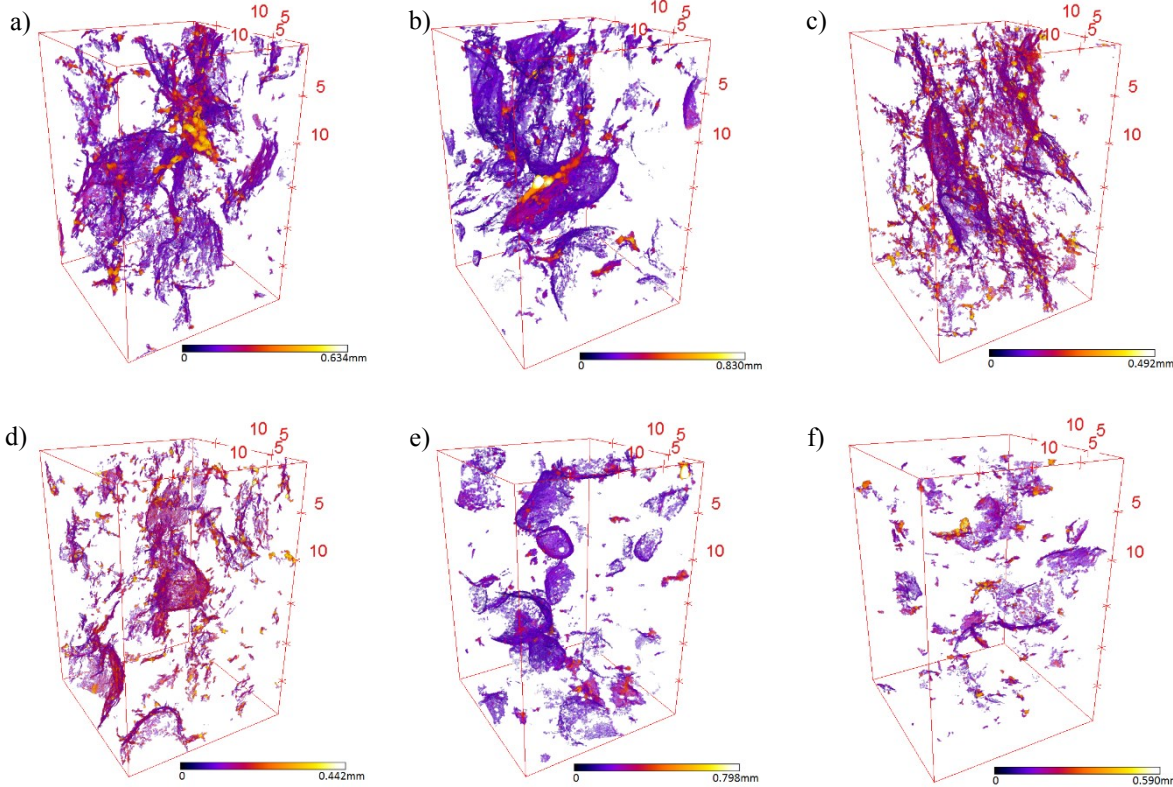


Figure 8-9 Microcrack width distribution in concretes with different water to binder ratios: a) 0.20SF-10/68-14, b) 0.25SF-10/68-14, c) 0.30SF-10/68-14- (w/b ratio replica), d) 0.35SF-10/68-14, e) 0.40SF-10/68-14 and f) 0.45SF-10/68-14 based on local thickness measurements in BoneJ. Colours indicates microcrack width range.

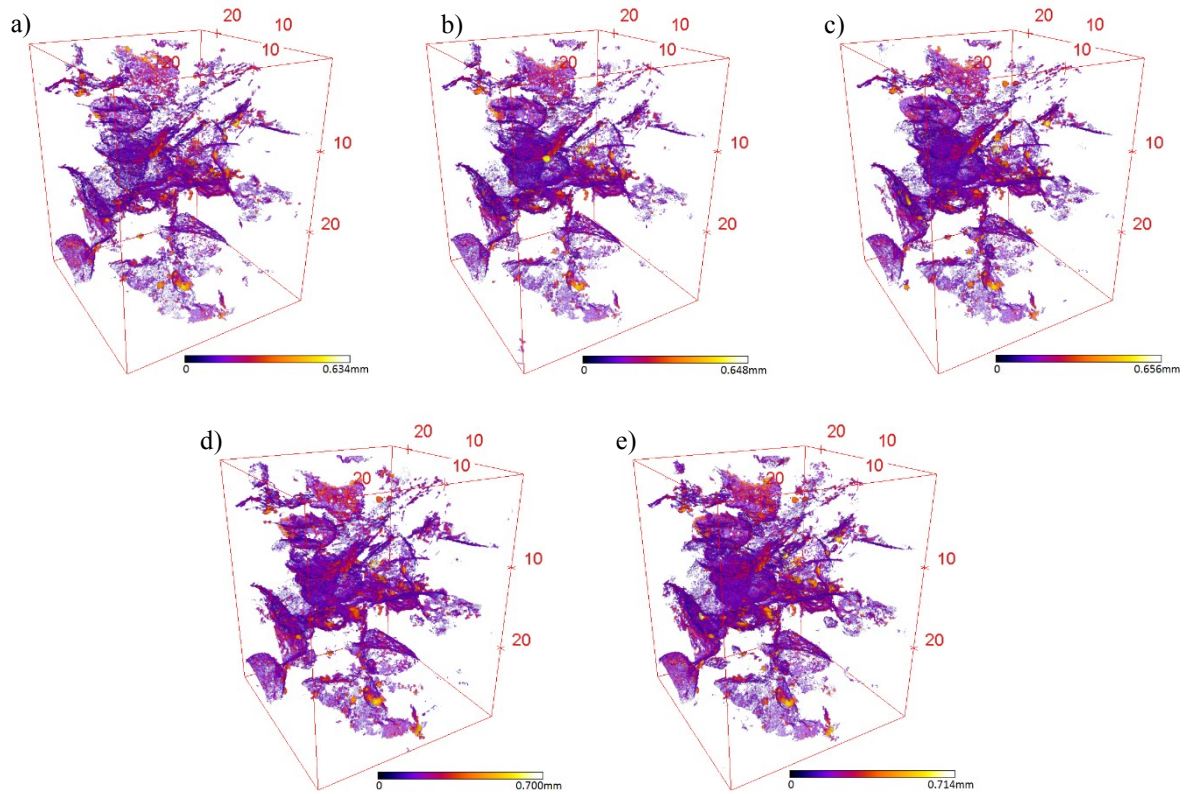


Figure 8-10 Microcrack width distribution in concretes at different age a) 0.30SF-10/68-1, b) 0.30SF-10/68-3, c) 0.30SF-10/68-7, d) 0.30SF-10/68-14-(age replica) and e) 0.30SF-10/68-28 based on local thickness measurements in BoneJ. Colour indicates microcrack width range.

	0.30C-10/68-14	0.30SF-10/68-14*	0.30S-10/68-14	0.20SF-10/68-14	0.25SF-10/68-14	0.30SF-10/68-14*	0.35SF-10/68-14	0.40SF-10/68-14	0.45SF-10/68-14	0.30SF-10/68-1	0.30SF-10/68-3	0.30SF-10/68-7	0.30SF-10/68-14*	0.30SF-10/68-28
W_{mean}	148	178	205	177	186	169	176	172	178	169	171	176	177	191
[μm]	±3.5	±5.2	±4.5	±5.1	±6.2	±4.2	±3.3	±5.1	±5.9	±5.2	±5.3	±5.5	±5.3	±5.5

Table 8-2 Average microcrack widths in μm with standard errors. (* - refers to relevant replicas).

From the measured local thickness of the microcracks, a volume-weighted mean thickness (i.e. microcrack average width) and the microcrack width distribution were estimated. The results are presented in Table 8-2 and Figure 8-11 respectively.

In general, Table 8-2 shows similar trends in the average microcrack width between the different samples to those obtained in the 2D analysis from LSCM in Chapter 7. The type of binder appears to be the most important influencing parameter for average microcrack width, in comparison to w/b ratio or concrete age. The highest average microcrack width with the value of 205 μm was found for concrete with GGBS (0.30S-10/68-

14) and the lowest average microcrack width with the value of 148 μm for neat Portland cement concrete (0.30C-10/68-14). Water to binder ratio does not appear to have a significant effect on the microcracks width, its average value oscillates around 175 μm . Furthermore, curing age has a slight impact on the microcracks width. The growth of microcracks with time is especially noticeable between 14th and 28th day, where the mean width increased by about 14 μm .

These tendencies are reinforced in Figure 8-11 showing the cumulative distribution of microcrack widths. It is clearly visible (Figure 8.11 -a) that microcracks in concretes with SCMs are wider than those in neat OPC concrete. The cumulative distribution curves for concretes with silica fume and GGBS are shifted towards larger values. Microcracks with widths below 100 μm represent 38%, 23% and 10% of the population for samples with neat OPC, 9% of silica fume and 70% of GGBS respectively, while microcracks with widths above 200 μm represent 7%, 20% and 35% of the population for samples with OPC, silica fume and GGBS respectively.

On the contrary, the cumulative distribution curves for samples with different w/b ratios practically overlap each other (Figure 8.11 -b). This highlights the insignificant correlation of microcrack widths with w/b ratio, which is consistent to the results obtained from 2D analysis in Chapter 7. The curves are very steep. Hence, most of the microcracks (approximately 70-80%) in these samples have widths in a narrow range of 100 - 200 μm . The same applies to samples analysed at different ages. However, here we observed a greater number of small microcracks (< 50 μm) of about 10% compared to the replicate samples which were drilled from a larger volume of concrete. This is probably due to the effect of directly casting concrete into a small cylindrical mould, which led to sample size effects on microcracking as discussed in detail in Chapter 7.

Moreover, the width of microcracks was also affected by the development of autogenous shrinkage with time. Evidence of that can be found by looking at the percentages of the smallest and the largest microcracks in the sample scanned over time. The amount of microcracks with crack width below 100 μm decreased continuously from 28%, 25%, 23%, 19% to only 12%, respectively in samples analysed at 1, 3, 7, 14 and 28 days, while for microcracks with crack width above 200 μm , their percentage increased gradually from 20%, 21%, 22%, 24% up to 30%, respectively in sample at 1, 3, 7, 14 and 28 days.

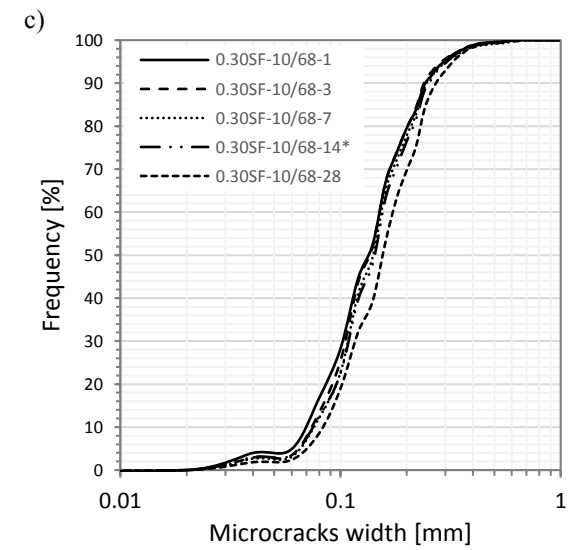
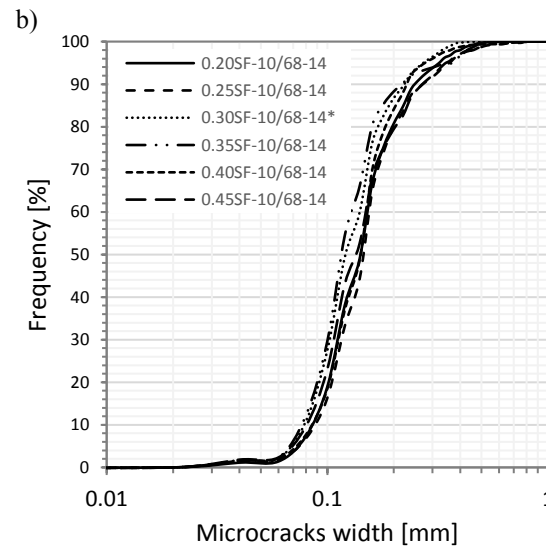
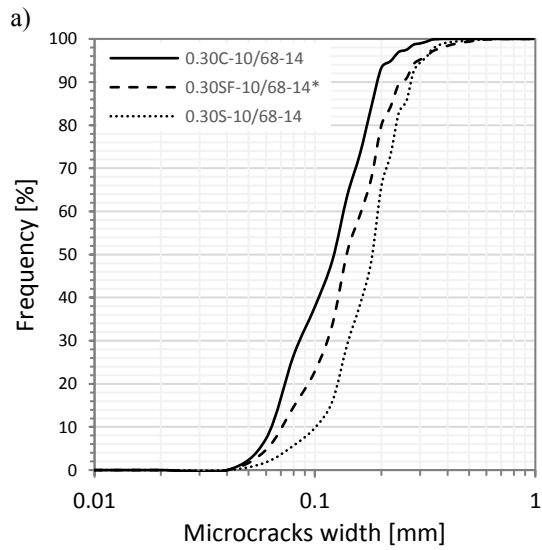


Figure 8-11 Cumulative width distribution of microcracks in concretes with different a) type of binder, b) w/c ratio and c) age. (* - refers to relevant replicas).

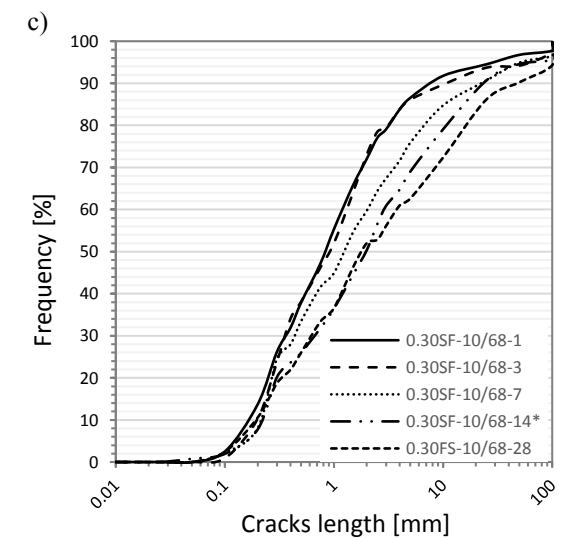
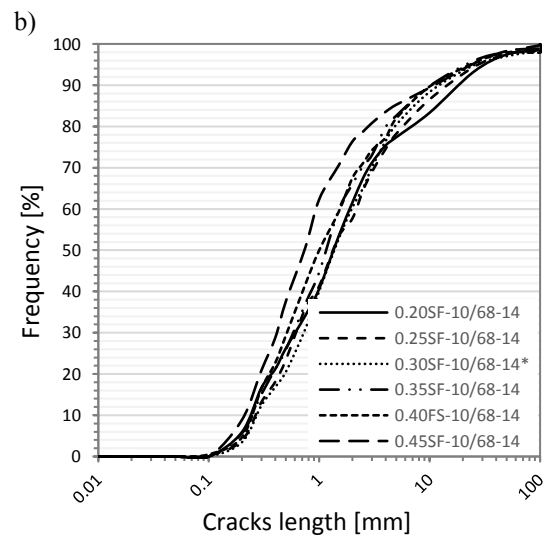
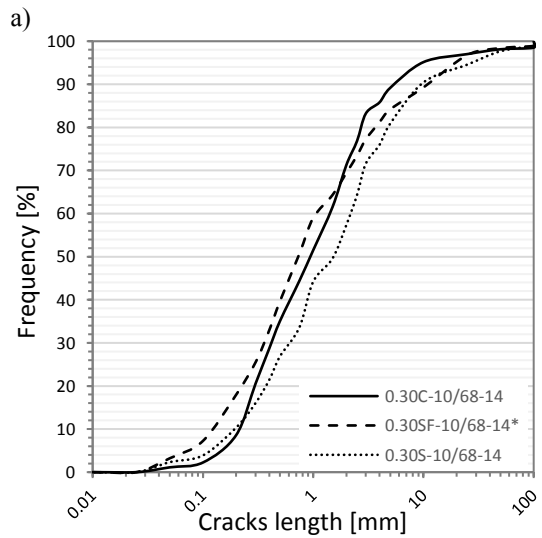


Figure 8-12 Cumulative length distribution of microcracks in concretes with different a) type of binder, b) w/c ratio and c) age. (* - refers to relevant replicas).

8.3.4 Length

Length of the microcracks (L) was measured as dendritic length of the 3D skeletonised microcracks and each measured value was used to calculate a mean length (L_{mean}) and to obtain the distribution of microcrack lengths. The 3D skeletons of microcracks were obtained by applying 3D thinning algorithm implemented in BoneJ (Lee et al., 1994) and the images of skeletonised microcracks are shown in Figure 8-13, 8-14 and 8-15 (Section 8.3.5). For full description of the methodology, please refer to Section 6.4.

Results from the analysis are presented in Table 8-3 (mean and total lengths) and in Figure 8-12 (crack length distributions) for samples with different binder type, w/b ratio and age respectively.

	0.30C-10/68-14	0.30SF-10/68-14*	0.30S-10/68-14	0.20SF-10/68-14	0.25SF-10/68-14	0.30SF-10/68-14*	0.35SF-10/68-14	0.40SF-10/68-14	0.45SF-10/68-14	0.30SF-10/68-1	0.30SF-10/68-3	0.30SF-10/68-7	0.30SF-10/68-14*	0.30SF-10/68-28
L_{mean} [mm]	5.9 ±2.0	17.8 ±7.6	29.4 ±25.0	15.0 ±7.6	13.6 ±5.4	11.0 ±5.0	10.5 ±2.9	9.9 ±4.2	5.5 ±1.2	16.2 ±7.5	17.1 ±12.2	27.5 ±14.2	25.3 ±15.5	26.0 ±18.6
L_{tot} [m]	1.67	6.51	11.6	6.45	6.25	6.23	4.30	3.17	1.62	7.14	7.21	8.11	8.86	9.41

Table 8-3 Average and total microcrack lengths in mm with standard errors.
(* - refers to relevant replicas).

The analysed microcracks have a wide range of lengths from 50 μm up to 100 mm. The average length is between 6 and 30 mm depending on sample type. Results show that microcracks in concrete with SCMs are much longer than in neat Portland cement. The average crack length is three times longer in samples with silica fume, and five times longer in samples containing GGBS, in comparison to neat Portland cement concrete. The average length of microcracks also increased with decrease in water to binder ratio from 5.5 mm at w/b = 0.45 to 15 mm at w/b = 0.20. The average length also increased with concrete age, the highest increase was observed between third and seventh day.

Further analysis of the length distribution shows that most of the microcracks (70-85% of the population) have lengths ranging from 0.2 mm to 10 mm. The sample with neat Portland cement has a very small population of microcracks longer than 10 mm (4.9%), while concretes with SCMs have twice as many of these microcracks, precisely 9.6% (OPC + SF) and 10.7% (OPC +GGBS). Microcracks that are shorter than 0.20 mm represent 8.6% of the population in samples with neat OPC and 10% in samples containing GGBS, while concrete with silica fume have up to 18% of these microcracks.

The length distribution curves (Figure 8-12 b, c) also indicate differences caused by water to binder ratio and concrete age. The lengths of microcracks increase with decrease in w/b ratio as seen by the slight translation of the distribution curves towards larger values. This is evident especially for w/b of 0.45, as this sample was the least affected by autogenous shrinkage and associated with microcracking. The percentage of microcracks longer than 5 mm increases from 14.7% to 17.4%, 18.0%, 19.6%, 21.8%, to 22.7% for samples with

w/b of 0.45, 0.40, 0.35, 0.30, 0.25 and 0.20, respectively. The increase in microcrack length is clearly visible for sample analysed at different ages. The crack length distribution curves show a substantial shift to larger values, apart from the early age samples (one and three days old) that had overlapping curves. The greatest change in crack lengths occurred in the first two weeks. The last curve (28 days old sample) does not diverge much from the curve of the 14 days old sample. This is evidence of microcracks propagating with time and its rate can be correlated to the development of autogenous shrinkage (see Section 7.3).

8.3.5 Density

Microcrack dendritic density was measured on the 3D skeletons of microcracks as ratio between total length of the skeleton to the image volume. Images of the skeletonised microcracks are presented in Figures 8-13, 8-14 and 8-15 for concretes with different binders, w/b ratios and curing ages respectively. These images clearly indicate that the type of binder and water to binder ratio have the greatest impact on microcrack density. However, concrete age has a less noticeable effect based on visual comparison.

The visual assessment is reinforced by quantitative image analysis presented in Figure 8-16. The highest microcrack density was measured in samples containing GGBS, followed by silica fume, while the sample with neat Portland cement had the lowest density, at 1.00, 0.62 and 0.14 mm/mm³ respectively. This corresponds to the results from linear deformation measurement, where concretes with SCMs showed much higher shrinkage compared to Portland cement concrete (see Section 7.3). Therefore, these samples were expected to crack more severely.

The measured microcrack density of concretes with very low w/b ratios of 0.20, 0.25 and 0.30 were consistent (ranging from 0.56 to 0.59 mm/mm³), but much higher than those at w/b ratios of 0.35, 0.40 and 0.45 (at 0.40, 0.29 and 0.15 mm/mm³ respectively). Samples with w/b of 0.20, 0.25 and 0.30 had very similar characteristics in terms of density and volume fraction of microcracks (as can be seen in Section 8.3.2). These results are also consistent with linear shrinkage measurements where large differences were seen between samples with different water to binder ratios.

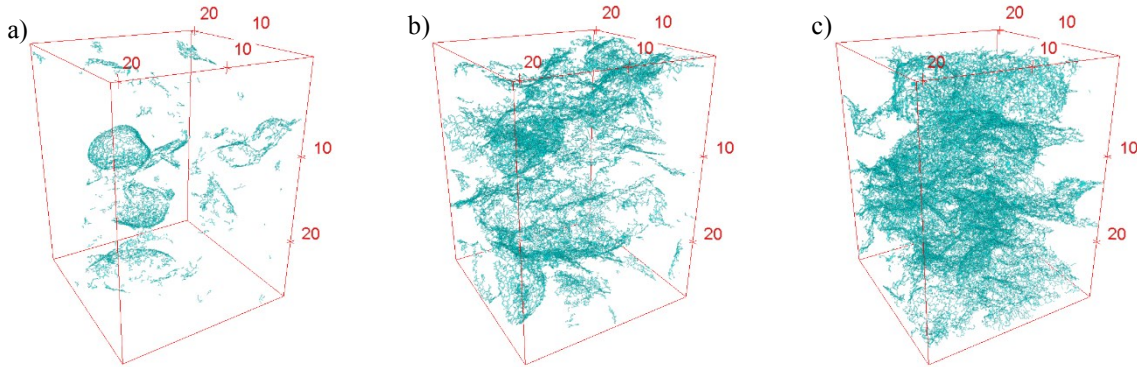


Figure 8-13 Skeleton of microcracks in concretes with different binders
a) 0.30C-10/68-14, b) 0.30SF-10/68-14- (binder replica), c) 0.30S-10/68-14.

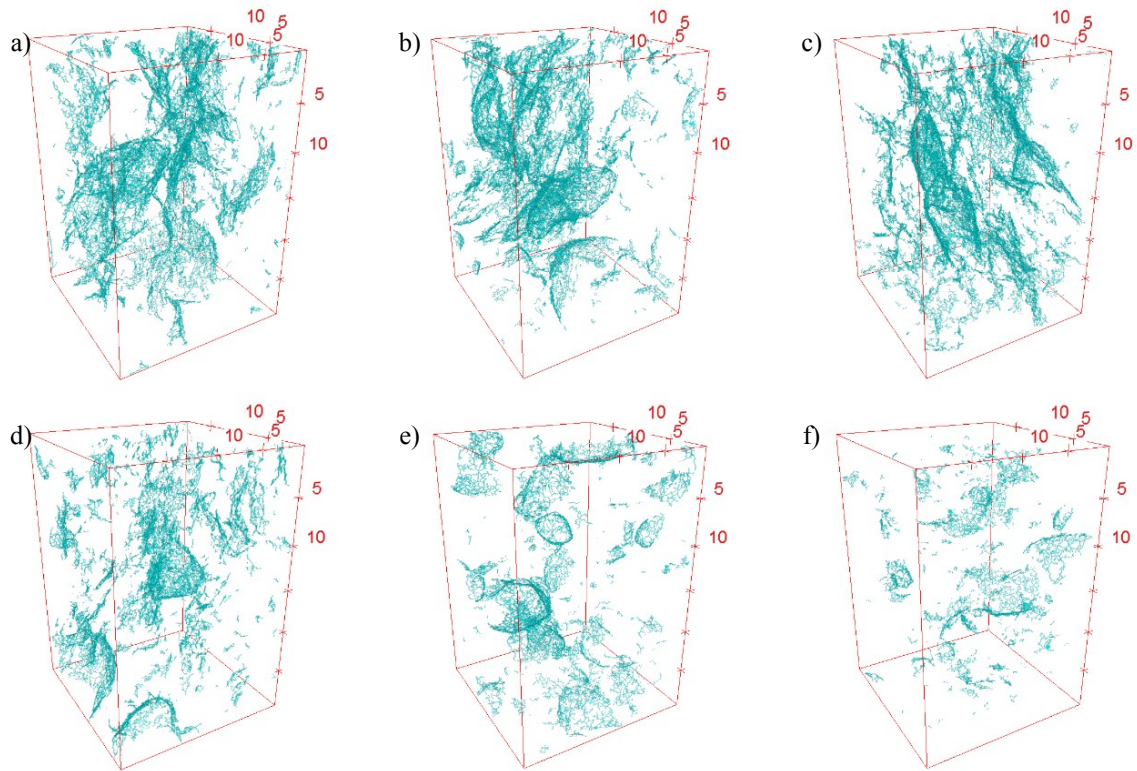


Figure 8-14 Skeleton of microcracks in concretes with different water to binder ratios: a) **0.20SF-10/68-14**, b) **0.25SF-10/68-14**, c) **0.30SF-10/68-14-** (w/b ratio replica), d) **0.35SF-10/68-14**, e) **0.40SF-10/68-14**, and f) **0.45SF-10/68-14**.

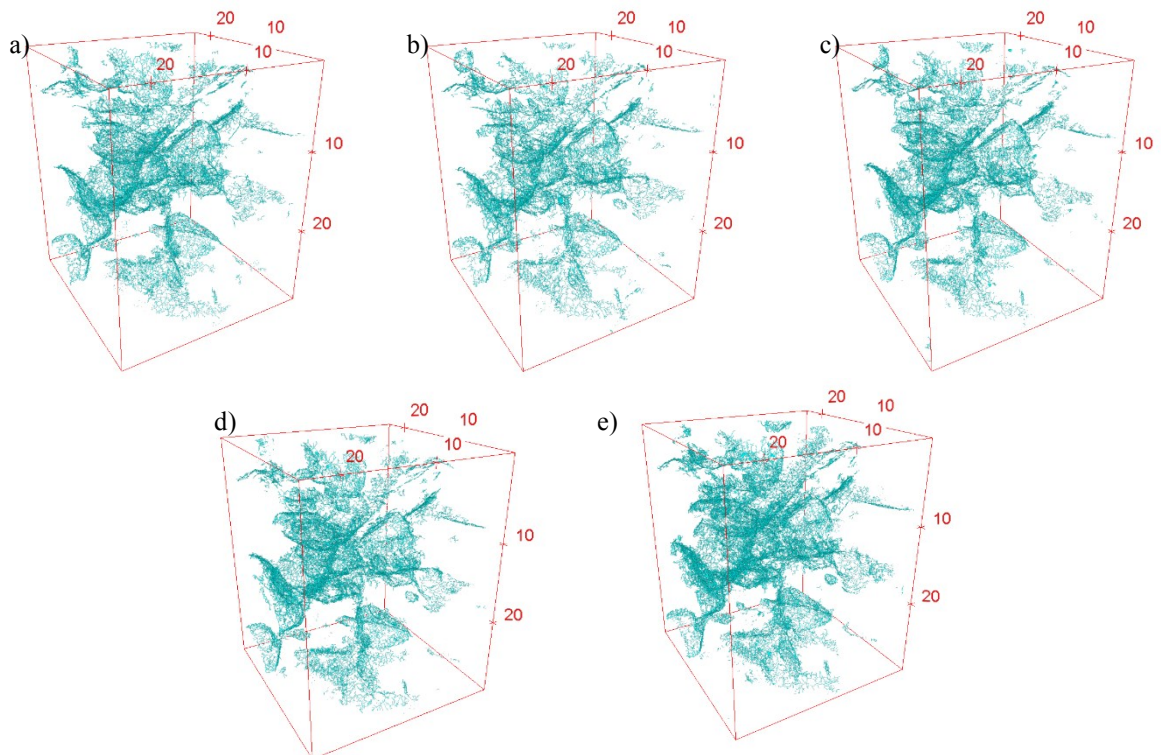


Figure 8-15 Skeleton of microcracks in concretes at different ages: a) **0.30SF-10/68-1**, b) **0.30SF-10/68-3**, c) **0.30SF-10/68-7**, d) **0.30SF-10/68-14-** (age replica) and e) **0.30SF-10/68-28**.

The results from measurements made at different ages demonstrate that development of microcracking occurs mainly in the first two weeks, which also confirms the findings from shrinkage measurements. Most of the microcracks formed in the first 24 hours. The total number of microcracks (labelled clusters) after the first day did not increase substantially in subsequent measurements. Thus, the microcracks were mainly branching with little tendency to form new, separated cracks at later stages. The microcrack density at age of 1, 3, 7, 14 and 28 days was 0.29, 0.33, 0.38, 0.45 and 0.49 mm/mm³ respectively, which correspond to shrinkage development over time (31.3 μ strain in the 1st day, increasing to 13.4, 45.9, 52.6 and 22.6 μ strain in the 3rd, 7th, 14th and 28th day, respectively).

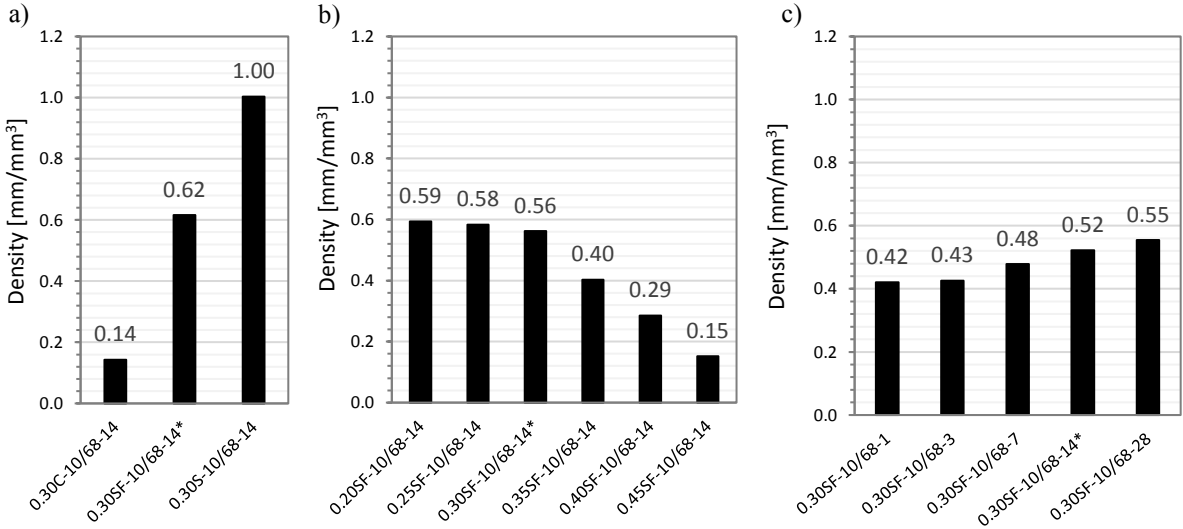


Figure 8-16 Dendritic density of microcracks in concretes with a) different binders, b) different water to binder ratios and c) at different ages. (*- refers to relevant replicas).

8.3.6 Degree of anisotropy

Degree of anisotropy of microcracks was estimated by application of the mean intercept length method (MIL) in 3D (see Section 6.4.3). The visualisation of microcrack orientation is presented in Appendix IV. These images present the 3D visualisation of the MIL vector cloud, shown in orthogonal views in the XY, XZ and YZ directions. Note that the X and Y axes are perpendicular to the casting direction. Additionally, the 2D orientation of microcracks at 0°, 45°, 90°, 135° angles in XY, XZ and YZ directions was determined (see Section 6.4.1 for detailed explanation). It is presented in the form of rose of intercepts (thick black lines) that matches the shape of the MIL vector cloud's orthogonal views.

Orientation of the microcracks varied quite significantly between different directions within the sample. On the XY orthogonal views, the microcracks in all samples seem to be uniformly oriented (isotropic structures). However, on the XZ and YZ orthogonal views they appear to have one privileged orientation usually towards 0-180° direction (on the XZ plane) and 90-270° direction (on the YZ plane). The orientation of microcracks within the volume may be related to sample size. Note that the shape of the moulds in which the samples were cast was cylindrical with a diameter of about 1.5 times the height of the mould for samples with different binders and w/b ratios (drilled samples) and with a diameter of about 0.5 times the height of the mould for samples scanned over

time (cast sample). Therefore, the autogenous shrinkage could be affected by these dimensions; from being uniform across the XY plane to being distorted along the Z-axis. Moreover, the orientation of aggregates as well as casting and compacting concrete mixes in layers may influence the microcrack orientation. However, the sample size effect seems to have the strongest influence on the orientation of microcracks.

The overall (3D) degree of anisotropy of microcracks which is a number between 0 (complete isotropy) and 1 (complete anisotropy), was above 0.6 for most of the samples (see Figure 8-17). Samples with degree of anisotropy lower than 0.6 experienced much less microcracking (e.g. samples: 0.30C-10/68-14, 0.40SF-10/68-14 and 0.45SF-10/68-14).

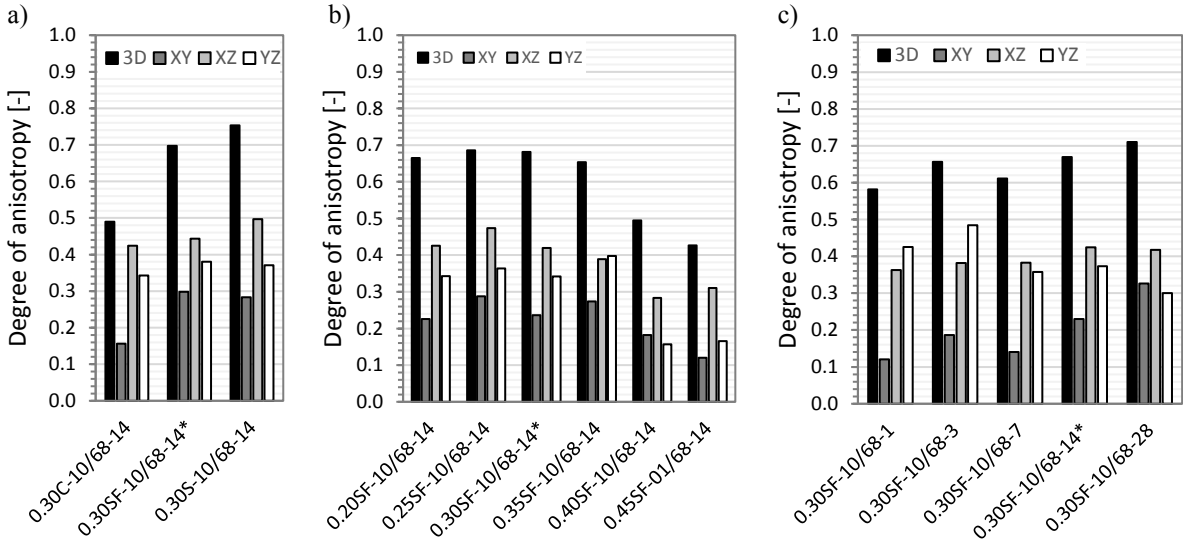


Figure 8-17 Degree of anisotropy of microcracks in concrete with different c) type of binder, b) w/b ratio and c) age. The results were calculated for the whole 3D volume and with 2D interpretation in XY, XZ and YZ.

8.3.7 Connectivity

Connectivity of microcracks was expressed in percentage of the volume of the largest interconnected microcrack over the total volume of all microcracks. In addition, the density of connections was measured as the number of junctions of the skeletonised microcracks divided by image volume. Results are shown in Figure 8-18 a), b) and c) for samples with different binders, w/b ratios and ages respectively. The results for connectivity show a large spread of values between samples with different binders (23 to 89%) and w/b ratios (3 to 54%). Connectivity increased substantially with the presence of SCMs and with decrease in w/b ratio. Similarly, the density of microcrack connections also show an increasing trend for samples with lower w/b ratio and samples containing SCMs. These clearly indicates that both the type of binder and w/b ratio influence the connectivity of microcracks, as these parameters in general have an impact on the degree of autogenous shrinkage-induced microcracking.

Connectivity of microcracks in samples scanned at different ages was rather constant, around 47%. However, the density of connections shows a significant increase with increase in age. This increase may be caused by formation of new microcracks and propagation and branching of already existing microcracks with

time. It may also indicate that the crack growth is uniform since the volume ratio of the largest microcrack to all microcracks was maintained throughout the experiment.

8.3.8 Tortuosity

Tortuosity of microcracks was determined by two parameters i.e. geometric tortuosity and centroid path tortuosity measured in X-, Y and Z- directions. These are defined in Section 6.4.1. Results from this analysis are presented in Figure 8-19 a, b and c for microcracks in concretes with different binders, various w/b ratio and age respectively. The geometric tortuosity of the microcracks is fairly uniform, approximately 1.28 for every sample. This is considered a low value ($\tau_g=1$ means that the structure is not tortuous, e.g. a straight pipe) and the findings indicate that autogenous induced microcracks have a fairly low tortuosity. Such results were caused by presence of a large number of short and relatively straight branches of the 3D skeletonised microcracks. Note that the geometric tortuosity was calculated as the sum of the length of the branches divided by the sum of their Euclidean lengths.

On the contrary, the centroid path tortuosity measurements showed more differential results not only between sample types, but also between the directions of the measurements. The reason is that the centroid path tortuosity is the ratio of the path formed by centroids of each 2D slice along one axis to the number of the 2D slices along that axis. Therefore, it is strongly related to the orientation of the microcracks. The more orientated microcracks (higher degree of anisotropy), the lower centroid path tortuosity. For instance, most of the samples exhibited the highest centroid path tortuosity in Z direction, which is consistent with the lowest degree of anisotropy on the XY planes, along z-axis.

Microcracks in concrete with SCMs, especially with GGBS were less tortuous than in pure Portland cement concrete. An increase of w/b ratio resulted in an increase of the centroid path tortuosity, and with age the centroid path tortuosity decreased. The differences between individual samples are strictly related to the quantity, distribution and orientation of microcracks. Samples that cracked more severely have lower tortuosity, because the path length through the computed centroids is shorter than in samples containing less microcracks. The obtained results are consistent with the degree of anisotropy, volume fraction and density results provided in Sections 8.3.6; 8-3-1 and 8-3-5.

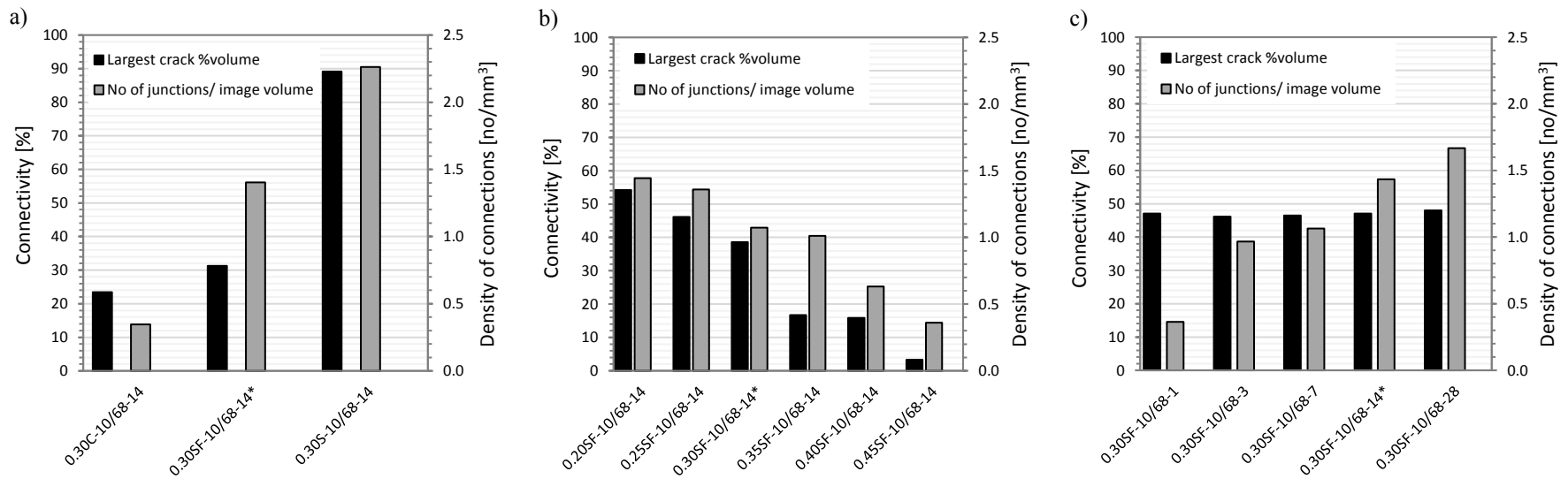


Figure 8-18 Connectivity of microcracks and density connections in concretes with different a) binders, b) w/b ratios and c) age. *- refers to relevant replicas.

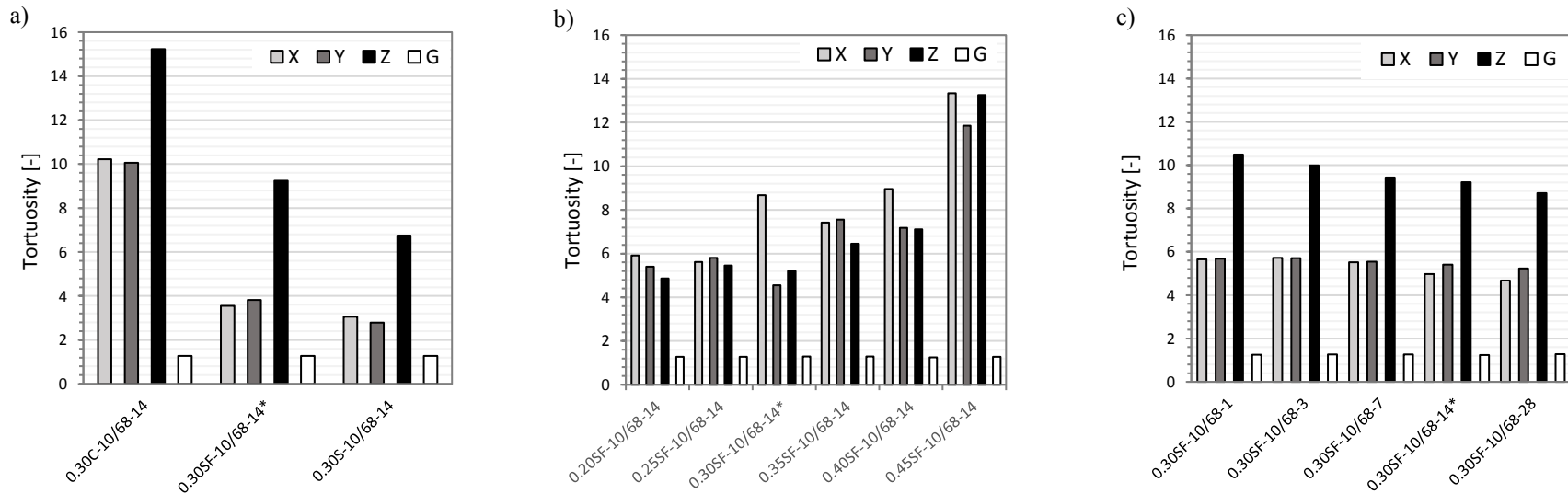


Figure 8-19 Geometric (G) and centroid path tortuosity along X-, Y- and Z- axes for concretes with different a) binders, b) w/c ratio and c) age. *- refers to relevant replicas

8.4 Statistical approach

An accurate image analysis of microcracks is very difficult to achieve. On the one hand, it is important to image a representative image volume at sufficient resolution, and this aspect was already discussed in Section 6.6. On the other hand, it is required to analyse a number of replicates to ensure adequate statistical analysis.

The statistical approach was demonstrated on three replicate samples (0.30SF-10/68-14* - binder, w/b ratio and age replicas). Note that the binder and w/b ratio replicas were drilled out of a larger volume (two cylinders of 95 mm in diameter and 65 mm height), while the age replica was directly cast into a small mould (a cylinder of 30 mm in diameter and 65 mm height). This could have an impact on the autogenous shrinkage development and consequently on the microcrack characteristics due to sample size effects.

Results from the measurements for all three replicas are tabulated in Table 8-4. Additionally, the average value and standard deviation for each parameter was calculated first for all three replicas (binder, w/b ratio and age) and then for cored replicas only (binder and w/b ratio).

Parameter	0.30SF-10/68-14*			Cored & cast replicas average	Cored & cast replicas st. dev.	Cored replicas average	Cored replicas st. dev.
	cored		Cast				
	binder replica	w/b ratio replica	age replica				
Volume fraction [%]	1.67	1.56	1.26	1.50	0.17	1.62	0.05
Density [mm/mm ³]	0.62	0.56	0.52	0.57	0.04	0.59	0.03
Specific surface area (LICM) [mm ⁻¹]	21.24	23.57	21.62	22.14	1.02	22.41	1.17
Surface density (LICM) [mm ⁻¹]	0.35	0.37	0.27	0.33	0.04	0.36	0.01
Average width [μm]	178	169	177	174.67	4.03	173.50	4.50
Average length [mm]	17.8	11	25.3	18.03	5.84	14.40	3.40
Total length [m]	6.51	6.23	8.86	7.20	1.18	6.37	0.14
Degree of anisotropy [-]	0.697	0.682	0.669	0.680	0.01	0.690	0.01
Connectivity [%]	31.24	38.57	47.08	38.96	6.47	34.91	3.67
No of junction/image volume [no/mm ³]	1.40	1.07	1.43	1.30	0.16	1.24	0.17
Tortuosity [-]	1.27	1.29	1.24	1.27	0.02	1.28	0.01

Table 8-4 Characteristics of microcracks in three replicate samples (binder, w/b ratio and age replicas) and averages with standard deviations of the measured parameters.

The results between replicate samples are very similar for all measurements, therefore the standard deviations are low, especially for cored samples. Noticeable differences might be observed for parameters such as volume fraction, microcrack length (average and total values) and connectivity between cored and cast replicas. However, as mentioned earlier, this could be associated with sample size effect on microcracking. Such influences were also observed in the 2D image analysis (see Section 7.4 for more details).

8.5 Comparison between 2D image analysis (LSCM and μ -CT) and 3D image analysis (μ -CT)

Each imaging technique, whether 2D or 3D image analysis, has its advantages and limitations over the others. This study gives an excellent opportunity to demonstrate them because the same sample sets were imaged with two different techniques (LSCM – Section 7.4 and μ -CT – Section 8.3) and the image analysis of microcracks was carried out in 2D (images from LSCM and μ -CT) and in 3D (images from μ -CT). The differences between 2D and 3D analysis were discussed in Chapter 6.5.1. Here, further discussion of results from 2D analysis of microcracks acquired with LSCM are presented. The comparison was made on three samples (0.30C-10/68-14, 0.30SF-10/68-14 and 0.30S-10/68-14). These samples were selected because they have the most diversified characteristics of microcracks among all the analysed samples. Results from the analysis are tabulated in Table 8-5.

			0.30C-10/68-14	0.30SF-10/68-14*	0.30S-10/68-14
Volume (area) fraction	μ -CT	3D	0.28 %	1.67 %	3.28 %
		2D	0.28 %	1.67 %	3.28 %
	LSCM	2D	1.62 %	1.79 %	2.08 %
Surface area: SSA/SD (LICM)	μ -CT	3D	27.12/ 0.07 mm ⁻¹	21.24/ 0.35 mm ⁻¹	18.27/ 0.60 mm ⁻¹
		2D	4.89/ 0.01 mm ⁻¹	6.98/ 0.12 mm ⁻¹	8.10/ 0.27 mm ⁻¹
	LSCM	2D	9.27/ 0.15 mm ⁻¹	8.85/ 0.16 mm ⁻¹	7.88/ 0.16 mm ⁻¹
Average Width	μ -CT	3D	148 μ m	178 μ m	205 μ m
		2D	179 μ m	263 μ m	283 μ m
	LSCM	2D	38 μ m	50 μ m	70 μ m
Average Length	μ -CT	3D	5.925 mm	17.756 mm	29.439 mm
		2D	1.166 mm	2.475 mm	4.122 mm
	LSCM	2D	0.161 mm	0.194 mm	0.174 mm
Density	μ -CT	3D	0.14 mm/mm ³	0.62 mm/mm ³	1.00 mm/mm ³
		2D	0.02 mm/mm ²	0.10 mm/mm ²	0.18 mm/mm ²
	LSCM	2D	0.42 mm/mm ²	0.36 mm/mm ²	0.30 mm/mm ²
Degree of anisotropy	μ -CT	3D	0.49	0.70	0.75
		2D	0.16 XY, 0.42 XZ, 0.34 YZ	0.30 XY, 0.44 XZ, 0.38 YZ	0.28 XY, 0.50 XZ, 0.37 YZ
	LSCM	2D	0.34	0.37	0.36
Connectivity (C ₁ and D _{CN})	μ -CT	3D	23.41 %/ 0.35	31.24 %/ 1.40	89.12 %/ 2.26
		2D	N/A	N/A	N/A
	LSCM	2D	N/A	N/A	N/A
Tortuosity (τ_g and τ_{CP})	μ -CT	3D	1.28/ 10.22 x, 10.06 y, 15.23 z	1.27/ 3.55 x, 3.81 y, 9.24 z	1.27/ 3.06 x, 2.78 y, 6.75 z
		2D	N/A	N/A	N/A
	LSCM	2D	N/A	N/A	N/A

Table 8-5 Comparison of microcrack analysis using different methods: 3D (μ -CT), 2D (μ -CT) and 2D (LSCM) of three selected samples (0.30C-10/68-14, 0.30SF-10/68-14* - binder replica and 0.30S-10/68-14).

There are three values for each characteristic parameter of microcracks: the first value from 3D analysis of the whole image volume acquired with μ -CT, the second value from a 2D interpretation of the same image (as a stack of 2D images, where each 2D slice of the 3D image was analysed), and third value from 2D analysis of image montage (stitched mosaic of 2D images) conducted on the same concrete mix, but not particularly on the same samples imaged with LSCM. Thus, any differences between the first two values are associated only to the effect of interpreting the analysed image volumes in 2D or 3D. On the contrary, the measured parameters in both 2D analyses (the second and third values) might vary for three reasons: a) differences in image sampling area; b) higher resolution of the LSCM technique that can detect finer microcracks compared to μ -CT; and c) sample preparation prior to LSCM imaging may have introduced artificial microcracks as explained in Section 3.3.1 – reference sample. However, contribution of these microcracks to the total area fraction of microcracks should be smaller than 6% ($A_A=0.07\%$ for reference sample), see Section 3.3.1.

The comparison of values from different analyses reported here has yielded several noteworthy results. Most of these results (three values for the same parameter) varied to some extent depending on the imaging technique and image analysis approach. There is only one parameter i.e. volume fraction from 3D analysis of μ -CT image and its 2D correspondent – area fraction from 2D analyses of μ -CT image which has exactly the same value. The area fraction obtained from LSCM imaging are generally higher due to the higher detectability of very small microcracks (higher resolution of the LSCM technique). An exception was the sample containing GGBS (0.30S-10/68-14) which had slightly lower area fraction compared to results from μ -CT imaging. This is because microcracks in samples with slag were wider and therefore better resolved by μ -CT. Another explanation can be simply related to sampling issue. It must be noted that only one core was analysed and slight differences in measurement between replicate samples could occur as demonstrated in Section 8.4. Thus, several cores drilled from different regions of the same sample should be analysed from a statistical point of view.

Due to the better resolution of the LSCM technique, surface area expressed as specific surface area (SSA) and surface density (SD) are slightly higher in 2D LSCM compared to 2D μ -CT, apart from GGBS sample owing to the factors explained above. Comparing 3D analysis versus 2D analysis, it is observed that 3D surface areas (SSA or SD) are much higher than corresponding values measured as 2D projections of three-dimensional structures.

Analysing sample cross-sections (2D analysis) rather than sample volumes (3D analysis) produces a substantial effect on the measured crack width and length. The average width of microcracks measured with the same method (the local thickness measurement) is of about 20-45% higher in 2D compared to 3D analysis of the same μ -CT images. Even more evident is the disparity in microcrack length measurements, where the average crack length is about 80-90% lower in 2D compared to corresponding 3D analysis. Such differences were not unexpected since 2D analysis measures only some fragments of microcracks, while real three-dimensional structures are separated into many shorter and often wider cracks depending on the orientation of microcracks to the slicing direction. Moreover, 2D analysis of LSCM images gave several times lower values for both average microcrack width and length due to its higher resolution and better detectability of the smallest microcracks. The average crack width is of about 4-5 times smaller than those from μ -CT measurements, while the average length is about one order of magnitude shorter. These findings show that 2D analysis methods produce misleading results and are unreliable for microcrack width and length measurements.

The density of microcracks as a parameter related to its dendritic length is affected by the skeletonisation algorithm, which gives different results in 2D and 3D. The actual length of microcracks, and consequently their density, are underestimated in 2D because the skeletonisation processes are performed only on one plane (e.g. x-y plane) without any insights in the third dimension (z-direction). Furthermore, in samples that were imaged with LSCM, the 2D density of microcracks is much larger compared to the corresponding samples imaged with μ -CT. This is again caused by the lower resolution of X-ray microtomography, which limits its ability to resolve the smallest microcracks.

Degree of anisotropy of microcracks is a very controversial parameter, especially when measured in 2D. As can be seen from the 2D analysis of μ -CT images (Table 8-5), microcracks can have a privileged orientation and their degree of anisotropy may vary with the direction of analysis, from very low near-zero values (e.g. XY plane) where it can be assumed that the microcracks are strongly isotropic structures, to relatively high values (e.g. XZ), where such an assumption is completely incorrect. In the case of LSCM imaging, the image analysis is usually performed on one randomly selected cross-section, here represented by the YZ plane. Such one directional analysis is not reliable regardless of the technique used to acquire the images for analysis. Under these circumstances the only accurate results will be given by the 3D analysis, for which the degree of anisotropy is much higher than each of the directional measurements.

Another advantage of the 3D analysis over the 2D analysis is the capability of measuring parameters such as connectivity and tortuosity of microcracks, which are essential for understanding and modelling mass transport processes. Thereby, μ -CT as a three-dimensional imaging technique is more advantageous despite the much higher resolution of the LSCM conventional 2D imaging.

8.6 Summary

The overall trends of the measured 3D parameters are summarised in Table 8-6, where a colour code indicates increasing (red), decreasing (green) and no changing (yellow) tendencies. These results are consistent with those obtained from the 2D analysis of LSCM images reported in Chapter 7 (Table 7-6), even though the data are not directly comparable due to the fact, that different analysis approaches and imaging techniques were involved in the characterisation of the autogenous shrinkage induced microcracking. The severity of microcracking was primarily influenced by the greater development of autogenous shrinkage in samples with SCMs compared to neat Portland cement samples. Presence of silica fume and GGBS increase volume fraction and density of microcracks, especially in the case of GGBS. The microcracks formed were wider and much longer and have greater connectivity. However, parameters such as tortuosity and degree of anisotropy of the microcracks were not substantially affected by the type of binder.

A much higher degree of microcracking was also observed in samples with lower water to binder ratio. Concretes with w/b ratio of 0.20 and 0.25 were the most severely damaged (highest volume fraction and density of microcracks). The degree of microcracking (as measured from volume fraction and density) gradually decreases with increasing w/b ratio to 0.40 and 0.45, where the microcracking was the least severe. Apart from volume fraction and density of microcracks, their length and connectivity significantly decreased with increase in w/b ratio. However, parameters such as microcrack width and geometric tortuosity was practically not

affected by w/b ratio (stable results for all samples) while other parameters such as degree of anisotropy decreased only for higher w/b ratio (w/b 0.40 and 0.45) and centroid path tortuosity increased with an increase in w/b ratio. The 3D analysis shows that most of the microcracking develops during the first two weeks and this is consistent with the results from linear autogenous shrinkage development and 2D analysis of microcracks in Chapter 7. The possibility of monitoring microcrack growth in the same concrete core at different ages, which is enabled by using non-destructive 3D imaging technique, gave some interesting observations. In particular, the large number of microcracks formed within the first 24 hour (0.98% volume fraction). This increased to 1.26% and 1.37% after two and four weeks respectively, which are relatively small increments compared to the one-day result. Therefore, it is questionable whether the measured shrinkage at one day old samples, which was about 30 μ strain (for 0.30SF-10/68-1, see Section 7.3), could cause such damage. In contrast, the measured shrinkage for one and two-week old samples were about three to five times greater than the one-day values. This could be due to the uncertainty with defining and errors with measuring the initial sample length at time “zero”. It is not possible to determine shrinkage in the time between casting and final setting of the concrete because the sample is too weak and fragile for length measurement. Therefore, the shrinkage that developed during that time was not considered. Nevertheless, the results show how crucial the first 24 hours is for the development of microcracking in samples without proper curing. Other parameters besides volume fraction change over time, which indicates that once formed the microcracks tend to branch and grow, in addition to generation of new microcracks. This is supported by the increase in the density, width, length and number of connection of microcracks measured at later ages.

	Binder type	w/c ratio	Age [days]
	C»SF»S	0.20»0.25»0.30»0.35»0.40»0.45	1»3»7»14»28
V_V			
W			
SSA			
SD			
D_D			
L			
DA			
C			
D_{CN}			
τ_g			
τ_{CP}			

Table 8-6 Overall trends of the measured parameters indicated by colour codes.
 V_V – volume fraction, W – crack width, SSA – specific surface area, SD – surface density,
 D_D = dendritic density, L – crack length, DA – degree of anisotropy, C – connectivity,
 D_{CN} – density of connection, τ_g – geometric tortuosity, τ_{CP} – centroid path tortuosity.

Colour code: increase, decrease, no change.

Chapter 9

9.1 Conclusions

This thesis shows the difficulties and challenges associated with 3D imaging and image analysis of microcracks in cement-based materials. On the one hand, 3D characterisation of microcracks in concrete is highly desirable for better understanding of transport processes and long-term durability of cement-based materials. On the other hand, existing 3D imaging techniques that could detect the whole range of microcracks ($1\mu\text{m} < \text{crack width} < 1\text{mm}$) in a representative volume of concrete do not exist. Thus far, this topic has been overlooked by researchers.

One of the aim of this thesis was to apply and further develop 3D imaging techniques such as FIB-nt, BIB-SEM, LSCM and μ -CT for 3D imaging and quantification of microcracks induced in a laboratory environment. Unfortunately, the existing 3D imaging techniques are unable to achieve simultaneously the spatial resolution and image volume required for meaningful characterisation of the 3D microcrack network.

FIB-nt is able to achieve 3D imaging at nanometre resolution, but the imaging plane and imaging depth are limited to a volume of few tens of μm^3 . Extending the imaging plane by BIB polishing could overcome this, but still there are limitations on the imaging depth, poor Z-resolution, the time consuming and costly BIB irradiation of new layers. Because of the restricted image volume, none of the two techniques should be considered as potential tools for 3D imaging of microcracks in cement-based materials.

Conventional imaging with LSCM is able to achieve 3D images at submicron resolution, but limited to a few microns imaging depth. Therefore, a new method that combines serial sectioning with LSCM to extend the imaging depth of cement-based materials was proposed in this thesis. The method produces a series of Z-stacks containing overlapping regions for stitching based on phase correlation. It can also be extended in the XY plane to further increase the overall image volume. The method was tested to build up a reconstruction of microcracked concrete with imaging plane of $700 \times 700 \mu\text{m}^2$ and up to a $165 \mu\text{m}$ in depth at XY and Z resolutions down to $\sim 0.2 \mu\text{m}$ and $\sim 0.5 \mu\text{m}$ respectively. However, it must be pointed out that this method is very tedious and time consuming because of the repetitive process of sectioning, imaging and reconstruction that will be needed. Therefore, the method is not yet ideal and practical for imaging large volumes of microcracked concrete.

The image volume issue is completely resolved by using X-ray microtomography. This technique can image wide range of sample sizes from hundreds of μm^3 to hundreds of mm^3 , depending on the type of the μ -CT scanner. However, the sample size strongly affects the achievable resolution (voxel size = $1/2000$ sample size for modern CT scanners), which requires a thoughtful compromise between both requirements.

The experimental review of existing 3D imaging techniques presented in this thesis not only discloses their limitations, but also shows their advantages in potential applications to study various microstructural aspects of cement-based materials. For example, the proposed method of combining serial sectioning and LSCM fills the gap between X-ray μ -CT and FIB-nt in terms of spatial resolution and image volume and may be used for example for characterising pore structure of cement-based materials (Yio et al., 2017, 2019). The X-ray microtomography instead could be used to characterise air voids or aggregates shape in concrete. Such application (air voids characterisation) was further discussed in this work. An algorithm for extracting air voids from the 3D image and quantification tools was proposed that can be easily applied in related works.

Moreover, the fluorescence LSCM is ideal for real-time imaging of cement-based materials for example, for monitoring of water penetration into a microcracked concrete as shown in Figure 9-1. In this short experiment, a fluorescein sodium-dyed water was applied from one direction and the appearance of fluorescence in the pores and cracks was imaged. This can be quantified by means of image analysis to help understand how microcrack and pore structure contribute to water ingress at pore-scale level.

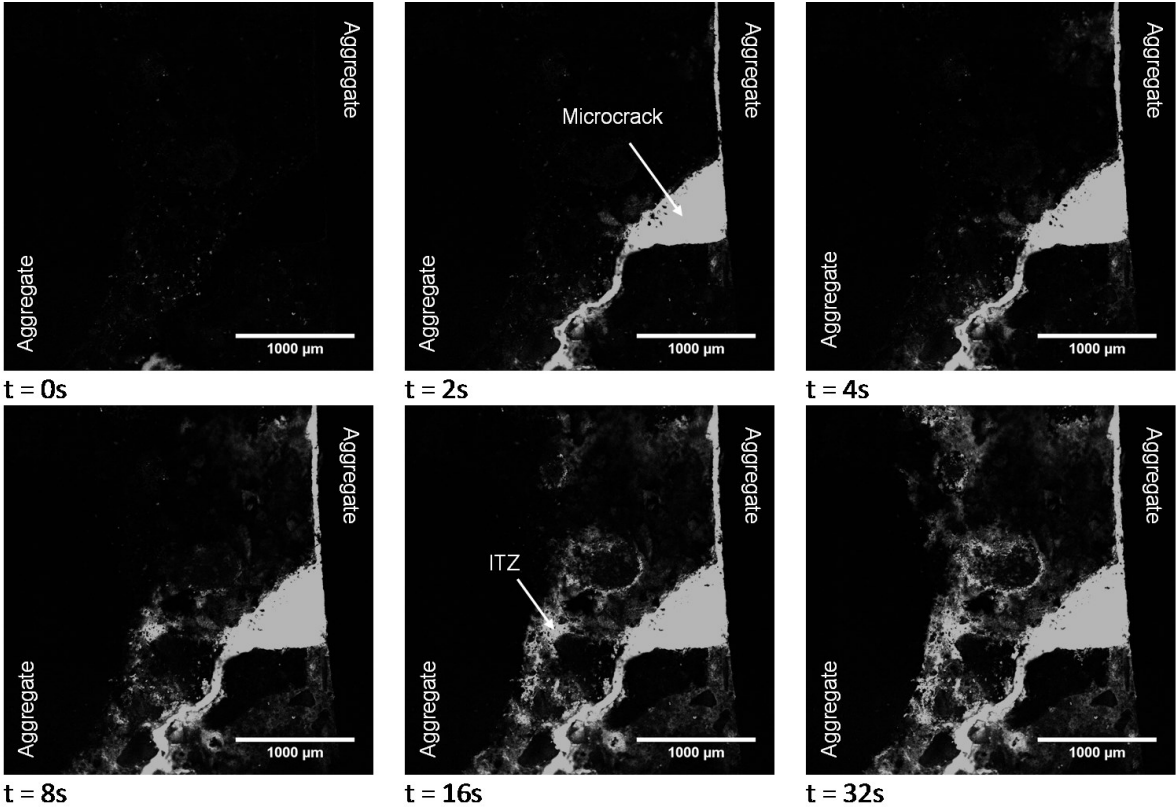


Figure 9-1 Demonstration of fluorescence LSCM for real-time imaging of water penetration into a microcracked concrete subjected to cyclical freezing and thawing (in collaboration with Marcus Yio).

In this thesis, large sample volumes (cylinders $\text{Ø}30\text{mm}$ and 30mm in height) were scanned with μ -CT scanner, but at lower resolution (voxel size of $15.5 \mu\text{m}$). This brings the question of whether the size range of the detectable microcracks is sufficient and whether the imaged volume is sufficiently large for representative image analysis of the microcracks. This of course, depends on the type of microcracks and their morphology, in other words, the phenomenon that caused the concrete to crack. This made the thesis even more challenging because

there are so many physical and chemical processes that may lead to microcracking. Several ways of introducing microcracks to cementitious samples were tested to find the most realistic approach in a laboratory environment conditions. This in fact is a difficult task since many real structures are subjected to more complex exposure environments and deterioration processes. From the approaches examined i.e. drying shrinkage with internal and external restrained (different regime of oven drying), frost attack (cycles of freezing and thawing) and autogenous shrinkage (sealed curing of low water to binder ratio concretes), the latter was chosen for more detailed study.

Autogenous shrinkage is an inherent attribute to every cement-based material. However, the lower water to binder ratio, the higher the development of autogenous shrinkage and consequently, the potential risk of microcracking. High autogenous shrinkage leads to internal cracking, while drying shrinkage is associated mainly with surface cracking or cracking through when the concrete structure is externally restrained. Therefore, not only the characteristic parameters of microcracks, but also their localization (internal/ surface cracking) within concrete members may influence mass transport properties of concrete and its ultimate failure. For this reason, internal cracking should be a primary concern. The assessment of different crack-inducing tactics helps to visualise how the localization of microcracks is affected by the origin of its formation and thereby endorses the decision to focus on autogenous shrinkage induced microcracks in this work.

Besides finding the proper imaging technique and the relevant microcracks, image analysis either in 2D and 3D was also a very demanding task. This is due to the fact that microcracks appear to have to share similar grey scale intensities with other porous features (pores in aggregates, air voids, capillary pores) in the image brightness histogram. The overlapping grey scale intensity means that additional steps are required during image processing to facilitate separation of microcracks from such features. An algorithm to achieve this was developed in this work. Moreover, quantification measurements enabling extensive analysis of the characteristic parameters of microcracks were proposed. The developed image processing algorithm and quantification tools were applied to 3D images of all microcracked samples throughout this thesis.

The 3D images acquired by X-ray microtomography were analysed twice; firstly, as a whole volume (3D analysis) and secondly, as a stack of image planes, slice by slice (2D analysis). Comparison of results obtained with such different interpretations highlighted some well-known, but also some unexpected conclusions. In general, it is known that the 3D analysis has the advantage over 2D analysis in characterising microcrack connectivity and tortuosity, but other parameters such as volume fraction, 3D density, crack width, crack length and orientation were estimated based on 2D results. The present work proved that this is true for volume fraction and crack width, but other parameters particularly crack length and 3D orientation does not give inter-changeable results. Crack length is significantly shortened in 2D comparing to 3D interpretations and orientation of microcracks can be directional within the volume, which is difficult to observe on a 2D image, giving rise to misleading results.

Another concern related to the representative elementary volume (REV) for characterising microcracks and air voids in concrete was also discussed. This was pursued using a 'statistical' approach, where every microcrack and air void parameter was measured in a range of image volumes. Each subsequent image volume was 10% smaller than the previous image volume. The results showed that most of the measured parameters achieved stable values for image volumes above approximately $14.1 \times 14.1 \times 17.4 \text{ mm}^3$, which was 70% of the

original volume of the analysed image. An exception was spacing factor of air voids, and the width and length of microcracks. Further analysis on larger quantity of samples and perhaps using a larger sample size would be required to confirm these findings. If a smaller sample size gives representative results, a higher image resolution could be achieved whilst scanning and thereby a better detection of the smallest microcracks could be obtained. Nevertheless, this REV serves as a lower limit only since microcracks are prone to larger-scale heterogeneities.

In this thesis, a wide range of concrete samples were prepared and subjected to autogenous shrinkage by means of sealed curing. These samples were varied in binder type, water to binder ratio, age, maximum aggregate size and aggregate fraction, which gives a complex study of the influence of concrete mix design on autogenous shrinkage induced microcracking. In the first step, 2D LSCM was used in conjunction with linear deformation measurement to study the influence of each variable on the development of autogenous shrinkage and associated microcracking. In the next step, X-ray microtomography was applied to selected samples based on the results from 2D analysis.

Generally, good correlations were observed between 2D and 3D values of characteristic parameters of microcracks measured from LSCM and X-ray microtomography. However, direct comparison is not possible for two reasons. First, with LSCM much higher resolution was achieved compared to μ -CT. This allowed the detection of microcracks from 1 μm in width, while for μ -CT images, microcracks below 50 μm (i.e. $\sim 3 \times$ voxel size) were difficult to be resolved. Second, results from 2D and 3D analyses are not necessarily interchangeable and the 2D approach leads to a misleading interpretation of results for some parameters.

All samples prepared in this thesis exhibited microcracking. The degree of microcracking consistently increased with the decrease in water to binder ratio. Although microcracks were not avoided in samples prepared with higher w/b ratio of 0.45 and 0.40, there were far less microcracking compared to samples with w/b ratio of 0.35 – 0.20. Second crucial parameter influencing the degree of microcracking was type of the binder. Samples containing silica fume (SF) and GGBS (S) showed an increase in severity of microcracking compared to neat Portland cement concretes. The same trends were observed both in 2D and 3D analyses. It also agrees with the magnitude of linear deformation measurements. Additionally, these shrinkage measurements over time highlighted that most of the microcracks were produced in the first two weeks after casting.

Furthermore, the maximum aggregates size (MSA) and aggregate content were found to considerably influence the parameters of microcracks, particularly their length and width. Generally, samples with large MSA and low aggregate content produced wider and longer microcracks. In contrast, sample size had a lesser impact on the results. Nevertheless, samples cast in cylinders of 25 mm in diameter showed less severe microcracking than those cast in $\text{\O}50$ mm and $\text{\O}95$ mm, which had similar microcrack parameters.

It is interesting to note that these parameters: low water to binder ratio, use of SCMs (particularly silica fume), low aggregate content and aggregate size of 10/20 mm are incorporated in mix design for high performance concrete (HPC). This means that such concretes will struggle with early age microcracking and potentially other associated risks such as acceleration of mass transport via the presence of inter-connected, well-distributed microcrack networks.

9.2 Recommendations for further research

As future work, it would be worthwhile to assess the impact of microcracking on long-term durability. This could be achieved for example by using the obtained data as an input for modelling the contribution of microcracks to transport processes. It is also strongly recommended to link the measured microcrack characteristics with mass transport properties, especially in long-term experiments. A thorough understanding of this is important to ensure that the desire to achieve superior strength performance does not compromise long-term durability and service life of structures in aggressive environments. To answer this question, for instance, measurement of oxygen permeability, oxygen diffusivity, water sorptivity, chloride diffusivity, carbonation resistance and electrical conductivity should be performed and correlated to microcrack characteristics. Ideally, cracked and non-cracked samples should be investigated to isolate the effect of microcracks. Otherwise, the transport processes will be also affected by the pore structure. Decoupling and isolating the influence of microcracks and pore structure will require a combined multi-phase and multi-scale approach.

References

- ABYANEH, S. D., WONG, H. S. & BUENFELD, N. R. (2016). Simulating the effect of microcracks on the diffusivity and permeability of concrete using a three-dimensional model. *Computational Materials Science*, 119, 130-143.
- ABYANEH, S. D., WONG, H. S. & BUENFELD, N. R. (2013). Modelling the diffusivity of mortar and concrete using a three-dimensional mesostructure with several aggregate shapes. *Computational Materials Science*, 78, 63-73.
- AÏTCIN, P. C. (1998). *High Performance Concrete*, 1st Edition, E & FN Spon, London
- AMIN, M. N., KIM, J. S., DAT, T. T. & KIM, J. (2010). Improving test methods to measure early age autogenous shrinkage in concrete based on air cooling. Part A: *Civil and Structure Engineering*, 4, 244–256.
- AMMOUCHE, A., BREYSSE, D., HORNAIN, H., DIDRY, O. & MARCHAND, J. (2000). A new image analysis technique for the quantitative assessment of microcracks in cement based-materials. *Cement and Concrete Research*, 30(1), 25-35.
- ASTM-C1581/C1581M. Determining Age at Cracking and Induced Tensile Stress Characteristics of Mortar and Concrete under Restrained Shrinkage.
- BARCELO, L., BOIVIN, S., RIGAUD, S., ACKER, P., CLAVAUD, B. & BOULAY, C. (1999). Linear vs. volumetric autogenous shrinkage measurement: Material behaviour or experimental artefact? *Proceedings of the 2nd International Research Seminar on Self-desiccation and its Importance in Concrete Technology*, June 18, Lund, Sweden, 109-125.
- BARTLETT, J. D., JAANUS, S. D., FISCELLA, R., HOLDEMAN, N. & PROKOPICH, C. (2008). *Clinical ocular pharmacology*, St Louis, Missouri, Butterworth-Heinemann Elsevier.
- BASHEER, L., KROPP, J. & CLELAND, D. J. (2001). Assessment of the durability of concrete from its permeation properties: a review. *Construction and Building Materials*, 15(2-3), 93-103.
- BENTZ, D. P. (2007). Internal Curing of High Performance Blended Cement Mortars. *ACI Materials Journal*, 104(4), 408-414.
- BISSCHOP, J. & VAN MIER, J. G. M. (2002). How to study drying shrinkage micro-cracking in cement-based materials using optical and scanning electron microscopy? *Cement and Concrete Research*, 32(2), 279-827.
- BISSCHOP, J. & WITTEL, F. K. (2011). Contraction gradient induced microcracking in hardened cement paste. *Cement and Concrete Research*, 33(4), 466-473.
- BISSCHOP, J. (2002). *Drying shrinkage microcracking in cement-based materials*. Delf University Press.
- BISSCHOP, J., LURA, P. & VAN MIER, J. (2002). Shrinkage microcracking in cement-based materials with low water-cement ratio. PRO 23: EAC'01: *International RILEM Conference on Early Age Cracking in Cementitious Systems*, 79-88.
- BISSONNETTE, B., PIERRE, P. & PIGEON, M. (1999). Influence of key parameters on drying shrinkage of cementitious materials. *Cement and Concrete Research*, 29(10), 1655-1662.
- BLUNT, M. J., BIJELJIC, B., DONG, H., GHARBI, O., IGLAUER, S., MOSTAGHIMI, P., PALUSZNY, A. & PENTLAND, C. (2013). Pore-scale imaging and modelling. *Advances in Water Resources*, 51, 197-216.
- BONEJ: <http://bonej.org>
- BS 882: 1992 Specification for aggregates from natural sources for concrete

BS EN 12620: 2002 + A1: 2008 Aggregates for concrete

BS EN 934 – 2: 2009 +A1: 2012 Admixtures for concrete, mortar and grout. Concrete admixtures. Definitions, requirements, conformity, marking and labelling.

BUENFELD, N. R., ZOBEL, M., ZIMMERMAN, R. W. & WONG, H. S. (2009). Influence of the interfacial transition zone and microcracking on the diffusivity, permeability and sorptivity of cement-based materials after drying. *Magazine of Concrete Research*, 61(8), 571-589.

BURLION, N., BERNARD, D. & CHEN, D. (2006). X-ray microtomography: Application to microstructure analysis of a cementitious material during leaching process. *Cement and Concrete Research*, 36(2), 346-357.

CAMP, J. J., HANN, C. R., JOHNSON, D. H., TARARA, J. E. & ROBB, R. A. (1997). Three-dimensional reconstruction of aqueous channels in human trabecular meshwork using light microscopy and confocal microscopy. *Scanning*, 19(4), 258-263.

CASTLEMAN, K.R. (1996). *Digital image processing*. Prentice Hall, Englewood Cliffs.

CEN/TR 15177: 2006 Testing the freeze-thaw resistance of concrete - Internal structural damage.

CHENA, X. T., DAVYA, C. A., SHAO, J. F. & SKOCZYLAS, F. (2010). Experimental and micro-mechanical analysis of the mechanical and transport properties of mortar containing heat-induced micro-cracks. *Cement and Concrete Composites*, 32(9), 678-85.

CHIAIA, B., VAN MIER, J. G. M. & VERVUURT, A. (1998). Crack growth mechanisms in four different concretes: microscopic observations and fractal analysis. *Cement and Concrete Research*, 28(1), 103-114.

COLLIER, N. C., SHARP, J. H., MILESTONE, N. B., HILL, J. & GODFREY, I. H. (2008). The influence of water removal techniques on the composition and microstructure of hardened cement pastes. *Cement and Concrete Research*, 38(6), 737-744.

COSTER, M. & CHERMANT, J. L. (2001). Image analysis and mathematical morphology for civil engineering materials. *Cement and Concrete Composites*, 23(2-3), 133-151.

CRAEYE, B., GEIRNAERT, M. & DE-SCHUTTER, G. (2011). Super absorbing polymers as an internal curing agent for mitigation of early-age cracking of high-performance concrete bridge decks - review. *Construction and Building Materials*, 25(1), 1-13.

DAVIS, H.E. (1940). Autogenous volume changes of concrete, American Society for Testing Materials, ASTM, proceedings 32(40), 1103-1112.

DESBOIS, G., URAI, J. L. & KUKLA, P. A. (2009). Morphology of the pore space in claystone's – evidence from BIB/FIB ion beam sectioning and cryo-SEM observations. *e-Earth*, 4, 15-22.

DESBOIS, G., URAI, J. L., HOUBEN, M. E. & SHOLOKHOVA, Y. (2010). Typology, morphology and connectivity of pore space in claystones from reference site for research using BIB, FIB and cryo-SEM methods. 14th International Conference on Experimental Mechanics, EPJ Web of Conferences, 6, 22005(1-6).

DESBOIS, G., URAI, J. L., PÉREZ-WILLARD, F., RADI, Z., OFFERN, S., BURKART, I., KUKLA, P. A. & WOLLENBERG, U. (2013). Argon broad ion beam tomography in a cryogenic scanning electron microscope: a novel tool for the investigation of representative microstructures in sedimentary rocks containing pore fluid. *Journal of Microscopy*, 249(3), 215-235.

DOROZHKIN, S.V. (2010). Bioceramics of calcium orthophosphates. *Biomaterials*, 31(7), 1465-1485.

DOUBE, M., KŁOSOWSKI, M. M., ARGANDA-CARRERAS, I., CORDELIÉRES, F., DOUGHERTY, R. P., JACKSON, J., SCHMID, B., HUTCHINSON, J. R. & SHEFELBINE, S. J. (2010). BoneJ: free and extensible bone image analysis in ImageJ. *Bone*, 47(6), 1076-1079.

- DOUGHERTY, R. & KUNZELMANN, K. (2007). Computing local thickness of 3D structures with ImageJ. *Microscopy and Microanalysis*, 13(S02), 1678-1679.
- EFFORD, N. (2000). *Digital Image Processing: A Practical Introduction Using Java™*. Pearson Education.
- FICKER, T., MARTIŠEK, D., & JENNINGS, H. M. (2010). Roughness of fracture surfaces and compressive strength of hydrated cement pastes, *Cement and Concrete Research*, 40(6), 947-955.
- FIJI/ ImageJ: <http://fijisc/Fiji>
- GALLÉ, C. (2001). Effect of drying on cement-based materials pore structure as identified by mercury intrusion porosimetry: a comparative study between oven-, vacuum-, and freeze-drying. *Cement and Concrete Research*, 31(10), 1467–1477.
- GALLUCCI, E., SCRIVENER, K., GROSO, A., STAMPANONI, M. & MARGARITONDO, G. (2007). 3D experimental investigation of the microstructure of cement pastes using synchrotron X-ray microtomography (μ CT). *Cement and Concrete Research*, 37(3), 360-368.
- GARBOCZI, E. J. & BULLARD, J. W. (2004). Shape analysis of a reference cement. *Cement and Concrete Research*, 34(10), 1933-1937.
- GHANBARIAN, B., HUNT, A. G., EWING, R. P. & SAHIMI, M. (2013). Tortuosity in porous media: A critical review. *Science Society of America Journal*, 77(5), 1461-1477.
- GIANNUZZI, L. A. & STEVIE, F. A. (2005). *Introduction to Focused Ion Beams - Instrumentation, Theory, Techniques and Practice*. Springer.
- GLASBEY, C. A. (1993). An analysis of histogram-based thresholding algorithms. *CVGIP: Graphical Models and Image Processing*, 55(6), 532-537.
- GOLTERMANN, P. (1995). Mechanical Predictions of Concrete Deterioration. Part 2: Classification of Crack Patterns. *ACI Materials Journal*, 92(1), 58-63.
- GRASSL, P., WONG, H. S. & BUENFELD, N. R. (2010). Influence of aggregate size and volume fraction on shrinkage induced micro-cracking of concrete and mortar. *Cement and Concrete Research*, 40(1), 85-93.
- GRIT/COLLECTION STITCHING: http://fijisc/Grid/Collection_Stitching_Plugin.
- GUAYASAMIN, A. S. V. (2015) Influence of autogenous shrinkage on mass transport properties of concrete. Msc. Thesis from Imperial College London, Department of Civil and Environmental Engineering.
- HAMMER, T. A., BJØNTEGAARD, Ø. & SELLEVOLD, E. J. (2002). Early age cracking in cementitious systems. Report of RILEM Technical Committee TC 181-EAS. Measurement methods for testing of early age autogenous strain. Section 6.2, 207-217.
- HAN, J., SUN, W., PAN, G., WANG, C. & RONG, H. (2012). Application of X-ray computed tomography in characterization microstructure changes of cement pastes in carbonation process. *Journal of Wuhan University of Technology – Materials Science Edition*, 27(2), 358-63.
- HANEHARA, S., HIRAO, H. & UCHIKAWA, H. (1999). Relationship between autogenous shrinkage and the microstructure and humidity changes at inner part of hardened cement pastes at early ages. *Proceeding International Workshop Autoshrink'98*, ed. E.-I. Tazawa, Hiroshima, Japan, E & FN SPON, London, 89-100.
- HARRIGAN, T. P. & MANN, R. W. (1984). Characterization of microstructural anisotropy in orthotropic materials using a second rank tensor. *Journal of Materials Science*, 19, 761-767.
- HEAD, M. K. & BUENFELD, N. R. (2006). Confocal imaging of porosity in hardened concrete. *Cement and Concrete Research*, 36(5), 896-911.

- HEAD, M. K., WONG, H. S. & BUENFELD, N. R. (2006). Characterisation of 'Hadley' grains by confocal microscopy. *Cement and Concrete Research*, 36(8), 1483-1489.
- HEAD, M. K., WONG, H. S. & BUENFELD, N. R. (2008). Characterising aggregate surface geometry in thin-sections of mortar and concrete. *Cement and Concrete Research*, 38(10), 1227-1231.
- HILDEBRAND, T. & RÜEGSEGG, P. (1997). A new method for the model-independent assessment of thickness in three-dimensional images. *Journal of Microscopy*, 185(1), 67-75.
- HOLZER, L., FLATT, R. J., ERDOĞAN, S. T., BULLARD, J. W. & GARBOCZI, E. J. (2010). Shape comparison between 0.4–2.0 and 20–60 μm cement particles. *Journal of the American Ceramic Society*, 93(6), 1626-1633.
- HOLZER, L., GASSER, P. H., KAECH, A., WEGMANN, M., ZINGG, A., WEPF, R. & MUENCH, B. (2007). Cryo-FIB-nanotomography for quantitative analysis of particle structures in cement suspensions. *Journal of Microscopy*, 227(3), 216-228.
- HOLZER, L., MUNCH, B., WEGMANN, M. & GASSER, P. H. (2006). FIB-Nanotomography of Particulate Systems – Part I: Particle Shape and Topology of Interfaces. *Journal of the American Ceramic Society*, 89(8), 2577-2585.
- HRNČIŘ, T., LOPOUR, F., ZADRAŽIL, M., JIRUŠE, J., DELOBBE, A., SALORD, O., ET AL. (2012). Novel plasma FIB/SEM for high speed failure analysis, 3D tomography and other applications. ISTFA Conference Proceedings from the 38th International Symposium for Testing and Failure Analysis. November 11-15, Phoenix, Arizona, USA, 26-38.
- HSIEH, J. (2009). *Computed Tomography - Principles, Design, Artifacts, and Recent Advances*. SPIE.
- HU, Z., SHI, C., CAO, Z., OU, Z., WANG, D., WU, Z., & HE, L. (2013). A review on testing methods for autogenous shrinkage measurements of cement-based materials. *Sustainable Cement-Based Materials*, 2(2), 161-171.
- HUANG, Y. & KLETTE, R. (2004). A comparison of property estimators in stereology and digital geometry. 10th International Workshop of Combinatorial Image Analysis (IWCIA 2004), Lecture Notes in Computer Science, 3322, 421-431.
- HUO, X. S. & WONG, L. U. (2006). Experimental study of early-age behaviour of high performance concrete deck slabs under different curing methods. *Construction and Building Materials*, 20(10), 1049-1056.
- IDIART, A. E., LOPEZ, C. M. & CAROL, I. (2011). Modeling of drying shrinkage of concrete specimens at the meso-level. *Materials and Structures*, 44, 415-435.
- IDIART, A., BISSCHOP, J., CABALLERO, A. & LURA, P. (2012). A numerical and experimental study of aggregate-induced shrinkage cracking in cementitious composites. *Cement and Concrete Research*, 2012(42), 272-281.
- IGARASHI, S., BENTUR, A. & KOVLER, K. (2000). Autogenous shrinkage and induced restraining stresses in high-performance concretes. *Cement and Concrete Research*, 30(11), 1701-1707.
- JACOBS, L. J. & WHITCOMB, R. W. (1997). Laser generation and detection of ultrasound in concrete. *Journal of Non-destructive Evaluation*, 16(2), 57-65.
- JACOBSEN, S., MARCHAND, J. & BOISVERT, L. (1996). Effect of cracking and healing on chloride transport in OPC concrete. *Cement and Concrete Research*, 26(6), 869-881.
- JENSEN, O. M. & HANSEN, P. F. (1996). Autogenous deformation and change of the relative humidity in silica fume-modified cement paste. *ACI Materials Journal*, 93(6), 539-543.

- JIANG, C., YANG, Y., WANG, Y., ZHOU, Y. & MA, C. (2014). Autogenous shrinkage of high performance concrete containing mineral admixtures under different curing temperatures. *Construction and Building Materials*, 61, 260-269.
- KESNER, K., SANSALONE, M. & POSTON, R. W. (2004). Detection of distributed damage in concrete using transient stress waves. *ACI Materials Journal*, 101(4), 318-326.
- KURDOWSKI, W. (2002). Chloride corrosion of concrete. *Cement Wapno Beton*, 7/69(2), 56-60.
- KURTIS, K. E., EL-ASHKAR, N. H., COLLINS, C. L. & NAIK, N. N. (2003). Examining cement-based materials by laser scanning confocal microscopy. *Cement and concrete composites*, 25, 695-701.
- LANDIS, E. N., ZHANG, T., NAGY, E. N., NAGY, G. & FRANKLIN, W. R. (2006). Cracking, damage and fracture in four dimensions. *Materials and Structures*, 40(4), 357-364.
- LANGE, D. A., JENNINGS, H. M. & SHAH, S. P. (1993). Relationship between fracture surface roughness and fracture behaviour of cement paste and mortar. *Journal of the American Ceramic Society*, 76(3), 589-597.
- LAUNEAU, P. & ROBIN, P. Y. F. (1996). Fabric analysis using the intercept method. *Tectonophysics*, 267(1-4), 91-119.
- LEE, T. C., KASHYAP, R. L. & CHU, C. N. (1994). Building skeleton models via 3-D medial surface axis thinning algorithms. *CVGIP: Computer Vision Graphical Models and Image Processing*, 56(6), 462-478.
- LEE, T. P. (1992). *Deterioration mechanisms*. Chapter 2. E&FN Spon
- LITROWICZ, A. (2006). Identification and quantification of cracks in concrete by optical fluorescent microscopy. *Cement and Concrete Research*, 36(8), 1508-1515.
- LORENSEN, W. E. & CLINE, H. E. (1987). Marching cubes: A high resolution 3D surface construction algorithm. In *Proceedings of the 14th annual conference on Computer Graphics and Interactive Techniques*, Association for Computing Machinery, 163-169.
- LU, S., LANDIS, E. N. & KEANE, D. T. (2006). X-ray micro tomographic study of pore structure and permeability in Portland cement concrete. *Materials and Structures*, 39(6), 611-620.
- LURA, P. (2003). *Autogenous deformation and internal curing of concrete*. Delf University Press, PhD thesis.
- LURA, P., JENSEN, O. M. & VAN BREUGEL, K. (2003). Autogenous shrinkage in high-performance cement paste: An evaluation of basic mechanisms. *Cement and Concrete Research*, 33(2), 223-232.
- LURA, P., JENSEN, O. M. & WEISS, J. (2009). Cracking in cement paste induced by autogenous shrinkage. *Materials and Structures*, 42(8), 1089-1099.
- MARCHAND, J., PLEAU, R. & GAGNÉ, R. (1995). *Deterioration of concrete due to freezing and thawing*. Materials Science of Concrete, Vol. IV, American Ceramic Society, Westerville, OH, 283-354.
- MARION, A. (1991). *Introduction to Image Processing*. Springer, 1st Edition, 283-244.
- MAUKO, A., MUCK, T. & MLADENOVIC A. (2009). 3D visualization and quantification of bowing marble microstructure. *Construction and Building Materials*, 23(6), 2380-2385.
- MERKLE, A. & GELB, J. (2013). The ascent of 3D X-ray microscopy in the laboratory. *Microscopy Today*, 21(02), 10-5.
- MEYER, M. D., WATSON, L. S., WALTON, C. M. BOARD, SKINNER, R. E. J., ET AL. (2006). *Control of Cracking in Concrete - State of the Art*. Transportation Research Circular E-C107. Transportation Research Board of the National Academies.

- MIRCEA, C. (2009). Overview upon restrained shrinkage cracking of RC structures. Proceedings of the 3rd International Conference on Concrete Solutions, Padua, Italy, 22-25 June, Concrete Solutions, Taylor & Francis Group, London, 172-177.
- MORIOKA, M., HORI, A., HAGIWARA H. & SAKAI, E. D. M., (1999). Measurements of autogenous length changes by laser sensors equipped with digital computer system. Autogenous Shrinkage of Concrete. E. Tazawa, ed., Taylor & Francis Group, London & New York.
- MUNCH, B. & HOLZER, L. (2008) Contradicting Geometrical Concepts in Pore Size Analysis Attained with Electron Microscopy and Mercury Intrusion. *Journal of the American Ceramic Society*, 91(12), 4059-4067.
- MUNCH, B., GASSER, P. H. & HOLZER, L. (2006). FIB-Nanotomography of Particulate Systems – Part II: Particle Recognition and Effect of Boundary Truncation. *Journal of the American Ceramic Society*, 89(8), 2568-2595.
- MUNCH, B., TRTIK, P., MARONE, F. & STAMPANONI, M. (2009). Stripe and ring artefact removal with combined wavelet - Fourier filtering. *Optics Express*, 17(10), 8567-8591.
- NAIK, N. N., JUPE, A. C., STOCK, S. R., WILKINSON, A. P., LEE, P. L. & KURTIS, K. E. (2006) Sulphate attack monitored by micro-CT and EDXRD: Influence of cement type, water-to-cement ratio, and aggregate. *Cement and Concrete Research*, 36(1), 144-159.
- NEVILLE, A. M. (1995). *Properties of Concrete*. 5th Edition. Pearson Education Limited, Essex, England.
- NEVILLE, A.M. & AİTCIN, P. C. (1998). High performance concrete – An overview. *Materials and Structures*, 31(2), 111-117.
- NGUYEN, T. T. (2015). Modeling of complex microcracking in cement-based materials by combining numerical simulations based on a phase-field method and experimental 3D imaging. PhD Thesis from University of Luxembourg.
- NICHOLS, A. B. & LANGE, D. A. (2006). 3D surface image analysis for fracture modeling of cement-based materials. *Cement and Concrete Research*, 36(6), 1098-1107.
- ODGAARD, A. (1997). Three-dimensional methods for quantification of cancellous bone architecture. *Bone* 20, 315-328.
- OHTSU, M., SHIGEISHIA, M. & SAKATA, Y. (1998). Non-destructive evaluation of defects in concrete by quantitative acoustic emission and ultrasonics. *Ultrasonics*, 36(1-5), 187-195.
- OUYANG, C., LANDIS, E. N. & SHAH, S. (1991). Damage Assessment in Concrete Using Quantitative Acoustic Emission. *Journal of Engineering Mechanics*, 117(11), 2681-2698.
- PAWLEY, J. B. (1995). *Handbook of biological confocal microscopy*. Springer.
- PD-CEN/TR-15177:2006. Testing the freeze-thaw resistance of concrete. Internal structural damage.
- PETFORD, N., DAVIDSON, G. & MILLER, J. (2001). Investigation of the petrophysical properties of a porous sandstone sample using confocal scanning laser microscopy, *Petroleum Geoscience*, 7, 99-105.
- PIGEON, M., MARCHAND, J. & PLEAU, R. (1996). Frost resistant concrete. *Construction and Building Materials*, 10(5), 339-348.
- POWERS, T. C. (1949) The air requirement of frost-resistant concrete. *Proc. Highway Res. Board* 29, 184-202.
- PREIBISCH, S., SAALFELD, S. & TOMANCAK, P. (2009). Globally optimal stitching of tiled 3D microscopic image acquisitions. *Bioinformatics*, 25(11), 1463-1465.

- PREWITT, J. M. & MENDELSON, M. L. (1966). The analysis of cell images. *Annals of the New York Academy of Sciences*, 128(3), 1035-1053.
- PROMENTILLA, M. A. B. & SUGIYAMA, T. (2010). X-Ray Microtomography of Mortars Exposed to Freezing-Thawing Action. *Journal of Advanced Concrete Technology*, 8(2), 97-111.
- PROMENTILLA, M. A. B., SUGIYAMA, T., HIOTOMI, T. & TAKEDA, N. (2008). Characterizing the 3D pore structure of hardened cement paste with Synchrotron microtomography. *Journal of Advance Concrete Technology*, 6(2), 273-286.
- REN, W., YANG, Z., SHARMA, R., McDONALD, S. A. & MUMMERY, P. (2018). Three-dimensional in situ XCT characterisation and FE modelling of cracking in concrete. *Complexity*, Wiley Hindawi, 1-11.
- RINGOT, E. & BASCOUL, A. (2001). About the analysis of microcracking in concrete. *Cement and Concrete Composites*, 23(2-3), 261-266.
- RINGOT, E. (1988). Automatic quantification of microcracks network by stereological method of total projections in mortars and concretes. *Cement and Concrete Research*, 18(1), 35-43.
- ROBSON, P. (1975). The sand and gravel resources of the Thames Valley, the country around Cricklade, Wiltshire: Description of 1:25 000 resource sheets SU 09/19 and parts of SP 00/10. Mineral Assessment Report Institute of Geological Sciences, No. 18.
- SAMAHA, H. R. & HOVER, K. C. (1992). Influence of microcracking on the mass transport properties of concrete. *Materials Journal*, 89(4), 416-424.
- SANGEETHA, V., VAITHIYANATHAN, V., SIVAGAMI, R., DIVYALAKSHMI, K., JOSEPH ABRAHAM SUNDAR, K. & IFJAZ AHMED, M. (2015). Skeletonisation Approaches for Determining Paths in an Image: A Review. *Indian Journal of Science and Technology*, 8(35), 1-7.
- SAUVOLA, J. & PIETAKSINEN, M. (2000). Adaptive Document Image Binarization. *Pattern Recognition*, 33(2), 225-236
- SCHEYDT, C., & MULLER, S. (2012). Microstructure of ultra high performance concrete (UHPC) and its impact on durability. In *Proceedings of the 3rd International Symposium on UHPC and Nanotechnology for High Performance Construction Materials*, Kassel, Germany, 349-356.
- SCRIVENER, K. L. (2004). Backscattered electron imaging of cementitious microstructures: understanding and quantification. *Cement and Concrete Composites*, 26(8), 935-945.
- SHIOTANI, T., BISSCHOP, J. & VAN MIER, J. G. M. (2003). Temporal and spatial development of drying shrinkage cracking in cement-based materials. *Engineering Fracture Mechanics*, 70(12), 1509-1525.
- SOILLE, P. (2004). *Morphological Image Analysis: Principles and Applications*. Springer, 2nd Edition, Section 3.8, 63-103.
- SOROUSHIANA, P., ELZAFRANEY, M. & NOSSONI, A. (2003). Specimen preparation and image processing and analysis techniques for automated quantification of concrete microcracks and voids. *Cement and Concrete Research*, 33(12), 1949-1962.
- STOCK, S. R., IGNATIEV, K., WILKINSON, A. P., NAIK, N. & KURTIS, K. E. (2002). Sulphate attack of Portland cement studied by X-ray microtomography (micro-CT). *Advances in X-ray Analysis*, 45, 128-132.
- STUTZMAN, P. E. & CLIFRON, J. R. (1999) Specimen preparation for scanning electron microscopy. 21st International Conference on Cement Microscopy. April 25-29, Las Vegas, Nevada, USA, 10-22.
- TAZAWA, E. & MIYAZAWA, S. (1995). Influence of cement and admixture on autogenous shrinkage of cement paste. *Cement and Concrete Research*, 25(2), 281-287.

TAZAWA, E. (1998). Autogenous Shrinkage of Concrete. Proceedings of the International Workshop organized by JCI (Japan Concrete Institute). Section 3 and 4, Taylor & Francis Group, London & New York.

TAZAWA, E. (1999). Autogenous Shrinkage of Concrete. Part four: Effect of materials on autogenous shrinkage. E & FN Spon, London, 173-241.

TEMPLATE MATCHING: <https://sites.google.com/site/qingzongtseng/template-matching-ij-plugin>.

THÉVENAZ, P., RUTTIMANN, U. E. & UNSER, M. A. (1998). Pyramid approach to subpixel registration based on intensity. IEEE Transactions on Image Processing, 7(1), 27-41.

TRTIK, P., DUAL, J., MUNCH, B & HOLZER, L. (2008). Limitation in obtainable surface roughness of hardened cement paste: 'virtual' topographic experiment based on focussed ion beam nanotomography datasets. Journal of Microscopy, 232(2), 200-206.

TRTIK, P., MUNCH, B., GASSER, P., LEEMANN, A., LOSER, R., WEPF, R. & LURA, P. (2010). Focused ion beam nanotomography reveals the 3D morphology of different solid phases in hardened cement pastes. Journal of Microscopy, 241(3), 234-242.

TSAI, W. H. (1985). Moment-preserving thresholding: A new approach. Computer Vision, Graphics, and Image Processing, 29(3), 273-285.

WADELL, H. (1935). Volume, Shape and Roundness of Quartz Particles. Journal of Geology, 43(3), 250-280.

WHITE, A. H., AAGAARD, V. A. & CHRISTENSEN, A. O. L. (1928). Cracking in concrete and the growth of hair cracks into structural cracks. Journal Proceedings 24(2), 190-201.

WONG, H. S. (2006). Quantifying the pore structure of cement-based materials using backscattered electron microscopy. Imperial College London, PhD thesis.

WONG, H. S., ZOBEL, M., BUENFELD, N. R. & ZIMMERMAN, R. W. (2009). Influence of the interfacial transition zone and microcracking on the diffusivity, permeability and sorptivity of cement-based materials after drying. Magazine of Concrete Research, 61(8), 571-589.

WONG, H.S. & BUENFELD, N.R. (2006). Patch microstructure in cement-based materials: Fact or artefact? Cement and Concrete Research, 36(5), 990-997.

WU, Z. (2014). Influence of Microcracks on the Transport Properties of Concrete. PhD Thesis from Imperial College London, Department of Civil and Environmental Engineering.

WU, Z. WONG, H. S., CHEN, C. & BUENFELD, N. R. (2019). Anomalous water absorption in cement-based materials caused by drying shrinkage induced microcracks. Cement and Concrete Research, 115, 90-104.

WU, Z., WONG, H. S. & BUENFELD, N. R. (2017). Transport properties of concrete after drying-wetting regimes to elucidate the effects of moisture content, hysteresis and microcracking. Cement and Concrete Research, 98, 136-154.

WU, Z., WONG, H.S. & BUENFELD, N.R. (2015). Influence of drying-induced microcracking and related size effects on mass transport properties of concrete. Cement and Concrete Research, 68, 35-48.

YANG, Z., REN, W., SHARMA, R., MCDONALD, S. MOSTAFAVI, M., VERTYAGINA, Y. & MARROW, T. J. (2017). In-situ X-ray computed tomography characterisation of 3D fracture evolution and image-based numerical homogenisation of concrete. Cement and Concrete Composites, 75, 74-83.

YANG, Z., WEISS, W. J. & OLEK, J. (2006). Water transport in concrete damaged by tensile loading and freeze-thaw cycling. Journal of Materials in Civil Engineering, 18(3), 424-434.

YIO, M. H. N., MAC, M. J., WONG, H. S. & BUENFELD, N. R. (2015). 3D imaging of cement - based materials at submicron resolution by combining laser scanning confocal microscopy with serial sectioning. *Journal of microscopy*, 258(2), 151-169.

YIO, M. H. N., WONG, H. S. & BUENFELD, N. R. 2016. 3D Monte Carlo simulation of backscattered electron signal variation across pore-solid boundaries in cement-based materials. *Cement and Concrete Research*, 89, 320-331.

YIO, M. H. N., WONG, H. S. & BUENFELD, N. R. (2017). Representative elementary volume (REV) of cementitious materials from three-dimensional pore structure analysis. *Cement and Concrete Research*, 102, 187-202.

YIO, M. H. N., WONG, H. S. & BUENFELD, N. R. (2019). 3D pore structure and mass transport properties of blended cementitious materials. *Cement and Concrete Research*, 117, 23-37.

ZEISS BROCHURE. (2013). Resolution of a 3D X-ray microscopy. Carl Zeiss Microscopy.

ZHANG, J. & SCHERER, G. W. (2011). Comparison of methods for arresting hydration of cement. *Cement and Concrete Research*, 41(10), 1024-1036.

ZHUTOVSKY, S. & KOVLER, K. (2012). Effect of internal curing on durability-related properties of high performance concrete. *Cement and Concrete Research*, 42(1), 20-26.

ZHUTOVSKY, S., KOVLER, K. & BENTUR, A. (2013). Effect of hybrid curing on cracking potential of high-performance concrete. *Cement and Concrete Research*, 54, 36-42.

Appendices

APPENDIX I: Microcrack width - cumulative distribution curves (Chapter 7)

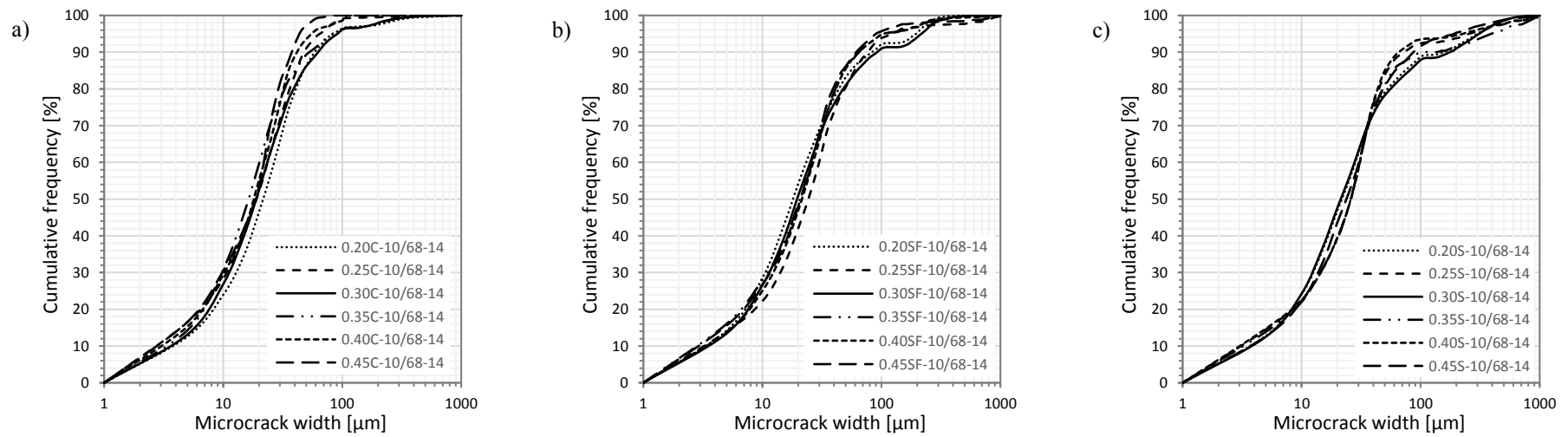


Figure I- 1 Cumulative distribution of microcrack width in concretes with different w/b ratios (0.20, 0.25, 0.30, 0.35, 0.40, 0.45) and a) Portland cement (C), b) silica fume (SF) and c) GGBS (S) as binders.

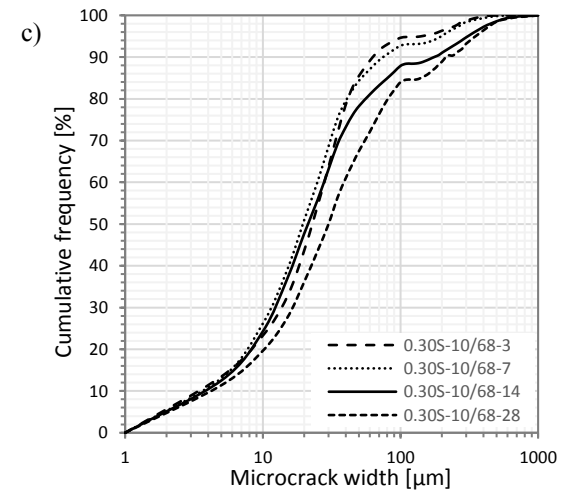
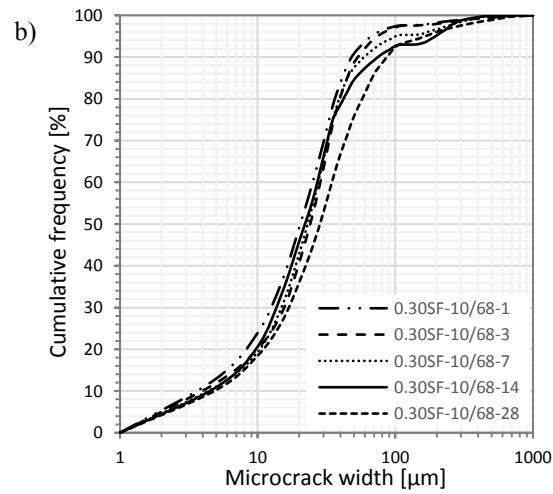
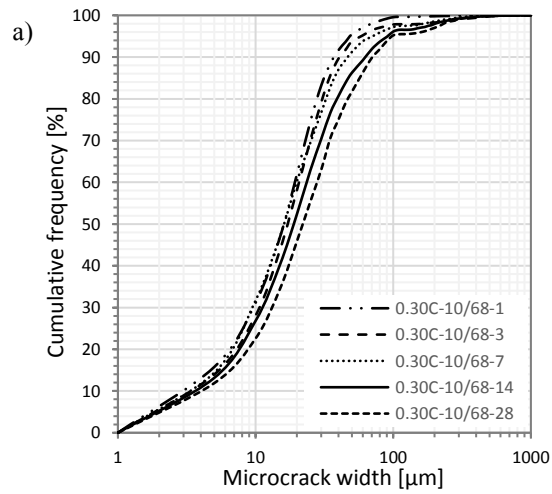


Figure I-2 Cumulative distribution of microcrack width in concretes at different ages (1, 3, 7, 14 and 28 days) and a) Portland cement (C), b) silica fume (SF) and c) GGBS (S) as binders.

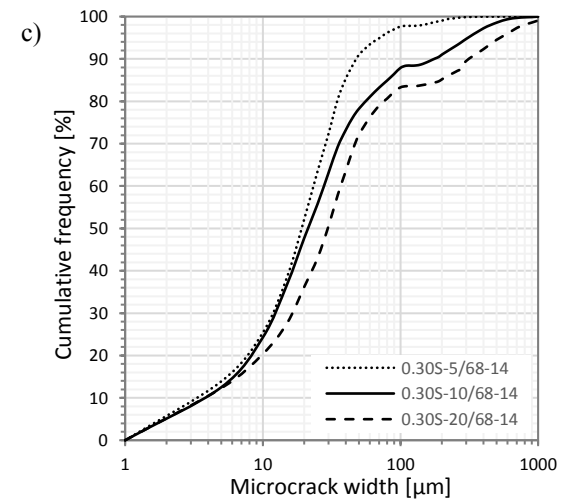
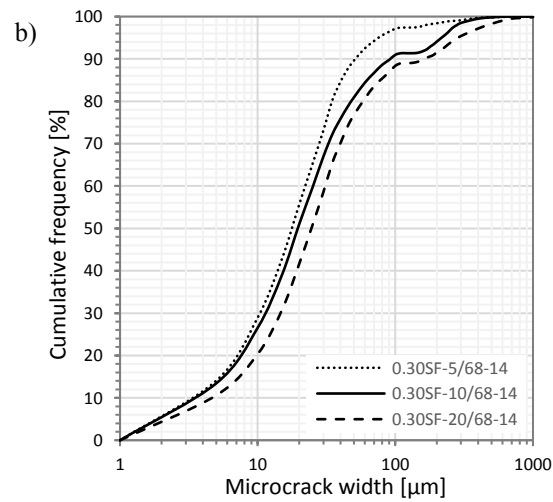
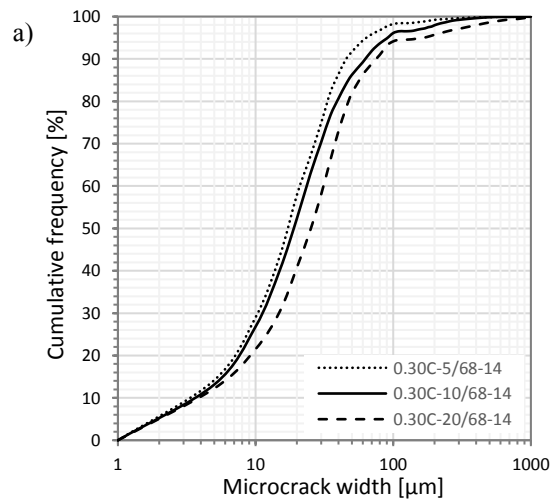


Figure I-3 Cumulative distribution of microcrack width in concretes with different MSA (5 mm, 10mm, 20 mm) and a) Portland cement (C), b) silica fume (SF) and c) GGBS (S) as binders.

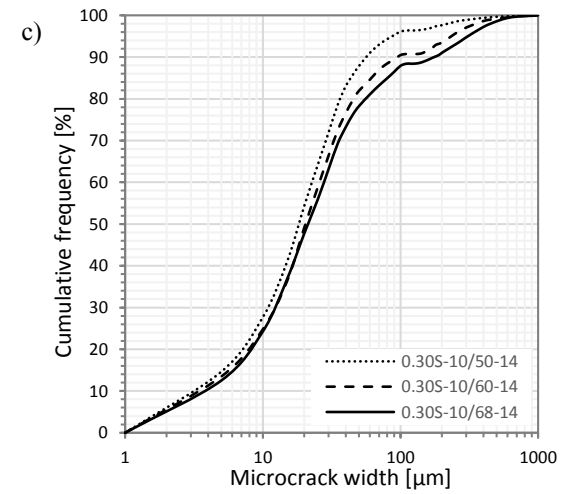
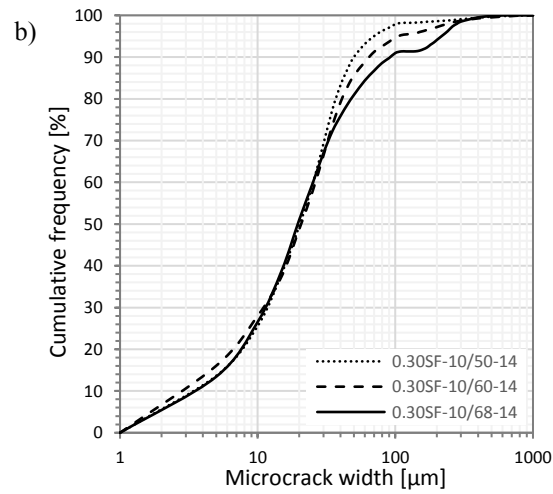
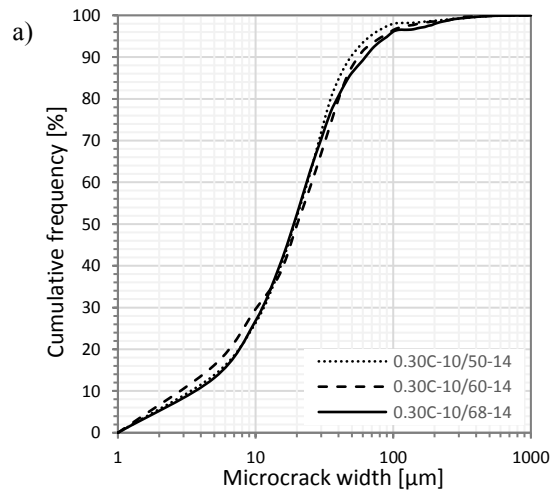


Figure I-4 Cumulative distribution of microcrack width in concretes with different aggregate fraction (50%, 60%, 68%) and a) Portland cement (C), b) silica fume (SF), c) GGBS (S) as binders.

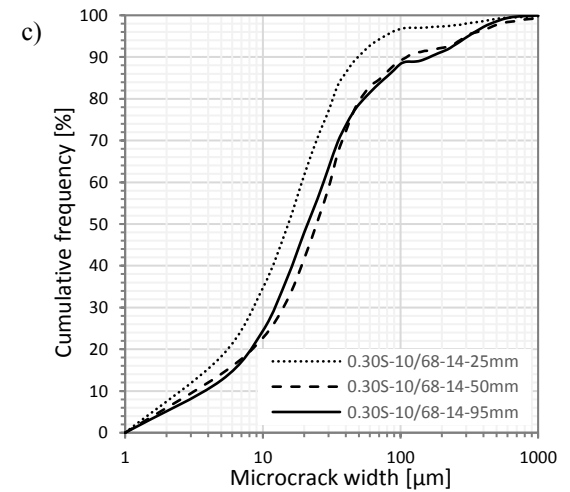
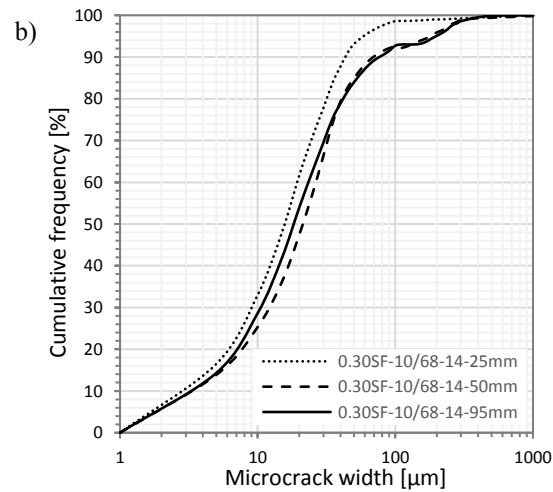
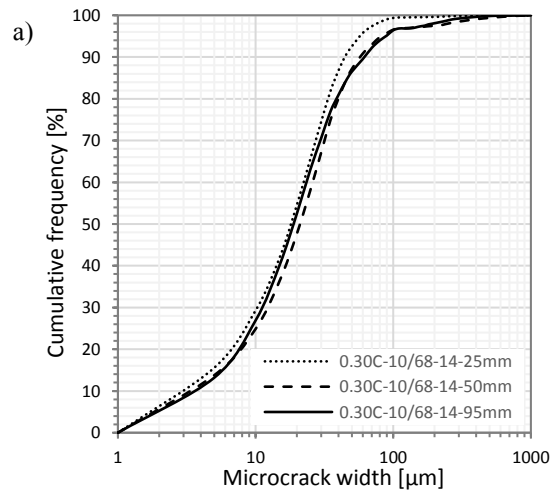


Figure I-5 Cumulative distribution of microcrack width in concretes with different sample sizes (Ø25 mm, Ø50 mm, Ø95 mm) and a) Portland cement (C), b) silica fume (SF) and c) GGBS (S) as binders.

APPENDIX II: Microcrack length - cumulative distribution curves (Chapter 7)

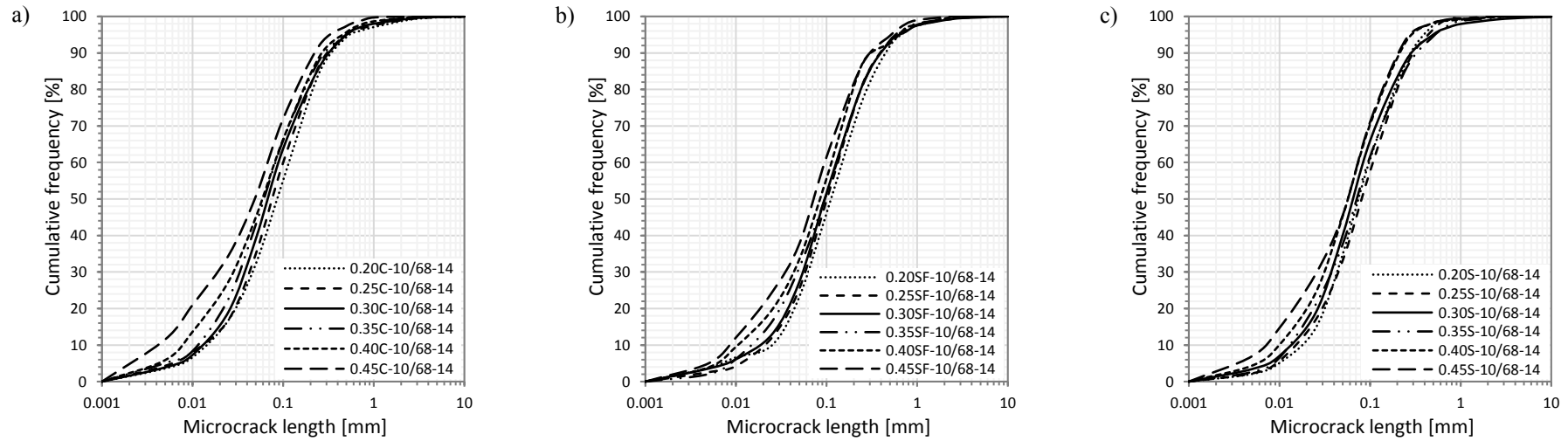


Figure II-1 Cumulative distribution of microcrack length in concretes with different w/b ratio (0.20, 0.25, 0.30, 0.35, 0.40 and 0.45) and a) Portland cement (C), b) silica fume (SF) and c) GGBS (S) as binders.

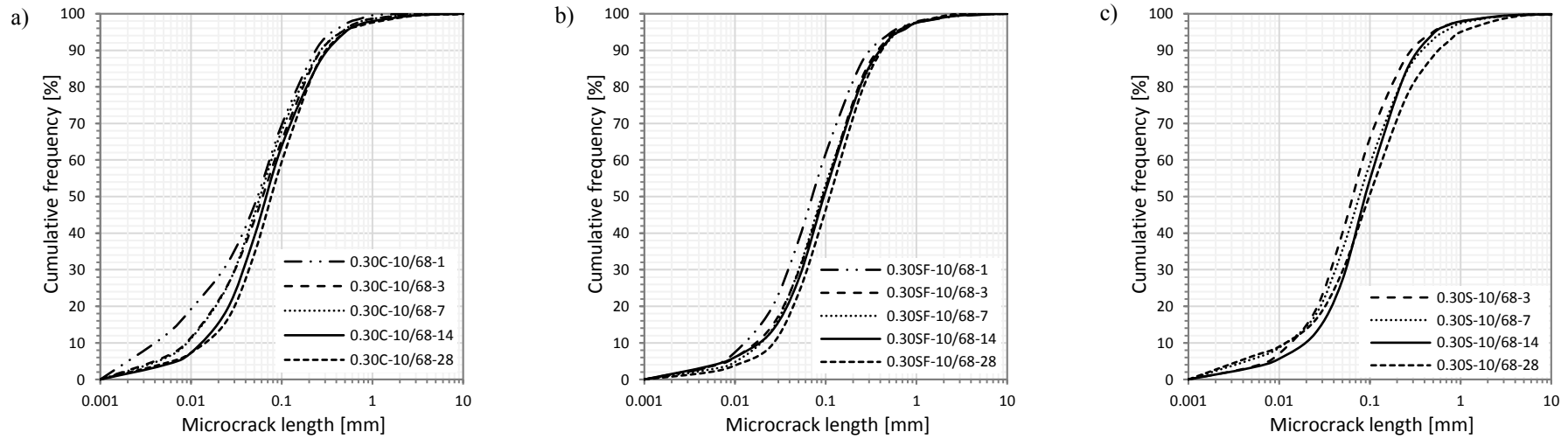


Figure II-2 Cumulative distribution of microcrack length in concretes at different ages (1, 3, 7, 14 and 28 days) and a) Portland cement (C), b) silica fume (SF) and c) GGBS (S) as binders.

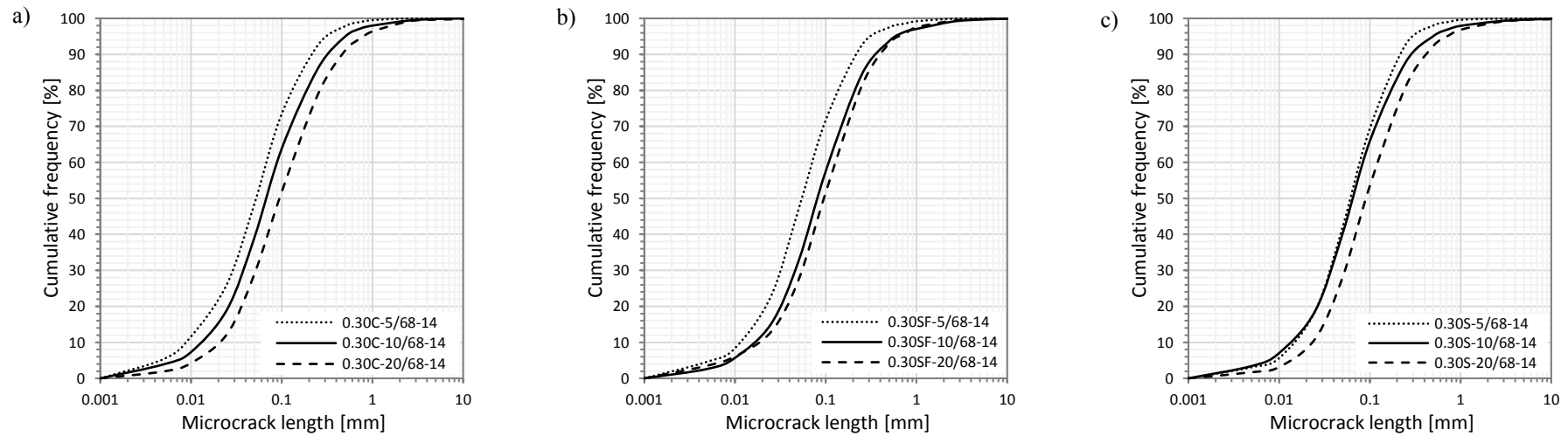


Figure II-3 Cumulative distribution of microcrack length in concretes with different MSA (5, 10 and 20 mm) and a) Portland cement (C), b) silica fume (SF) and c) GGBS (S) as binders.

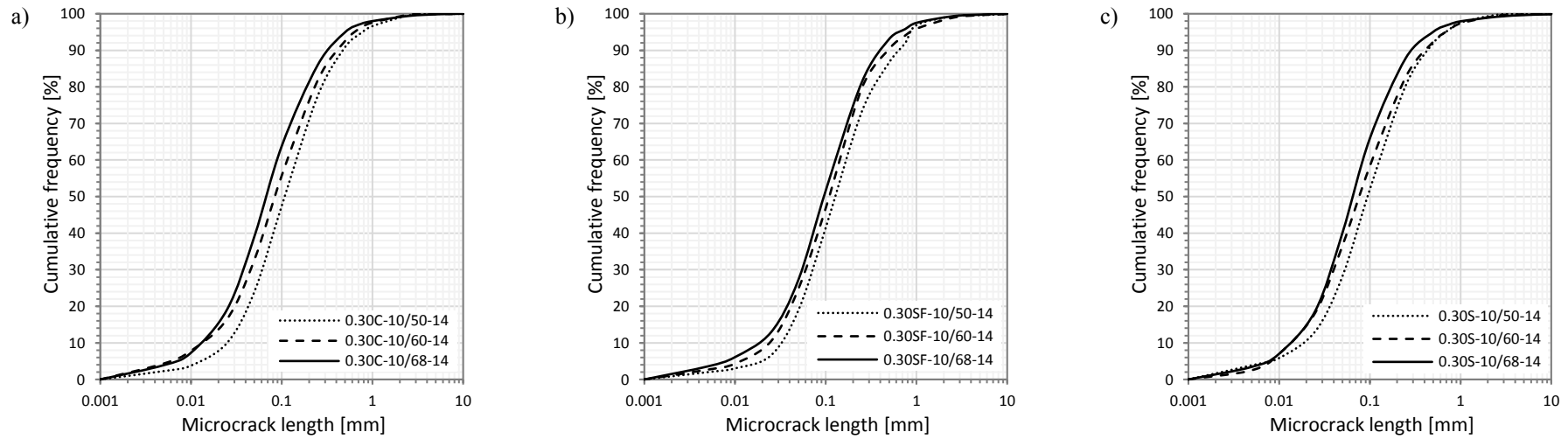


Figure II-4 Cumulative distribution of microcrack length in concretes with different volume fraction of aggregates (50%, 60% and 68%) and a) Portland cement (C), b) silica fume (SF), c) GGBS (S) as binders.

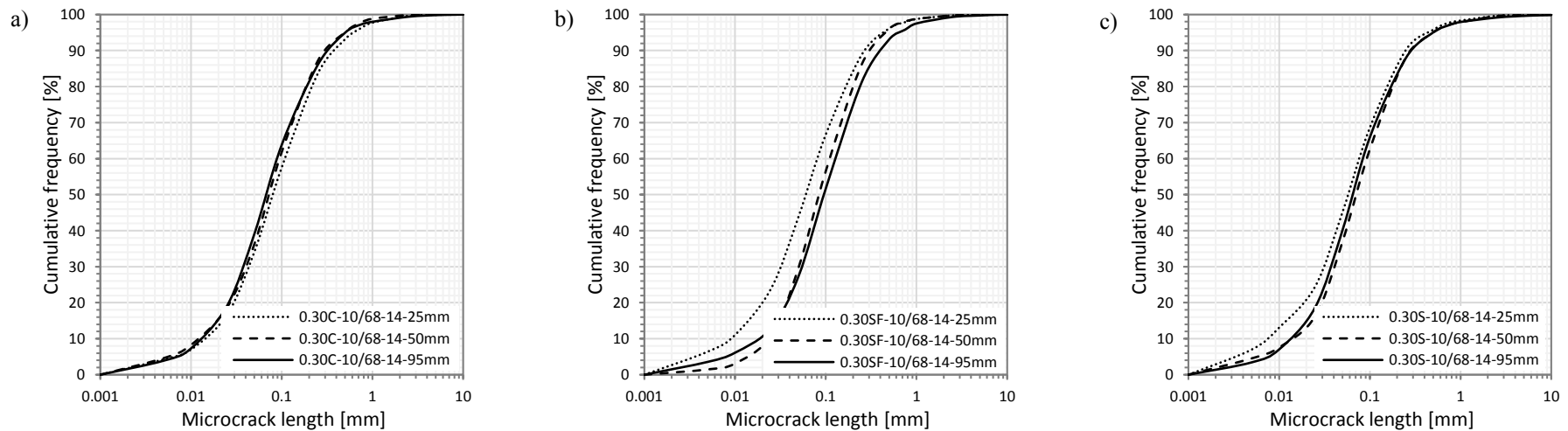
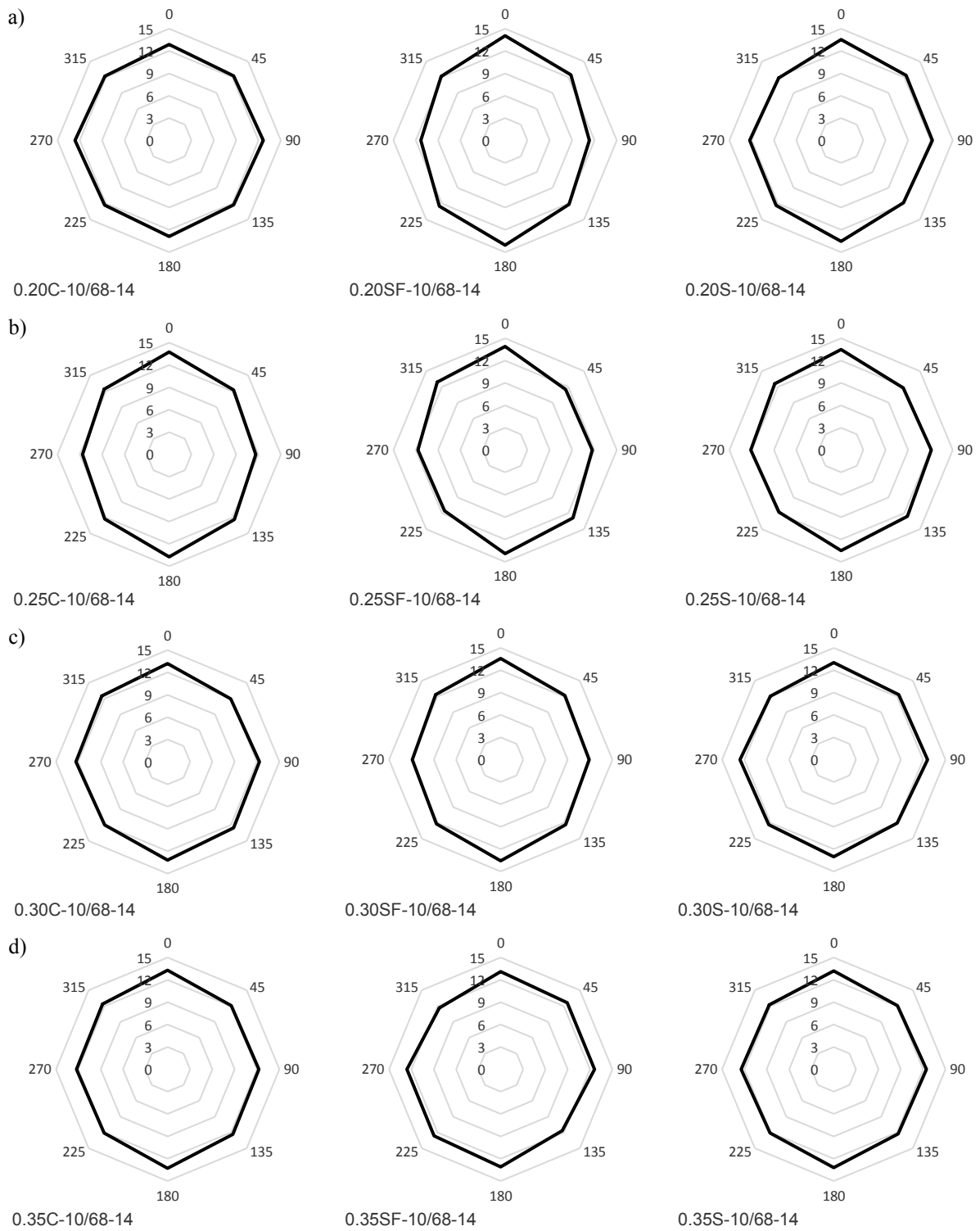


Figure II-5 Cumulative distribution of microcrack length in concretes with different sample size (25, 50 and 95 mm diameter) and a) Portland cement (C), b) silica fume (SF) and c) GGBS (S) as binders.

APPENDIX III: 2D orientation of microcracks induced by autogenous shrinkage (Chapter 7)



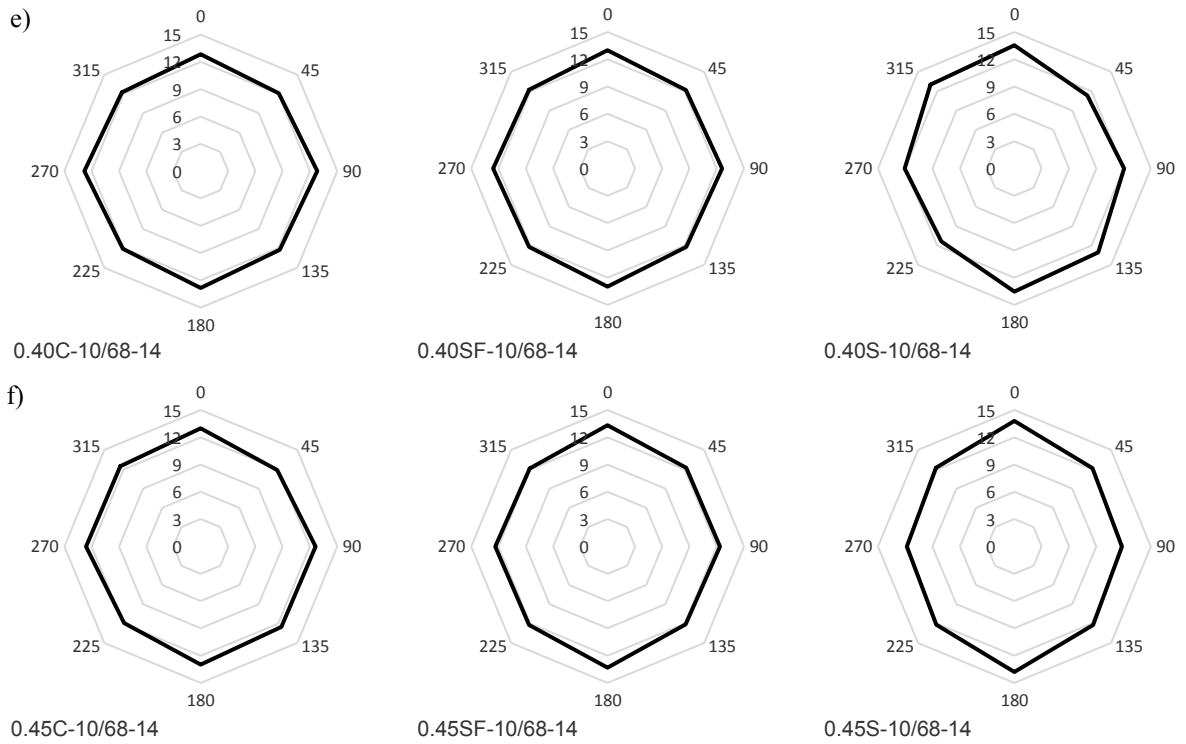
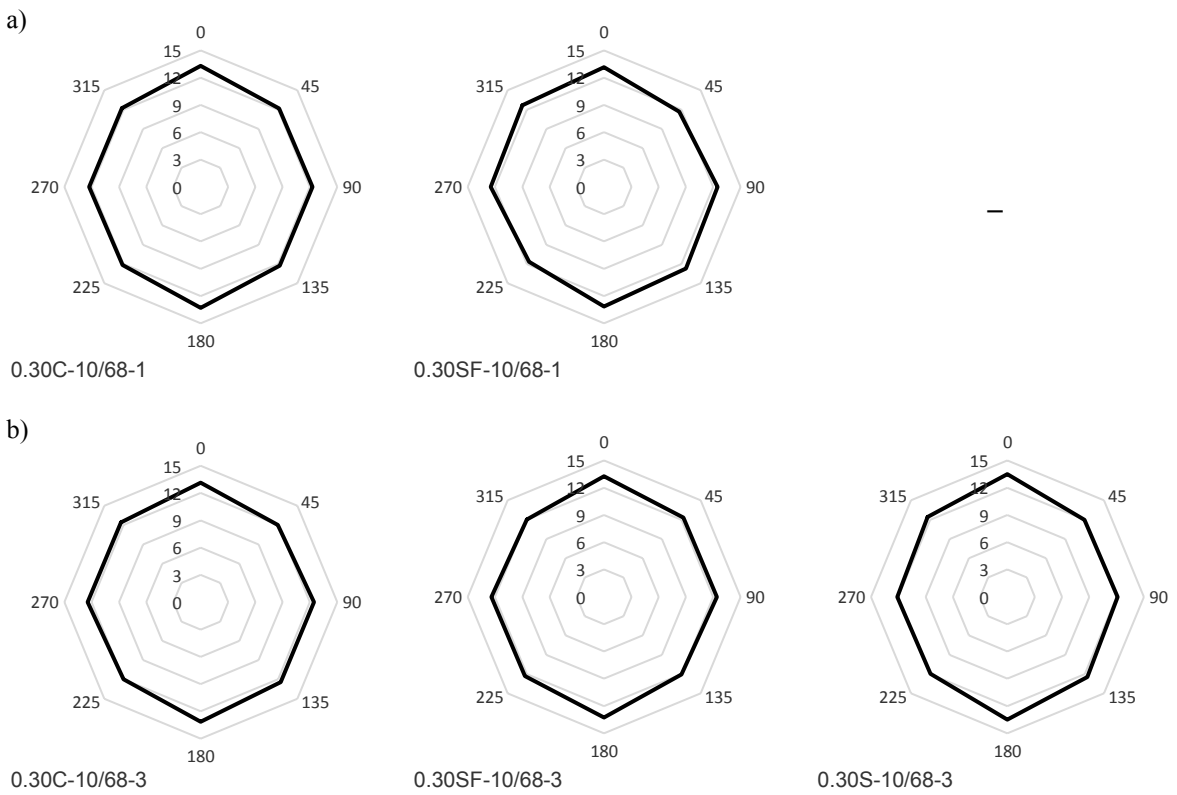


Figure III-1 Orientation of microcracks in concretes with different binders and w/b ratio of a) 0.20, b) 0.25 c) 0.30, d) 0.35, e) 0.40 and f) 0.45, presented by means of rose of intercepts at 0°, 45° 90° and 135°.



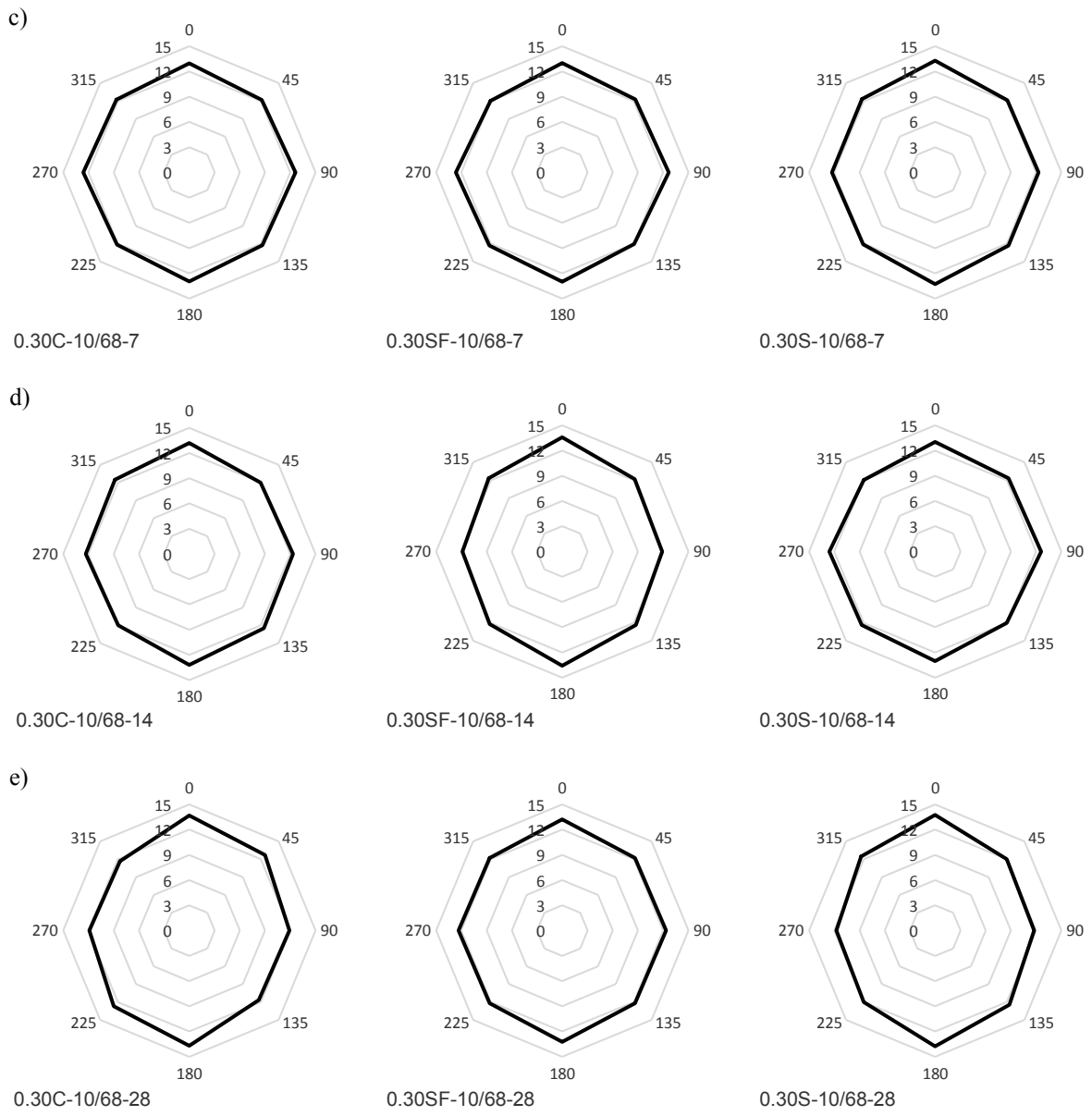


Figure III-2 Orientation of microcracks in concretes with different binders at age of a) 1 day, b) 3 days c) 7 days, d) 14 days and e) 28 days, presented by means of rose of intercepts at 0°, 45°, 90° and 135°.

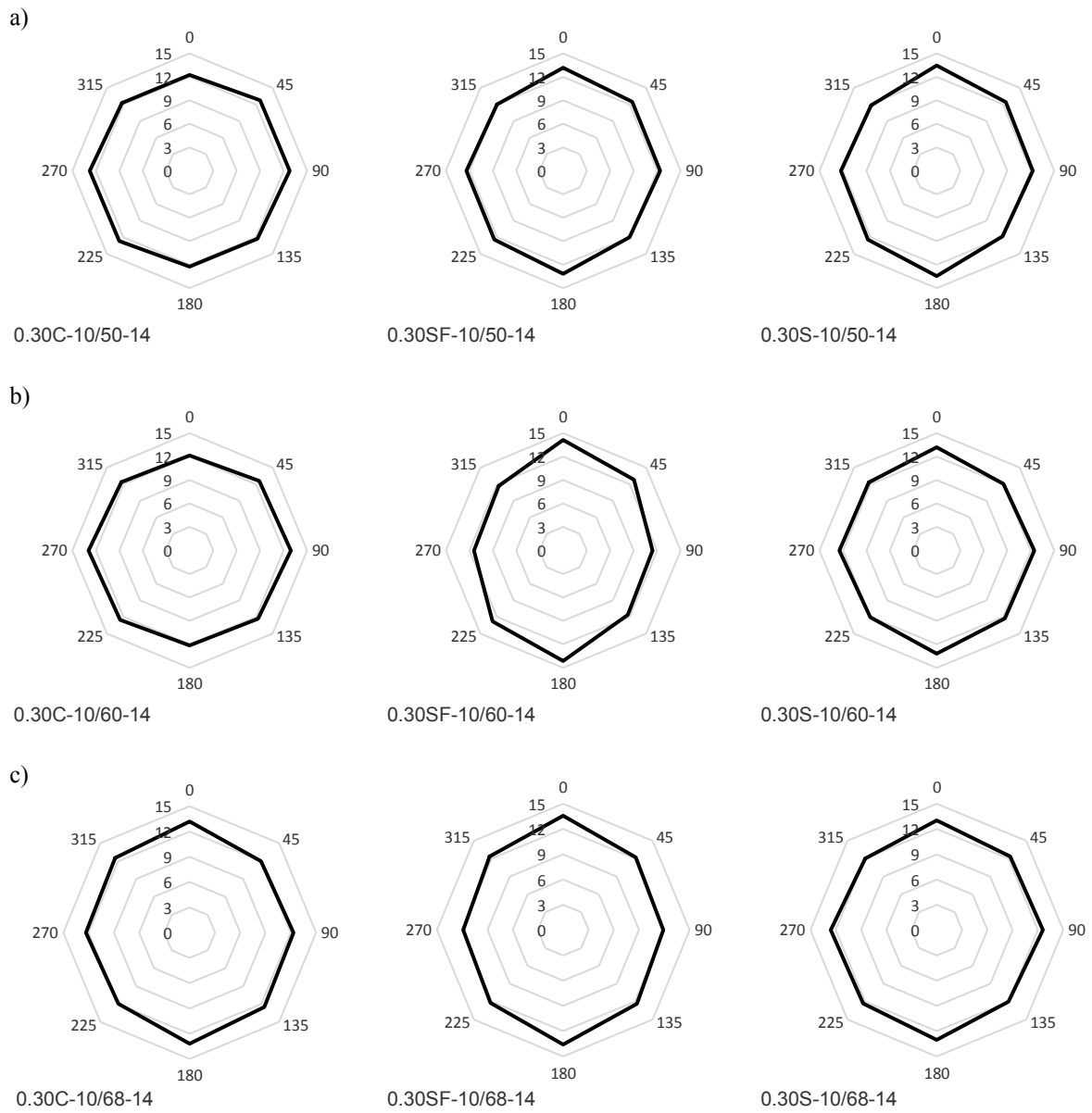


Figure III-3 Orientation of microcracks in concretes with different binders and aggregate volume fraction of a) 50%, b) 60% and c) 68%, presented by means of rose of intercepts at 0°, 45° 90° and 135°.

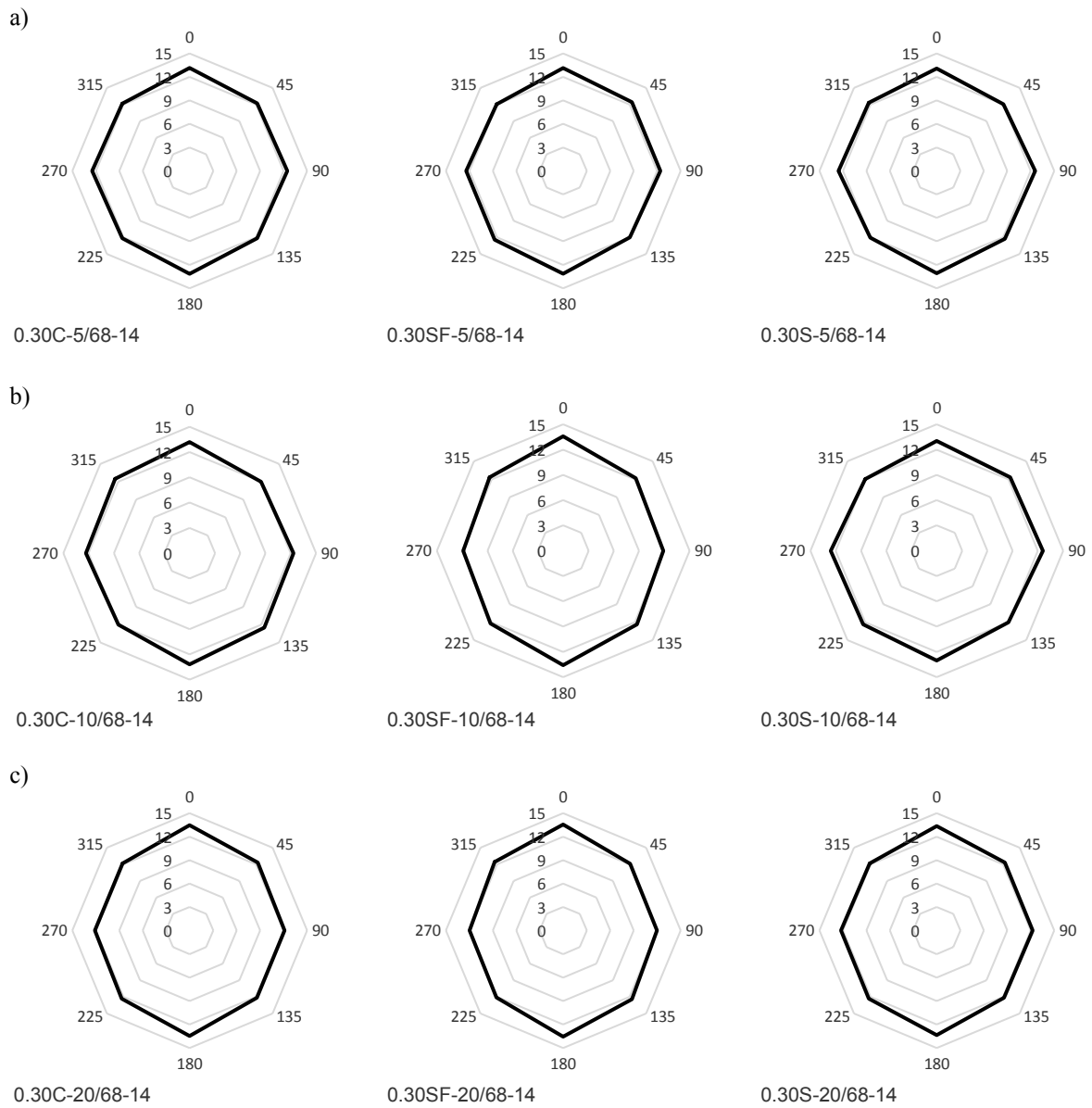


Figure III-4 Orientation of microcracks in concretes with different binder types and MSA of a) 5 mm, b) 10 mm and c) 20 mm, presented by means of rose of intercepts at 0°, 45° 90° and 135°.

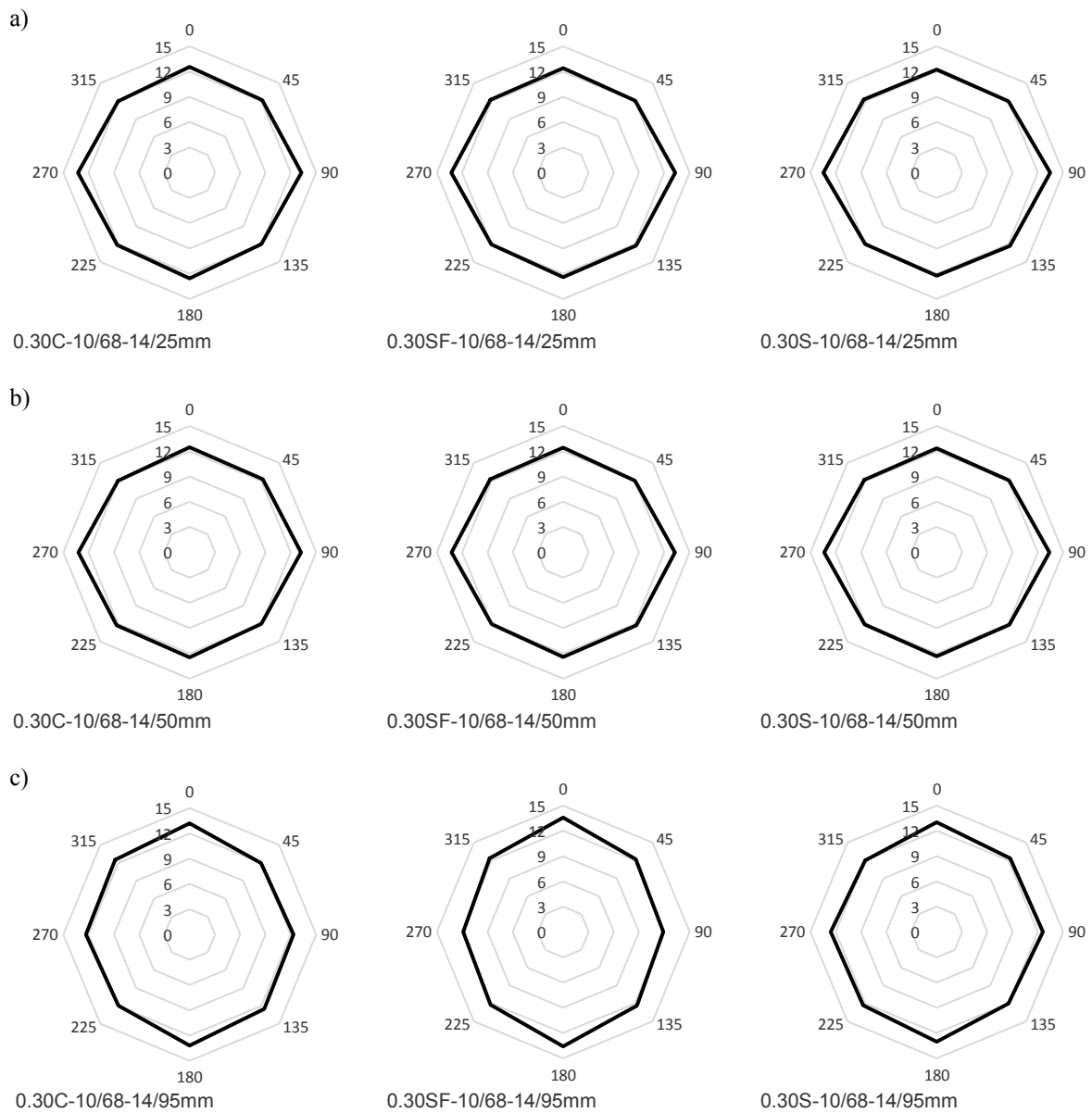


Figure III-5 Orientation of microcracks in concretes with different binders and sample sizes of a) 25 mm, b) 50 mm and c) 95 mm in diameter, presented by means of rose of intercepts at 0°, 45° 90° and 135°.

APPENDIX IV: 3D orientation of microcracks induced by autogenous shrinkage (Chapter 8)

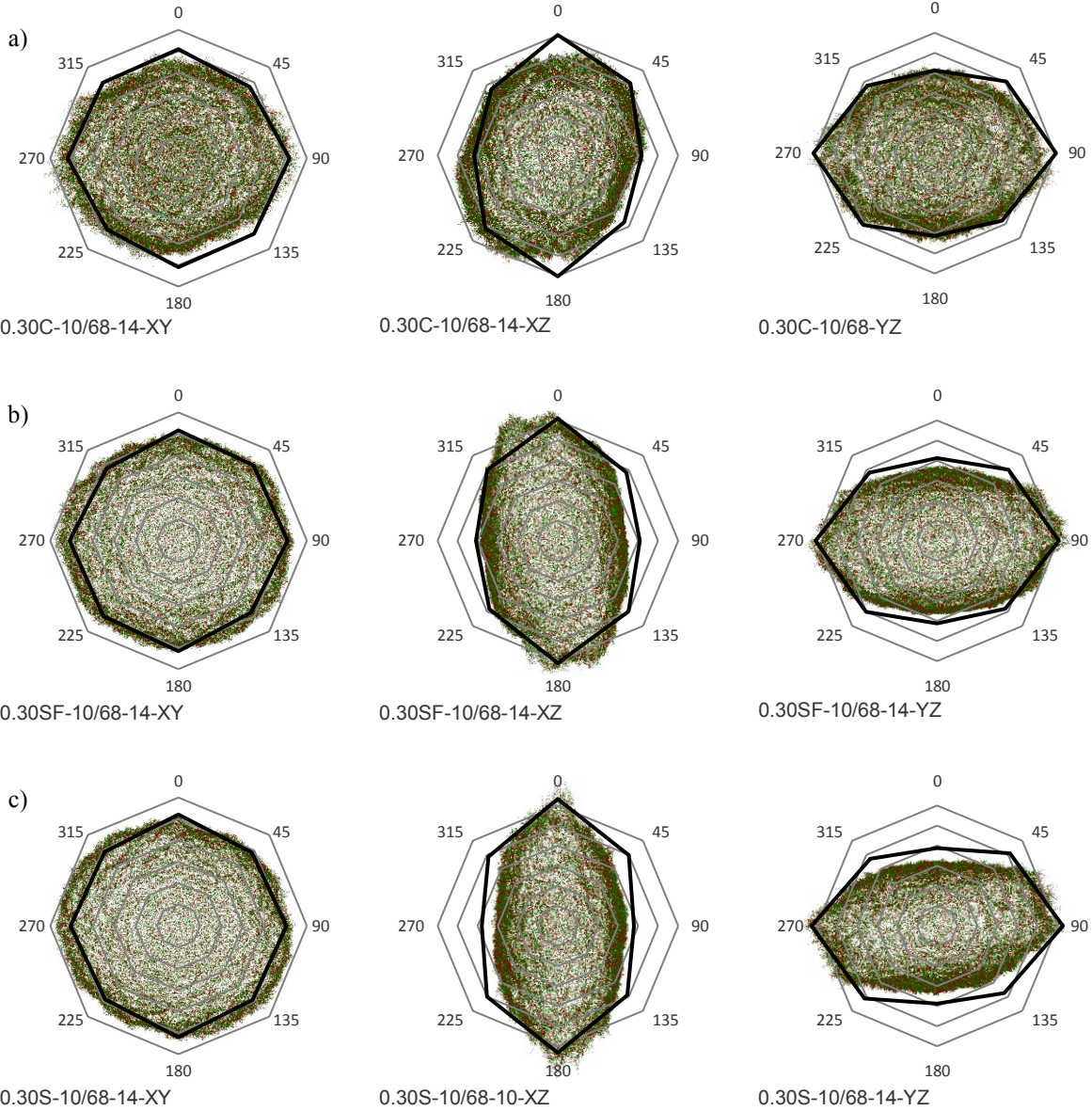
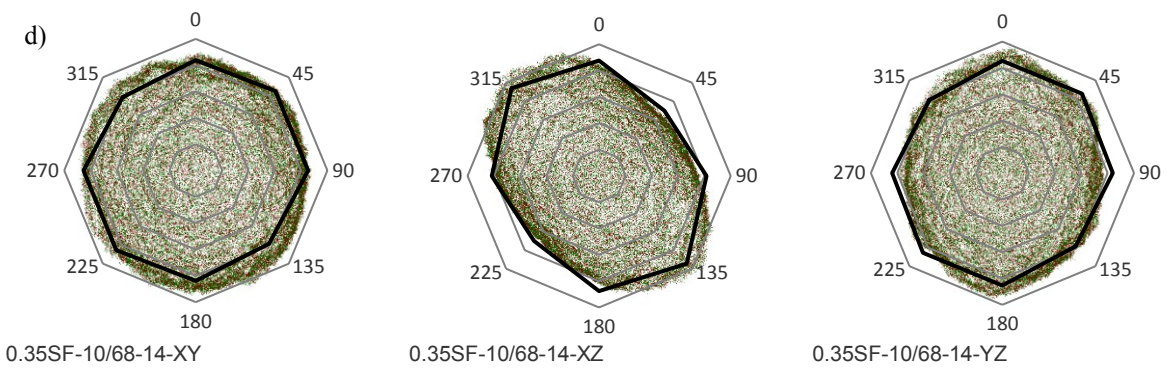
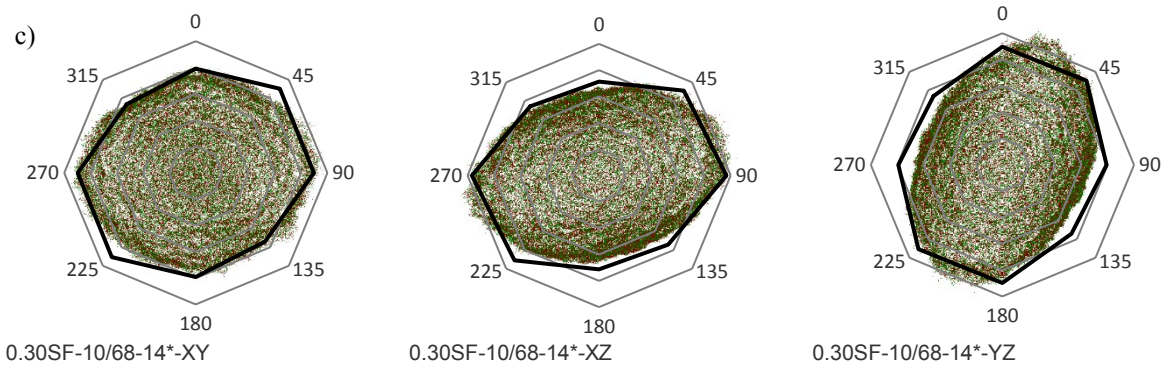
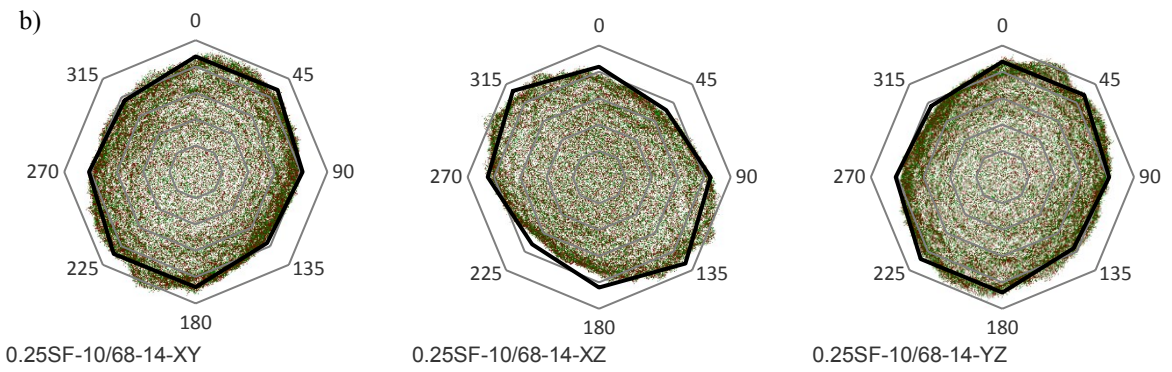
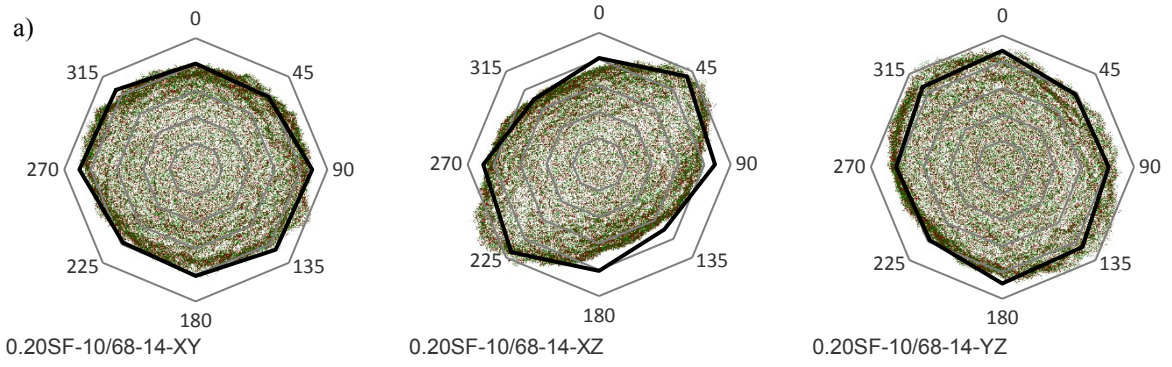


Figure IV-1 Orientation of microcracks in concretes with three different binders: a) 0.30C-10/68-14, b) 0.30SF-10/68-14- (binder replica), c) 0.30S-10/68-14 presented in 2D by means of rose of intercepts at 0°, 45° 90° and 135° angle (black lines) and 3D visualisation of the MIL vector cloud in XY, XZ and YZ directions.



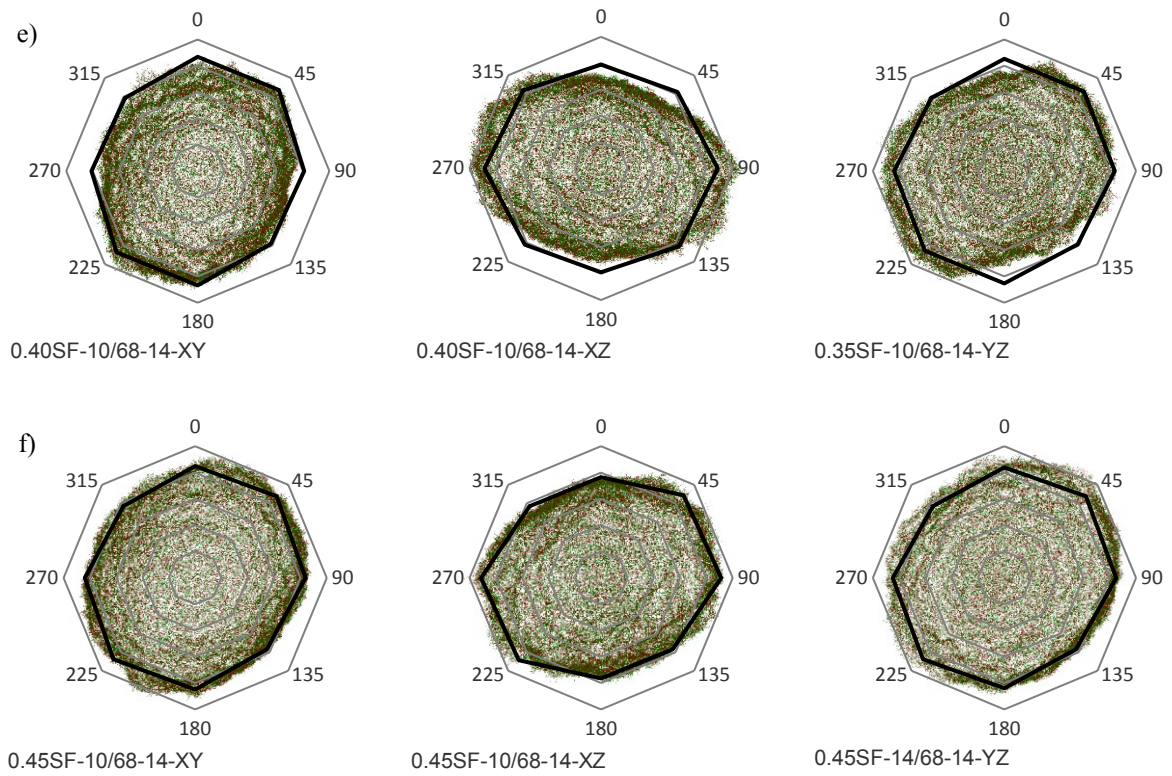
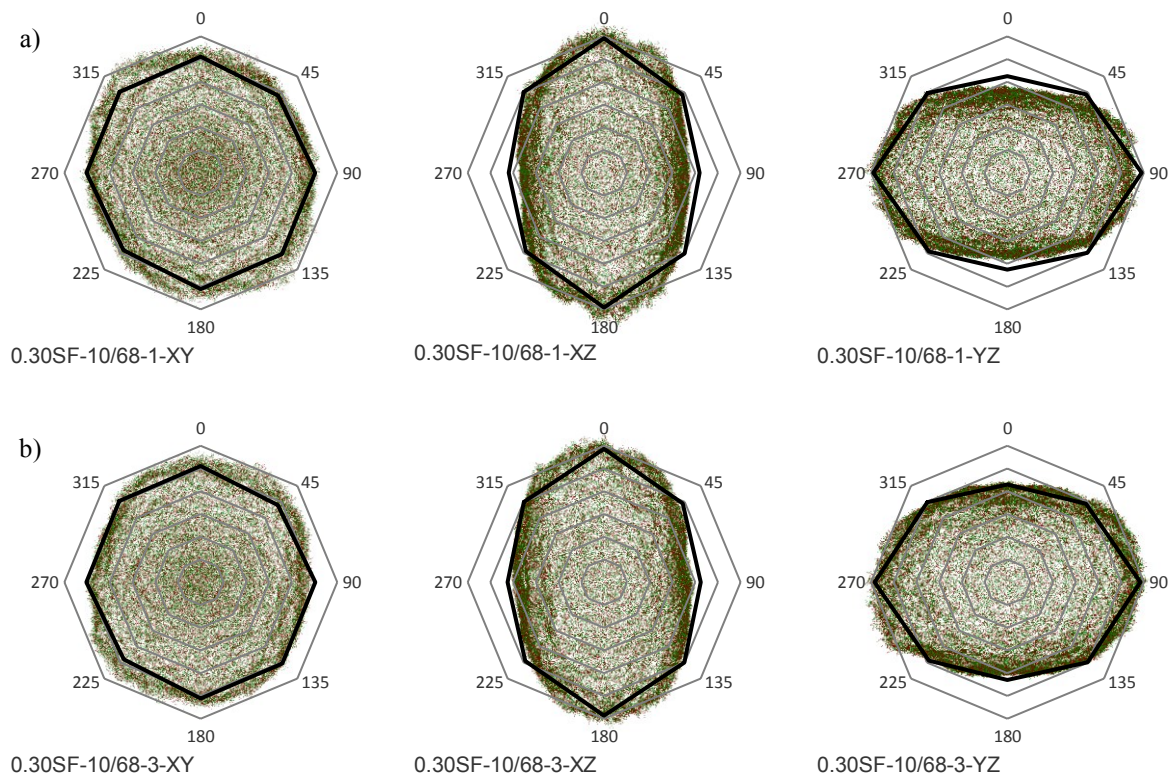


Figure IV-2 Orientation of microcracks in concretes with different water to binder ratios: a) **0.20SF-10/68-14**, b) **0.25SF-10/68-14**, c) **0.30SF-10/68-14**- (w/b ratio replica), d) **0.35SF-10/68-14**, e) **0.40SF-10/68-14** and f) **0.45SF-10/68-14** presented in 2D by means of rose of intercepts at 0°, 45° 90° and 135° angle (black lines) and 3D visualisation of the MIL vector cloud in XY, XZ and YZ directions.



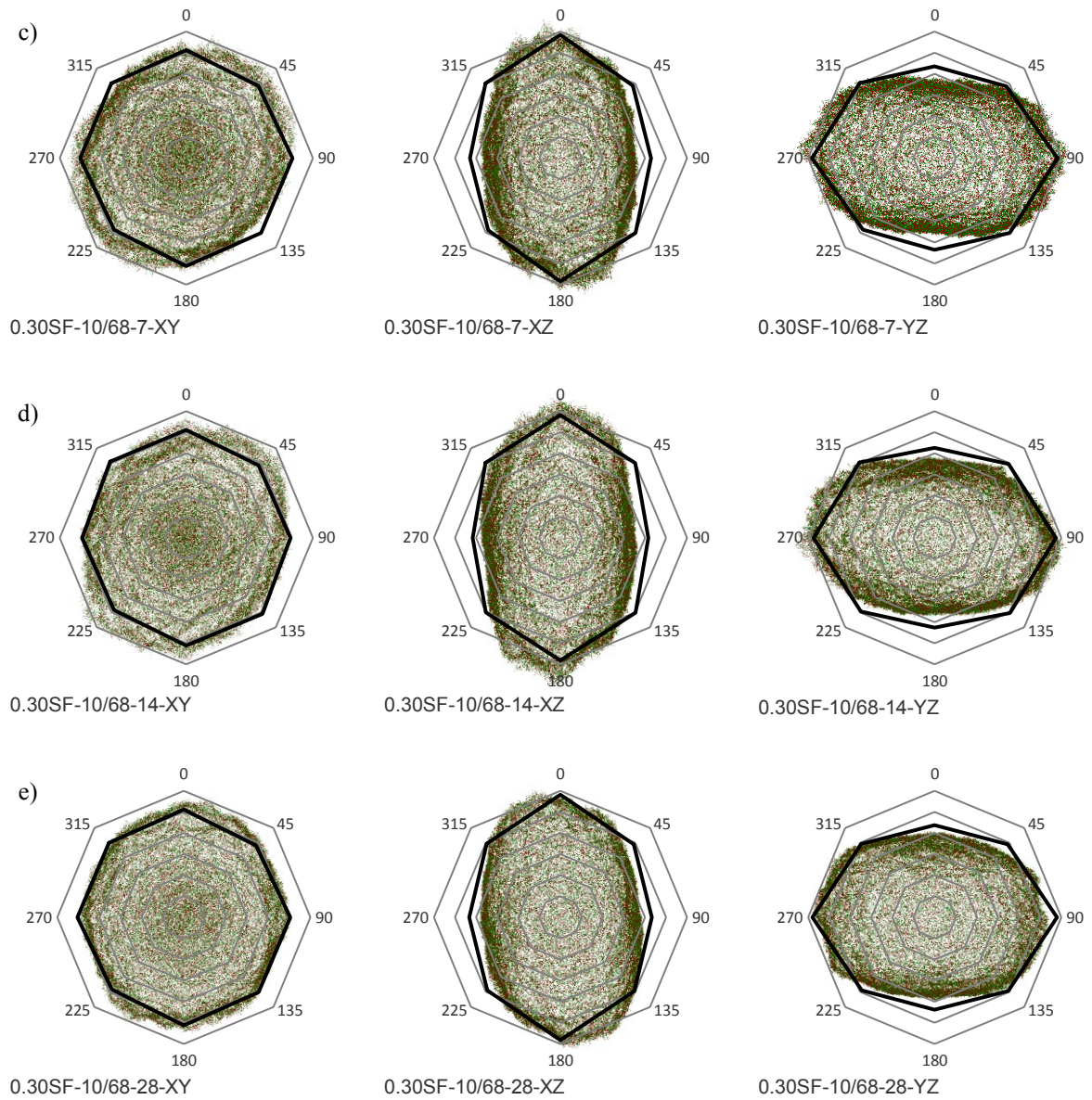


Figure IV-3 Orientation of microcracks in concretes at different ages:
 a) 0.30SF-10/68-1, b) 0.30SF-10/68-3, c) 0.30SF-10/68-7, d) 0.30SF-10/68-14-(age replica) and
 e) 0.30SF-10/68-28 presented in 2D by means of rose of intercepts at 0°, 45° 90° and 135° angle (black lines)
 and 3D visualisation of the MIL vector cloud in XY, XZ and YZ directions.

APPENDIX V: Publications arising from this research

Journal papers

M.H.N. Yio, M.J. Mac, H.S. Wong, N.R. Buenfeld, 3D imaging of cement-based materials at submicron resolution by combining laser scanning confocal microscopy with serial sectioning, *Journal of Microscopy*, 258 (2015) 151–169.

M.J. Mac, M.H.N. Yio, G. Desbois, I. Casanova, H.S. Wong, N.R. Buenfeld, 3D imaging of microcracks in cementitious materials, (under preparation for *Journal of Microscopy*)

M.J. Mac, H.S. Wong, N.R. Buenfeld, 3D characterisation of autogenous shrinkage induced microcracks in concrete containing supplementary cementitious materials, (under preparation for *Cement and Concrete Research*)

Conference proceedings

M. Mac, G. Desbois, P. Pardo, I. Casanova, Ion beam tomography of the nano- and microstructure of cementitious materials. International Symposium on Nanotechnology in Construction (NICOM 4th), Agios Nikolaos, Crete, Greece, May 20, 2012.

Z. Wu, M.J. Mac, H.S. Wong, N.R. Buenfeld, Characterisation of microcracks and their influence on transport properties of concrete, TRANSCEND Conference: Water transport in cementitious materials, 2013 November 3-6, Guildford, UK.